



# TECHNICAL REPORTS

## 29



Determination of the methane budget of the  
Amazon region utilizing airborne methane  
observations in combination with atmospheric  
transport and vegetation modeling

by  
Veronika Beck



## Technical Reports - Max-Planck-Institut für Biogeochemie 29, 2012

Max-Planck-Institut für Biogeochemie  
P.O.Box 10 01 64  
07701 Jena/Germany  
phone: +49 3641 576-0  
fax: + 49 3641 577300  
<http://www.bgc-jena.mpg.de>



## Technical Reports - Max-Planck-Institut für Biogeochemie 29, 2012

Max-Planck-Institut für Biogeochemie  
P.O.Box 10 01 64  
07701 Jena/Germany  
phone: +49 3641 576-0  
fax: + 49 3641 577300  
<http://www.bgc-jena.mpg.de>

Determination of the methane budget of the  
Amazon region utilizing airborne methane  
observations in combination with atmospheric  
transport and vegetation modeling

**Dissertation**

zur Erlangung des akademischen Grades doctor rerum naturalium  
(Dr. rer. nat)

durchgeführt am Max-Planck-Institut für Biogeochemie  
vorgelegt dem Rat der Chemisch-Geowissenschaftlichen Fakultät  
der  
Friedrich-Schiller-Universität Jena



von Dipl. Phys. Veronika Beck  
geboren am 12. Januar 1983  
in Aalen/Ostalbkreis

Gutachter:

1. Dr. habil. Christoph Gerbig, Max-Planck-Institut für Biogeochemie
2. Prof. Dr. Kai-Uwe Totsche, Institut für Hydrogeologie

Tag der öffentlichen Verteidigung: 17. Oktober 2012

## Abstract

The Amazon basin is an important player in the global methane cycle, because of its huge amount of wetland area. To estimate the future impact of climate change on the methane emissions in the Amazon basin, a thorough understanding of the underlying processes is required. However, observations of methane are still sparse in the Amazon basin and only available on the local scale. Satellite observations have global coverage, but only limited accuracy. For an entire understanding of the processes in the Amazon basin, high-resolution observations at the regional scale are essential.

Within the Balanço Atmosférico Regional de Carbono na Amazônia project (BARCA) two airborne measurement campaigns were conducted in the Amazon basin, one at the end of the dry season in November 2008 and one at the end of the wet season in May 2009. For the first time in the Amazon basin, continuous measurements of methane onboard an aircraft were obtained during the second campaign. In total almost 400 flasks were collected during both campaigns and analyzed for methane in the gas lab.

To quantify the source strength of the Amazon basin, three different methods were used within this work: (1) minimization of the difference between BARCA methane observations and global methane inversions; (2) high-resolution forward simulations with the Greenhouse Gas model coupled to the Weather Research and Forecasting model WRF (WRF-GHG) using combinations of two different wetland models and three different wetland inundation maps; (3) regional methane inversion utilizing observations from the 35 m high TT34 tower in the central Amazon basin.

WRF-GHG was developed within this work to perform high-resolution simulations of atmospheric methane over the Amazon basin. It includes online calculation of biospheric methane fluxes from wetlands, termites, and soil uptake. The already existing model for the online calculation of biospheric carbon dioxide fluxes and a plumerise model were also integrated in WRF-GHG. The code is part of the official WRF-Chem V3.4 release from spring 2012 onwards.

The comparison of flask and continuous observations obtained from the two BARCA campaigns with background measurements made at three tower stations confirmed that the Amazon basin is a strong source of methane. The atmospheric methane mixing ratio in the Amazon basin was found to be lower at the end of the dry season in November 2008 ( $1817 \pm 39$  ppb in the planetary boundary layer and  $1794 \pm 12$  ppb in the lower free troposphere) compared to the end of the wet season in May 2009 ( $1841 \pm 37$  ppb and  $1806 \pm 38$  ppb, respectively). Isotope analysis in the flask samples identified the main methane source component to be biogenic. Anthropogenic emissions from major cities in the Amazon basin, e.g. Manaus were also determined to have biogenic origin. Comparisons of the BARCA observations to global methane inversions illustrate the benefit of satellite observations in inversion systems. From the minimized model-observation mismatch the monthly budget for the Amazon lowland region was derived to  $5.7 \pm 0.7$  for November 2008 and  $6.9 \pm 1.1$  Tg for May 2009.

High-resolution methane simulations over the Amazon were performed for the two months of the BARCA campaigns using WRF-GHG. Four simulations with combinations of two different

wetland models (Kaplan, Walter) and three different wetland inundation maps (Kaplan, JERS-1SAR, Prigent) were carried out. The modeled methane mixing ratios were adjusted to match the mean of the corresponding observations for selected flights with a good representation of the atmospheric transport in the model during the second campaign. Comparisons to BARCA observations indicate that the location of a particular wetland is more important than its actual emission strength in representing airborne observations. Flights, for which the WRF-Chem model showed a good representation of the convective transport, matched the observations better compared to flights with a poorer representation of the atmospheric transport in the model. Budget estimates for the Amazon lowland region from the WRF-GHG simulations were derived to  $3.9 \pm 0.8$  Tg for November 2008 and  $4.0 \pm 0.8$  Tg for May 2009.

A regional methane inversion utilizing the Jena two-step inversion system TM3-STILT was conducted for the entire year 2009 with three different a-priori methane flux distributions and observations from the TT34 tower 60 km north-west of Manaus. The Walter wetland model (with different meteorological forcing) and the JERS-1SAR and Prigent wetland inundation map were used. Differences originating from different meteorological forcing were found to be small for the Amazon mainstream area. Locally, differences up to 50 ppb occurred in the simulated atmospheric methane mixing ratios, which could be traced back to differences in the soil temperature. Explanations for a 25 ppb mean difference in the simulated atmospheric methane mixing ratio at the TT34 tower from simulations using two different regional atmospheric transport models (WRF and STILT) were found in the simulated atmospheric background mixing ratio, the height of the planetary boundary layer, and the convective parametrization. The regional inversion demonstrated improvements in the representation of the seasonality of the methane emissions in the Amazon basin. However, observations from one single 35 m tower were not sufficient enough to constrain the methane fluxes in the entire Amazon basin. Budget estimates from the regional inversions are calculated to  $1.9 \pm 0.02$  Tg and  $4.4 \pm 0.01$  Tg for the Amazon lowland region in May 2009 and to  $24.9 \pm 0.5$  Tg and  $61.2 \pm 0.8$  Tg for 2009 depending on the choice of the a-priori flux distribution.

## Zusammenfassung

Das Amazonasgebiet ist aufgrund seiner großen Feuchtgebiete (sogenannten „Wetlands“) ein wichtiger Bestandteil des globalen Methankreislaufes. Um den Effekt des Klimawandels auf die Methanemissionen im Amazonasgebiet für die Zukunft besser abschätzen zu können, ist ein tiefergehendes Verständnis der beteiligten Prozesse vonnöten. Beobachtungen von Methanflüssen oder atmosphärischen Mischungsverhältnissen von Methan sind jedoch nur sehr spärlich und auf wenige Stellen begrenzt im Amazonasgebiet vorhanden. Satellitenbeobachtungen stehen hingegen weltweit zur Verfügung. Sie besitzen jedoch meistens nur eine grobe Auflösung. Für ein vollständiges Verständnis der Methanemissions-Prozesse im Amazonasgebiet sind räumlich und zeitlich hochaufgelöste Beobachtungen von Methanmischungsverhältnissen auf regionaler Skala unerlässlich.

Innerhalb des Projektes BARCA (Balanço Atmosférico Regional de Carbono na Amazônia) wurden zwei Flugzeugmesskampagnen im Amazonasgebiet durchgeführt, eine im November 2008 zum Ende der Trockenperiode (BARCA-A) und eine weitere im Mai 2009 am Ende der Regenzeit (BARCA-B). Während der zweiten Flugkampagne wurden zum ersten Mal kontinuierliche Methanmessungen auf einem Flugzeug im Amazonasgebiet durchgeführt. Es wurden jeweils ca. 200 Luftproben genommen und im Gaslabor auf Methan hin analysiert.

Die Hauptaufgabe der vorliegenden Arbeit bestand im Aufbau eines regionalen Vorwärts- und Inversionsmodellsystems zur Bestimmung der Methanbilanz in tropischen Regionen, z.B. dem Amazonasgebiet. Da die Zahl der Methanbeobachtungen in den Tropen, speziell im Amazonasgebiet, durch neue Messtürme und Flugzeugkampagnen in den nächsten Jahren stark ansteigen wird, ist diese Arbeit auch als eine Art „Benchmark-Studie“ für die zukünftige Anwendung von regionalen Vorwärts- und Inversionsmodellsystemen in den Tropen zu verstehen.

Um die Methanemissionen im Amazonasgebiet zu quantifizieren wurden in dieser Arbeit drei verschiedene Methoden angewandt: (1) Minimierung der Differenz zwischen BARCA Beobachtungen und Simulationen von globalen Methaninversionen; (2) hochaufgelöste Vorwärtssimulationen mit dem an das Weather Research and Forecasting Modell WRF gekoppelte Greenhouse Gas Modell unter Verwendung von verschiedenen Wetland Modellen und Wetland Karten; (3) regionale Methaninversionen mittels Methanbeobachtungen des 35 m hohen TT34-Messturmes im mittleren Amazonasgebiet und zwei verschiedenen Wetland Karten.

Um hochaufgelöste Methansimulationen mit dem WRF-Modell durchführen zu können, wurde das Greenhouse Gas Modell in dieser Arbeit entwickelt und an das WRF-Modell gekoppelt (WRF-GHG). Es erlaubt die direkte Berechnung von Methanflüssen aus Wetlands, Termiten und Bodenaufnahme in simultaner Berechnung mit der WRF Meteorologie. Des Weiteren wurde das bereits bestehende Modell zur Berechnung von biosphärischen Kohlenstoffdioxidflüssen und ein Modell zur Berechnung der Eintrittshöhe von Emissionen aus Biomassenverbrennung in WRF-GHG eingebunden. Der Transport der Spurengase Methan, Kohlenstoffdioxid und Kohlenstoffmonoxid findet hierbei ohne chemische Reaktionen in der Atmosphäre statt, d.h. als passiver Transport. Der in dieser Arbeit erstellte WRF-GHG-Modellcode steht in leicht veränderter Form innerhalb der offiziellen WRF-Chem Version 3.4 zu wissenschaftlichen Zwecken frei zur Verfügung.



Der Vergleich von BARCA-Methanbeobachtungen mit Methanbeobachtungen von angrenzenden Bodenstationen östlich und nordöstlich des Amazonasgebietes bestätigt, dass das Amazonasgebiet eine starke Methanquelle ist. Die Methanmischungsverhältnisse im Amazonasgebiet sind am Ende der Trockenperiode im November 2008 etwas niedriger ( $1817 \pm 39$  ppb in der planetaren Grenzschicht und  $1794 \pm 12$  ppb in der unteren freien Troposphäre) als im Mai 2009 am Ende der Regenzeit ( $1841 \pm 37$  ppb bzw.  $1806 \pm 38$  ppb). Isotopenmessungen von ausgewählten Luftproben zeigen, dass der Großteil der Methanbeobachtungen der zwei Flugzeugkampagnen biogenen Ursprung hat und somit größtenteils aus Wetlands stammt. Biogenes Methan wurde während der Flugkampagnen aber auch für Emissionen von größeren Städten im Amazonasgebiet z.B. Manaus nachgewiesen. Der Vergleich von BARCA-Methanbeobachtungen mit Simulationen von globalen Methaninversionen zeigt, dass die Inversionen, die zusätzlich Satellitenbeobachtungen benutzen, die Methanverteilung im Amazonasgebiet am besten wiedergeben. Ein monatlicher Methangesamtfluss des Amazonastieflandes wurde aus der Minimierung der Differenz zwischen Simulationen und Beobachtungen zu  $5,7 \pm 0,7$  Tg für November 2008 und  $6,9 \pm 1,1$  Tg für Mai 2009 ermittelt.

Die Methanverteilung im Amazonasgebiet wurde mit dem WRF-GHG-Modell für die zwei Monate der BARCA-Messkampagnen in hoher Auflösung simuliert. Hierzu wurden vier verschiedene Simulationen mit Kombinationen aus zwei verschiedenen Wetland Modellen (Kaplan-Modell und Walter-Modell) und drei verschiedenen Wetland Karten (Kaplan, JERS-1SAR, Prigent), die die Verteilung der Wetlands im Amazonasgebiet wiedergeben, durchgeführt. Die Werte der Methanemissionen von Wetlands wurden so angepasst, dass der Mittelwert der Simulationen demjenigen aus den Beobachtungen der zweiten Messkampagne für ausgewählte Flüge mit einer guten Darstellung des atmosphärischen Transports im Modell entspricht. Aus dem Vergleich zu den Beobachtungen ist ersichtlich, dass die Wahl der Wetland Karte für eine gute Wiedergabe der Flugzeugbeobachtungen entscheidender ist als die Wahl des Wetland Modells. Flüge, für die das WRF-Modell eine bessere Darstellung des konvektiven Transports in der Atmosphäre ermöglicht, zeigen eine größere Übereinstimmung mit den Beobachtungen als Flüge, bei denen der konvektive Transport im Modell schlecht wiedergegeben wird. Die Güte des konvektiven Transports wurde anhand eines Vergleichs mit Niederschlagsdaten ermittelt. Der Methangesamtfluss für das Amazonastiefland berechnet sich aus den WRF-GHG Simulationen zu  $3,9 \pm 0,8$  Tg für November 2008 und  $4,0 \pm 0,8$  Tg für Mai 2009.

Eine regionale Methaninversion mit dem zweistufigen Jenaer Inversionssystem TM3-STILT unter Verwendung der Beobachtungen des 35 m hohen TT34-Messturms 60 km nordwestlich von Manaus wurde für das gesamte Jahr 2009 durchgeführt. Die regionale Inversion wurde mit drei verschiedenen a-priori Flussverteilungen realisiert. Hierfür wurden die JERS-1SAR und Prigent Wetland Karten sowie das Walter-Modell, jedoch mit anderen meteorologischen Antriebsdaten, verwendet. Die Untersuchung von verschiedenen meteorologischen Antriebsdaten für das Walter Wetland Modell zeigte geringe Unterschiede bezogen auf das zentrale Amazonasgebiet. Jedoch betragen die Unterschiede in den Mischungsverhältnissen lokal bis zu 50 ppb. Hauptursache hierfür sind Unterschiede in der Bodentemperatur in den Antriebsdaten. Ein Vergleich von Simulationen der Methanmischungsverhältnisse mit den TT34 Beobachtungen von zwei regionalen Atmosphärentransportmodellen WRF und STILT zeigte eine mittlere Differenz von 25 ppb zwischen den beiden Modellen. Erklärungen hierfür sind Unterschiede im Hintergrundmischungsverhältnis, der Höhe der planetaren Grenzschicht im Modell und der konvektiven Parametrisierung. Anhand von Flugzeugdaten aus der Santarém Region wurde für die optimale Konfiguration der re-

gionalen Inversion eine räumliche Korrelationslänge von ca. 160 km und eine zeitliche Korrelation von ca. einer Woche bestimmt. Die regionale Inversion zeigte deutliche Verbesserungen in der saisonalen Verteilung der Methanemissionen im Amazonasgebiet. Jedoch reichen Beobachtungen von einem 35 m hohen Messturm alleine nicht aus, um den Methanfluss im gesamten Amazonasgebiet anhand von Beobachtungen aus der Atmosphäre genau bestimmen zu können. Je nach a-priori Methanflussverteilung berechnete sich der Gesamtfluss für das Amazonas Tiefland zu  $1,9 \pm 0,02$  Tg und  $4,4 \pm 0,01$  Tg für Mai 2009 und  $24,9 \pm 0,5$  Tg und  $61,2 \pm 0,8$  Tg für das gesamte Jahr 2009.

Insgesamt zeigt dies, dass die Bestimmung der Methanemissionen im Amazonasgebiet immer noch mit großen Unsicherheiten behaftet ist. Der Daten-basierte Ansatz zur Bestimmung der Methanemissionen im Amazonasgebiet führt zu deutlich höheren Werten als die beiden Modellbasierten Methoden. Um die Methanemissionen im Amazonasgebiet innerhalb eines geringeren Unsicherheitsbereiches bestimmen zu können, sind mehrere neue Messstationen idealerweise im Abstand von maximal 1000 km nötig. Zusätzlich muss auch die Repräsentation des konvektiven Transports in hochaufgelösten regionalen Atmosphärentransportmodellen verbessert werden, um von der höheren Auflösung gegenüber globalen Atmosphärentransportmodellen bei der Simulation von Spurengasen zu profitieren.



# Contents

<b>1</b>	<b>Introduction</b>	<b>1</b>
<b>2</b>	<b>Methane and the Amazon</b>	<b>5</b>
2.1	Methane . . . . .	5
2.1.1	Isotopic composition . . . . .	7
2.1.2	Natural sources . . . . .	8
2.1.3	Anthropogenic sources . . . . .	12
2.1.4	Sinks . . . . .	15
2.2	Amazon . . . . .	16
2.2.1	Meteorology and climatology . . . . .	17
2.2.2	Methane emissions . . . . .	19
2.3	Summary . . . . .	23
<b>3</b>	<b>Methods</b>	<b>25</b>
3.1	Top-down approach . . . . .	25
3.2	Observations . . . . .	27
3.2.1	Flux measurements . . . . .	28
3.2.2	Atmospheric mixing ratio observations . . . . .	29
3.3	Atmospheric transport models . . . . .	34
3.3.1	Weather Research and Forecasting model (WRF) . . . . .	34
3.3.2	Tracer transport models TM3 and TM5 . . . . .	38
3.3.3	Stochastic Time Inverted Lagrangian Transport model (STILT) . . . . .	38
3.4	Jena Inversion System . . . . .	40
3.5	Statistical methods . . . . .	44
3.6	Summary . . . . .	46
<b>4</b>	<b>WRF Greenhouse Gas model (WRF-GHG)</b>	<b>47</b>
4.1	Flux models . . . . .	47
4.1.1	Biospheric flux models implemented in WRF-GHG . . . . .	47
4.1.2	External fluxes . . . . .	53
4.2	Structure of WRF-GHG . . . . .	57
4.3	Initial and boundary conditions . . . . .	62
4.4	WRF-GHG in official WRF-Chem release . . . . .	63
4.5	Conclusions . . . . .	65

<b>5</b>	<b>Data analysis and comparison to global models</b>	<b>69</b>
5.1	Data collection during the two BARCA campaigns . . . . .	69
5.2	Methane data analysis . . . . .	70
5.2.1	BARCA-A vs. BARCA-B . . . . .	70
5.2.2	Methane source identification . . . . .	75
5.3	Comparison to global models . . . . .	78
5.4	Conclusions . . . . .	87
<b>6</b>	<b>WRF-GHG simulations in the Amazon basin</b>	<b>89</b>
6.1	Modeling framework description . . . . .	90
6.1.1	WRF model and meteorology set up for the Amazon basin . . . . .	90
6.1.2	Methane tracers and fluxes for WRF-GHG in the Amazon basin . . . . .	90
6.1.3	Wetland inundation maps . . . . .	91
6.2	Results and discussion . . . . .	94
6.2.1	Meteorology . . . . .	95
6.2.2	Wetland fluxes . . . . .	96
6.2.3	Comparison to BARCA observations . . . . .	98
6.2.4	Amazon basin budget calculations . . . . .	107
6.3	Conclusions . . . . .	111
<b>7</b>	<b>Annual methane budget of the Amazon basin</b>	<b>113</b>
7.1	Two-step regional inversion set up . . . . .	113
7.1.1	A-priori flux distribution . . . . .	115
7.1.2	Atmospheric transport . . . . .	119
7.1.3	Conducted regional inversions . . . . .	121
7.2	Results and discussion . . . . .	122
7.2.1	TT34 observations . . . . .	122
7.2.2	Global TM3 inversion . . . . .	125
7.2.3	Regional TM3-STILT inversion . . . . .	126
7.2.4	Budget estimates . . . . .	134
7.3	Conclusions . . . . .	138
<b>8</b>	<b>Summary and outlook</b>	<b>139</b>
8.1	Summary . . . . .	139
8.2	Outlook . . . . .	143
<b>A</b>	<b>Additional figures and tables</b>	<b>145</b>
<b>B</b>	<b>List of acronyms and symbols</b>	<b>173</b>
<b>C</b>	<b>Data documentation</b>	<b>187</b>
	List of figures . . . . .	204
	Bibliography . . . . .	205

# Chapter 1

## Introduction

Climate change, global warming, and the anthropogenic greenhouse effect are currently rising national and international interest and the scientific community is asked to answer the questions of the society. Without the natural greenhouse effect, the earth's natural temperature would be at  $-18^{\circ}\text{C}$  and life on earth would not be possible. Since the Industrial Revolution, the amount of carbon dioxide ( $\text{CO}_2$ ) and methane ( $\text{CH}_4$ ) in the atmosphere has risen dramatically [IPCC, 2007]. As a consequence, the amount of thermal radiation absorbed by these molecules in the atmosphere and emitted back to the earth has also risen. This results in a rise of the earth's average temperature. To quantify the impact of different molecules on the anthropogenic greenhouse effect, the term "radiative forcing" was introduced. It quantifies externally posed disturbances of the earth's radiation balance [IPCC, 2001]. The increase in the atmospheric mixing ratio of  $\text{CO}_2$  since pre-industrial times has resulted in a current radiative forcing due to this substance of  $1.66 \text{ Wm}^{-2}$  [IPCC, 2007]. Even though the impact of  $\text{CH}_4$  on the total radiation balance is small compared to  $\text{CO}_2$  ( $0.48 \text{ Wm}^{-2}$ ), a single  $\text{CH}_4$  molecule is 40 times more powerful in absorbing and emitting thermal radiation compared to a single  $\text{CO}_2$  molecule [Archer, 2010], making  $\text{CH}_4$  the second most important greenhouse gas [IPCC, 2007]. Almost 70% of the global  $\text{CH}_4$  sources ( $\sim 500 \text{ Tg a}^{-1}$ ) originate from anthropogenic sources. The other 30% have a natural origin. Emissions from anaerobic production by microbes in wetlands dominate the natural sources (approx. 70% of all natural sources) [Wuebbles and Hayhoe, 2002].

Tropical regions account for 60% of global wetland emissions [Bartlett and Harris, 1993, Bloom et al., 2010]. The Amazon basin with its estimated wetland area of  $5.19 \times 10^6 \text{ km}^2$  is a strong natural source of  $\text{CH}_4$  [Melack et al., 2004] and an important player in the global  $\text{CH}_4$  cycle. Apart from  $\text{CH}_4$  emissions from wetlands, anthropogenic sources such as biomass burning and fossil fuel emissions contribute significantly to the  $\text{CH}_4$  emissions in the Amazon basin [Bousquet et al., 2006]. In the future, wetland (and biomass burning) emissions might be affected by changing climate and human land-use activities. To estimate the human impact on these natural sources, a thorough understanding of the processes is required.

Several studies of  $\text{CH}_4$  flux measurements have been carried out since the 1980s to quantify the wetland source and other natural sources such as soils or bromeliads [Bartlett et al., 1990, Crill et al., 1988, Devol et al., 1988, do Carmo et al., 2006, Martinson et al., 2010]. The contribution to the atmosphere from biomass burning was investigated by several aircraft campaigns over the Amazon basin, when flask samples were taken during flights and analyzed for  $\text{CH}_4$  [Harriss et al., 1988, Ferek et al., 1998, Andreae and Merlet, 2001, Guyon et al., 2005, Yokelson et al., 2007, Lloyd



et al., 2007]. From 2000 to the present, the National Oceanic and Atmospheric Administration Earth System Research Laboratory (NOAA-ESRL) has collected flask samples to create stationary vertical profiles at fixed locations over Manaus and Santarém on a regular basis [Miller et al., 2007]. In addition to ground-based and airborne measurements, total column measurements of  $\text{CH}_4$  from space are available since 2003 from the SCanning Imaging Absorption spectroMeter for Atmospheric ChartographY (SCIAMACHY) onboard ENVISAT [Frankenberg et al., 2005, 2008, 2011].

It is worth noting that  $\text{CH}_4$  (and also  $\text{CO}_2$ ) atmospheric observations in the Amazon basin are in most instances only available on the local scale, i.e., flux towers and stationary airborne profiles. Satellite observations (e.g. from SCIAMACHY) have quasi global coverage, but only limited accuracy. For a full understanding of the ongoing processes in the Amazon basin and for the determination of the location of sources and sinks of  $\text{CH}_4$ , data collection at the regional scale is essential. To accomplish this, regional-scale airborne measurements of greenhouse gases, aerosols, and ozone covering nearly the entire Amazon basin were conducted within the Balanço Atmosférico Regional de Carbono na Amazônia project (BARCA). It is part of the Large-scale Biosphere-Atmosphere Experiment in Amazonia (LBA) [Keller et al., 2009]. The main goal of the BARCA project is to quantify the greenhouse gas budgets for the Amazon basin by combining the observations from aircraft campaigns with observations from flux towers and process-based land surface models. Two aircraft campaigns were conducted within the BARCA project, one in November 2008 at the end of the dry season (called “BARCA-A”) and one in May 2009 at the end of the wet season (called “BARCA-B”). In addition, continuous  $\text{CH}_4$  observations for more than one year (11/2008–04/2010) were obtained at the TT34 tower (located 60 km northwest of Manaus) in the central Amazon basin. In the future, the amount of atmospheric  $\text{CH}_4$  observations in the Amazon basin is expected to grow significantly. With the upcoming Amazonian Tall Tower Observatory (ATTO, <http://www.mpic.de/ATTO.125.0.html>) and the AMAZON Integrated Carbon Analysis project (AMAZONICA, <http://www.geog.leeds.ac.uk/projects/amazonica/>), the Amazon basin will become a focus region for regional  $\text{CH}_4$  studies.

To quantify the  $\text{CH}_4$  source strength of the Amazon basin, four different approaches have been used so far: (1) calculation of the Amazon  $\text{CH}_4$  budget based on upscaling of observations from local flux measurements [Bartlett et al., 1988, Devol et al., 1990, Melack et al., 2004]; (2) estimation of the annual  $\text{CH}_4$  wetland contribution of the Amazon basin as function of the water table depths, and surface temperature obtained from satellite observations (Gravity Recovery and Climate Experiment GRACE) [Bloom et al., 2010]; (3) calculations of the source strength based on observed enhancements in atmospheric  $\text{CH}_4$  within the Amazon basin compared to  $\text{CH}_4$  mixing ratios observed at remote background surface station in Ascension Island and Ragged Point Barbados from the National Oceanic and Atmospheric Administration Earth System Research Laboratory (NOAA-ESRL) [Miller et al., 2007]; and (4) estimations from global inversion systems [Bousquet et al., 2006, Chen and Prinn, 2006, Bergamaschi et al., 2007, Spahni et al., 2011]. The latter two methods are thought of as a “top-down” approach. They use observations of atmospheric trace gases (e.g.  $\text{CO}_2$ ,  $\text{CH}_4$ ) within atmospheric transport models to retrieve surface-atmosphere fluxes. This is possible as the atmosphere mixes and integrates surface fluxes that vary temporally and spatially [IPCC, 2007]. However, Meirink et al. [2008b] and Bergamaschi et al. [2009] state that estimates of the global  $\text{CH}_4$  budget obtained from global atmospheric inversions still show high uncertainties, particularly in the tropics.

To improve the occasionally high uncertainties in global atmospheric inversions, a top-down approach is widely used at the regional scale to estimate CH<sub>4</sub> budgets in northern mid-latitudes [Vermeulen et al., 1999, Kort et al., 2008, Zhao et al., 2009, Pickett-Heaps et al., 2011]. High-resolution regional atmospheric transport models are better able to capture mesoscale transport processes such as land-sea breeze or mountain-valley circulation [Ahmadov et al., 2007, Pillai et al., 2011]. They allow for a more accurate representation of the observations in the model and a budget estimate with smaller uncertainties [Dolmann et al., 2006, Gerbig et al., 2009]. The tropical regions are still lacking those applications at the regional scale. So far, only one study [Deutscher et al., 2010] has estimated the tropical Australian wetland source using a regional modeling framework. Until now a regional-scale forward and inverse modeling framework for the estimation of the CH<sub>4</sub> budget has not yet been implemented for the Amazon basin. Of course, one requirement of applying such a modeling framework is sufficient availability and coverage of atmospheric observations within the region of interest. With the aircraft observations of the two BARCA campaigns and more than one year ground-based observations at the TT34 tower, the time is ripe for an implementation of a regional forward and inverse modeling framework to contribute to the following scientific questions:

- What is the CH<sub>4</sub> budget of the Amazon basin?
- What are the main underlying processes that influence the CH<sub>4</sub> budget in the Amazon basin? What is their distribution within the Amazon basin?
- How can aircraft and tower observations help us to obtain reliable estimates of the CH<sub>4</sub> budget in the Amazon basin?
- How well are aircraft and tower observations in the Amazon basin represented by global and regional atmospheric transport models when coupled with high resolution flux models?

The main challenge of the presented work is to establish a forward and inverse modeling framework at the regional scale to quantify the CH<sub>4</sub> budget in the Amazon basin within reduced uncertainty. For this purpose, the Greenhouse Gas model for the Weather Research and Forecasting model (WRF-GHG) was developed. It performs high-resolution forward simulations of the atmospheric CH<sub>4</sub> distribution. In order to obtain data-constrained budgets, two process-based models for the calculation of CH<sub>4</sub> wetland emissions, in combination with three different wetland inundation maps (indicating the area of inundation per grid cell) were evaluated against atmospheric observations obtained during BARCA. The BARCA CH<sub>4</sub> observations were analyzed for seasonal differences and CH<sub>4</sub> source components, and compared to global TM5-based CH<sub>4</sub> atmospheric inversions. The two-step Jena regional inversion scheme was adapted to the Amazon basin to obtain an annual estimate of the CH<sub>4</sub> budget for the Amazon basin using TT34 tower observations. The main purpose of this work is to serve as a benchmark study for future CH<sub>4</sub> forward and inverse modeling applications within tropical regions, especially the Amazon basin.

Chapter 2 gives a summary of the current knowledge of methane and the Amazon. Formation of CH<sub>4</sub> from natural and anthropogenic processes is described including processes in the Amazon basin. Contributions to the global annual CH<sub>4</sub> budget are discussed. The climatological and meteorological conditions in the Amazon basin during the two BARCA campaigns are given.

Chapter 3 presents the methods utilized within this work. The “top-down” approach and the Jena two-step inversion scheme are explained. Different measurement techniques for CH<sub>4</sub> atmospheric and flux observations, from which data is used within this work, are specified. The global and regional atmospheric transport models applied within this work are described.

The development of the Greenhouse Gas model for the Weather Research and Forecasting model (WRF-GHG) is the substantial part of Chapter 4. The flux models for the calculation of biospheric CO<sub>2</sub> and CH<sub>4</sub> fluxes that are integrated into the WRF-GHG code are described. Flux fields from external sources, such as prescribed anthropogenic emissions or emissions from biomass burning are discussed. The code structure of WRF-GHG is explained in detail and the required changes for the integration of the Greenhouse Gas model in the official WRF-Chem release version 3.4 are denoted.

Data analysis of the CH<sub>4</sub> observations obtained during the two BARCA campaigns is presented in Chapter 5. The observations are discussed within the context of observations from surrounding background stations. The observations are attributed to different CH<sub>4</sub> source processes. The performance of five different global CH<sub>4</sub> inversions based on the same global atmospheric transport model TM5 in the Amazon basin is evaluated by a comparison to the BARCA observations. From this comparison, an improved CH<sub>4</sub> budget of the Amazon basin for November 2008 and May 2009 is derived.

In Chapter 6 high-resolution WRF-GHG simulations of the atmospheric CH<sub>4</sub> distribution in the Amazon basin and their comparison to BARCA CH<sub>4</sub> observations are described. Simulations with two different wetland models and three wetland inundation maps are presented. Wetland emissions are adjusted to match the mean value of the observations of selected flights with a good representation of the atmospheric transport in the model during BARCA-B. The comparison to the observations is separately evaluated for flights for which a good representation of the atmospheric transport is obtained, and for flights with a poorer representation of the atmospheric transport. From four different WRF-GHG simulations, a range of the monthly CH<sub>4</sub> budget of the Amazon basin for November 2008 and May 2009 is derived.

The estimation of the annual CH<sub>4</sub> budget of the Amazon basin from a two-step regional inversion using the TM3-STILT model is the main focus of Chapter 7. The TT34 tower observations are utilized here. These are compared to WRF-GHG simulations for assessing the representation of the atmospheric transport at tower stations. A comparison of regional inversions using different a-priori wetland fluxes and inversion configurations is presented.

Finally, the key findings of this work are highlighted in the Summary, and topics for future investigation are suggested in the Outlook section.

## Chapter 2

# Methane and the Amazon

Methane is the second most important greenhouse gas; its contribution to the anthropogenic greenhouse gas effect and the resulting global warming cannot be neglected. In this chapter, the evolution of atmospheric  $\text{CH}_4$  since the late Pleistocene is illustrated with a focus on the last 20 years. The different source and sink processes that influence the global  $\text{CH}_4$  budget are explained. Sources are divided into anthropogenic and natural origin focusing on the relevant  $\text{CH}_4$  sources for the Amazon basin. Methane isotopes that can be used to distinguish between different  $\text{CH}_4$  source components are introduced. Climatological and meteorological conditions in the Amazon basin, especially during the two BARCA campaigns, are described.

### 2.1 Methane

Methane is a transparent and odorless gas. Each  $\text{CH}_4$  molecule consists of one carbon and four hydrogen atoms with a total molar mass of 16 g. Like other hydrocarbons it is relatively insoluble in water. If the volume fraction of  $\text{CH}_4$  in the air reaches values between 5% and 15% the mixture can be highly explosive. The mole fraction of methane in the atmosphere is currently 0.0001774% which corresponds to an atmospheric mixing ratio of 1774 ppb (parts per billion, here used in the notation nanomole mole<sup>-1</sup>) based on the IPCC [2007] estimates for the year 2005. In contrast to  $\text{CO}_2$ , which accumulates in the atmosphere,  $\text{CH}_4$  is a transient gas with a lifetime of  $\tau = 8.7 \pm 1.3$  a [IPCC, 2007]. It is oxidized in the atmosphere mainly by a reaction with the hydroxyl radical OH. Consumption of atmospheric  $\text{CH}_4$  by soils is the only terrestrial sink.

Natural sources of  $\text{CH}_4$  are anaerobic production of  $\text{CH}_4$  by microbes in wetlands,  $\text{CH}_4$  emissions by termites, hydrates, geological sources such as mud volcanoes, and anaerobic production by microbes in the ocean. Wildfires and wild animals add only a minor contribution to the natural  $\text{CH}_4$  emissions. They are not further discussed within this work.

Since the beginning of the Industrial Revolution, anthropogenic  $\text{CH}_4$  sources have increased to a size twice as high as natural  $\text{CH}_4$  sources. Anthropogenic  $\text{CH}_4$  sources include coal mining, emissions from the gas and oil industry, ruminants, biomass burning, rice agriculture, and landfills. Fig. 2.1 illustrates the contributions of the different  $\text{CH}_4$  source components. The total annual amount of  $\text{CH}_4$  released to the atmosphere ranges between 503–610 Tg, while the total sink is estimated to be 492–581 Tg according to the IPCC [2007]. Table 2.1 illustrates an overview of the estimates of the single  $\text{CH}_4$  source processes contributing to the total annual  $\text{CH}_4$  budget. The single processes are described later in detail.

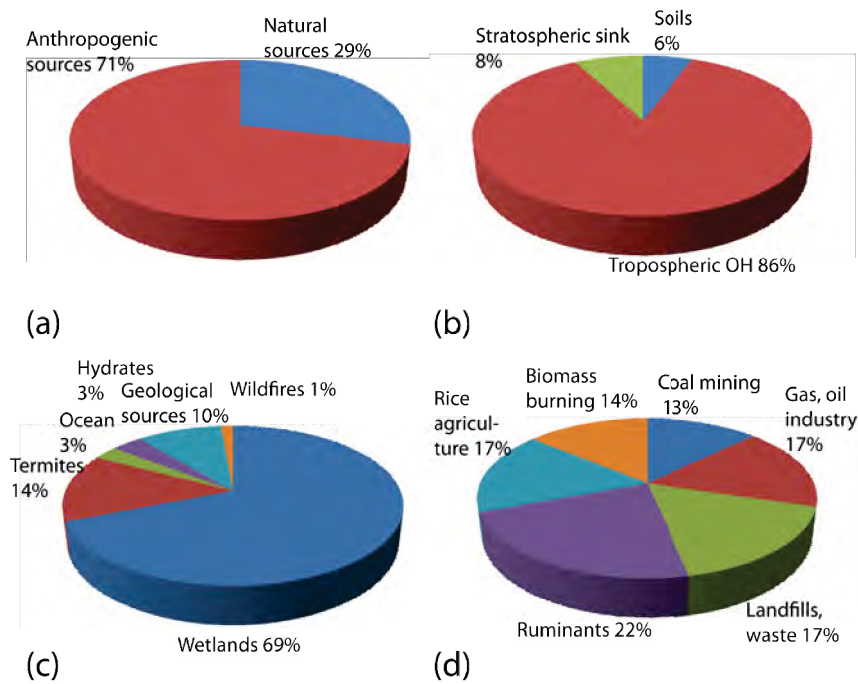


Figure 2.1: Distribution of different  $\text{CH}_4$  sources based on Wuebbles and Hayhoe [2002]. (a) illustrates the fraction of anthropogenic vs. natural sources of  $\text{CH}_4$  while in (b) the distribution of  $\text{CH}_4$  sinks is demonstrated. (c) shows the distribution of the natural  $\text{CH}_4$  sources and (d) the distribution of the corresponding anthropogenic sources.

Based on ice-core measurements the atmospheric mixing ratio of  $\text{CH}_4$  has been reconstructed until 650,000 years before present. The mixing ratio has ranged between 400 ppb during glacial and 700 ppb during interglacial time periods [Spahni et al., 2005]. However, the atmospheric mixing ratio of  $\text{CH}_4$  since pre-industrial times ( $\leq 700$  ppb) has more than doubled until the end of the last century [Etheridge et al., 1998]. In particular, the time period from the year 1945 to 1990 is marked by high  $\text{CH}_4$  growth rates [Etheridge et al., 1998]. Fig. 2.2 illustrates observations of the  $\text{CH}_4$  atmospheric mixing ratio from several surface stations around the globe since 1986. Dlugokencky et al. [1998] reported a declining growth rate in atmospheric  $\text{CH}_4$  since the year 1984 (cf. Fig. 2.2b). The large annual growth rate in 1998 is explained by enhanced emissions from boreal and tropical wetlands and boreal biomass burning. Enhanced wetland emissions might have been induced through the strong El Niño event in 1997/1998 leading to positive temperature anomalies [Dlugokencky et al., 2001]. Since the year 1999 the observed  $\text{CH}_4$  atmospheric mixing ratios show rather constant values for the time period 1999–2007 [Dlugokencky et al., 2003] (cf. Fig. 2.2a). Different research groups found possible explanations for this “flattening” of the  $\text{CH}_4$  atmospheric mixing ratio curve (also called the “ $\text{CH}_4$  enigma”), such as a decrease in fossil fuel emissions [Aydin et al., 2011] (Worthy et al. [2000] suggest a decrease in fossil fuel emissions over Europe and Siberia), or the decrease in the  $\text{CH}_4$  emissions from rice paddies [Kai et al., 2011]. However, the exact reason is still a subject of current research [Heimann, 2011]. Rigby et al. [2008] report on a new enhancement in the atmospheric mixing ratio of  $\text{CH}_4$  since the year 2007 for stations on both hemispheres, which is confirmed by Dlugokencky et al. [2009], who analyzed data from 46 surface stations around the globe.

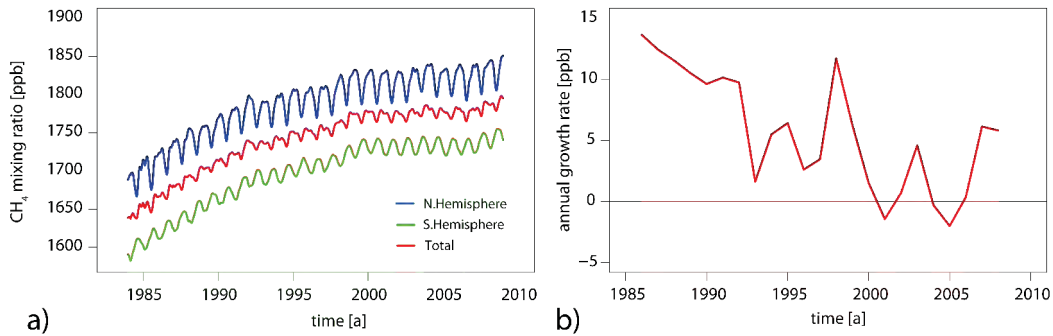


Figure 2.2: (a) Methane atmospheric mixing ratio of marine surface stations (latitudinal interpolation) of the years 1985–2008 separated for northern (blue) and southern Hemisphere (green) and the total average (red). (b) illustrates the changes in the annual growth rates from 1986 to 2008. Data are obtained from NOAA GLOBALVIEW CH<sub>4</sub> ([http://www.esrl.noaa.gov/gmd/ccgg/globalview/ch4/ch4\\_intro.html](http://www.esrl.noaa.gov/gmd/ccgg/globalview/ch4/ch4_intro.html)).

### 2.1.1 Isotopic composition

Isotopes are defined as atoms containing the same number of protons and electrons, but different number of neutrons. For CH<sub>4</sub>, two isotopes are of major importance: <sup>13</sup>CH<sub>4</sub> and <sup>2</sup>H (also known as “D” for Deuterium). Further, <sup>14</sup>CH<sub>4</sub> can be used to separate between the anthropogenic and biogenic contribution of CH<sub>4</sub> sources. The <sup>14</sup>CH<sub>4</sub> signature from fossil fuel emissions (resulting from time periods before nuclear weapon tests) is much lower compared to the signature of biogenic emissions [Stevens and Wahlen, 2000]. The standard notation for isotopes is the  $\delta$  notation. It expresses the relative abundance (expressed in [‰]) of, for example, <sup>13</sup>CH<sub>4</sub> in a sample ( $R_{SA}$ ), compared to a reference sample ( $R_{ST}$ ). It is calculated according to the following formula [Archer, 2010]:

$$\delta = \frac{R_{SA}}{R_{ST}} - 1 \times 1.0\text{‰} \quad (2.1)$$

The standards for  $\delta^{13}\text{CH}_4$  observations are the Vienna Pee Dee belemnite (PDB; consisting of CaCO<sub>3</sub>) and the Vienna Standard Mean Ocean Water (SMOW) for  $\delta\text{D}$  [Archer, 2010]. Isotopes are fractionated by biological processes, as lighter isotopes tend to react faster compared to heavier isotopes [Archer, 2010]. Hence, different CH<sub>4</sub> source processes yield different isotopic signatures. Atmospheric observations of the isotopic composition of CH<sub>4</sub> are used to distinguish between different CH<sub>4</sub> source processes as shown by Lassey et al. [2007]. Fig. 2.3 gives an overview of the  $\delta^{13}\text{CH}_4$  and  $\delta\text{D}$  signature of different CH<sub>4</sub> source processes.



Source category	Global annual CH <sub>4</sub> budget contribution [Tg]	Reference
<b>Natural sources</b>		
Wetlands	100–231	IPCC [2007] Bastviken et al. [2011]
Termites	2–26	Seiler et al. [1984], Fraser et al. [1986], Khalil et al. [1990], Martius et al. [1993], Sanderson [1996]
Hydrates	170–1270 (estimation of stored carbon in CH <sub>4</sub> hydrates)	Dickens [2011], Boswell and Collett [2011]
Permafrost	25–30	Kvenvolden and Lorenson [1993]
Geological sources	14–70	Judd et al. [2002], Etiopie and Klusman [2002], Etiopie et al. [2008]
<b>Anthropogenic sources</b>		
Biomass burning	11–88	Crutzen and Andreae [1990], Levine et al. [2000], IPCC [2007]
Landfills	40	Hein et al. [1997]
Wastewater treatment	35–69	IPCC [2007]
Ruminants	76–94	Johnson et al. [2000], Crutzen et al. [1986], IPCC [2007]
Rice agriculture	31–112	IPCC [2007], Shearer and Khalil [2000], Bouwman [1991], Wassmann et al. [1993]
Coal mining	46	Kirchgessner et al. [1993]
Natural gas and oil industry	36–68	IPCC [2007]
<b>Sinks of methane</b>		
Tropospheric OH	428–507	IPCC [2007]
Stratospheric sink	30–45	IPCC [2007]
Uptake by soils	26–34	Dörr et al. [1993], Smith et al. [2000], IPCC [2007]

Table 2.1: Contributions of the individual CH<sub>4</sub> source components to the global annual CH<sub>4</sub> budget.

### 2.1.2 Natural sources

Methane emissions from anaerobic production by microbes in wetlands are by far the most important natural source of CH<sub>4</sub>, followed by CH<sub>4</sub> emissions from termites [Wuebbles and Hayhoe, 2002]. Recently, CH<sub>4</sub> emissions from geological sources such as mud volcanoes have gained more attention as an underestimated natural source. Potential future CH<sub>4</sub> emissions from hydrates or permafrost could contribute significantly to the natural CH<sub>4</sub> budget [Archer, 2007].

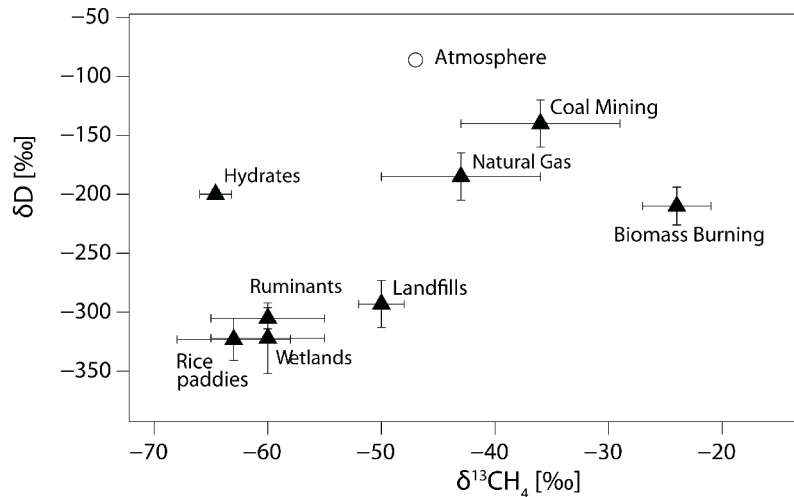


Figure 2.3: Isotopic composition of different  $CH_4$  sources based on Quay et al. [1999], Snover et al. [2000], and Hachikubo et al. [2010].  $\delta D$  indicates the deviation from SMOW in [‰],  $\delta^{13}CH_4$  the deviation from PDB in [‰]. The error bars indicate the 1- $\sigma$  uncertainty. The isotopic composition of the well-mixed atmosphere is denoted as black circle.

### Production pathways of biogenic methane

Acetate splitting and  $CO_2$  reduction are the two main pathways through which biogenic  $CH_4$  can be produced. The chemical reaction for acetate splitting is written to:



Whiticar [1999] summarizes that acetate splitting is responsible for 70% of the  $CH_4$  produced in freshwater environments. The isotopic carbon signature of the  $CH_4$  from acetate splitting ranges between -40 ‰ and -60 ‰ [Chanton et al., 2005]. In freshwater systems,  $CH_4$  is also produced by reduction of  $CO_2$  with hydrogen [Chanton et al., 2005]:



Methane produced by  $CO_2$  reduction has an isotopic carbon signature of ranging from -60 ‰ to -90 ‰ [Chanton et al., 2005].

### Natural wetlands

Methane emissions from natural wetlands are produced by anaerobic production by microbes in freshwater environments through decomposition of soil organic matter by the above described two different pathways. Chanton et al. [2005] describe that in freshwater wetlands, especially in peat, the  $CH_4$  production mechanism moves from acetate-splitting to  $CO_2$  reduction with increasing depths.

The  $CH_4$  production in wetlands can be described as a function of the height of the water table, soil temperature, and substrate availability [Schlesinger, 1997]. The height of the water table acts as a separator between anoxic soil layers of  $CH_4$  production and oxic soil layers of  $CH_4$  oxidation

[Bartlett and Harris, 1993]. Whiting and Chanton [1993] found a positive correlation between net ecosystem production and  $\text{CH}_4$  emissions in wetlands. Bartlett and Harris [1993] describe the increase in  $\text{CH}_4$  emissions with increasing soil temperature especially for temperate wetlands. Methane produced in anoxic soil layers is transported through three different pathways to the atmosphere: molecular diffusion, ebullition, and plant-mediated transport [Schlesinger, 1997]. According to Schlesinger [1997], Bartlett and Harris [1993], and Devol et al. [1988], the highest  $\text{CH}_4$  flux is obtained when  $\text{CH}_4$  forms gas bubbles (occurs if  $\text{CH}_4$  dissolved in soil exceeds the hydrostatic pressure of the overlying water) and is released to the atmosphere via ebullition. By the diffusion of  $\text{CH}_4$  through oxic soil layers or water, part of the  $\text{CH}_4$  is already oxidized and less  $\text{CH}_4$  reaches the atmosphere. The transport of  $\text{CH}_4$  to the atmosphere through plants often prevents the  $\text{CH}_4$  of being oxidized [Bartlett et al., 1992]. Fig. 2.4 illustrates schematically the different transport ways of  $\text{CH}_4$  to the atmosphere.

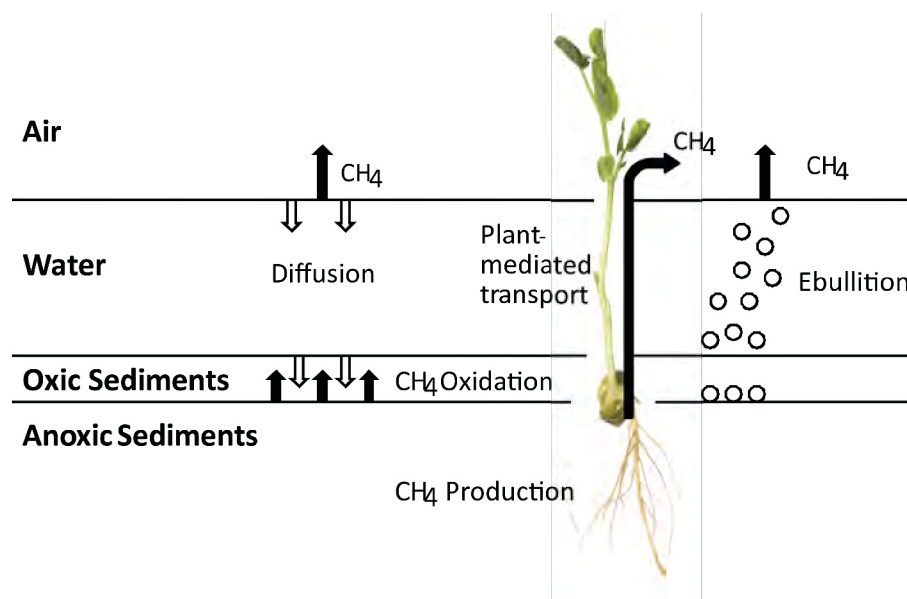


Figure 2.4: Illustration of the three different pathways (molecular diffusion, ebullition, and plant-mediated transport) of  $\text{CH}_4$  to the atmosphere (modified from Schlesinger [1997]).

The average  $\text{CH}_4$  flux from wetlands depends on region (e.g. tropics or high-latitudes), season (winter vs. summer for high-latitudes or wet vs. dry season for the tropics), and wetland type. In high-latitudes wetland types such as lakes, bogs, and freshwater marshes dominate. In tropical regions  $\text{CH}_4$  wetland emissions from swamp forests, flooded forests, and flood plains are more important [Lehner and Döll, 2004]. Observed  $\text{CH}_4$  fluxes can easily cover three orders of magnitude at the same measurement location [Baldocchi et al., 2012, Baulch et al., 2011]. They are found to range between  $27\text{--}346 \text{ mg m}^{-2} \text{ d}^{-1}$  for tropical regions,  $29\text{--}237 \text{ mg m}^{-2} \text{ d}^{-1}$  in the boreal zone, and  $65\text{--}254 \text{ mg m}^{-2} \text{ d}^{-1}$  in the tundra [Bartlett and Harris, 1993]. Cao et al. [1996] estimate the  $\text{CH}_4$  flux of tropical wetlands on average five times higher than the flux of northern wetlands and 30% higher compared to temperate wetlands. For the estimation of the global contribution of wetland emissions not only the  $\text{CH}_4$  flux magnitude in wetlands is of importance, but also the extent of the wetland area. The estimates of the global wetland area range from  $2.16 \times 10^{12} \text{ m}^2$  to  $11.0 \times 10^{12} \text{ m}^2$  [Prigent et al., 2001a, Lehner and Döll, 2004, Matthews and Fung, 1987, Kaplan,

2002] (Fig. 2.5 demonstrates an overview over the potential global wetland area as calculated by Kaplan [2002]). This makes the quantification of the natural wetland source very difficult, as both the flux observations and the estimates for the wetland area are highly uncertain (cf. Table 2.1).

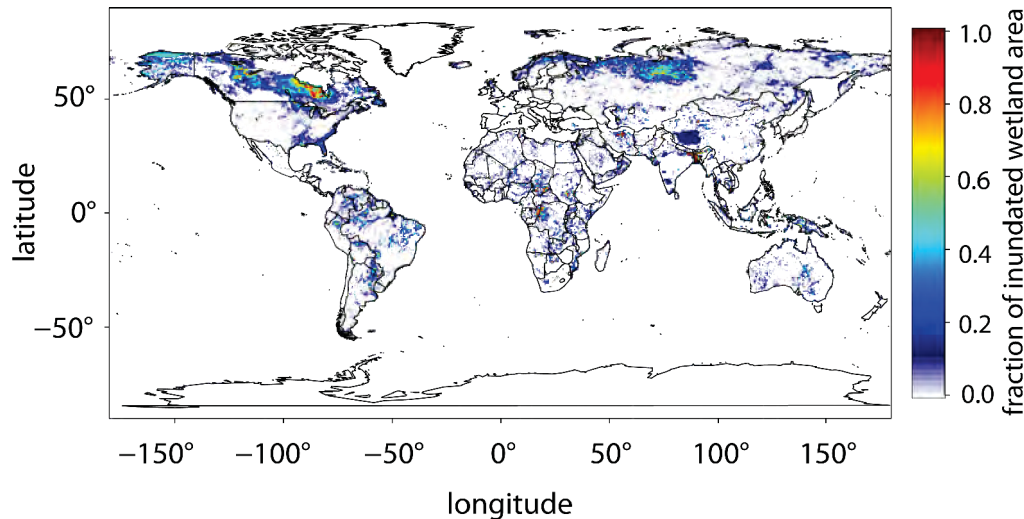


Figure 2.5: *The global wetland distribution based on the geographical potential wetland inundation map from Kaplan [2002] at  $0.5^\circ \times 0.5^\circ$  horizontal resolution. It indicates areas where wetlands can develop due to suitable orographic conditions. The wetland fraction per grid cell ranges from 0.0 to 1.0 (a wetland fraction of 1.0 denotes that the grid cell is fully covered by wetlands).*

### Termites

Another natural source of  $\text{CH}_4$  are termites. Methane is produced through anaerobic digestion of organic matter in their guts [Archer, 2010]. Cellulose is broken up and splitted into acetate,  $\text{CO}_2$ , and hydrogen.  $\text{CH}_4$  is then produced by  $\text{CO}_2$  reduction (cf. Eq. (2.3)) [Sanderson, 1996]. Sanderson [1996] states that most of the  $\text{CH}_4$  emissions originating from termites are located in tropical regions.

### Hydrates, oceanic sources, permafrost, and geological sources

Methane in the ocean is produced in sediments beneath the sea floor. The major contribution results from  $\text{CO}_2$  reduction (cf. Eq. (2.3)). It is hardly produced in the upper marine layer due to the abundance of seawater sulfate ( $\text{SO}_4^{2-}$ ), which primarily leads to sulfur reduction [Schlesinger, 1997]. A second source is thermogenic  $\text{CH}_4$  produced through the heating of soil organic matter, especially in the Gulf of Mexico. Solomon et al. [2009] observed such  $\text{CH}_4$  fluxes in the range of  $197\text{--}6520 \text{ mg m}^{-2} \text{ d}^{-1}$  in the Gulf of Mexico. Most of the  $\text{CH}_4$  produced beneath the sea floor is stored in hydrates.

The majority of hydrates are composed of biogenic  $\text{CH}_4$  [Archer, 2007] indicated by a carbon isotope value of  $-65\text{‰}$  [Kennett et al., 2000]. Hydrates are solids that form from water and  $\text{CH}_4$  in sediments. For this process high pressure (3–5 MPa), low temperature and sufficient  $\text{CH}_4$  gas concentration is required [Ruppel, 2011]. Thus the stability of hydrates is determined by water

depths (due to pressure increase) and temperature. In the context of climate change and global warming, leading to an increase in water temperature, dissociation of hydrates and release of  $\text{CH}_4$  to the atmosphere is a potential scenario [Kennett et al., 2000]. Shakhova [2010] already observed elevated  $\text{CH}_4$  mixing ratios over the Laptev Sea in the East Siberian Arctic Shelf. A 10% release of the hydrates would have an impact on the radiative forcing that is 10 times higher than for  $\text{CO}_2$  at the present estimated by Archer [2007]. However, Archer [2010] states that it will take thousands of years to warm and melt most of the hydrates in the ocean.

Of higher importance are potential  $\text{CH}_4$  emissions from melting permafrost. In arctic permafrost regions huge amounts of frozen organic carbon are stored accounting for almost 50% of the global below ground carbon pool [Tarnocai et al., 2009]. Due to an increase in global atmospheric temperature, the temperature in permafrost regions rises as well and parts of the frozen organic carbon are expected to melt [Romanovsky et al., 2002]. The melting of the permafrost exposes organic carbon to microbial degradation [Schuur et al., 2008], leading to  $\text{CH}_4$  emissions produced by anaerobic production by microbes in water covered areas, e.g. Siberia thaw lakes [Walter et al., 2006, Schaefer et al., 2011]. Anisimov [2007] predicts the contribution of  $\text{CH}_4$  emissions from Siberian permafrost to the global annual  $\text{CH}_4$  budget to increase by 6–8 Tg by the mid 21st century. This corresponds to an increase in the atmospheric mixing ratio of 40 ppb.

In the last years, the geological source of  $\text{CH}_4$  emissions gained more attention. Geologic  $\text{CH}_4$  can either be formed by biogenic processes such as anaerobic production by microbes, thermogenic processes (decomposition of organic matter at high temperatures) or by abiogenic processes such as inorganic synthesis and outgassing from the earth mantle [Judd, 2000]. Beside the formation of gas hydrates as described above, there are two more important pathways of geological  $\text{CH}_4$  to the atmosphere: Natural gas seeps that can occur both on land and in the ocean, and mud volcanoes that expulse water, gas, and mud from sediment sequences [Judd et al., 2002]. Judd [2000] estimated  $\text{CH}_4$  emissions from natural gas seeps to be in the order of 0.6–13.1 Tg  $\text{a}^{-1}$ , while the estimates for  $\text{CH}_4$  emissions from mud volcanoes range between 6.0–10.1 Tg  $\text{a}^{-1}$  as described by Judd et al. [2002] and Etiope and Milkov [2004].

### 2.1.3 Anthropogenic sources

The different sources of anthropogenic  $\text{CH}_4$  emissions range from human induced biomass burning activities to emissions from coal mining and the oil and gas industry. Methane emissions from rice agriculture, land fills or waste water treatments, and ruminants are accounted for as well in the anthropogenic  $\text{CH}_4$  sources.

#### Biomass burning

Biomass burning is defined as the combustion of living and dead biomass in forests and savannas, combustion of agricultural waste, and the burning of fuel wood [Levine et al., 2000]. In case of ideal conditions of hot, dry fires with sufficient oxygen supply, the combustion process is described as [Delmas et al., 1995, Levine et al., 2000]:



$\text{CH}_2\text{O}$  describes the average composition of biomass material [Levine et al., 2000]. However, the combustion of biomass is often an incomplete combustion process that leads to the emissions of

other species than  $CO_2$  like carbon monoxide (CO),  $CH_4$  or non-methane hydrocarbons [Levine et al., 2000]. Delmas et al. [1995] describe the emissions of different species as function of the duration of the fire. In the flaming phase almost complete combustion with mainly  $CO_2$  emissions is observed while in the smoldering phase the fraction of CO and  $CH_4$  emissions is higher. To determine the fraction of a tracer (different from  $CO_2$ ) that is emitted by the fire, the notation of the emission ratio (ER) is used. Depending on the vegetation type, it allows the calculation of the amount of emitted tracer  $X$  in relation to the reference tracer (e.g.  $CO_2$ ) [Levine et al., 2000]. It is defined through the following equation:

$$ER_{XCO_2} = \frac{\Delta X}{\Delta CO_2} \quad (2.5)$$

with

$$\Delta X = X_{obs} - X_b \quad (2.6)$$

$$\Delta CO_2 = CO_{2,obs} - CO_{2,b} \quad (2.7)$$

$X_{obs}$  indicates the observed atmospheric mixing ratio of tracer  $X$  within the biomass burning plume,  $CO_{2,obs}$  the atmospheric mixing ratio of the reference species  $CO_2$  in the biomass burning plume.  $X_b$  and  $CO_{2,b}$  are the background atmospheric mixing ratios of the corresponding tracers. As described in Andreae and Merlet [2001], CO is often used as reference tracer, too (cf. Ch. 5). The emission factor (EF) is defined as the amount of a tracer released compared to the amount of dry fuel consumed. It is expressed by the following equation [Andreae and Merlet, 2001]:

$$EF_X = \frac{M_X}{M_c} [C]_{biomass}. \quad (2.8)$$

$M_X$  indicates the released mass of the tracer  $X$ ,  $M_c$  the mass of the carbon emitted and  $[C]_{biomass}$  the carbon concentration in the biomass burned. Emission ratio and emission factor are related via the following equation [Andreae and Merlet, 2001]:

$$EF_X = ER_{XCO_2} \frac{MW_X}{MW_{CO_2}} EF_{CO_2}. \quad (2.9)$$

$EF_{CO_2}$  indicates the emission factor of the reference tracer  $CO_2$ ,  $ER_{XCO_2}$  the emission ratio of the specific tracer  $X$  in relation to the reference tracer  $CO_2$ , and  $MW_X$  and  $MW_{CO_2}$  the molecular weights of both tracers. The total amount of a specific tracer emitted by one single fire  $M_X^{fire}$  is determined by the following relationship (based on Seiler and Crutzen [1980] and modified by Longo et al. [2010]):

$$M_X^{fire} = \alpha_{veg} \times \beta_{veg} \times EF_X \times a_{fire} \quad (2.10)$$

with  $\alpha_{veg}$  being the available above ground biomass for burning,  $\beta_{veg}$  the combustion fraction,  $EF_X$  the emission factor of the corresponding tracer, and  $a_{fire}$  the size of the burned area per fire. The burned area per fire is determined by satellite observations, e.g. from the Geostationary Operational Environmental Satellite - Wildfire Automated Biomass Burning Algorithm (GOES WF\_ABBA; [Prins et al., 1998]). van der Werf [2010] estimated that from the total global  $CH_4$  emissions from biomass burning almost half of the contribution is from deforestation, degradation, and peat fires in the tropics.



### **Landfills and wastewater, ruminants, and rice agriculture**

Methane emissions in landfills occur through decomposition of organic waste under anaerobic conditions. The decomposition process typically starts 1–2 years after the waste was placed in the landfill [EPA, 2006]. The  $\text{CH}_4$  emissions from landfills increase with a higher organic share (e.g. paper or organic waste) and higher moisture content in the waste. In landfills with a soil cover, part of the  $\text{CH}_4$  produced is already oxidized again in the soil and not released to the atmosphere [Bogner and Spokas, 1993]. However, especially in developing countries no strict regulations on the amount of  $\text{CH}_4$  emissions from landfills exists, resulting in potentially higher  $\text{CH}_4$  emissions from landfills [EPA, 2006].

Methane emissions are also produced during waste water treatment where organic waste is decomposed by microorganisms. This leads to  $\text{CH}_4$  emissions under anaerobic conditions and  $\text{CO}_2$  emissions under aerobic conditions. EPA [2006] numbers the contribution of the waste water sector to contribute 9% of the global total  $\text{CH}_4$  emissions (including natural and anthropogenic emissions).

Animals, especially ruminants (primarily cattle and buffaloes), contribute to the global  $\text{CH}_4$  emissions by two different pathways: (1) through microbial digestion in their stomachs (rumen) and (2) through microbial degradation of their excrements (manure) [Johnson et al., 2000]. The  $\text{CH}_4$  emissions depend on the diet and the digestive system of the animal and are estimated to be in the order of 2–12% of the feed energy consumed [Johnson et al., 2000]. A lower feed quality (lower grain content) and a higher feed uptake lead to higher  $\text{CH}_4$  emissions [EPA, 2006].  $\text{CH}_4$  emissions from manure are high if it is stored under anaerobic conditions, while depositing it on pasture reduces the  $\text{CH}_4$  emissions significantly [EPA, 2006]. Laubach and Kelliher [2005, 2004] and Lassey et al. [1997] report on  $\text{CH}_4$  emissions from cows ranging from 263–402  $\text{g d}^{-1} \text{cow}^{-1}$ , while Lassey et al. [1997] observed  $\text{CH}_4$  emissions from sheep to be in the order of 19  $\text{g d}^{-1} \text{sheep}^{-1}$ .

Another anthropogenic  $\text{CH}_4$  source are emissions from rice paddies. Those emissions follow the same chemical reactions as the  $\text{CH}_4$  emissions from natural wetlands through anaerobic decomposition of soil organic matter. Sass et al. [1992] observed that 90% of the  $\text{CH}_4$  produced in rice paddies is directly oxidized in the soil. The remaining 10% are emitted to the atmosphere mainly via plant-mediated transport (90%), while only a minor part of  $\text{CH}_4$  is released via ebullition (10%) and diffusion (<1%) according to Schütz et al. [1989]. Neue and Roger [2000] state that rice cultivation in wetlands under anaerobic conditions produces significant amounts of  $\text{CH}_4$ , while the  $\text{CH}_4$  emissions from rice cultivation in uplands are negligible. In Brazil most of the rice is cultivated in upland regions [EPA, 2006].

### **Coal mining and natural gas and oil industry**

Through coal mining processes  $\text{CH}_4$  stored in the pockets of a coal seam is released. As  $\text{CH}_4$  is highly explosive in atmospheric concentrations of 5–15%, it has to be degassed to the atmosphere in order to keep the  $\text{CH}_4$  concentration in the coal mines below 1% [EPA, 2006].

The main source of  $\text{CH}_4$  emissions in the natural gas industry arises from equipment and pipeline leaks and venting activities. Methane emissions to the atmosphere can occur throughout all four production processes of natural gas: production, processing of the gas, transportation and storage, and the final distribution to the consumer [EPA, 2006]. Dedikov et al. [1999] estimate the contribution from the natural gas industry in Russia to be in the order of 4  $\text{Tg a}^{-1}$ . Pétron et

al. [2012] claim in their recent study for Colorado, US, that the emissions from leaks and storage tanks are most likely underestimated.

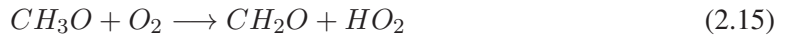
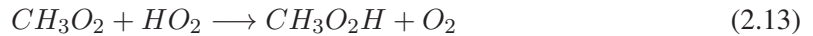
In the oil industry most of the  $\text{CH}_4$  emissions occur in the oil production stage through flaring, venting, and accidental leaks. This is especially true for offshore oil production. For onshore oil production,  $\text{CH}_4$  is captured and transported for energy usage [EPA, 2006]. For the oil industry,  $\text{CH}_4$  emissions from refinement or transport play only a minor role.

### 2.1.4 Sinks

Methane is a transient gas in the atmosphere with an average atmospheric lifetime of  $\tau = 8.7$  a [IPCC, 2007]. The main sink process of  $\text{CH}_4$ , the destruction by the hydroxyl (OH) is described in the following. The processes and reactions leading to  $\text{CH}_4$  loss in the stratosphere and the uptake of atmospheric  $\text{CH}_4$  by soils are discussed briefly.

#### Atmospheric sink

More than 90% of atmospheric  $\text{CH}_4$  is destroyed by the reaction with OH in the troposphere [Schlesinger, 1997] via the following reaction chain:



leading to the overall equation:



Hydroxyl radicals with a lifetime of only a few seconds in the atmosphere are produced via ozone destruction:



Another OH production pathway is the reaction of nitrogen oxides ( $\text{NO}_x$ ) with water vapour [Archer, 2010]:



The OH atmospheric mixing ratio is highest in the tropical latitudes (due to stronger incoming UV radiation) and during daytime [Schlesinger, 1997]. The atmospheric  $\text{CH}_4$  mixing ratio at high-latitudes is marked by a seasonal cycle with a minimum in the late summer (corresponding to a maximum in the OH mixing ratio; cf. Fig. 2.2). With increasing  $\text{CH}_4$  and CO atmospheric mixing ratio in the atmosphere, one would expect a decrease in the OH atmospheric mixing ratio and therefore, a prolongation of the  $\text{CH}_4$  lifetime. However, Dentener et al. [2003] and Montzka et al. [2011] state that changes in the OH atmospheric mixing ratio are dominantly driven by

meteorological changes, such as the tropospheric water vapour content, and not by an increase in the  $\text{CH}_4$  atmospheric mixing ratio.

Formaldehyde ( $\text{CH}_2\text{O}$ ) produced in the chemical reaction described in Eq. (2.16) further reacts with OH to CO, which is later oxidized to  $\text{CO}_2$ . The net reaction for this process is described by:



Therefore, on the long term oxidation of  $\text{CH}_4$  leads to accumulation of  $\text{CO}_2$  in the atmosphere [Schlesinger, 1997].

The only “source” of  $\text{CH}_4$  in the stratosphere is the atmospheric transport of  $\text{CH}_4$  from the troposphere to the stratosphere. Methane loss in the stratosphere occurs through reactions with OH,  $\text{O}({}^1\text{D})$ , Cl and  $h\nu$  according to the following chemical reactions [Cicerone and Oremland, 1988, Schlesinger, 1997]:



Due to no additional source of  $\text{CH}_4$  in the stratosphere, the atmospheric mixing ratio of  $\text{CH}_4$  in the stratosphere decreases continually from  $\sim 1770$  to 250 ppb with increasing altitude and latitude along the stratospheric circulation path [Röckmann et al., 2011].

### Terrestrial sink

The only terrestrial sink of atmospheric  $\text{CH}_4$  is uptake by soils [IPCC, 2007]. Atmospheric  $\text{CH}_4$  is consumed in soils via oxidation through aerobic microorganisms [Bender and Conrad, 1993]. This oxidation takes places in the top few centimeters of the soil [Crill, 1991, Striegler, 1993]. The ability of soil to take up atmospheric  $\text{CH}_4$  decreases with increased soil moisture content (shift to anaerobic  $\text{CH}_4$  production conditions) [Adamsen and King, 1993, Steudler et al., 1989, Itoh et al., 2009]. Nitrogen fertilizers and changes in landuse from tropical forest to pasture reduces the uptake of atmospheric  $\text{CH}_4$  [Ojima et al., 1993, Steudler et al., 1996]. The uptake of  $\text{CH}_4$  was observed to be higher in tropical regions compared to temperate or subarctic regions (observed  $\text{CH}_4$  flux into the soil of  $10\text{--}12 \text{ mg m}^{-2} \text{ d}^{-1}$  for tropical regions [Singh et al., 1997] compared to  $1\text{--}5 \text{ mg m}^{-2} \text{ d}^{-1}$  in temperate and arctic regions [Adamsen and King, 1993, Crill, 1991]). Verchot et al. [2000] claim that tropical soils account for 10–20% of the global terrestrial  $\text{CH}_4$  sink.

## 2.2 Amazon

The Amazon river is one of the longest rivers in the world with a total length of 6448 km and contributions of 1100 rivers. The source is located in the Nevado Mismi mountains in Peru at 5170 m a.s.l.. The Amazon river carries 20% of the river water in the world with an annual discharge of  $6300 \text{ km}^3$  before flowing into the Atlantic ocean close to the city of Belém.

### 2.2.1 Meteorology and climatology

Compared to higher latitudes, which are influenced by large synoptic scale variability caused by a stronger effect of the Coriolis force and resulting higher pressure gradients, the atmosphere in the tropics has relatively low variability. Minimal temperature difference between day and night (max. 10 K at a mean annual temperature of 26.6°C [Junk and Piedade, 2005]) combined with a weak Coriolis force result in weak pressure gradients that form a fairly steady circulation with winds coming preferably from the East [Laing and Evans, 2011]. For this reason, local and mesoscale effects have a more dominant influence on the tropical weather compared to higher latitudes.

Due to a surplus in radiation in the tropics (the sum of “positive” incoming solar radiation and

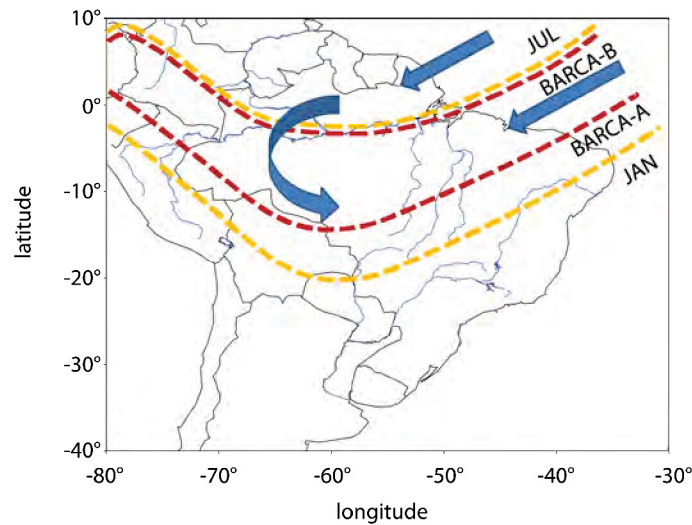


Figure 2.6: Illustration of the ITCZ location (orange dashed line) during January (JAN) and July (JUL) and wind flow (blue arrows) entering the Amazon basin and within the Amazon basin [Laing and Evans, 2011]. The location of the ITCZ during the two BARCA campaigns in November 2008 (BARCA-A) and May 2009 (BARCA-B) is marked by the dark red dashed line and was obtained from GOES8 satellite observations.

“negative” outgoing longwave radiation in the tropics is positive), air parcels are rising and leading to low convective systems along the belt of maximum surplus of the radiation - also known as the intertropical convergence zone (ITCZ). The location of the ITCZ over South America for January and July (orange dashed line) is illustrated in Fig. 2.6. In January the location of the ITCZ is basically determined by the Andes and the Atlantic ocean. For the two months of the BARCA campaigns (November 2008 and May 2009), the ITCZ was located on the southern edge of the Amazon basin in November 2008 and just over the Amazon mainstream along Manaus to Belém during May 2009 (red dashed line Fig. 2.6). The ITCZ location during BARCA-B coincides well with the July location of the ITCZ marked in Fig. 2.6.

The trade winds entering the Amazon basin from the north-east or south-east transport moist air to the interior of the Amazon basin. These winds are then deflected along the Andes changing their direction from north-east to south-west. In the tropics precipitation is mainly produced by organized cloud systems with a length scale ranging from 100–1,000 km and a lifetime of several hours to days [Johnson et al., 1999]. They are called Mesoscale Convective Systems (MCS). These

MCSs are responsible for the convective precipitation. Stratiform precipitation is caused by older, less active MCSs [Laing and Evans, 2011]. Shallow convection contributes only 10% to the total rainfall in the Amazon basin [Pereira and Rutledge, 2006]. The diurnal cycle of precipitation in the tropics depends on surface properties, e.g. land or ocean, topographically induced circulations such as land or sea breeze, and propagating MCSs [Nesbitt and Zipser, 2003]. In the Amazon basin, i.e. over land regions, the total maximum of the precipitation occurs usually in the afternoon hours (local time). The peak in precipitation depends on the region within the Amazon basin. The maximum precipitation occurs around noon at the mouth of the Amazon basin (close to Belém) due to the sea-breeze effect that helps to trigger convection. While moving southwestwards into the Amazon basin, the maximum precipitation shifts to the evening hours.

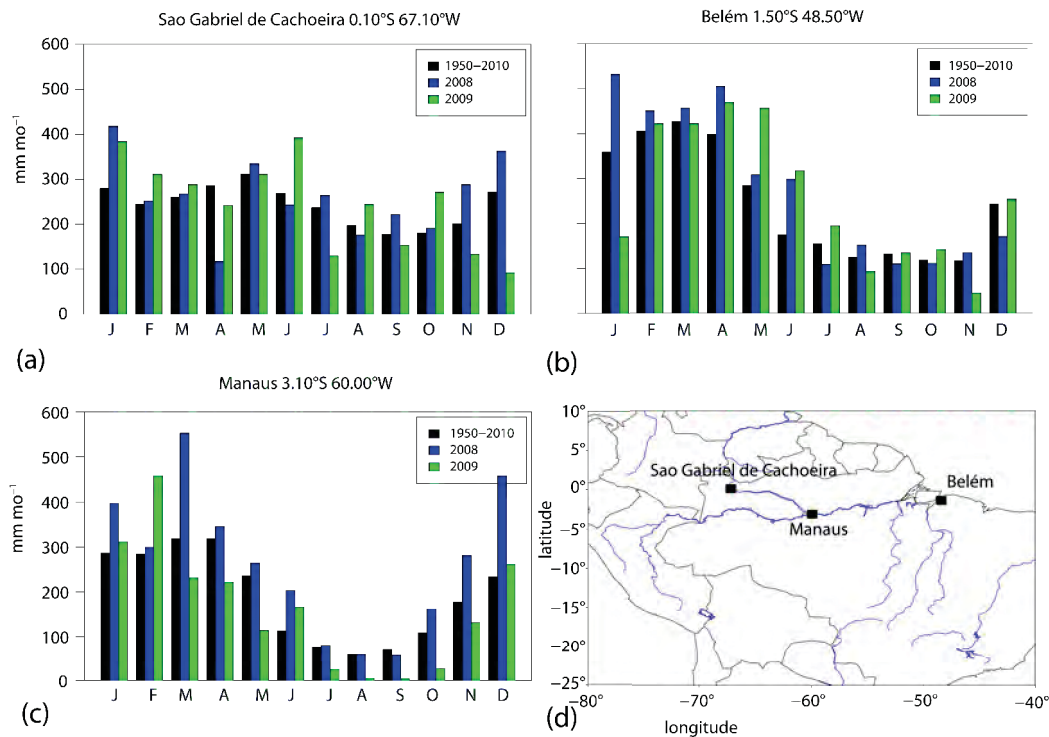


Figure 2.7: Averaged monthly rainfall during the years 1950–2010 (black) and for the two years of the BARCA campaigns 2008 (blue) and 2009 (green) for the cities of Sao Gabriel de Cachoeira (a), Belém (b), and Manaus (c) in the Amazon basin. (d) illustrates the location of the cities within the Amazon basin. Precipitation data from the Global Historical Climatology Network (GHCN) [Easterling and Peterson, 1995, Peterson and Easterling, 1994].

Three areas of abundant rainfall can be identified in the Amazon basin. The north-western part of the Amazon basin with annual rainfall of more than 3600 mm due to uplift effect of the air along the Andes, the center part  $\sim 5^\circ\text{S}$  with 2400 mm annual rainfall and the mouth of the Amazon river with 2800 mm, which is thought to originate from nighttime convergence of the easterly trade winds with the land breeze [Liebmann and Marengo, 2001, Marengo, 2007]. The main sources of precipitation in the Amazon basin are the recycling of moisture through evapotranspiration and the contribution of the tropical South Atlantic trade winds. The recycling of moisture accounts for roughly 45% of the precipitation in the Amazon basin and is a fairly constant source with

less interannual variability (IAV) [Marengo, 2007]. The precipitation originating from the South Atlantic trade winds has a higher seasonal variation. In Fig. 2.7 monthly precipitation for three different cities within the Amazon basin (Manaus, Belém, and Sao Gabriel de Cachoeira) averaged for the time reference period of 1950–2010 (black) and for the two years of the BARCA campaigns (2008–blue and 2009–green) is illustrated. Compared to the mean annual average the year 2008 was wetter for all the three cities. In 2009 enhanced precipitation is denoted only in Belém in May during the time of the BARCA-B campaign. This is not in contrast to the fact that in 2009 one of the worst flooding in the Amazon during the last 50 years occurred, which was mainly caused by heavy rainfall in the northern part of the Amazon basin.

Associated with vertical transport, the height of the planetary boundary layer (PBL) in tropical regions, especially the Amazon basin, was found to depend on the vegetation type. Nobre et al. [1996] obtained the PBL heights for forest and pasture from radiosonde and balloon profiles in the Ji-Paraná region of Rondônia (Table 2.2). Fisch et al. [2004] point out that the differences in the height of the PBL between pasture and forest are more dominant during the dry season due to larger sensible heat fluxes at pasture sites compared to the wet season.

	Forest	Pasture
Local time [h]	PBL height [m]	PBL height [m]
08:00	200	110
11:00	580	1590
14:00	1150	2100
17:00	1250	2220

Table 2.2: *Observations of PBL heights obtained over two vegetation types (forest and pasture) at different times of the day in the Ji-Paraná region of Rondônia [Nobre et al., 1996].*

A further impact on the variability of the precipitation comes from the El Niño Southern Oscillation (ENSO). It causes negative rainfall anomalies in the northern and center part of the Amazon basin and below average summer rainfall in the southern part of the Amazon basin during El Niño events. The negative rainfall anomalies are generated by weaker trade winds leading to a reduced moisture flux during strong El Niño events. For La Niña events, the wet season in the northern and center Amazon basin is more predominant. It affects the river discharge, which generally peaks 3–4 months after the precipitation maximum during the wet season, with lower river levels during El Niño events and higher river levels during La Niña events [Marengo, 2007]. The Multivariate El Niño Index during the time periods of the BARCA campaigns (Fig. 2.8) shows a La Niña event throughout the year 2008 (including the November 2008 when BARCA-A took place) and a transition period from La Niña to El Niño in May 2009 (BARCA-B). It is in very good agreement with the precipitation observations shown in Fig. 2.7 with above average precipitation for 2008 and the beginning of 2009 and below average precipitation for the second half of 2009.

### 2.2.2 Methane emissions

Methane emissions in the Amazon basin are dominated by emissions from anaerobic production by microbes in wetlands. Emissions from biomass burning, cattle, and pasture soils play a minor role as stated by Davidson and Artaxo [2004]. In the last years, CH<sub>4</sub> emissions from hydroelectric reservoirs in the tropics gained more attention as a substantial source of atmospheric CH<sub>4</sub>



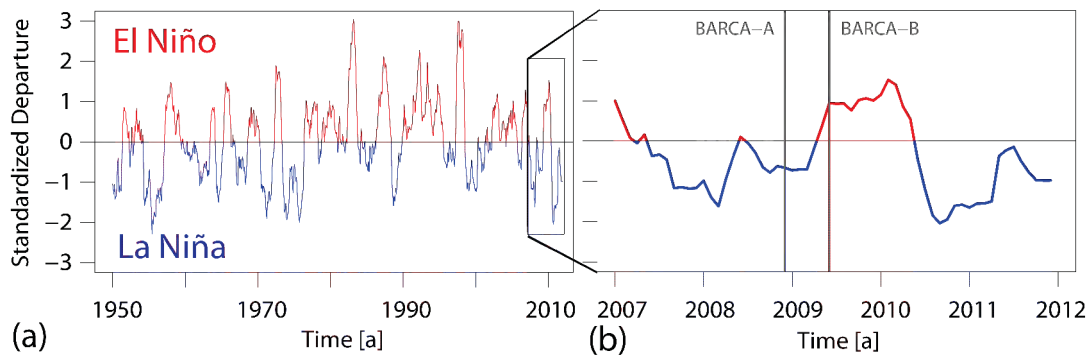


Figure 2.8: (a) illustrates the Multivariate El Niño Index (MEI) for the years 1950 to the present. The MEI is based on observations of six main variables including atmosphere and ocean variables (sea-level pressure, zonal and meridional wind components of surface winds, sea surface temperature, surface air temperature, and total cloudiness fraction of the sky) over the tropical Pacific ocean [Wolter and Timlin, 2011]. The MEI is positive for El Niño periods and negative for La Niña periods. In (b) a zoom into the years 2007 to 2012 is illustrated and the time periods of the two BARCA campaigns are denoted with gray lines. Data for the graphic were obtained from <http://www.esrl.noaa.gov/psd/enso/mei.ext/table.ext.html>.

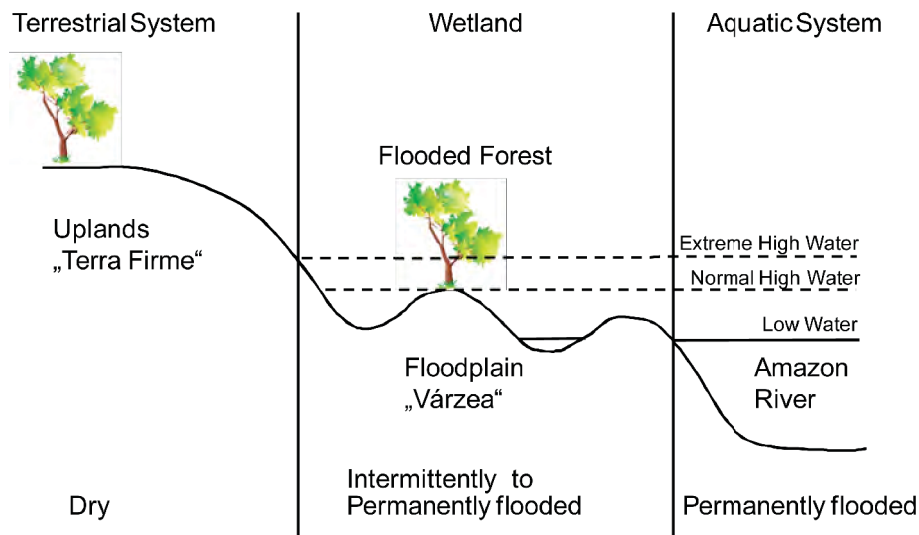


Figure 2.9: Horizontal cross-section through the Amazon river, wetlands, and uplands simplified from Maltby [2009].

[Kemenes et al., 2007]. As for all tropical regions,  $\text{CH}_4$  emissions from termites and atmospheric uptake of  $\text{CH}_4$  by soils have to be considered.

Wetlands in the Amazon are mainly extensive inundated floodplains, which are covered by open water, flooded forest or aquatic macrophytes [Melack et al., 2004]. The annual floods of the floodplains last for several months. Fig. 2.9 illustrates a typical cross-section through the Amazon river plain showing the transition from the Amazon main river to wetlands and the dry uplands. For regions with a significant dry season, savannas can occur. Those are exposed to seasonal flooding from rain and rivers [Melack et al., 2004]. Roraima in Brazil and Llanos de Mojos in



Bolivia are two examples for savannah wetlands within the Amazon basin. These two wetlands are marked with blue (Roraíma) and green (Llanos de Mojos) color in Fig. 2.10. This figure also illustrates the maximum inundated wetland area as seen by the Japanese Earth Resources Satellite 1 Synthetic Aperture Radar (JERS-1SAR) in the Amazon lowland region (<500 m) defined by Melack et al. [2004]. 17% of the Amazon mainstream area (yellow rectangle in Fig. 2.10) could be identified as wetlands while 83% of this area are uplands [Melack and Hess, 2011]. 96% of this wetland area is flooded at high water stages, while only 26% of this area is flooded at low water stages. Flooded forest occupies nearly 70% of the wetlands [Melack and Hess, 2011]. The differences in the estimates of the total wetland area in the Amazon are substantially large, varying from 203,100 km<sup>2</sup> to over 800,000 km<sup>2</sup> as described by Melack and Hess [2011].

Wetlands in the Amazon can be classified into different wetland types depending on the vegetation type (non-vegetated, herbaceous, shrub, woodland, forest) and inundation stage (flooded vs. non-flooded) [Melack and Hess, 2011]. Melack [2009] estimates the contribution of different habitat areas to the total CH<sub>4</sub> wetland emissions in the Amazon basin to be 3% from the river channel, 5% from open water areas, 13% from herbaceous, and 79% from forest/shrubs. Extensive CH<sub>4</sub> flux measurements were conducted in the Amazon basin mainly in the late 1980s with a few measurement campaigns following afterwards. Crill et al. [1988] and Engle and Melack [2003] found CH<sub>4</sub> fluxes of 2–158 mg m<sup>-2</sup> d<sup>-1</sup> with a mean of 27 mg m<sup>-2</sup> d<sup>-1</sup> for open lakes (i.e., Lake Calado, 60 km west of Manaus). Bartlett et al. [1988, 1990], Devol et al. [1988] and Wassmann et al. [1992] observed CH<sub>4</sub> fluxes for different habitats ranging from 5–120 mg m<sup>-2</sup> d<sup>-1</sup> for open water areas over 110–192 mg m<sup>-2</sup> d<sup>-1</sup> for flooded forest to the highest values of 201–590 mg m<sup>-2</sup> d<sup>-1</sup> for floating grass mats (during high water levels). They all report a significant (>50%) contribution from ebullition to the transport pathways of CH<sub>4</sub> to the atmosphere. Wassmann et al. [1992] found that flooded forests have the highest CH<sub>4</sub> flux during high water periods, while the flux from floating grass mats is highest when the water level starts to fall. Devol et al. [1990] reports about a lower CH<sub>4</sub> flux during low water periods. Both Devol et al. [1988] and Wassmann et al. [1992] confirmed with the help of  $\delta^{13}\text{C}_{\text{CH}_4}$  isotope measurements that most of the CH<sub>4</sub> released from wetlands in the Amazon basin has its origin in acetate splitting. The calculated CH<sub>4</sub> budget estimates from flux measurements for the total Amazon basin increased from 5.1–10 Tg in the 1980s [Devol et al., 1988, 1990] to the most recent estimate of 29.3 Tg as reported by Melack et al. [2004].

Methane emissions from hydroelectric reservoirs evolve in a similar way as CH<sub>4</sub> emissions from wetlands. Organic matter in the flooded area of the reservoir is decomposed. These emissions can be considered as man-made emissions of “artificial wetlands”. While the direct CH<sub>4</sub> emissions of the reservoir to the atmosphere (through diffusion and ebullition) were found to decrease substantially with time, the degassing of CH<sub>4</sub> downstream of the turbines remains constant [Abril et al., 2005, dos Santos et al., 2005]. Guérin et al. [2006] found significant CH<sub>4</sub> fluxes downstream of reservoirs in the order of 48–960 mg m<sup>-2</sup> d<sup>-1</sup>. Kemenes et al. [2007] estimate the CH<sub>4</sub> emissions downstream of the Balbina reservoir, which is the largest hydroelectric reservoir in the Amazon (cf. Fig. 2.10 red), to contribute 3% of the total CH<sub>4</sub> released in the Amazon basin. Investigations already started to use these CH<sub>4</sub> emissions as renewable energy source, e.g. by capturing the CH<sub>4</sub> and refining it [Bambace et al., 2007].

Other anthropogenic CH<sub>4</sub> sources in the Amazon basin are CH<sub>4</sub> emissions from biomass burning and cattle ranching. Even though a steep decline in forest cleaning due to governmental efforts is observed (decrease in deforested area from 28,000 km<sup>2</sup> a<sup>-1</sup> in 2004 to 7,000 km<sup>2</sup> a<sup>-1</sup> in 2011)

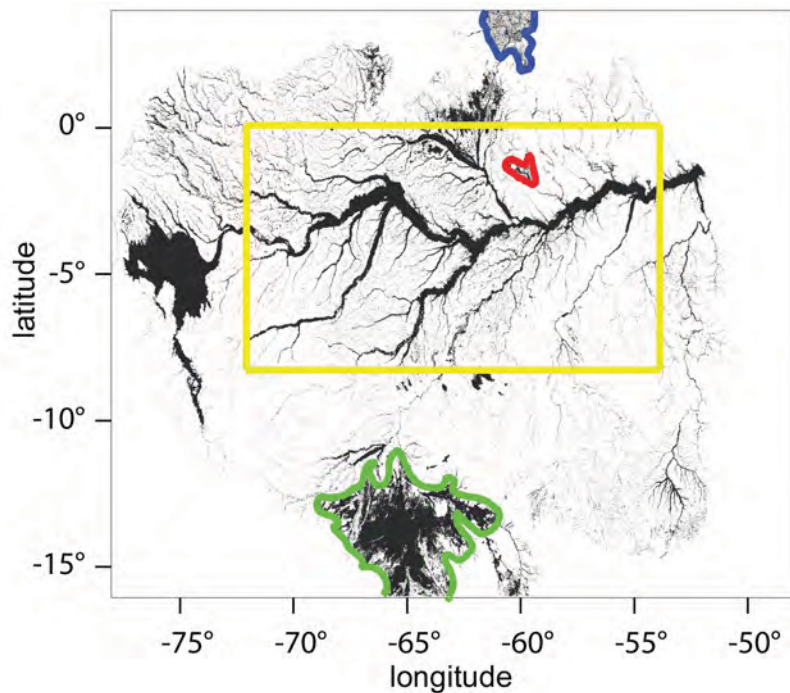


Figure 2.10: Wetland area of the Amazon lowland region ( $<500\text{ m}$ ) as seen by the JERS-1SAR satellite [Hess et al., 2003]. The savannah wetland areas Roraima (blue) and Llanos de Mojo (green), the Amazon mainstream floodplain (yellow), and the Balbina reservoir (red) are indicated.

[Davidson et al., 2012], cattle ranching is responsible for 80% of the Amazon deforestation resulting in increased  $\text{CH}_4$  emissions [Nepstad et al., 2009]. Davidson and Artaxo [2004] state that still changes in land-use have only minor effects on  $\text{CH}_4$  emissions in the Amazon basin as the majority of the emission originates from the wetlands in the intact forest.

Observations of  $\text{CH}_4$  emissions or uptake by soils in the Amazon are reported by Verchot et al. [2000]. They found soils in the primary forest to be a source of  $0.03\text{ mg m}^{-2}\text{ d}^{-1}$  during the wet season and a  $\text{CH}_4$  sink of  $-0.98\text{ mg m}^{-2}\text{ d}^{-1}$  during the dry season. do Carmo et al. [2006] obtained  $\text{CH}_4$  fluxes in the order of  $2\text{--}21\text{ mg m}^{-2}\text{ d}^{-1}$  from the canopy layer of undisturbed upland forest, which could be confirmed by Querino et al. [2011], who found a  $\text{CH}_4$  flux of  $2.8\text{ mg m}^{-2}\text{ d}^{-1}$  for upland forest. However, the biological processes behind these canopy emissions still remain unknown.

## 2.3 Summary

This chapter introduces the reader to atmospheric  $\text{CH}_4$  and the Amazon. Anthropogenic  $\text{CH}_4$  emissions from different production processes led to a doubling of  $\text{CH}_4$  emissions into the atmosphere since pre-industrial times. Relevant anthropogenic emissions sources for the Amazon basin are biomass burning, emission from ruminants, and waste water treatment. The dominant  $\text{CH}_4$  emission source in the Amazon basin are natural emissions from anaerobic production by microbes in natural wetlands. Emission from termites play a minor role. The different  $\text{CH}_4$  source components can be distinguished by differences in the isotopic composition of carbon and hydrogen atoms in  $\text{CH}_4$ . Recently attention was drawn to  $\text{CH}_4$  emissions from hydroelectric reservoirs and upland forests in the Amazon basin. In the Amazon basin, the weather is dominated by mesoscale convective systems. The climate is influenced by large-scale variations as the El Niño Southern Oscillation.



# Chapter 3

## Methods

In this chapter the method of calculating greenhouse gas flux distributions from atmospheric observations (the so-called “top-down approach” using the technique of “atmospheric inversions”) is described. The approach uses a combination of atmospheric observations and atmospheric transport models in order to constrain flux fields of CH<sub>4</sub> and other greenhouse gases. Fluxes constrained by observations are derived for a certain region and time period (“budget estimate”). Both components, the atmospheric observations and the atmospheric transport models, are introduced in detail in this chapter. Different methods for CH<sub>4</sub> flux measurements and CH<sub>4</sub> atmospheric mixing ratio measurements at different spatial and temporal scales (tower-based, airborne, and satellite observations) are discussed. The basic equations of both, global and regional, atmospheric transport models and the inversion mechanism with respect to the relevance of this work are presented. The statistical methods applied within this work are explained.

### 3.1 Top-down approach

Under the framework of the Kyoto Protocol [1997], the world’s countries were requested to reduce their greenhouse gas emissions until the commitment period of 2008–2012 by 5% compared to the year 1990. The scientific community was asked to develop methods for the supervision of greenhouse gas emissions from a single country. One approach consists of the collection of data at several measurement locations and scaling them up to the specific regions of interest. This approach is called “bottom-up” and was used, e.g. within the CarboEurope project to estimate the European CO<sub>2</sub> balance [Schulze et al., 2010]. Over the last years a complementary technique, the so-called “top-down” approach has been established. It uses atmospheric observations and atmospheric transport models to gain information on the surface flux distribution of greenhouse gases. The atmosphere mixes and integrates surface fluxes that vary spatially and temporally [IPCC, 2007]. The method is called “atmospheric inversion”. As illustrated in Fig. 3.1, a prescribed flux field of the tracer of interest is coupled to an atmospheric transport model and the distribution of the atmospheric mixing ratio of that tracer in the atmosphere is simulated. The simulated atmospheric mixing ratio is compared to the observed atmospheric mixing ratio and the flux distribution is optimized in a way that the difference between the modeled and observed atmospheric mixing ratio is minimized (see Sec. 3.4 for details). From the obtained “best guess” of the flux field (called “a-posteriori flux”) the budget estimate of the tracer is calculated. The flux model provides an “initial guess” of the flux field (called “a-priori flux distribution”) for the inversion algorithm. Gurney

et al. [2002] describe the inverse modeling technique as a valuable tool to derive information about the source and sink distribution of trace gases (sources are associated with positive fluxes into the atmosphere and sinks with negative fluxes or uptake of trace gases from the atmosphere by the biosphere).

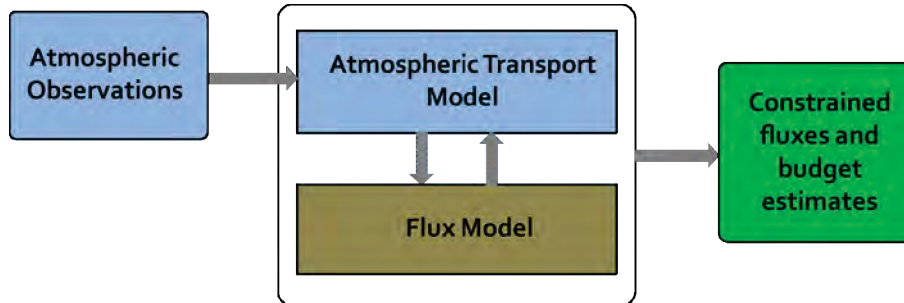


Figure 3.1: Sketch of the budget estimate calculation using atmospheric and biospheric observations within the top-down approach modified from Gerbig et al. [2009].

A first attempt on atmospheric  $\text{CH}_4$  inversions was made in the late 1990s using the TM3 atmospheric transport model [Hein et al., 1997, Houweling et al., 1999]. Nowadays different scientific groups work on global atmospheric  $\text{CH}_4$  inversions [Bergamaschi et al., 2007, 2009, Bousquet et al., 2006, Meirink et al., 2008b, Chen and Prinn, 2006, Mikaloff Fletcher et al., 2004]. The approaches of these groups differ in their choice of the atmospheric transport model using for instance the TM3 model [Hein et al., 1997, Mikaloff Fletcher et al., 2004], the more advanced TM5 version [Bergamaschi et al., 2007, 2009, Meirink et al., 2008b] or other three-dimensional atmospheric chemistry models [Bousquet et al., 2006, Chen and Prinn, 2006]. Further differences lie in their number of atmospheric observations from surface stations used in the atmospheric inversion, the choice of the prescribed a-priori fluxes, and the numerical solution of the inverse problem (Ensemble Kalman Filter [Peters et al., 2004], four-dimensional variational assimilation (4DVAR) [Meirink et al., 2008b], geostatistical approach [Michalak et al., 2004], or the iterative approach of the Jena Inversion System [Rödenbeck, 2005]). Due to the increasing amount of observations from space, Bergamaschi et al. [2007] and Meirink et al. [2008b] started to use observations from the SCanning Imaging Absorption spectroMeter for Atmospheric CHartography (SCIAMACHY) satellite in their inversion scheme besides the standard usage of observations from surface stations.

Two main uncertainty components are involved in this method: the uncertainty of the a-priori fluxes and the uncertainty resulting from the inadequate representation of the observation in the transport model. The uncertainty of the observed atmospheric mixing ratio is small compared to the other two components as identified for  $\text{CO}_2$  by Rödenbeck [2005]. In atmospheric inversion systems, the distribution of observation locations influences the uncertainty reduction for fluxes on grid scale. Studies were conducted to determine the optimal observation network design that would lead to a high uncertainty reduction in the a-posteriori fluxes, e.g. described by Gloor et al. [2000]. Marquis and Tans [2008] claim that a higher density of observations would improve the a-posteriori flux estimates significantly. For global atmospheric inversions, Houweling et al. [1999] found that the uncertainty reduction for the a-posteriori flux field is 75% at the global scale, while the reduction on grid scale was only in the order of 1%. This originates mainly from the fact that global long range transport models cannot resolve the fine-scale features that originate from spatially very heterogeneous flux patterns, e.g. from fossil fuel emissions [Geels et al., 2007]. The

atmospheric transport model uncertainty of global atmospheric transport models was assessed within the TransCom CH<sub>4</sub> project (Chemistry Transport Model InterComparison, [Patra et al., 2009]). Simulations of CH<sub>4</sub> atmospheric mixing ratio with different global atmospheric chemistry transport models using identical CH<sub>4</sub> flux fields have been performed to gain information on the uncertainty of the atmospheric transport [Patra et al., 2009]. The derived atmospheric transport uncertainty calculated in relation to the total obtained annual CH<sub>4</sub> flux of 513 Tg from the models was estimated to 9–14 Tg. This is in the order of 2% [Patra et al., 2011].

To reduce the uncertainty in the a-posteriori flux estimates evolving from unresolved fine-scale structure in global atmospheric transport models, the number of atmospheric CH<sub>4</sub> inversion studies at the regional scale starts to grow continuously [Kort et al., 2008, Zhao et al., 2009, Deutscher et al., 2010, Villani et al., 2010]. The regional atmospheric inversions utilize high-resolution regional atmospheric transport models, e.g. the coupled Weather Research and Forecasting model (WRF) to the Stochastic Time Inverted Lagrangian Transport model (STILT) [Kort et al., 2008, Zhao et al., 2009, Pillai, 2011]. The high-resolution regional atmospheric transport models are able to better represent the short-term variability of the point observations compared to global atmospheric transport models [Geels et al., 2007, Ahmadov et al., 2009, Pillai et al., 2011]. As shown in Ahmadov et al. [2007] and Pillai et al. [2011], regional atmospheric transport models can perform reasonably well in capturing mesoscale meteorological effects such as the land-sea breeze or mountain-valley circulation even in complex terrain. High-resolution regional atmospheric transport models still have uncertainties in the representation of the atmospheric transport. Gerbig et al. [2009] identified that the uncertainties in the representation of vertical mixing in the PBL in regional atmospheric transport models have a high impact on the simulation of the CO<sub>2</sub> distribution in the atmosphere. Uncertainties in the representation of advective transport in the model or the grid resolution have impact on the simulated CO<sub>2</sub> distribution [Gerbig et al., 2009]. However, an estimate of the uncertainty of convective transport processes, which have a large impact on the simulation of the tracer distribution in tropical regions, is not yet reported. The knowledge of the uncertainty in the representation of the atmospheric transport in the model is of major importance in order to distinguish between far field (background) and near field (in the surroundings of the measurement location) influence on the flux signals [Marquis and Tans, 2008, Gerbig et al., 2009].

In the following sections the different single components required for an atmospheric inversion system (observations, atmospheric transport model, and inversion algorithm) are described in more detail. Biospheric flux models for the calculation of a-priori fluxes are discussed in Ch. 4.

## 3.2 Observations

Methane observations can either be obtained as direct flux measurements (emitted from different source processes from or near the ground) or as measurements of the atmospheric mixing ratio. Local flux measurements are frequently used to derive bottom-up budget estimates by upscaling of flux observations to specific regions. For this purpose, two different methods, flux chamber measurements and the eddy-covariance technique, are used. Observations of the CH<sub>4</sub> atmospheric mixing ratio on different spatial scales (e.g. measurements on towers, aircrafts, and satellites) provide additional information on the CH<sub>4</sub> mixing ratio in the atmosphere.



### 3.2.1 Flux measurements

Methane flux measurements are either obtained by direct flux chamber measurements or from calculations based on the eddy-covariance technique. Both are described within this section.

#### Flux chamber measurements

Direct measurements of the  $\text{CH}_4$  flux with flux chambers on the soil-air or water-air interface are continuously used since the 1980s [Sebacher and Harriss, 1982, Bubier et al., 1993, Verchot et al., 2000, Kiese et al., 2003, do Carmo et al., 2006, Baird et al., 2009]. Measurements of the  $\text{CH}_4$  gas concentration is either performed online - with a  $\text{CH}_4$  analyzer in close vicinity of the flux chamber, or offline by syringe sampling at regular time intervals, e.g. of 5 min [Bartlett et al., 1988] and subsequent analysis with the gas chromatography flame ionization detector (GC-FID) [Baird et al., 2009]. Changes in the  $\text{CH}_4$  concentration are continuously monitored with the online method. This method enables a separation between ebullitive and diffusive flux [Bartlett et al., 1988, Crill et al., 1988, Devol et al., 1988]. The ebullitive flux is calculated from the increase in  $\text{CH}_4$  concentration during bubbling episodes [Bartlett et al., 1988]. Flux chambers are still the only way to obtain information on the parameters controlling the  $\text{CH}_4$  flux from the surface to the atmosphere such as water table position or soil temperature [Baird et al., 2009]. However, to derive  $\text{CH}_4$  flux information on a larger spatial scale, flux chambers might be unsuited as they are limited to small areas ( $\sim 1 \text{ m}^2$ ) [Verma et al., 1992]. Here, the eddy-covariance technique could lead to improvements.

#### Eddy-covariance measurements

Based on measurements of the  $\text{CH}_4$  atmospheric mixing ratio and the vertical wind velocity (typically located a few meters above the ground),  $\text{CH}_4$  fluxes are calculated with the eddy-covariance technique [Baldocchi et al., 2012, Verma et al., 1992]. The calculation is based on the conservation equation of a scalar [Aubinet et al., 2000]:

$$\frac{\partial \rho_{CH_4}}{\partial t} + u \frac{\partial \rho_{CH_4}}{\partial x} + v \frac{\partial \rho_{CH_4}}{\partial y} + w \frac{\partial \rho_{CH_4}}{\partial z} = S + D_{air}. \quad (3.1)$$

Here  $\rho_{CH_4}$  denotes the density of atmospheric  $\text{CH}_4$  (mixing ratio multiplied by air density),  $u$ ,  $v$ , and  $w$  are the wind velocity components in horizontal ( $x, y$ ) and vertical  $z$  direction,  $S$  the source (flux) and  $D_{air}$  the diffusion term in free air. After the Reynolds decomposition ( $\rho_{CH_4} = \overline{\rho_{CH_4}} + \rho'_{CH_4}$ ), neglect of diffusion and assumption of atmospheric stationarity and horizontal homogeneity, the equation for the calculation of the  $\text{CH}_4$  flux is simplified to [Aubinet et al., 2000]:

$$\int_0^{h_m} S dz = \overline{w' \rho'_{CH_4}} \quad (3.2)$$

with  $h_m$  indicating the height of the sensor above ground level. The calculated fluxes are integrated over 30 min time periods [Baldocchi et al., 2012, Verma et al., 1992] and values with low turbulence are removed [Rinne et al., 2007]. However, during calm nights when accumulation of  $\text{CH}_4$  occurs close to the surface and in cases where horizontal gradients of the mixing ratio emerge, the eddy-covariance method might lead to an underestimation of the flux as not all above mentioned terms of Eq. (3.1) can be neglected any more. Eddy-covariance measurements of  $\text{CH}_4$

fluxes started in the 1990s [Verma et al., 1992] and became more important recently [Rinne et al., 2007, Hendricks et al., 2008, Smeets et al., 2009, Teh et al., 2011, Querino et al., 2011, Baldocchi et al., 2012]. With this technique flux observations are obtained that are representative for a larger area compared to flux chamber measurements [Smeets et al., 2009]. However, observed  $\text{CH}_4$  fluxes can range within three orders of magnitude at one single station (also for the flux chamber measurements), which makes the interpretation of the obtained fluxes very difficult. They depend on many factors such as geographical, site-management, biophysical or biochemical factors [Baldocchi et al., 2012].

### 3.2.2 Atmospheric mixing ratio observations

#### Ground-based observations

Atmospheric observations of greenhouse gases (especially  $\text{CO}_2$ ) started back in 1958 at the Mauna Loa observatory in Hawaii [Keeling et al., 1976]. Since 1983 atmospheric  $\text{CH}_4$  observations (mostly from flasks, more recently also from continuous measurements) were established at several stations distributed around the globe by the NOAA Earth System Research Laboratory (NOAA-ESRL) [Dlugokencky et al., 1994]. The Advanced Global Atmospheric Gas Experiment (AGAGE) network already started in 1978 with observations of  $\text{CH}_4$  at surface stations [Prinn et al., 2000]. The Commonwealth Scientific and Industrial Research Organization (CSIRO) runs a number of stations with  $\text{CH}_4$  measurements preferably in remote areas [Langenfelds et al., 2002]. As reported by the Global Atmospheric Watch of the World Meteorological Organization (WMO) (<http://www.wmo.int/gaw>)  $\text{CH}_4$  measurements at 160 surface stations in 147 locations distributed over the whole globe are currently (or have been) conducted (see Fig. 3.2 green triangles, stations with additional  $\delta^{13}\text{CH}_4$  measurements are colored in blue). This provides an excellent overview over the global atmospheric  $\text{CH}_4$  distribution. Almost half of the stations (68) are operated by the NOAA-ESRL Global Monitoring Division, while the other stations are run by other networks such as AGAGE or CSIRO or by organizations on country level. Surface stations have not only been established at remote sites in order to obtain information on the atmospheric  $\text{CH}_4$  background mixing ratio, but also closer to industrial areas to gain information on local emission sources. This was required to obtain reliable constraints on the estimates of the land emission sources in inverse models [Gloor et al., 2000]. Besides the observations from the surface stations of the global networks, more than one year of continuous  $\text{CH}_4$  observations (11/2008–04/2010) at the TT34 tower located 60 km north-west of Manaus in the central Amazon are utilized within this work. The location of the TT34 tower is marked as black triangle in Fig. 3.2.

From tall tower measurements, additional information on emission sources can be obtained. Sampling at different heights up to  $\sim 500$  m above the ground allows for a separation between signals from local emission sources (near-field influence) and signals originating from the regional scale (far field) [Gloor et al., 2001a]. Besides providing information on emission sources or polluted areas, tall towers allow detailed studies of the biological exchange, boundary layer dynamics, and advective and vertical transport of trace gases [Bakwin et al., 1998]. The first tall towers were built in the United States in 1992–1994 (North Carolina (610 m) and Wisconsin (447 m)) [Bakwin et al., 1998]. In Europe within the Continuous High-precision Tall Tower Observations of greenhouse gases project (CHIOTTO) eight tall towers were established between 1998–2005. The tall towers are mainly distributed over central Europe and have one to five measurement levels [Vermeulen et al., 2007]. Methane measurements are conducted at each of the eight towers. The

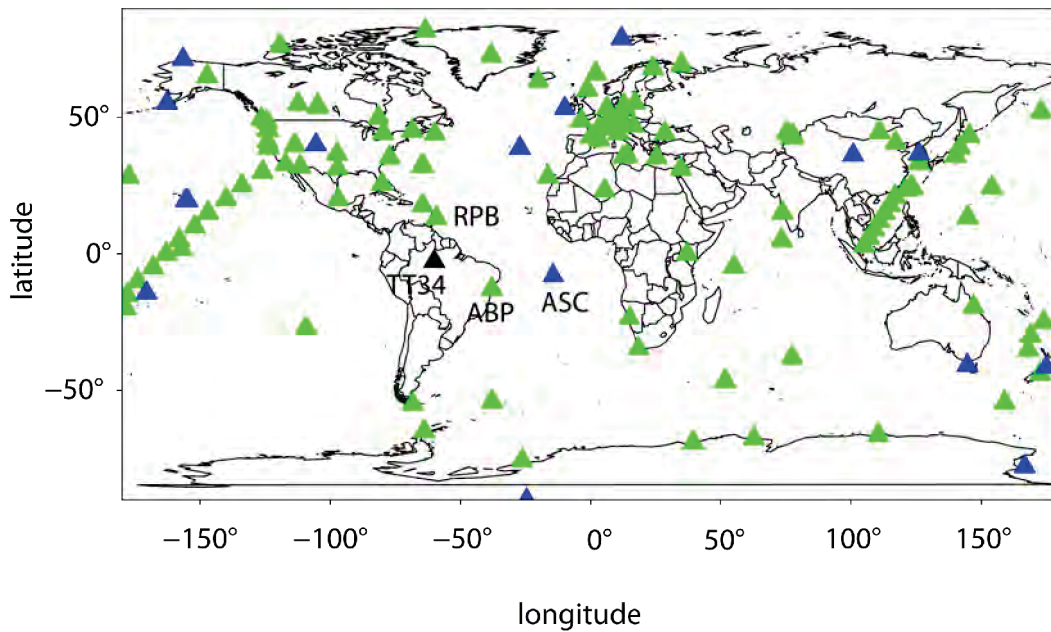


Figure 3.2: Overview over the  $\text{CH}_4$  measurement locations (green). Stations which additionally measure  $\delta^{13}\text{CH}_4$  are marked in blue. The background stations around the Amazon basin are indicated with letters (RPB–Ragged Point Barbados (BDS), ASC–Ascension Island (UK), ABP–Arembepe (BZ)). The TT34 tower in the Amazon basin is denoted as a black triangle. Data were obtained from WMO Global Atmospheric Watch (<http://gaw.kishou.go.jp/cgi-bin/wdcgg>).

Integrated Carbon Observing System (ICOS) ([www.icos-infrastructure.eu](http://www.icos-infrastructure.eu)) together with the Earth Networks Company ([www.earthnetworks.com](http://www.earthnetworks.com)) will establish  $\sim 50$  new observation stations (including surface stations and tall towers) within Europe in the next years. The Max Planck Institute for Biogeochemistry (MPI-BGC) operates two of the already existing eight tall towers in Europe: the tower in Bialystok, Poland [Popa et al., 2010] and the Ochsenkopf tower in the Fichtelgebirge, Germany [Thompson et al., 2009]. In addition, the ZOTino Tall Tower Observatory (ZOTTO) in Siberia where  $\text{CH}_4$  measurements were already conducted by MPI-BGC in the years 2005–2006 [Kozlova et al., 2008] was newly equipped in 2009 with a continuous measurement system measuring simultaneously at six different heights [Winderlich et al., 2010]. In the near future the Amazonia Tall Tower Observatory (ATTO) will be established close to Manaus in the Amazon basin (<http://www.mpic.de/ATTO.125.0.html>).

### Airborne observations

Airborne observations are a powerful technique to obtain detailed information on the vertical and horizontal  $\text{CH}_4$  distribution in the atmosphere up to the lower stratosphere in heights of 10–12 km [Brenninkmeijer et al., 1995]. The observations onboard of aircrafts close the data gap at the regional scale between the local observations at surface stations (as reported above) and the global observations from space (discussed below) [Dolmann et al., 2006]. These observations provide high spatial coverage and budget estimates at the regional scale can be derived with the additional use of atmospheric transport models [Gerbig et al., 2003a,b]. Airborne observations are used to

validate total column measurements (observation of the atmospheric mixing ratio of a tracer in the total atmospheric column ranging from the earth's surface to space) or to evaluate atmospheric transport models [Geibel et al., 2012, Wecht et al., 2012, Ahmadov et al., 2009]. They further provide the chance to study the troposphere-stratosphere exchange of trace gases [Zahn et al., 2004a,b, Schuck et al., 2009]. In principle three different types of aircraft observations for research purposes are conducted. They differ in their temporal and spatial resolution:

1. **Local stationary airborne profiles** at regular time intervals, e.g. over Manaus and Santarém in the Amazon basin [Miller et al., 2007], over several stations in Siberia [Arshinov et al., 2009], and at several sites in the United States conducted by NOAA-ESRL;
2. **Measurements onboard of commercial airliners**, which cover a wider range still on regular time intervals have been established since the 1990s [Brenninkmeijer et al., 2007]. Those observations are especially suited for studying the troposphere-stratosphere exchange as they regularly reach high altitudes. Most prominent projects are the Civil Aircraft for Regular Investigation of the Atmosphere Based on an Instrument Container project (CARIBIC) [Brenninkmeijer et al., 2007], the MOZAIC project (Measurement of Ozone and Water Vapor by Airbus In-Service Aircraft) [Marengo et al., 1998], and the Comprehensive Observation Network for Trace gases by AirLiner (CONTRAIL) [Machida et al., 2008]. Matsueda and Inoue [1996] already reported of CH<sub>4</sub> and CO<sub>2</sub> observations onboard of commercial airliners in the years 1993–1994. In the next years the IAGOS project (In-service Aircraft for a Global Observing System) will follow up the two European projects MOZAIC and CARIBIC to ensure aircraft observations of trace gases, including greenhouse gases onboard commercial airliners [Volz-Thomas et al., 2009];
3. **Aircraft campaigns at the regional scale** with low time intervals enable a very detailed snap-shot of the vertical distribution of trace gases in the troposphere. Examples for these aircraft campaigns are the CO<sub>2</sub> Budget and Rectification Airborne study (COBRA) over the United States [Gerbig et al., 2003a, Kort et al., 2008], the Carbo Europe Regional Experiment Strategy (CERES) [Dolmann et al., 2006, Sarrat et al., 2009], or the HIAPER Pole-to-Pole Observations (HIPPO) [Wofsy, 2011]. Over the Amazon basin, several aircraft campaigns were conducted starting already in the 1980s with the Amazon Boundary Layer Experiment (ABLE2A+B) [Harriss et al., 1988, 1990], the Smoke, Clouds, and Radiation study (SCAR-B) in 1995 [Ferek et al., 1998], the Cooperative LBA Airborne Regional Experiment (LBA-CLAIRE 2001) [Andreae et al., 2002, Lloyd et al., 2007], and The Tropical Forest and Fire Emissions Experiment (TROFFEE) in 2004 [Yokelson et al., 2007]. While most of these airborne campaigns in the Amazon focused on emissions from biomass burning, the aim of the two aircraft campaigns conducted within the BARCA project was to assess the carbon balance of the Amazon basin [Andreae et al., 2012] (cf. Ch. 5).

## Satellite observations

Observations from space gain more and more importance as they draw a global picture of various climate dependent variables. Observations of atmospheric greenhouse gases, detection of fires, precipitation or estimation of the inundated wetland area from space are only a small fraction of the various applications. In the following the instruments from which observations within this work are utilized are explained in more detail:

### Optical sensors for the observation of greenhouse gases from space

Instruments with optical sensors are particularly suitable for observations of greenhouse gases and other atmospheric constituents. They either determine the  $\text{CH}_4$  atmospheric mixing ratio by the absorption of the reflected solar radiation by the  $\text{CH}_4$  molecules (near infrared–NIR) or by measuring the thermal infrared emission from greenhouse gases in the atmosphere (thermal infrared–TIR). Thermal infrared emissions from atmospheric  $\text{CH}_4$  molecules have a lower intensity compared to the infrared emissions from the earth due to the cooler temperature [Archer, 2010]. The frequencies at which the molecules emit the infrared radiation are determined by the vibrational modes of the molecules. For  $\text{CH}_4$  the main absorption bands lie in the near-infrared in the region of 7.7  $\mu\text{m}$ , 3.31  $\mu\text{m}$ , 2.35  $\mu\text{m}$ , and 1.66  $\mu\text{m}$  [Cooley, 1925, Norris and Unger, 1933].

The observation of  $\text{CH}_4$  from space started already in the early 1990s with the Halogen Occultation Experiment (HALOE) [Park et al., 1996]. Later instruments are the Atmospheric InfraRed Sounder (AIRS) [Aumann et al., 2003, Xiong et al., 2008] or the Infrared Atmospheric Sounding Interferometer [Crevoisier et al., 2009] that provided measurements of the total atmospheric  $\text{CH}_4$  column. The first total column measurements of  $\text{CH}_4$  that found applications in atmospheric inversion systems are from the SCanning Imaging Absorption spectroMeter for Atmospheric CHartography (SCIAMACHY) instrument onboard ENVISAT [Bergamaschi et al., 2007]. The SCIAMACHY instrument has a spectral range of 0.24–2.38  $\mu\text{m}$  ranging from ultraviolet to near-infrared with a spectral resolution of 0.2–1.5 nm. The footprint size is 25 km and the global coverage is achieved every six days [Bovensmann et al., 1999]. Due to its large spectral range, tropospheric columns of various atmospheric constituents such as  $\text{O}_3$ ,  $\text{NO}_2$ , CO,  $\text{CH}_4$  or  $\text{H}_2\text{O}$  are derived [Bovensmann et al., 1999]. Two different groups (one at the University of Bremen and one at the Netherlands Institute for Space Research (SRON)) have been working on retrieval algorithms for total atmospheric  $\text{CH}_4$  columns from SCIAMACHY [Buchwitz et al., 2006, Frankenberg et al., 2005, 2008] and now present continuous time series of the years 2003–2009 [Schneising et al., 2011, Frankenberg et al., 2011]. They both use  $\text{CH}_4$  obtained from channel 6 with a spectral range of 1.5–1.7  $\mu\text{m}$  [Schneising et al., 2011, Frankenberg et al., 2011]. So far only the SRON retrievals [Frankenberg et al., 2008] are utilized in global atmospheric inversions [Bergamaschi et al., 2007, Meirink et al., 2008b].

Recently the Greenhouse gas Observing SATellite (GOSAT) was launched (2009), which provides total atmospheric column measurements of  $\text{CO}_2$  and  $\text{CH}_4$  with a footprint of 10.5 km. The global coverage is achieved every three days [Morino et al., 2011]. Upcoming space-borne missions for  $\text{CH}_4$  in the next years are the joint French-German Methane Remote Sensing Lidar Mission (MERLIN) ([http://www.dlr.de/pa/desktopdefault.aspx/tabid-2342/6725\\_read-26662/](http://www.dlr.de/pa/desktopdefault.aspx/tabid-2342/6725_read-26662/)) that is planned for 2014 or the Carbon Monitoring Satellite (CarbonSat) mission for  $\text{CO}_2$  and  $\text{CH}_4$  to be launched in 2018 [Bovensmann et al., 2010].



Additionally, atmospheric total column measurements are conducted with ground-based Fourier-Transform-Spectrometers (FTS). These instruments are currently located at more than 20 stations around the globe and connected via the Total Carbon Column Observation Network (TCCON) [Geibel et al., 2010, Petersen et al., 2010, Messerschmidt et al., 2011a]. Those observations are preferably taken for the comparison to satellite observations, e.g. to SCIAMACHY [Sussmann et al., 2005, Schneising et al., 2012] or GOSAT [Parker et al., 2011, Morino et al., 2011]. On the other hand FTS observations are validated against insitu observations of airborne campaigns [Geibel et al., 2012, Messerschmidt et al., 2011b].

#### **Active and passive microwave sensors for the observation of wetland area**

Active and passive microwave sensors, e.g. Radio Detection and Ranging (RADAR) instruments with wavelengths of  $\lambda \approx 1\text{--}80$  cm are useful for microwave imaging of the earth's surface. The Synthetic Aperture RADAR (SAR) technique, as used by the Japanese Earth Resources Satellite 1 Synthetic Aperture Radar (JERS-1SAR), has high spatial resolution (20 km–20 m) and very limited temporal availability [Hess et al., 2003]. With an active microwave sensor the Doppler history of objects that changes when moving towards or away from them based on the reflectance and backscatter is determined. The so-called L-Band with a wavelength of  $\lambda \sim 20\text{--}30$  cm has the ability to penetrate through the canopy capturing double bounce scattering from flooded forest. This characteristic makes SAR observations particularly applicable for estimations of the wetland area [Hess et al., 2003]. Compared to optical sensors, the advantage of active microwave sensors is the independence of sunlight and meteorological conditions (especially clouds), i.e. 100% transmission through clouds.

The Special Sensor Microwave/Images (SSM/I) onboard the Defense Meteorological Satellite Programm (DMSP) polar orbiters measures the microwave brightness temperatures of the earth twice daily at four different frequencies between 19–85 GHz (corresponding to wavelength of 3.5–16  $\mu\text{m}$ ) with vertical and horizontal polarization. The surface emissivity is derived after removing the contributions from atmospheric clouds [Prigent et al., 2001b]. Open water surfaces (lakes and inundated areas) can be detected by passive microwave measurements because of their very low emissivity in vertical and horizontal polarization and the high polarization difference between vertical and horizontal polarization [Prigent et al., 2001b]. Generally, passive microwave sensors have a low spatial resolution  $\sim 27$  km and higher temporal resolution compared to SAR as reported by Sippel et al. [1998].

#### **Satellite observations for fire pixel detection**

Satellites are valuable to detect fires and their corresponding burned area from space. Wavelength for fire detection are located in the range of the near to the thermal infrared. The Moderate Resolution Imaging Spectroradiometer (MODIS) instrument observes biological and physical processes on earth and the lower atmosphere and among other variables the surface temperature [EO Handbook, 2011]. For MODIS the burned area is derived from the reflectance product at the surface (describing the ratio of reflected radiation to incident radiation at the earth's surface) [Giglio et al., 2010] and the fire pixels are calculated from the brightness temperature (defined as the temperature of the surface assuming an emissivity of 1.0) [Justice et al., 2002]. From the Advanced Very High Resolution Radiometer (AVHRR), e.g. land and sea surface temperatures and vegetation indices are obtained. It measures reflected and emitted radiation at wavelength of 0.58–12.5  $\mu\text{m}$  with a spatial resolution of 1 km [Giglio et al., 1999]. From the temperature at the surface and the

reflectance, the location of the fires are determined [Setzer and Pereira, 1997]. The Geostationary Operational Environmental Satellite - Wildfire Automated Biomass Burning Algorithm (GOES WF\_ABBA) uses the sensitivity of the shortwave infrared band to high temperature anomalies of subpixels to derive fire pixels [Prins et al., 1998].

#### **Satellite observations of precipitation**

The most prominent observation of precipitation from space is the Tropical Rainfall Monitoring Mission (TRMM), which was launched in 1997 sampling between  $35^{\circ}\text{N}$  and  $35^{\circ}\text{S}$ . The precipitation radar instrument measures the precipitation rate in the tropics. It operates at a single frequency of 13.8 GHz (corresponding to a wavelength of  $22\ \mu\text{m}$ ) and a horizontal resolution of 5 km at ground. Vertical profiles of rain are identified up to heights of 20 km. Rainfall is detected above a minimum rate of  $0.7\ \text{mm h}^{-1}$ . Precipitation estimates from TRMM are obtained at  $0.25^{\circ}\times 0.25^{\circ}$  horizontal and 3 h temporal resolution (<http://trmm.gsfc.nasa.gov>).

### **3.3 Atmospheric transport models**

Atmospheric transport models simulate the distribution of greenhouse gas tracers (e.g.  $\text{CO}_2$  or  $\text{CH}_4$ ) in the atmosphere. Depending on the type of transport model they cover different horizontal resolutions (coarse resolution of  $\sim 5^{\circ}\times 5^{\circ}$  for global atmospheric transport models to  $2\ \text{km}\times 2\ \text{km}$  for regional atmospheric transport models). Global atmospheric transport models reach a maximum horizontal resolution of  $1^{\circ}\times 1^{\circ}$  due to computational power constraints. They are a useful tool for describing the global variability and long term change of the atmospheric mixing ratio of trace gases. The long range transport and the trace gas exchange between troposphere and stratosphere are further study objects of global atmospheric transport models [Krol et al., 2005]. Regional atmospheric transport models find their application in the study of high-resolution simulations of the tracer distribution in the atmosphere. They include mesoscale atmospheric effects such as land-sea breeze or mountain-valley circulation and resolve subgrid-scale variability compared to global atmospheric transport models [Gerbig et al., 2009, Ahmadov et al., 2009]. Regional atmospheric transport models are utilized for tracer transport simulations at a maximum horizontal resolution of 2 km [Pillai et al., 2011]. In this section, both the regional atmospheric transport models WRF and STILT and the global atmospheric transport models TM3 (and TM5) are briefly described with respect to their applications in the following chapters.

#### **3.3.1 Weather Research and Forecasting model (WRF)**

The Weather Research and Forecasting model (WRF) evolved from the MM5 model, a mesoscale model that was developed by Pennsylvania State University and the National Center of Atmospheric Research (NCAR, Boulder) in the United States in the 1960s. The WRF model was officially released in 2002. It is a mesoscale numerical weather prediction model serving both applications, operational numerical weather prediction and atmospheric research (<http://www.wrf-model.org/index.php>). Two versions of WRF with different cores exist: Advanced Research WRF (ARW) and Non-hydrostatic Mesoscale Model (WRF-NMM). Both versions differ, e.g. in their temporal and spatial discretization and have been developed at two different institutions (ARW at NCAR and WRF-NMM at the National Center for Environmental Prediction (NCEP), Maryland, US). The following description refers only to the ARW core and is mainly



based on Michalakes et al. [2005], Skamarock et al. [2008], and Peckham et al. [2009], if not stated differently.

The governing equations of the WRF model are the Euler equations as special case of the Navier-Stokes equations. They are written in flux form in terms of the terrain-following hydrostatic pressure vertical coordinate  $\eta$ :

$$\partial_t U + (\nabla \cdot \mathbf{V}u) - \partial_x(p\partial_\eta\Phi) + \partial_\eta(p\partial_x\Phi) = F_U \quad (3.3)$$

$$\partial_t V + (\nabla \cdot \mathbf{V}v) - \partial_y(p\partial_\eta\Phi) + \partial_\eta(p\partial_y\Phi) = F_V \quad (3.4)$$

$$\partial_t W + (\nabla \cdot \mathbf{V}w) - g(\partial_\eta p - \mu_{mod}) = F_W \quad (3.5)$$

$$\partial_t \Theta + (\nabla \cdot \mathbf{V}\theta) = F_\Theta \quad (3.6)$$

$$\partial_t \mu_{mod} + (\nabla \cdot \mathbf{V}) = 0 \quad (3.7)$$

$$\partial_t \Phi + \mu_{mod}^{-1}[(\mathbf{V} \cdot \nabla \Phi) - gW] = 0 \quad (3.8)$$

together with the diagnostic relation for the inverse air density  $\alpha$ :

$$\partial_\eta \Phi = -\alpha \mu_{mod} \quad (3.9)$$

and the equation of state:

$$p = p_0 (R_d \theta / p_0 \alpha)^\gamma. \quad (3.10)$$

The terrain-following hydrostatic pressure vertical coordinate  $\eta$  is defined as:

$$\eta = (p_h - p_{ht}) / \mu_{mod} \quad (3.11)$$

with

$$\mu_{mod} = p_s - p_{ht} \quad (3.12)$$

$p_h$  represents the hydrostatic pressure,  $p_{ht}$  the pressure at the model top and  $p_s$  the pressure at the earth's surface.  $\mu_{mod}(x, y)$  expresses the mass per unit area for the total atmospheric column. The flux form variables, e.g. the velocity vector or the potential temperature are defined as  $\mathbf{V} = \mu \mathbf{v} = (U, V, W)$  and  $\Theta = \mu \theta$ , respectively. Further variables used in eqs. (3.3) to (3.10) are the geopotential  $\Phi = gz$  with  $g$  being the standard gravity, the pressure  $p$ , the reference pressure  $p_0 = 10^5$  Pa, the inverse air density  $\alpha = 1/\rho_{air}$ , the gas constant for dry air  $R_d$ , the ratio of the heat capacity for dry air  $\gamma = c_p/c_v$ , and the forcing terms  $F_U, F_V, F_W, F_\Theta$ . The forcing terms originate from the model physics, turbulent mixing, projections, and earth rotation.

The spatial discretization in horizontal direction is based on the Arakawa C grid. For the temporal discretization the 3rd order Runge-Kutta time-split integration scheme is used. WRF permits several different map projections such as the Lambert Conic Conformal projection, mercator projection, polar projection or lat-lon projection. Lateral boundary conditions for "real-data" cases are placed at the coarse domain on all four sides of the domain with a fixed external value and a relaxation zone of five grid cells to adjust to the model value. WRF additionally allows for both one-way and two-way nesting: In case of one-way nesting the coarse grid provides only the lateral boundary conditions for the nested grid. For two-way nesting, the values calculated within the nested grid replace those of the coarse grid without relaxation zones.

In Fig. 3.3 the structure of the WRF model is illustrated. The WRF Preprocessing System (WPS) interpolates meteorological forcing fields horizontally and vertically to the desired projection and

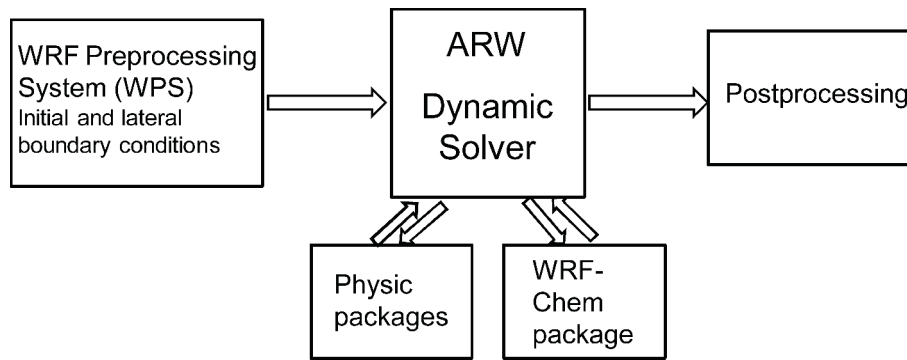


Figure 3.3: Simplified illustration of the main components of the WRF model using the ARW core (based on Michalakes et al. [2005], Skamarock et al. [2008], Peckham et al. [2009]).

vertical pressure levels. The main part of the WRF model is the dynamic solver that contains the above described Euler equations, nesting capabilities, time integration, etc.. Prognostic variables of the WRF model are the velocity components  $(u, v, w)$ , the potential temperature, geopotential, and surface pressure of dry air. Between two time-steps of the dynamic solver, different physic schemes calculate tendencies of the prognostic variables. Most of the physic schemes are one-dimensional column models calculating the tendency for the corresponding grid cell or column, respectively. In the same way, the WRF-Chem modules feed emissions of various trace gases between two time-steps into the dynamic solver. In the following, the relevant physic schemes and the main aspects of the chemistry part of the WRF model (WRF-Chem) are explained.

Five different physic schemes of the WRF model are explained in more detail here: microphysics, convective scheme, PBL scheme, radiation scheme, and the land-surface model. The PBL scheme and the land-surface model are called every time step. The interval for the other schemes is specified by the user. For each scheme, one can choose between several options. The options later used in this work are explained briefly.

The microphysics scheme explicitly describes the physical processes of cloud formation including precipitation processes. The WRF Single-Moment 5-class scheme (WSM5) resolves the five variables water vapour, cloud water, cloud ice, snow, and rain. The WSM6 microphysics scheme additionally includes graupel as sixth variable.

Convective schemes are important for representing convective or shallow clouds when the horizontal resolution does not allow resolving these processes with the microphysics scheme. Vertical fluxes from unresolved up- and downdrafts are described. They provide the convective component of the precipitation. These schemes are useful for gridsizes  $>10$  km. For gridsizes  $<5$  km when single clouds can be resolved by the model, those schemes are less useful. In the WRF model, one of the most prominent convective schemes is the Grell-Dévényi (GD) convective scheme [Grell and Dévényi, 2005]. This scheme is constructed as an ensemble cumulus scheme consisting of 144 ensemble members. The ensemble members are run at each grid box for the total column and the results are averaged and reported back to the dynamic solver. The relatively new Grell 3 scheme (G3) is similar to the GD convective scheme as it also uses the ensemble mean approach. Additionally, it enables spreading of subsidence effects to neighboring grid columns, which makes this scheme more suitable for gridsizes less than 10 km.

The PBL scheme in WRF prescribes the vertical subgrid scale flux from the eddy-transport in the total atmospheric column. The heat and moisture fluxes within the well-mixed boundary layer are determined and the tendencies for temperature and moisture are reported to the dynamic solver. For most of the WRF simulations in this work, the Mellor-Yamada-Janjic (MYJ) PBL scheme is used. The Mellor-Yamada-Nakanishi-Niino (MYNN) scheme is a further development of the MYJ PBL scheme correcting observed underestimations in the mixed-layer depths in the MYJ scheme [Nakanishi and Niino, 2004].

In the radiation scheme atmospheric heating is calculated using incoming shortwave and outgoing longwave radiation. For the calculation of the longwave radiation, the response to water vapour, CO<sub>2</sub>, O<sub>3</sub>, and other trace gases is considered that absorb and emit infrared and thermal radiation. The shortwave radiation is described by the visible and surrounding wavelengths of the solar spectrum. The Rapid Radiative Transfer Model (RRTM) uses prescribed tables for the representation of longwave emissions and absorption processes of water vapour, CO<sub>2</sub>, or O<sub>3</sub> in the atmosphere and accounts for the cloud optical depth [Mlawer et al., 1997]. The RRTMG radiation scheme is a further development of the RRTM mainly by improvements in the computational efficiency [Iacono et al., 2008].

The land-surface model calculates heat and moisture fluxes from the atmospheric variables and serves as a lower boundary condition for the vertical transport in the PBL scheme. Compared to the cumulus, PBL, and radiation scheme, the land-surface model does not provide any tendencies, but updates the land state variables. These variables include skin temperature (temperature at surface), soil temperature, soil moisture, snow cover, and possible canopy properties. Similar to the other schemes it is a one-dimensional column model without any interaction to the neighboring gridcells. The Noah Land Surface Model (NOAH-LSM) used in this work consists of four layers for soil moisture and soil temperature at depths (bottom) of 10 cm, 40 cm, 1 m, and 2 m. It includes a root zone, evapotranspiration, soil drainage, runoff, different vegetation categories, and information on soil texture.

The Chemistry part of the WRF model (WRF-Chem) provides emissions (anthropogenic and biogenic) of specified trace gases to the dynamics solver. Different chemical mechanisms that prescribe the chemical reactions of trace gases in the atmosphere such as aerosol interaction, photolysis, gas phase chemical mechanisms or dry deposition are implemented in the WRF-Chem code. The coupling of the full chemistry to the WRF code opens the chance for further applications of the WRF model such as air quality studies or studies considering climate change impacts.

In the context of atmospheric transport simulations of greenhouse gases, the WRF model is used in two different ways. First, it serves as meteorological input for regional greenhouse gas budget studies using the Stochastic Time Inverted Lagrangian Transport model (STILT; details below) as described in Nehrkorn et al. [2010], Kort et al. [2008], Zhao et al. [2009], Pillai et al. [2011]. Second, Ahmadov et al. [2007] coupled the Vegetation Photosynthesis and Respiration model (VPRM) [Mahadevan et al., 2008] to the WRF-Chem model to enable calculation of biospheric CO<sub>2</sub> fluxes within the WRF-Chem model. It allowed to use WRF for high-resolution forward simulations of CO<sub>2</sub> [Ahmadov et al., 2009, Pillai et al., 2010, 2011].

### 3.3.2 Tracer transport models TM3 and TM5

The TM3 model is a global atmospheric tracer transport model and a further development of the Tracer Transport Model (TM) originally written as TM2 by Heimann [1996]. It solves the continuity equation for tracer  $X$ :

$$\frac{\partial}{\partial t} \rho_{air} X + \nabla \times \rho_{air} \mathbf{v} X = S \quad (3.13)$$

Here  $\rho_{air}$  denotes the air density,  $\mathbf{v}$  the wind velocity vector and  $S$  the source or sink volume of the tracer [Heimann and Koerner, 2003]. The model accounts for advection, diffusion, and sub-grid scale vertical transport through vertical diffusion and cloud cumulus transport. The vertical coordinates are hybrid sigma-pressure coordinates. The pressure levels  $p_l$  are defined through real coefficients  $a_l$  and  $b_l$  of the corresponding vertical levels  $l$  and the surface pressure  $p_s$  via the following equation:

$$p_l = a_l + b_l \times p_s \quad (3.14)$$

For simulations using the NCEP meteorology, the vertical coordinates are pure sigma coordinates and  $a_l$  is set to zero [Heimann and Koerner, 2003]. Simulations with the TM3 model can be performed on different horizontal resolutions (including a different number of vertical levels) [Heimann and Koerner, 2003]. TM3 has already been used in a couple of inversion studies both for  $\text{CO}_2$  and  $\text{CH}_4$ , e.g. by Houweling et al. [1999] with the previous version TM2 or as described by Rödenbeck et al. [2003] for  $\text{CO}_2$  and Hein et al. [1997] and Mikaloff Fletcher et al. [2004] for  $\text{CH}_4$ .

Resolution	Acronym	Horizontal Resolution	No. vertical levels
coarse	cg	$\sim 10^\circ \times 8^\circ$	9
fine	fg	$\sim 5^\circ \times 4^\circ$	19
very fine	vfg	$\sim 1.875^\circ \times 1.875^\circ$	28/31
extra fine	xfg	$\sim 1.125^\circ \times 1.125^\circ$	31

Table 3.1: Description of the prescribed TM3 grids, the corresponding horizontal resolution, and number of vertical levels.

The TM5 model is a further development of the TM3 model. Krol et al. [2005] describe the zoom capability with two-way nesting as the most important new feature of TM5 compared to TM3. The TM5 model uses 25 out of 60 hybrid sigma-pressure levels provided by the European Center for Medium-Range Weather Forecasts (ECMWF) (cf. full Eq. 3.14). The default horizontal resolution of the TM5 model is  $6^\circ \times 4^\circ$ . For specific regions of interest, zoom capabilities enable simulations at higher resolution ( $3^\circ \times 2^\circ$  and  $1^\circ \times 1^\circ$ ). Several groups use the TM5 model as transport model for atmospheric inversion and chemistry applications [Bergamaschi et al., 2007, Peters et al., 2004, Villani et al., 2010].

### 3.3.3 Stochastic Time Inverted Lagrangian Transport model (STILT)

In contrast to the Eulerian atmospheric transport models, which simulate the three dimensional distribution of variables, Lagrangian Particle Dispersion Models (LPDM) simulate the trajectories of particles that represent air parcels. The trajectory of a particle can be calculated in forward and

backward mode. LPDMs are able to capture sub-grid scale atmospheric transport and represent turbulence [Stohl, 1998]. Advection and dispersion in the PBL are simulated by turbulent velocity statistics in the trajectories of the tracer particles. The air particles are treated as conserved entities [Stohl and Wotawa, 1995].

In the following the Stochastic Time Inverted Lagrangian Transport (STILT) model as an example for a LPDM is described in more detail. Further examples for LPDMs are the Hybrid Single-Particle Lagrangian Integrated Trajectory model (HYSPLIT) [Draxler and Hess, 1997] or the FLEXPART model [Stohl et al., 2005]. The following mathematical description of the STILT model follows Lin et al. [2003].

The particle velocity vector  $\mathbf{v}$  is decomposed via the Reynold's decomposition in a mean velocity part  $\bar{\mathbf{v}}$  and a turbulent part  $\mathbf{v}'$ . The turbulent part of the wind vector of the particle is described as:

$$\mathbf{v}'(t + \Delta t) = R(\Delta t)\mathbf{v}'(t) + \mathbf{v}''(t). \quad (3.15)$$

$R(\Delta t)$  denotes the random autocorrelation coefficient, which is given by an exponential decay function

$$R(\Delta t) = \exp\left(\frac{-\Delta t}{T_L}\right) \quad (3.16)$$

with  $T_L$  being the Lagrangian time scale ranging from  $T_L = 0$  for a random walk distribution to high values of  $T_L$  for advection through the mean wind.  $\mathbf{v}''$  illustrates the random velocity vector. This vector is shaped as a Gaussian distribution with zero mean and a standard deviation that is characterized by the variance of the vertical velocity vector.

In order to link surface fluxes to atmospheric mixing ratios, an influence function  $I(\mathbf{x}_r, t_r | \mathbf{x}, t)$  is defined relating sources and sinks at a given location  $(\mathbf{x}, t)$  (described through  $S(\mathbf{x}, t)$ ) to the atmospheric mixing ratio  $C(\mathbf{x}_r, t_r)$  at the receptor point  $(\mathbf{x}_r, t_r)$  in the following way:

$$C(\mathbf{x}_r, t_r) = \int_{t_0}^{t_r} dt \int_V d^3x I(\mathbf{x}_r, t_r | \mathbf{x}, t) S(\mathbf{x}, t) + \int_V d^3x I(\mathbf{x}_r, t_r | \mathbf{x}, t_0) C(\mathbf{x}, t_0). \quad (3.17)$$

The first term of the right hand side describes the change in the atmospheric mixing ratio resulting from sources and sinks located within the simulation domain. The second term denotes the contribution of the background atmospheric mixing ratio. The total atmospheric mixing ratio at the receptor location is the sum of the two terms as illustrated in Eq. (3.17). The influence function  $I(\mathbf{x}_r, t_r | \mathbf{x}, t)$  is calculated as the density  $\rho_{part}(\mathbf{x}_r, t_r | \mathbf{x}, t)$  of particles at location  $(\mathbf{x}, t)$  that were transported backwards from the receptor point  $(\mathbf{x}_r, t_r)$  normalized by the total number of particles released  $N_{tot}$ . This is written as follows:

$$I(\mathbf{x}_r, t_r | \mathbf{x}, t) = \frac{\rho_{part}(\mathbf{x}_r, t_r | \mathbf{x}, t)}{N_{tot}} = \frac{1}{N_{tot}} \sum_{pt=1}^{N_{tot}} \delta(\mathbf{x}_{pt}(t) - \mathbf{x}). \quad (3.18)$$

The  $\delta$ -function results in the value of 1 in case the particle  $pt$  is found at location  $\mathbf{x}$ . The influence function and the source and sink terms are discretized in time and space by finite intervals. A flux  $f(x, y, t)$  is related to the source (or sink) term  $S(\mathbf{x}, t)$  by

$$S(\mathbf{x}, t) = \frac{f(x, y, t) m_{air}}{h_m \bar{\rho}_{part}(x, y, z)} \quad (3.19)$$

for values of  $z$  below the assumed atmospheric column height  $h_m$  into which the flux  $f(x, y, t)$  is diluted ( $m_{air}$  indicates the air mass and  $\overline{\rho_{part}}(x, y, z)$  the average density below  $h_m$ ). Finally, the changes in the atmospheric mixing ratio  $\Delta C(\mathbf{x}_r, t_r)$  at the receptor point  $(\mathbf{x}_r, t_r)$  (corresponding to the first term on the right hand side of Eq. (3.17)) are described as the product of the footprint  $FP(\mathbf{x}_r, t_r | x, y, t)$  and the flux  $f(x, y, t)$ :

$$\Delta C(\mathbf{x}_r, t_r) = FP(\mathbf{x}_r, t_r | x, y, t) \times f(x, y, t). \quad (3.20)$$

The term footprint  $FP(\mathbf{x}_r, t_r | x, y, t)$  in context of LPDMs describes the surface sensitivity to upstream fluxes and is defined as :

$$FP(\mathbf{x}_r, t_r | x, y, t) = \frac{m_{air}}{h_m \overline{\rho_{part}}(x, y, t)} \frac{1}{N_{tot}} \sum_{p=1}^{N_{tot}} \Delta t_{p,x,y,z}. \quad (3.21)$$

Here  $\Delta t_{p,x,y,z}$  denotes the time a particle stays in the volume  $(x, y, z)$ .

The STILT model is built on the source code of the HYSPLIT model. The main difference to the HYSPLIT model is the different turbulent parametrization and the calculation of the PBL height. The STILT model has already been used in several studies to obtain information on the source distribution, the evaluation of footprints, and the estimation of greenhouse gas budgets at the regional scale [Gerbig et al., 2003b, Kort et al., 2008, Göckede et al., 2010, Pillai et al., 2011]. Nehrkorn et al. [2010] developed a coupler that allows for the usage of WRF meteorology to drive the STILT model. Pillai et al. [2012] investigated that the STILT model can be used as an adjoint transport model to the WRF model. In addition, the STILT model is now part of the Jena Inversion System TM3-STILT [Rödenbeck et al., 2009, Trusilova et al., 2010] that is described in detail in the next section.

### 3.4 Jena Inversion System

Atmospheric inversions derive optimized a-posteriori flux fields with the help of atmospheric observations. Observed atmospheric mixing ratios are compared to modeled atmospheric mixing ratios and the difference is minimized by adjusting the flux fields. One inversion system is the Jena Inversion System. The main equations of this inversion algorithm are described. The two-step inversion scheme using the two transport models TM3 and STILT is explained. This two-step inversion scheme enables global atmospheric inversions at a coarse horizontal resolution of  $\sim 5^\circ \times 4^\circ$  with the TM3 model and a second regional inversion for a specific region at high resolution (e.g.  $1^\circ \times 1^\circ$  or  $0.25^\circ \times 0.25^\circ$ ) with the STILT model. The description in this section is mainly based on Rödenbeck [2005], Rödenbeck et al. [2009], and Trusilova et al. [2010].

The calculation of the modeled atmospheric mixing ratio requires an atmospheric transport model (also referred to as transport matrix or transport operator in the following). The modeled atmospheric mixing ratio  $\mathbf{C}_{mod}$  at a specific location is obtained by the multiplication of the atmospheric transport operator  $\mathbf{A}$  with the flux field  $\mathbf{f}$  and the addition of the initial atmospheric mixing ratio  $\mathbf{C}_{ini}$ :

$$\mathbf{C}_{mod} = \mathbf{A}\mathbf{f} + \mathbf{C}_{ini}. \quad (3.22)$$

Additional constraints on the a-priori flux field are added:

$$\mathbf{f} = \mathbf{f}_{fix} + \mathbf{f}_{adPinv} \quad (3.23)$$



consisting of a fixed flux term  $\mathbf{f}_{\text{fix}}$  and an adjustable flux term  $\mathbf{f}_{\text{ad}} \times \mathbf{p}_{\text{inv}}$ . The parameters  $\mathbf{p}_{\text{inv}}$  are assumed to have zero mean and unit variance for their a-priori values. Fluxes can be defined for different components (e.g. anthropogenic, biogenic or oceanic fluxes). The following equation is a detailed description of the total flux field consisting of different components  $i = 1, \dots, N_{\text{com}}$  for one grid point in time and space:

$$f(x, y, t) = \sum_{i=1}^{N_{\text{com}}} (\beta_{\text{inv},i} f_{\text{fix},i}(x, y, t) + \alpha_{\text{inv},i} f_{\text{sh},i}(x, y, t) G_{\text{tcor}}(t) G_{\text{xycor}}(x, y) p_{\text{inv},i}). \quad (3.24)$$

The first term of the right hand side of Eq. (3.24) describes the fixed flux term. The second term is adjustable with zero mean. This results from the individual adjustable parameters  $p_{\text{inv}}$  that determine the strength and influence of the adjustable term, which are defined in a way that they have zero mean and variance. The temporal and spatial correlation length, i.e., a measure for the correlation of a-priori flux fields within a certain time interval and spatially distributed region is described via  $G_{\text{tcor}}(t)$  and  $G_{\text{xycor}}(x, y)$ . They determine the temporal and spatial decomposition into statistically a-priori independent elements. For the spatial correlation an exponential decay is assumed.  $f_{\text{sh}}(x, y, t)$  is called ‘‘shape function’’ and prescribes the distribution in space and time of the assumed underlying flux.  $\alpha_{\text{inv}}$  is an overall scaling factor for the adjustable flux term. The fixed flux term  $f_{\text{fix}}(x, y, t)$  can either be described by a zero flux or a prescribed flux inventory.  $\beta_{\text{inv}}$  is a scaling factor for the a-priori flux term.

The modeled atmospheric mixing ratio is now written as:

$$\mathbf{C}_{\text{mod}} = \mathbf{C}_{\text{mod,fix}} + \mathbf{A} \mathbf{f}_{\text{ad}} \mathbf{p}_{\text{inv}} \quad (3.25)$$

with

$$\mathbf{C}_{\text{mod,fix}} = \mathbf{A} \mathbf{f}_{\text{fix}} + \mathbf{C}_{\text{ini}}. \quad (3.26)$$

The aim of the inversion system is to optimize the adjustable part of the posterior flux  $\mathbf{f}_{\text{post}}$  (which coincides with  $\mathbf{f}_{\text{ad}} \mathbf{p}_{\text{inv}}$  in eqs. (3.24)–(3.26)) with respect to the mismatch between observed and modeled atmospheric mixing ratio ( $\mathbf{C}_{\text{obs}} - \mathbf{C}_{\text{mod}}$ ) according to the Bayes’ Theorem ( $P$  indicates the probability):

$$P(\mathbf{f}_{\text{post}} | (\mathbf{C}_{\text{obs}} - \mathbf{C}_{\text{mod}})) = \frac{P((\mathbf{C}_{\text{obs}} - \mathbf{C}_{\text{mod}}) | \mathbf{f}_{\text{post}}) P(\mathbf{f}_{\text{post}})}{P(\mathbf{C}_{\text{obs}} - \mathbf{C}_{\text{mod}})}. \quad (3.27)$$

$P((\mathbf{C}_{\text{obs}} - \mathbf{C}_{\text{mod}}) | \mathbf{f}_{\text{post}})$  is defined as:

$$P((\mathbf{C}_{\text{obs}} - \mathbf{C}_{\text{mod}}) | \mathbf{f}_{\text{post}}) \propto \exp\left(-\frac{1}{2}(\mathbf{C}_{\text{obs}} - \mathbf{C}_{\text{mod}})^T \mathbf{Q}_{\text{c}}^{-1} (\mathbf{C}_{\text{obs}} - \mathbf{C}_{\text{mod}})\right) \quad (3.28)$$

while  $P(\mathbf{f}_{\text{post}})$  is expressed as:

$$P(\mathbf{f}_{\text{post}}) \propto \exp\left(-\frac{\mu}{2} \mathbf{f}_{\text{post}}^T \mathbf{f}_{\text{post}}\right). \quad (3.29)$$

$\mathbf{Q}_{\text{c}}$  is defined as the error covariance matrix of the atmospheric mixing ratio mismatch. It consists only of diagonal elements because all off-diagonal elements are set to zero. The diagonal elements are expressed as  $\sigma_i^2$  for  $i = 1, \dots, N$  with  $N$  indicating the number of observations in the corresponding time interval. Observations are pre-selected (e.g. preferably daytime values of



continuous observations to avoid bad representation of the atmospheric transport at night) and a measurement uncertainty is assigned. It is typically chosen to be in the range of  $\sigma_{obs} \sim 0.3$  ppm for  $\text{CO}_2$  and  $\sigma_{obs} \sim 0.4$  ppb for  $\text{CH}_4$ . The transport model uncertainty is dependent on the type of observation (tower, aircraft, etc.) and location of the observation (e.g. background site or continental site) and is in the order of  $\sigma_{mod} = 1.0$  ppm for  $\text{CO}_2$  and  $\sigma_{mod} = 1.5$  ppb for  $\text{CH}_4$ . The total uncertainty  $\sigma_{tot}$  is calculated to:

$$\sigma_{tot} = \sqrt{\sigma_{mod}^2 + \sigma_{obs}^2}. \quad (3.30)$$

To avoid a higher impact of the more frequent continuous observations compared to the less frequent flask observations, a data density weighting is introduced that considers the number of observations  $N^*$  in a weekly time interval and the total uncertainty increases to:

$$\sigma_i = \sqrt{N^*} \sigma_{tot} \quad (3.31)$$

where  $\sigma_i^2$  displays the elements of the error covariance matrix  $\mathbf{Q}_c$ .

As already stated above, the aim of the inversion is to obtain the optimized posterior flux field  $\mathbf{f}_{post}$ . As result,  $P(\mathbf{f}_{post} | (\mathbf{C}_{obs} - \mathbf{C}_{mod}))$  has to be minimized with respect to  $\mathbf{f}_{post}$ . This is written as a minimization of the cost function  $J$ :

$$\begin{aligned} J &= -\ln(P(\mathbf{f}_{post} | (\mathbf{C}_{obs} - \mathbf{C}_{mod}))) \\ &= \frac{1}{2}(\mathbf{C}_{obs} - \mathbf{C}_{mod})^T \mathbf{Q}_c^{-1} (\mathbf{C}_{obs} - \mathbf{C}_{mod}) + \frac{\mu}{2} \mathbf{f}_{post}^T \mathbf{f}_{post} + C. \end{aligned} \quad (3.32)$$

Here, the first term of the second line of Eq.(3.32) corresponds to the observations while the second term in the second line describes the a-priori flux constraints. The minimization of the cost function is done iteratively using the conjugate gradient method with typically 70 iterations for the global inversion and 50 iteration for regional inversion (see below). The factor  $\mu$  was introduced to scale the impact of the a-priori constraint on the Bayesian Inversion. It determines the ratio between the a-priori information and data constraints. For  $\mu \rightarrow 0$  no prior information is used for minimizing the cost function. For high values of  $\mu$  the a-priori flux distribution has a high impact on the minimization of the cost function.

The application of the above presented inversion mechanism within the Jena two-step inversion scheme developed by Rödenbeck et al. [2009] is described as next step. A high-resolution regional inversion within a specified Domain of Interest (DoI) and time Period of Interest (PoI) is performed. Fig. 3.4 illustrates the required steps. First, a global atmospheric inversion with the TM3 transport model is conducted (called ‘‘Step 1 Global Inversion’’) usually for a time period of several years (‘‘FP’’ - full time period). In the first intermediate step, the atmospheric mixing ratios  $\mathbf{C}_{mod, glob}$  of all observation stations are obtained by a forward simulation of the TM3 model using the constrained a-posteriori fluxes  $\mathbf{f}_{glob, post}$  of Step 1:

$$\mathbf{C}_{mod, glob} = \mathbf{A}_{TM3} \mathbf{f}_{glob, post} \quad (3.33)$$

To calculate the influence of the background on the DoI (cf. Eq. (3.17)), a second intermediate step is required. A forward simulation of the TM3 model using the previous constraint a-posteriori fluxes is set up in a way that all fluxes and atmospheric mixing ratios except those within the DoI are set to zero. In this step, the contribution to the modeled atmospheric mixing ratios at the stations from the DoI is estimated (corresponds to the ‘‘near-field’’ contribution within the global

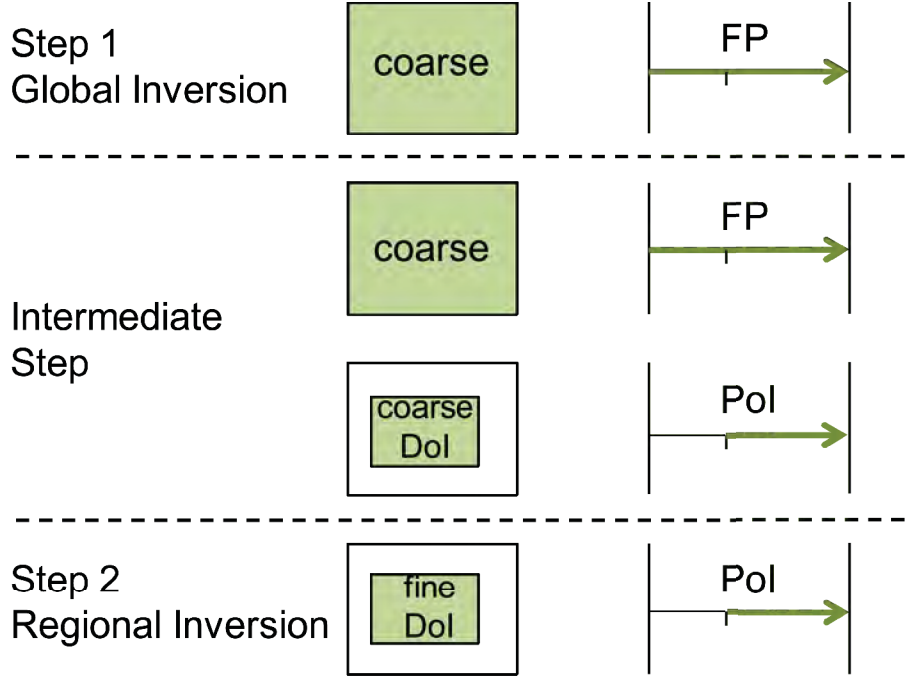


Figure 3.4: Illustration of the two-step inversion scheme (modified from Rödenbeck et al. [2009]). The global inversion with TM3 as the first inversion for the full time period (FP) at the global scale and the regional inversion as second inversion step only for the time period of interest (PoI) and the domain of interest (DoI) after two intermediate steps are demonstrated.

model, which will be replaced by the high-resolution contribution of the regional model in the second step):

$$C_{\text{mod,glob[DoI]}} = A'_{\text{TM3}} f_{\text{glob,post[DoI]}} \quad (3.34)$$

with  $A'_{\text{TM3}}$  being a modified transport operator of the TM3 model. It was modified in a way that tracers emitted within the DoI and PoI leaving the domain cannot re-enter it (achieved by setting tracer fields outside the DoI and PoI to zero). To calculate the contribution of the background to the atmospheric mixing ratio within the DoI ( $C_{\text{mod,back}}$ ),  $C_{\text{mod,glob[DoI]}}$  is subtracted from the atmospheric mixing ratio  $C_{\text{mod,glob}}$  from the first intermediate step:

$$C_{\text{mod,back}} = C_{\text{mod,glob}} - C_{\text{mod,glob[DoI]}} \quad (3.35)$$

The contribution to the atmospheric mixing ratio from the DoI  $C_{\text{mod,reg}}$  is calculated during the second inversion (called “Step 2 Regional Inversion”). The regional inversion uses a high-resolution atmospheric transport operator (e.g. the STILT model) and high-resolution a-priori fluxes  $f_{\text{reg}}$ . The contribution of the atmospheric mixing ratio of the regional inversion  $C_{\text{mod,reg}}$  is calculated to:

$$C_{\text{mod,reg}} = A_{\text{STILT}} f_{\text{reg}} \quad (3.36)$$

The flux  $f_{\text{reg}}$  is separated into a fixed and adjustable flux components analogous to Eq. (3.23). The transport operator  $A_{\text{STILT}}$  can be identified with the footprint definition in Eq. (3.21). The overall calculation of the atmospheric mixing ratio  $C_{\text{tot}}$  at a specified location using the two-step

inversion scheme results in:

$$C_{\text{mod,tot}} = C_{\text{mod,back}} + C_{\text{mod,reg}} \quad (3.37)$$

The described scheme was already successfully applied for CO<sub>2</sub> over Europe by Trusilova et al. [2010] and for CH<sub>4</sub> and N<sub>2</sub>O by U. Karstens within the NITROEUROPE (The nitrogen cycle and its influence on the European greenhouse gas balance) project ([www.nitroeuropa.com](http://www.nitroeuropa.com)). Winderlich [2011] applied it for CO<sub>2</sub> and CH<sub>4</sub> over Siberia.

### 3.5 Statistical methods

The description of the statistical methods utilized in this work is based on von Storch and Zwiers [1999] and Schönwiese [2000].

#### Mean

The mean value  $\bar{x}$  of a distribution is defined as

$$\bar{x} = \frac{1}{n} \sum_{i=1}^n x_i. \quad (3.38)$$

The weighted mean  $\overline{x_W}$  is written as

$$\overline{x_W} = \frac{1}{\sum_{i=1}^n w_i} \sum_{i=1}^n (w_i x_i). \quad (3.39)$$

In case of normalized weights,  $\sum_{i=1}^n w_i = 1$ .

#### Bias

Bias  $x_b$  is defined as the average deviation from the expected mean value  $\bar{x}$

$$x_b = \frac{1}{n} \sum_{i=1}^n |x_i - \bar{x}|. \quad (3.40)$$

A positive bias indicates an overestimation of the expected mean value and a negative bias an underestimation. In this work the notation bias is utilized as the mean difference between model and observations (mean of the residuals).

#### Standard deviation

The standard deviation specifies the strength of the dispersion around the mean value:

$$\sigma = \sqrt{\frac{1}{n-1} \left( \sum_{i=1}^n x_i^2 - \left( \frac{1}{n} \sum_{i=1}^n x_i \right)^2 \right)}. \quad (3.41)$$

Variance is defined as the square of the standard deviation ( $Var(x) = \sigma^2$ ). The standard error of the mean is the standard deviation divided by the square root of  $n$  ( $SE = \frac{\sigma}{\sqrt{n}}$ ).

### Confidence interval

The 95% confidence interval  $I_{conf}$  describes a constructed interval around the mean value  $\bar{x}$  in which the values  $x_i$  are located 95% of the time. In its easiest form (also used in this work) it is calculated as:

$$I_{conf} = \bar{x} \pm z_x \frac{\sigma}{\sqrt{n}} \quad (3.42)$$

with  $z_x$  being the argument of the standardized normal distribution.

### Correlation coefficient

The correlation  $r$  indicates the extend to which a linear relationship between two random variables  $x$  and  $y$  exists. It also called Pearson product-moment correlation coefficient and is defined as:

$$r = \frac{\sum_{i=1}^n x_i y_i - \frac{1}{n} \sum_{i=1}^n x_i \sum_{i=1}^n y_i}{\sqrt{\left[ \sum_{i=1}^n x_i^2 - \frac{1}{n} \left( \sum_{i=1}^n x_i \right)^2 \right] \left[ \sum_{i=1}^n y_i^2 - \frac{1}{n} \left( \sum_{i=1}^n y_i \right)^2 \right]}} \quad (3.43)$$

It can also be written as

$$r = \frac{Cov_{xy}}{\sqrt{Var(x)Var(y)}} \quad (3.44)$$

with  $Cov_{xy}$  indicating the covariance, i.e. the tendency of the jointly distributed variables  $x$  and  $y$  to vary jointly. The values of the correlation coefficient range between  $[-1,1]$  for which  $r = 1$  indicates a perfect linear relationship between  $x$  and  $y$ ,  $r = -1$  a negative linear relationship, and  $r = 0$  no linear relationship.

### Squared correlation

The squared correlation coefficient  $r^2$  is defined as the square of the Pearson product-moment correlation coefficient  $r$ . It describes the proportion of variance of, e.g. the variable  $y$  that can be represented linearly by the variance of  $x$ .

### Linear regression model

The linear regression model allows to obtain a linear equation through which the linear dependence of the variable  $y$  on the variable  $x$  can be described as:

$$y = A_{xy} + B_{xy}x \quad (3.45)$$

$A_{xy}$  and  $B_{xy}$  are the least square estimators for which the sum of the squared errors ( $\sum_{i=1}^n (y_i - A_{xy} - B_{xy}x_i)^2$ ) is minimized. This leads to the two following equation systems with the two unknowns  $A_{xy}$  and  $B_{xy}$ :

$$\bar{y} = A_{xy} + B_{xy}\bar{x} \quad (3.46)$$

$$\sum_{i=1}^n y_i x_i = A_{xy} \sum_{i=1}^n x_i + B_{xy} \sum_{i=1}^n x_i^2 \quad (3.47)$$

which can be solved to:

$$B_{xy} = \frac{\sum_{i=1}^n y_i x_i - \frac{1}{n} \sum_{i=1}^n y_i \sum_{i=1}^n x_i}{\sum_{i=1}^n x_i^2 - \left( \sum_{i=1}^n x_i \right)^2} \quad (3.48)$$

$$A_{xy} = \bar{y} - B_{xy}\bar{x}. \quad (3.49)$$

### 3.6 Summary

This chapter gives an overview over the different methods applied within this work. The top-down approach as a method to derive flux distributions from atmospheric observations is explained. The two components of the top-down approach, namely atmospheric observations and atmospheric transport models, are introduced with respect to their relevance to the following work. Observations of the  $\text{CH}_4$  atmospheric mixing ratio are utilized throughout this work: In Ch. 5 the airborne  $\text{CH}_4$  BARCA data are analyzed and compared to global atmospheric  $\text{CH}_4$  inversions that utilize SCIAMACHY observations. Surface stations from the WMO-GAW network and the TT34 tower observations are used in Ch. 7 for the two-step regional inversion. Simulated WRF precipitation is compared to TRMM observations in Ch. 6. Application of remote sensing based wetland inundation maps within the WRF-GHG model are described in Ch. 6. The location of fire pixels from space find their application in the calculation of  $\text{CH}_4$  emissions from fires as demonstrated in Ch. 4.

With respect to the atmospheric transport models the main focus in this chapter was on the presentation of the Weather Research and Forecasting model (WRF). It is the basis of the WRF Greenhouse Gas model development described in the next chapter. Comparison of BARCA  $\text{CH}_4$  observations to five different TM5 simulations are illustrated in Ch. 5. TM3 and STILT are applied in the Jena two-step regional inversion scheme for the estimation of the annual  $\text{CH}_4$  budget in the Amazon basin.

## Chapter 4

# WRF Greenhouse Gas model (WRF-GHG)

This chapter focusses on the development of the WRF Greenhouse Gas model (WRF-GHG) for high-resolution passive tracer transport (i.e., without any chemical reactions) of CH<sub>4</sub>, CO<sub>2</sub>, and CO. Within this work four new modules were established and implemented in the original WRF-Chem code. Biospheric CH<sub>4</sub> fluxes from wetlands, termites, and soil uptake are calculated “on-line”, i.e., the fluxes are calculated simultaneously with the WRF-Chem meteorology. To write the model code for these biospheric CH<sub>4</sub> flux models was part of this work. All flux models implemented in the WRF-GHG code (including the already existing model for biospheric CO<sub>2</sub> fluxes) and the external emissions inventories relevant for the following studies are described. The four new established modules are specified in detail. Recent modifications required for a distribution of the WRF-GHG code within the official WRF-Chem release from version 3.4 onwards are explained.

Main parts of this chapter are published in:

*Beck, V., T. Koch, R. Kretschmer, J. Marshall, R. Ahmadov, C. Gerbig, D. Pillai, and M. Heimann, (2011): The WRF Greenhouse Gas Model (WRF-GHG). Technical Report No. 25, Max Planck Institute for Biogeochemistry, Jena, Germany.*

### 4.1 Flux models

All flux models that are implemented in the WRF-GHG code, are described with focus on implementation and adaptation of these models to the WRF-Chem code. The external data sets and flux models are explained.

#### 4.1.1 Biospheric flux models implemented in WRF-GHG

Online calculated fluxes in WRF-GHG include biogenic emissions of CO<sub>2</sub> and CH<sub>4</sub> such as biogenic CO<sub>2</sub> fluxes using the Vegetation Photosynthesis and Respiration Model (VPRM), CH<sub>4</sub> fluxes from wetlands based on the wetland inventory of Kaplan, termite emissions of CO<sub>2</sub> and CH<sub>4</sub>, soil uptake of CH<sub>4</sub>, and CH<sub>4</sub> emissions from vegetation.



### The Vegetation Photosynthesis and Respiration Model (VPRM)

The VPRM model, a diagnostic biospheric model, estimates Net Ecosystem Exchange (NEE) on hourly timescale. For the CO<sub>2</sub> flux calculation, two vegetation indices from the Moderate Resolution Imaging Spectroradiometer (MODIS) (Land Surface Water Index (LSWI) and Enhanced Vegetation Index (EVI)), short wave radiation, and surface temperature obtained from WRF are required. A detailed description of the VPRM model is found in Mahadevan et al. [2008].

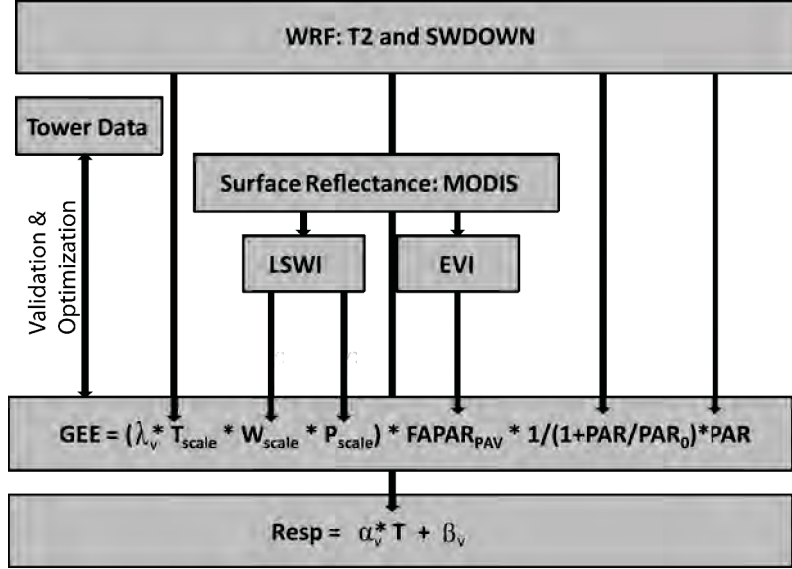


Figure 4.1: Schematic structure of the VPRM model for the estimation of Gross Ecosystem Exchange ( $GEE$ ) and Respiration ( $Resp$ ) based on MODIS surface reflectance and meteorological input variables from WRF. The VPRM parameters ( $\lambda_v$ ,  $PAR_0$ ,  $\alpha_v$ ,  $\beta_v$ ) are validated against observations from eddy-flux towers (adapted from Mahadevan et al. [2008]).

Fig. 4.1 illustrates the basic structure of the VPRM model. LSWI and EVI obtained from MODIS surface reflectance are included in the variables  $P_{scale}$  (accounting for effects of leaf age on photosynthesis) and  $W_{scale}$  (accounting for effects of water stress). The equation to calculate the Gross Ecosystem Exchange ( $GEE$ ) results in:

$$GEE = -\lambda_v \times T_{scale} \times P_{scale} \times W_{scale} \times FAPAR_{PAV} \times \frac{1}{1 + \frac{PAR}{PAR_0}} \times PAR. \quad (4.1)$$

The parameter  $\lambda_v$  describes the maximum quantum yield,  $PAR_0$  the half-saturation value of the photosynthetically active radiation ( $PAR$ ). Both parameters are adjustable and determined by comparison to observations from eddy-covariance towers. The variable  $T_{scale}$  represents the temperature dependence of the photosynthesis, depending on minimum, maximum, and optimal temperature ( $T_{min}$ ,  $T_{max}$  and  $T_{opt}$ ) of the photosynthesis process [Raich et al., 1991]. The short wave incoming radiation (SWDOWN) of the WRF model is used as a proxy for the photosynthetically active radiation ( $PAR$ ).  $FAPAR_{PAV}$  is defined as the Fraction of  $PAR$  absorbed by the photosynthetically active portion of the vegetation ( $PAV$ ) [Mahadevan et al., 2008].

The respiration process ( $Resp$ ) is parameterized as a function of temperature  $T$ :

$$Resp = \alpha_v \times T + \beta_v \quad (4.2)$$

with adjustable parameters  $\alpha_v$  and  $\beta_v$  that are determined by comparison with eddy-covariance measurements. For the temperature  $T$  [ $^{\circ}\text{C}$ ], the 2 m temperature (T2) from WRF is used. The total NEE is calculated as the sum of GEE and respiration:

$$NEE = GEE + Resp \quad (4.3)$$

The VPRM model uses 8 different vegetation classes (Evergreen forest, deciduous forest, mixed forest, shrubland, savanna, cropland, grassland, others) and the parameter set ( $\lambda_v$ ,  $PAR_0$ ,  $\alpha_v$ ,  $\beta_v$ ) is specified explicitly for each vegetation class.

### The Kaplan wetland inventory

The wetland inventory from Kaplan [2002] and Kaplan et al. [2006] with modifications of Drevet [2008] determines  $\text{CH}_4$  emissions from wetlands as fraction of the heterotrophic respiration [Christensen et al., 1996]. Heterotrophic respiration is defined as the release of  $\text{CO}_2$  and  $\text{CH}_4$  from soils to the atmosphere resulting from the decomposition of soil organic matter. Required external input fields for the Kaplan wetland inventory are the available substrate, e.g. from a fast carbon pool (CPOOL - from the Lund-Postdam-Jena (LPJ) model [Sitch et al., 2003]) and a wetland inundation map (WETMAP - Kaplan potential wetland map [Kaplan, 2002, Bergamaschi et al., 2007]; cf. Fig. 2.5) indicating the wetland fraction  $W_f$  per grid cell. The calculation of the carbon decomposition rate  $k_r$  (on hourly time interval) follows Sitch et al. [2003]. It is a measure of the carbon decomposed within a certain time period, and consequently a measure for the amount of released heterotrophic respiration  $h_r$ .  $k_r$  depends on soil moisture and soil temperature, both taken from WRF. The dependence is expressed through the soil moisture factor  $f_{SM}$  and the temperature factor  $g(T_{soil})$ :

$$k_r = \frac{1}{\tau_0} \times g(T_{soil}) \times f_{SM} \quad (4.4)$$

$\tau_0 = 2.86$  a describes the turnover time of the fast carbon pool. The soil moisture factor  $f_{SM}$  is written to:

$$f_{SM} = 0.25 + 0.75 \frac{sm}{sm_{sat}} \quad (4.5)$$

$sm$  indicates the mean value of the first two soil moisture layers (SMOIS) of the WRF model.  $sm_{sat}$  is the saturation value of the soil moisture depending on the soil type (obtained from the WRF soil parameter table).  $k_r$  depends further on the soil temperature  $T_{soil}$  (first layer of the WRF soil temperature TSLB is taken) in the following way:

$$g(T_{soil}) = \exp \left( 308.56 \times \left( \frac{1}{56.02} - \frac{1}{T_{soil} + 46.01} \right) \right) \quad (4.6)$$

In the WRF model, the soil temperature is only defined for land grid points. However, in some cases (especially for grid cells close to rivers and lakes) the WRF land-sea mask and the wetland inundation map do not coincide. For those grid cells where the soil temperature in WRF is not defined, the value of the skin temperature (TSK) is taken instead.

The decomposition of the carbon pool is described by an exponential decay. Heterotrophic respiration is assumed to be 70% of the decomposed carbon in the fast carbon pool. Using different scaling factors depending on the type of the wetland ( $w_{peat} = 0.05$  for peatland and  $w_{flood} = 0.19$  floodplain [Drevet, 2008]), the amount of  $\text{CH}_4$  emissions is calculated from the heterotrophic

respiration. If peatland and floodplain coexist (e.g. for global applications), a weighting factor  $P_l$  is introduced that depends on the mean annual temperature  $T_a$  (obtained from an external dataset) [Drevet, 2008]. The following overall equation describes the calculation of  $\text{CH}_4$  wetland emissions ( $\text{CH}_{4,wet}$ ):

$$\text{CH}_{4,wet} = P_l \times h_r \times w_{flood} \times W_f + (1 - P_l) \times h_r \times w_{peat} \times W_f. \quad (4.7)$$

The weighting factor  $P_l$  is denoted as:

$$P_l = \exp\left(\frac{T_a - 303.0}{8}\right). \quad (4.8)$$

For the WRF-GHG simulations in the Amazon basin described in Ch. 6, only the first part of the right hand side of Eq. (4.7) was utilized corresponding to only “floodplain” emissions.

### Termite emissions

The calculation of  $\text{CO}_2$  and  $\text{CH}_4$  emissions from termites follows the description of the global data base for termite emissions from Sanderson [1996]. The trace gas flux emitted by termites  $\text{CH}_{4,term}$  [ $\text{m}^{-2} \text{h}^{-1}$ ] is calculated as the product of biomass of termites  $biom$  [ $\text{g m}^{-2}$ ] and the flux of trace gas emitted from those termites  $f_{term}$  [ $\text{g gas g termite}^{-1} \text{h}^{-1}$ ]:

$$\text{CH}_{4,term} = biom \times f_{term}. \quad (4.9)$$

The values of  $f_{term}$  and  $biom$  depend on the vegetation type and were determined by measurements [Sanderson, 1996]. In the database daily constant termite emissions are assumed even though there is evidence for a diurnal variation of termite emissions [Sanderson, 1996]. Sanderson [1996] distinguishes between termite emissions in the “old” world (Europe, Asia, Africa) and the “new” world (America, Australia). Table 4.1 illustrates the mapping of the vegetation types used by Sanderson [1996] to the WRF vegetation types. The calculation of the biomass per grid cell and termite flux in WRF-GHG is based on these vegetation types.

### Soil uptake of methane

The soil uptake model developed by Ridgwell et al. [1999] is a process-based model to calculate the consumption of atmospheric  $\text{CH}_4$  by soils. The  $\text{CH}_4$  flux into the soil  $J_{\text{CH}_4}$  is given by:

$$J_{\text{CH}_4} = \frac{C_0 D_{soil}}{z_d} \left(1 - \frac{D_{soil}}{D_{soil} + k_d z_d}\right) \times K_{soil} \quad (4.10)$$

$D_{soil}$  is the diffusivity of the topsoil,  $C_0$  the atmospheric  $\text{CH}_4$  mixing ratio (here, the total  $\text{CH}_4$  mixing ratio of the WRF-GHG variable  $\text{CH}_4\_I$  is taken – for definition see Sec. 4.2),  $z_d$  the soil depth in [cm],  $k_d$  the first-order oxidation rate, and  $K_{soil}$  a factor of  $616.9 \text{ mg ppm}^{-1} \text{ cm}^{-1} \text{ CH}_4$  to account for unit conversions. This equation (based on Fick’s law with some modifications to account for changes in microbial oxidation activity) implies that the main part of the oxidation takes place at a soil depth of  $z_d = 6 \text{ cm}$ . The soil diffusivity  $D_{soil}$  is calculated to:

$$D_{soil} = G_{soil} \times G_T \times D_{air} \quad (4.11)$$

No.	WRF vegetation type (IVGTYP)	Vegetation type after Sanderson [1996]
1	Urban and built up land	-
2	Dry cropland and pasture	Farmland, settlement
3	Irrigated cropland, pasture	Farmland, settlement
4	Mixed dryland, irrigated cropland, pasture	Patchy wood, crop/grass
5	Cropland/grassland mosaic	Patchy wood, crop/grass
6	Cropland/woodland mosaic	Patchy wood, crop/grass
7	Grassland	Temperate grassland
8	Shrubland	Tree, shrub
9	Mixed grassland/shrubland	Tree, shrub
10	Savanna	Savannah/grassland - arid
11	Deciduous broadleaf forest	Temperate forest
12	Deciduous needleleaf forest	Temperate forest
13	Evergreen broadleaf forest	Tropical rainforest, raingreen forest, tropical montane forest
14	Evergreen needleleaf forest	Raingreen forest
15	Mixed forest	Temperate forest
16	Water bodies	-
17	Herbaceous wetland	-
18	Wooden wetland	-
19	Barren/sparsely vegetated	Dry highland/shrub
20	Herbaceous tundra	-
21	Wooded tundra	-
22	Mixed tundra	-
23	Bare ground tundra	-
24	Snow or ice	-

Table 4.1: Mapping of WRF vegetation types to vegetation types defined by Sanderson [1996] for the quantification of termite fluxes.

$D_{air}$  is the diffusivity of  $\text{CH}_4$  in free air.  $G_{soil}$  and  $G_T$  are factors that account for the effects of the soil structure and temperature, respectively. The variable  $G_{soil}$  is expressed as:

$$G_{soil} = V_p^{\frac{4}{3}} \left( \frac{\epsilon}{V_p} \right)^{1.5 + \frac{3}{b}}. \quad (4.12)$$

$V_p$  indicates the total pore volume and  $\epsilon$  the air-filled porosity. Both are taken according to the soil type from the WRF soil parameter table. The value of the sand content ( $I_{sand}$ ) of each soil type is obtained from the same table. The clay content ( $I_{clay}$ ) of each soil type is derived from Cosby et al. [1984]. From these values, the parameter  $b$  in Eq. (4.12) is calculated:

$$b = -3.140 - 0.00222 \times I_{clay}^2 - 3.484 \times 10^{-5} \times I_{sand}^2 \times I_{clay}. \quad (4.13)$$

The dependence on the temperature  $T$  is expressed as:

$$G_T(T) = 1.0 + 0.0055 \times T. \quad (4.14)$$

For the temperature  $T$  in [ $^{\circ}\text{C}$ ], the WRF 2 m temperature is taken. The  $\text{CH}_4$  oxidation rate  $k_d$  depends on three different influence factors: cultivation ( $r_N$ ), temperature ( $r_T$ ), and soil moisture ( $r_{SM}$ ) and is defined as:

$$k_d = r_N \times r_T \times r_{SM} \times k_0. \quad (4.15)$$

$k_0$  is the base oxidation rate, a constant for uncultivated soil at  $0^{\circ}\text{C}$ . Soil uptake is reduced due to agricultural activity and use of fertilizers. The cultivation factor  $r_N$  accounts for the cultivation activity of the vegetation type:

$$r_N = 1.0 - (0.75 \times I_{cult}). \quad (4.16)$$

$I_{cult}$  is a measure of the cultivation activity of the vegetation type and defined according to the WRF vegetation types (IVGTYP; cf. Table 4.1):

$$I_{cult} \begin{cases} 1 & IVGTYP \leq 5 \\ 0.5 & IVGTYP = 6 \\ 0 & IVGTYP > 6. \end{cases} \quad (4.17)$$

The dependence of the oxidation rate  $k_d$  on temperature is based on a  $Q_{10}$  approach:

$$r_T \begin{cases} \exp(0.0693 \times T - 8.56 \times 10^{-7} \times T^4) & T > 0^\circ C \\ 0 & T \leq 0^\circ C. \end{cases} \quad (4.18)$$

The soil moisture effect is characterized by:

$$r_{SM} \begin{cases} 1.0 & (pcp + sm)/et > 1.0 \\ (pcp + sm)/et & (pcp + sm)/et \leq 1.0. \end{cases} \quad (4.19)$$

It depends on precipitation  $pcp$ , soil moisture  $sm$ , and evapotranspiration  $et$ .

The following variables from WRF-GHG are used to drive the soil uptake model: Soil moisture (SMOIS), soil type (ISLTYP) and soil parameters (SOILPARM.TBL), total atmospheric  $CH_4$  mixing ratio ( $CH_4\_1$ ), precipitation (RAIN + RAINNC), potential evaporation (POTEVP), landuse (LANDUSE), 2 m temperature (T2), and wetland map (WETMAP). For grid cells that are dominated by wetlands (wetland inundation fraction  $>0.1$ ), the calculation of soil uptake is suppressed, as soil uptake does not occur in flooded areas.

### Methane emissions from vegetation

Keppler et al. [2006] published findings on  $CH_4$  emissions from plants. However, several studies could not confirm the high emissions values found by Keppler et al. [2006] and therefore, these emissions are now considered a source of minor relevance [Ferretti et al., 2007, Dueck et al., 2007, Beerling et al., 2008, Houweling et al., 2006, Nisbet et al., 2009, Querino et al., 2011]. For hypothesis testing, a  $CH_4$  vegetation source was implemented in WRF-GHG. The emissions for day and night ( $emiss\_day = 374 \times 10^{-9} \text{ kg } CH_4 \text{ kg biomass}^{-1} \text{ h}^{-1}$ ,  $emiss\_night = 119 \times 10^{-9} \text{ kg } CH_4 \text{ kg biomass}^{-1} \text{ h}^{-1}$ ) are scaled by the values of  $GEE$  and respiration ( $Resp$ ) from the VPRM model:

$$CH_{4,veg} = -2.0 \times emiss\_day \times GEE \quad (4.20)$$

for daytime emissions (i.e., when the incoming shortwave radiation (SWDOWN) exceeds a threshold value of  $50.0 \text{ W m}^{-2}$ ) and nighttime emissions:

$$CH_{4,veg} = 2.0 \times emiss\_night \times Resp \quad (4.21)$$

The factor of two accounts for the conversion of  $GEE$  and respiration to plant biomass. For WRF vegetation types with agriculture contribution (1–6, see Table 4.1), the emissions are assumed to be 88.5% of the emissions for undisturbed vegetation [Keppler et al., 2006].



### 4.1.2 External fluxes

External flux data sets are read into WRF-GHG and undergo the same transport mechanisms as the online calculated fluxes. Biomass burning emissions are calculated with the Brazilian Biomass Burning Emission Model (3BEM, [Longo et al., 2010]) included in the biomass burning preprocessor *Prep\_chem\_sources* [Freitas et al., 2010]. For anthropogenic emissions, the Emission Database of Global Atmospheric Research (EDGAR) is used [Olivier et al., 1996, 1999]. As additional model for the “offline” calculation of wetland fluxes with WRF meteorology, the Walter wetland model was utilized [Walter et al., 2001a].

#### Biomass burning emissions for CO<sub>2</sub>, CH<sub>4</sub>, and CO

Biomass burning emissions are calculated as daily emissions based on satellite fire spots by the WRF-Chem preprocessor *Prep\_chem\_sources* [Freitas et al., 2010, Longo et al., 2010].

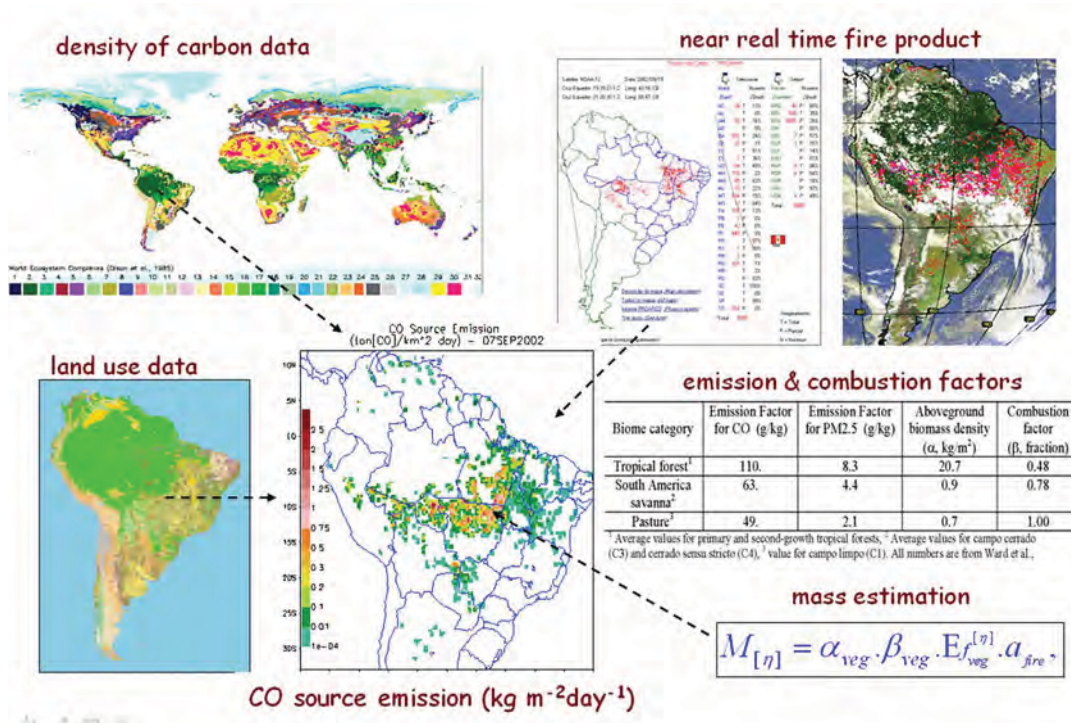


Figure 4.2: Schematic structure of all input parameters for the biomass burning preprocessor (from Longo et al. [2010]). See text for detailed explanation.

The satellite fire database uses three different satellites:

- GOES WF\_ABBA (Geostationary Operational Environmental Satellite - Wildfire Automated Biomass Burning Algorithm)
- Brazilian National Institute for Space Research fire product based on AVHRR (Advanced Very High Resolution Radiometer) onboard the NOAA polar orbiting satellite series
- MODIS (Moderate Resolution Imaging Spectroradiometer) fire product



A filter is applied to avoid double counting of fire pixels. For each detected fire pixel, the mass  $M_X$  of emitted tracers  $X$  is calculated using the following equation (cf. Eq. (2.10) in Ch. 2):

$$M_X = \alpha_{veg} \times \beta_{veg} \times EF_X \times a_{fire} \quad (4.22)$$

$\alpha_{veg}$  describes the above ground biomass available for burning,  $\beta_{veg}$  the combustion factor after Ward et al. [1992].  $EF_X$  is the emission factor for each tracer  $X$  after Andreae and Merlet [2001], and  $a_{fire}$  the burned area of the fire. The GOES WF\_ABBA satellite retrievals provide an estimate of the burned area of each detected fire pixel. In case of no available estimates of the firesize from the satellite observations, a mean fire size of 0.14 km<sup>2</sup> for GOES WF\_ABBA detected fires and 0.22 km<sup>2</sup> for MODIS and AVHRR detected fires is assumed [Longo et al., 2010].

The fire detection maps are merged with 1 km landuse maps and the carbon live vegetation dataset (Fig. 4.2). They are multiplied by the emission factors of Andreae and Merlet [2001] and the combustion factor for the different vegetation types. A diurnal cycle based on a Gaussian function centered around 18 UTC is applied to the biomass burning emissions [Prins et al., 1998]. Additional variables for the usage of the plumerise mechanism (calculation of the injection height of the fire emissions [Freitas et al., 2006, Grell et al., 2010]) in WRF-GHG (Sec. 4.2), such as the mean firesize, are calculated, too.

### Anthropogenic emissions for CO<sub>2</sub>, CH<sub>4</sub>, and CO

The Emission Database for Global Atmospheric Research version 4.1 (EDGAR v4.1; available online at <http://edgar.jrc.ec.europa.eu>) is globally available on 0.1° × 0.1° resolution for several greenhouse gases such as CO<sub>2</sub> and CH<sub>4</sub> and other trace gases, e.g. CO. Data can be obtained on yearly basis from 1970 until the year 2005. Alonso et al. [2010] established an updated version of EDGAR v4.1 for South American cities. The emissions are adjusted based on the correlation between city vehicle density and mobile source emissions of CO and nitrous oxides (NO<sub>x</sub>). These updated emissions are used as anthropogenic emissions for the simulations in the Amazon basin. Additionally, a diurnal cycle peaking twice daily at 08:00 and 20:00 local time using a double Gaussian function is applied to the EDGAR v4.1 emissions. It is included in *Prep\_chem\_sources* [Freitas et al., 2010].

### The Walter wetland model

The Walter wetland model [Walter et al., 1996, Walter and Heimann, 2000, Walter et al., 2001a,b] is a process-based model to calculate CH<sub>4</sub> emissions from wetlands. The important factors influencing CH<sub>4</sub> wetland emissions (cf. Sec. 2.1.2) are taken into account:

- Position of the water table to separate between anaerobic production of CH<sub>4</sub> and aerobic conditions for oxidation of CH<sub>4</sub>
- Soil temperature to control the rate of methanogenesis
- Transport of CH<sub>4</sub> to the atmosphere through the different mechanisms (plant mediated transport, ebullition, and diffusion)

The one-dimensional model consists of 170 layers à 1 cm. The change of  $\text{CH}_4$  concentration ( $C_{soil}$ ) with time at each soil layer ( $z$ ) is expressed through the following equation:

$$\frac{\partial}{\partial t} C_{soil}(t, z) = -\frac{\partial}{\partial z} F_{diff}(t, z) + Q_{ebull}(t, z) + Q_{plant}(t, z) + R_{prod}(t, z) + k_d(t, z). \quad (4.23)$$

The main terms are defined as follows:

- **$\text{CH}_4$  diffusion flux** ( $F_{diff}$ ) is based on Fick's law. It depends on the diffusion coefficient of  $\text{CH}_4$  ( $D_{soil}$ ) and the  $\text{CH}_4$  concentration gradient at depth  $z$ .  $f_{diff}$  is described through the following equation:

$$f_{diff}(t, z) = -D_{soil}(z) \frac{\partial}{\partial z} C_{soil}(t, z) \quad (4.24)$$

- **$\text{CH}_4$  ebullition flux rate** ( $Q_{ebull}$ ) is  $> 0$  if the  $\text{CH}_4$  concentration in a soil layer exceeds a certain threshold value  $V_{thresh}$ . Then 70% of the  $\text{CH}_4$  released in bubbles is transported to the layer at the height of the water table. The other 30% are trapped in the upper part of the water saturated layers.
- **The plant-mediated transport rate** ( $Q_{plant}$ ) describes how much  $\text{CH}_4$  is transported to the atmosphere through plants. It depends on the efficiency of plant-mediated transport, the growing state of the plants, the vertical distribution of the roots in the soil, and the  $\text{CH}_4$  concentration in the corresponding soil layer.
- **The  $\text{CH}_4$  production rate** ( $R_{prod}$ ) is a function of the substrate availability with soil depth, the amount of substrate itself (Net Primary Productivity-NPP), and the soil temperature  $T_{soil}(t, z)$ . It is expressed as:

$$R_{prod} = R_0 NPP_{org}(z) \left( 1 + \frac{NPP_{season}(t)}{NPP_{max}} \right) f(T_{soil}) Q_{10}^{\frac{T_{soil}(t,z) - T_{a,soil}}{10}} \quad (4.25)$$

$NPP_{org}(z)$  describes the substrate availability with soil depth. It is assumed to be constant throughout the rooting zone and decays exponentially below.  $NPP_{season}(t)$  indicates the seasonal availability of organic carbon for  $\text{CH}_4$  production.  $f(T_{soil})$  is a step-function inhibiting  $\text{CH}_4$  production for  $T_{soil} < 0^\circ \text{C}$ . The factor  $R_0$  is a measure for the amount and quality of substrate for methanogenesis. It was set to 2.80 for simulations in the Amazon basin according to the evaluation of Walter and Heimann [2000] for a tropical swamp in Panama.

- **The  $\text{CH}_4$  oxidation rate** ( $k_d$ ) follows the Michaelis-Menten kinetics with a  $Q_{10}$  soil temperature dependence:

$$k_d(t, z) = -\frac{V_{max} C_{soil}(t, z)}{K_m + C_{soil}(t, z)} Q_{10}^{\frac{T_{soil}(t,z) - T_{a,soil}}{10}}. \quad (4.26)$$

The Michaelis-Menten coefficients are set to  $V_{max} = 20 \mu\text{M}$  and  $K_m = 5 \mu\text{M}$  for tropical regions according to Walter and Heimann [2000].

The position of the water table is calculated from an adjoint hydrological model. It acts as the separator between the soil layers below the water table where  $\text{CH}_4$  is produced by anaerobic production by microbes and the soil layers above the water table (oxidation of  $\text{CH}_4$ ). The hydrological

model is constructed similar to the wetland model as a bucket model of 1.7 m depth with soil layers à 1 cm (a complete description of the hydrological model is found in Walter et al. [2001a]). The hydrological model calculates fluctuations of the water table as a function of climatological variables (precipitation, 2 m air temperature, surface solar radiation). Evapotranspiration, lateral inflow, and runoff are determined within the hydrological model to specify the position of the water table.

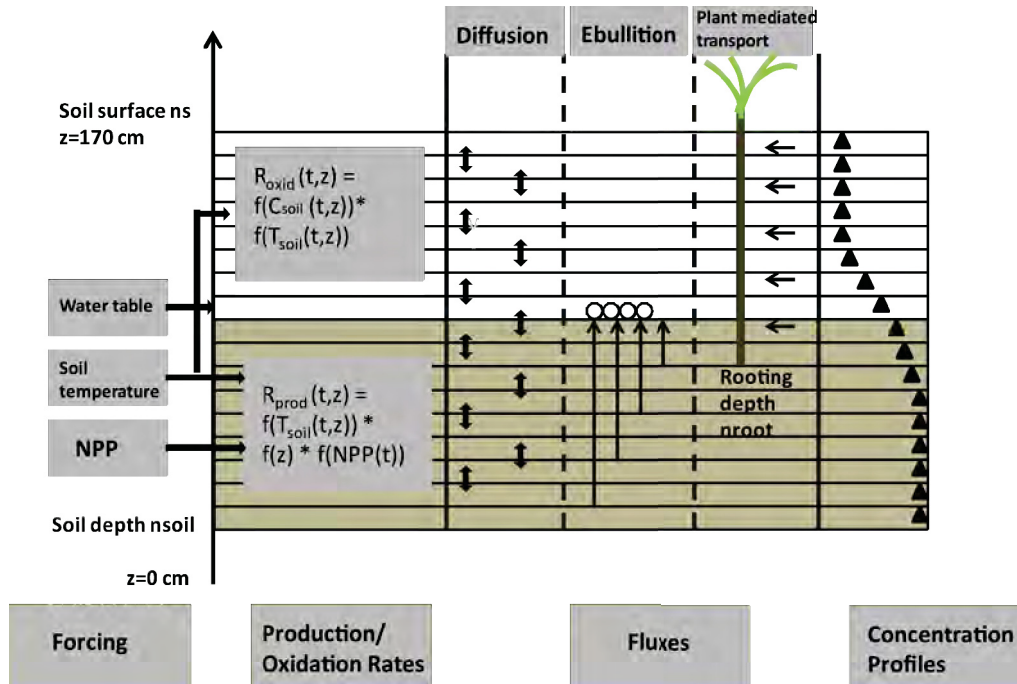


Figure 4.3: Schematic representation of the Walter wetland model structure (adapted from Walter and Heimann [2000]). Forcing variables are the position of the water table, soil temperature, and NPP. The CH<sub>4</sub> production and oxidation rates are calculated at each soil layer. Three transport mechanisms are implemented (diffusion, ebullition, and plant-mediated transport) for the release of CH<sub>4</sub> to the atmosphere.

The Walter wetland model is described in detail in Walter et al. [1996] and Walter and Heimann [2000]. Fig. 4.3 gives a short overview over the main aspects of the model. The CH<sub>4</sub> emissions are calculated separately at each wetland grid cell with the 1D column model. They are multiplied with the fractional coverage of wetland area of the corresponding grid cell. This information is obtained from a wetland inundation map.

The Walter wetland model is not implemented in the WRF-GHG code due to different programs that have to be run subsequently. It is driven offline by WRF meteorological output fields (Precipitation (RAIN+RAINNC), soil temperature (TSLB), radiation and heat fluxes (SWDOWN, GLW), and surface temperature (T2)). Soil and vegetation properties such as root and soil depth used in the Walter wetland model [Walter et al., 2001a] are derived from the WRF vegetation and soil types (details are found in Beck et al. [2011]).

Additional required variables besides the wetland inundation map are daily NPP from the Biosphere Energy Transfer and Hydrology model (BETHY) [Knorr, 1997], the terrain height (ETOPO5 - Earth Topography 5-minute; [Edwards, 1989]), and the mean annual soil temperature of the up-

per soil layer from simulations of the global atmospheric circulation model ECHAM (acronym of ECMWF and Hamburg). These are taken from the original Walter wetland model [Walter et al., 2001a].

## 4.2 Structure of WRF-GHG

WRF-GHG is an augmentation for CH<sub>4</sub> and CO of the coupled WRF-VPRM model developed by Ahmadov et al. [2007]. The complete tracer transport in WRF-GHG is performed in a passive way, i.e. no chemical reactions of the tracers with other species are allowed. All chemical mechanisms besides vertical mixing are turned off if the tracer transport option is used [Ahmadov et al., 2007]. The tracers are transported online, which implies that transport is performed simultaneously with the meteorological variables at each time step [Ahmadov et al., 2007]. Emissions are added at each time step to the tracer mixing ratio at the lowest model layer (except for biomass burning emissions). The tracers undergo the advection, PBL, and cumulus schemes similar to other chemical species. From WRF-Chem version 3.1.1 onwards an option for sub-grid convective transport of chemical species has been implemented [Peckham et al., 2009]. The GHG model is implemented as GHG\_TRACER package with chemistry option 98 (`chem_opt = 98`) in the WRF-Chem code.

To couple the Greenhouse Gas model (GHG model) to WRF-Chem four additional modules were established besides some minor modifications of the WRF-Chem code. In the new registry file (`registry.ghg`) the additional tracer and flux variables required for the GHG model are defined. The greenhouse gas module (`module_greenhouse_gases.F`) is the “heart” of the GHG model. It contains the code for the calculation of the previously described biospheric flux models for CO<sub>2</sub> and CH<sub>4</sub>. The routine for the addition of the fluxes to the corresponding tracer variable is located in `module_add_emissions.F`. The plumerise model calculates the injection height of the biomass burning emissions based on firesize, temperature, heat fluxes, and wind velocity. It is part of the standard WRF-Chem version [Grell et al., 2010] and was modified and adapted to the needs of the GHG model (`module_plumerise_ghg.F`). Fig. 4.4 illustrates how the four modules are embedded in the WRF-Chem code.

In the following the four additional established modules

- `registry.ghg`
- `module_add_emissions.F`
- `module_greenhouse_gases.F`
- `module_plumerise_ghg.F`

in the WRF-Chem code are described in more detail.

### 1. `registry.ghg`

In `registry.ghg` all additional required variables for tracers (describing the atmospheric mixing ratio) and fluxes of WRF-GHG are defined. The tracers are defined as four-dimensional `chem` arrays. The notation is `CO2_1, ..., CO2_6`, and `CO2_B` for CO<sub>2</sub>, `CH4_1, ..., CH4_7`, and `CH4_B`

Tracer variable (chem) [kg kg <sup>-1</sup> ]	Description
CO2_1	Total atmospheric CO <sub>2</sub> mixing ratio
CO2_2	Changes in CO <sub>2</sub> mixing ratio from biogenic activity
CO2_3	Changes in CO <sub>2</sub> mixing ratio from anthropogenic emissions
CO2_4	Changes in CO <sub>2</sub> mixing ratio from biomass burning
CO2_5	Changes in CO <sub>2</sub> mixing ratio from termites
CO2_6	Changes in CO <sub>2</sub> mixing ratio from ocean fluxes
CO2_B	Atmospheric CO <sub>2</sub> background mixing ratio
CH4_1	Total atmospheric CH <sub>4</sub> mixing ratio
CH4_2	Changes in CH <sub>4</sub> mixing ratio from wetland emissions
CH4_3	Changes in CH <sub>4</sub> mixing ratio from anthropogenic emissions
CH4_4	Changes in CH <sub>4</sub> mixing ratio from biomass burning
CH4_5	Changes in CH <sub>4</sub> mixing ratio from termite emissions
CH4_6	Changes in CH <sub>4</sub> mixing ratio from soil uptake
CH4_7	Changes in CH <sub>4</sub> mixing ratio from vegetation
CH4_B	Atmospheric CH <sub>4</sub> background mixing ratio
COT_1	Total atmospheric CO mixing ratio
COT_2	Changes in CO mixing ratio from biomass burning
COT_3	Changes in CO mixing ratio from anthropogenic emissions
COT_B	Atmospheric CO background mixing ratio

Table 4.2: Overview of all tracer variables defined in the `registry.ghg` file.

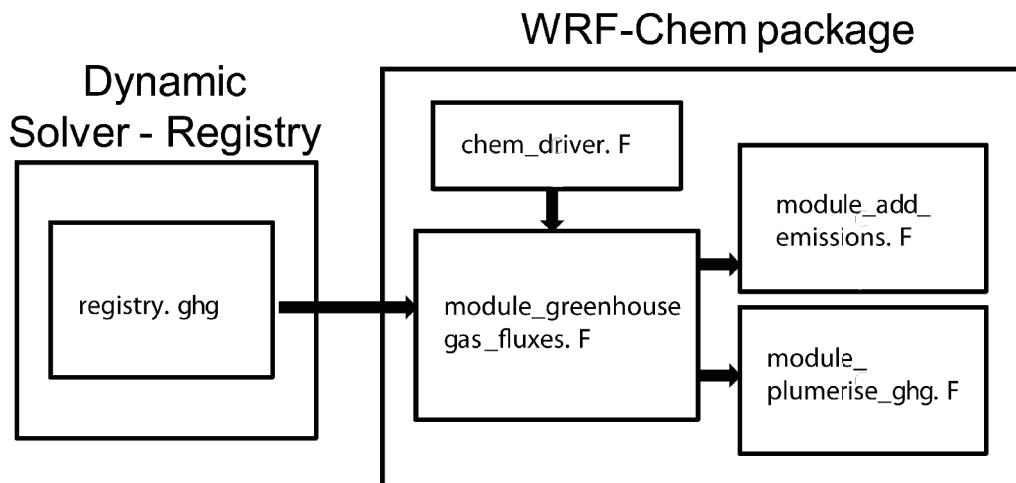


Figure 4.4: Embedded structure of the four new established modules in the WRF-Chem model structure.

for CH<sub>4</sub>, and *COT\_1*, ..., *COT\_3*, and *COT\_B* for CO. The assignment of the single tracer variables to different source and sink processes of CO<sub>2</sub>, CH<sub>4</sub>, and CO is illustrated in Table 4.2. All flux variables representing fluxes of different processes emitting or consuming CO<sub>2</sub>, CH<sub>4</sub>, and CO are defined in `registry.ghg`. Table 4.3 illustrates a full overview of all fluxes defined

in `registry.ghg`. All namelist options (cf. Tables 4.4 and 4.5) that were established for the WRF-GHG are defined in `registry.ghg`. The last line of the `registry.ghg` file illustrates how the WRF-GHG is defined: As chemistry option 98 (`chem_opt=98`) and package called `GHG_TRACER`.

Flux variable (chem_source) [kg m <sup>-2</sup> s <sup>-1</sup> ]	Description	Time Dimension
CO <sub>2</sub>		
fl_bio1	Biospheric [ext.]	Hourly [30]
fl_oce	Ocean [ext.]	Hourly [30]
fl_ant1	Anthropogenic [ext.]	Daily [1]
fl_antco2	Anthropogenic [ext.]	Hourly [30]
fl_bbco2	Biomass burning [ext.]	Daily [1]
bb_co2	3d biomass burning [int.]	WRF timestep
GEE	Gros-Ecosystem-Exchange [int.]	WRF timestep
RESP	Biospheric respiration [int.]	WRF timestep
co2_term	Termite emission [int.]	WRF timestep
CH <sub>4</sub>		
fl_wet	Wetland [ext.]	Hourly [30]
fl_ant4	Anthropogenic [ext.]	Daily [1]
fl_antch4	Anthropogenic [ext.]	Hourly [30]
fl_bbch4	Biomass burning [ext.]	Daily [1]
bb_ch4	3d biomass burning	WRF timestep
fl_term	Termite emission [ext.]	Daily [1]
fl_soilu	Soil uptake [ext.]	Hourly [30]
fl_veg	Vegetation [ext.]	Hourly [30]
ch4_emiss	Wetland [int.]	WRF timestep
ch4_term	Termite emission [int.]	WRF timestep
ch4_soil	Soil uptake [int.]	WRF timestep
ch4_veg	Vegetation [int.]	WRF timestep
CO		
fl_ant5	Ext. anthropogenic [ext.]	Daily [1]
fl_antco	Ext. anthropogenic [ext.]	Hourly [30]
fl_bbco	Ext. biomass burning [ext.]	Daily [1]
bb_co	3d Int. biomass burning [int.]	WRF timestep

Table 4.3: Overview over all flux variables used in the WRF-GHG model. [ext.] implies offline/external calculation of fluxes or use of emission inventories. [int.] denotes online calculation of fluxes and internal variables. The time step of the external fluxes is either set to daily or hourly. For the internal fluxes the time step of calculation depends on the time step of the WRF model.



## 2. module\_add\_emissions.F

`module_add_emissions.F` contains the addition of CO<sub>2</sub>, CH<sub>4</sub>, and CO fluxes to the corresponding atmospheric mixing ratios. Fluxes are added to the tracer variable at the first model layer. Biomass burning emissions are treated differently as they are injected at a specific model level calculated by the plumerise model. The different possibilities of adding fluxes to tracer variables in WRF-GHG are described in the following.

`module_add_emissions.F` consists of four routines

- `co2_surface_source_add`
- `co2_surface_source_ad2`
- `add_emis_anthro_ghg`
- `add_emis_burn_ghg`.

All follow the same principle in adding fluxes to atmospheric mixing ratios. The two-dimensional flux variable `chem_source(i, j)` (cf. Table 4.3) is multiplied by a conversion factor (`conv_rho(i, k, j)`) and added to the first layer of the three-dimensional tracer variable `chem(i, k, j)` (cf. Table 4.2). If the plumerise mechanism is used, biomass burning emissions are added at all vertical layers. The addition of fluxes to the atmospheric mixing ratios is written to:

$$\text{chem}(i, 1, j) = \text{chem\_source}(i, j) \left[ \frac{kg}{m^2 s} \right] \times \text{conv\_rho}(i, 1, j) \left[ \frac{sm^2}{kg} \right] \quad (4.27)$$

with

$$\text{conv\_rho}(i, 1, j) = \frac{1}{\text{rho}(i, 1, j) \left[ \frac{kg}{m^3} \right]} \times \frac{dt[s]}{dz8(i, 1, j)[m]}. \quad (4.28)$$

`rho(i, 1, j)` denotes the air density in the first model layer, `dt` the time step of the model and `dz8(i, 1, j)` the thickness of the first model layer in [m].

`co2_surfac_source_add` (`co2add` in Table 4.4) is used to add emissions to the first model layer using Eq. (4.27). If biomass burning emissions are added into the first model layer without using the plumerise mechanism `co2_surfac_source_ad2` (`co2ad2`) is utilized. A diurnal cycle peaking at 18 UTC (14:00 local time) for biomass burning emissions [Prins et al., 1998] is applied (multiplication factor for the emissions). `add_emis_anthro_ghg` (`emisantro`) adds a weekly cycle on, e.g. daily constant anthropogenic emissions to account for less traffic on the weekends compared to weekdays [Alonso et al., 2010]. The multiplication factors are denoted in the following way:

Sun	Mon	Tue	Wed	Thu	Fri	Sat
0.67	1.1	1.1	1.1	1.1	1.1	0.83

For three-dimensional addition of biomass burning emissions in connection with the plumerise mechanism, the subroutine `add_emis_burn_ghg` (`emisburn`) is deployed. In this case, a loop over all model levels  $k$  with their corresponding air density  $\text{rho}(i, k, j)$  and layer thickness  $\text{dz8}(i, k, j)$  is conducted in eqs. (4.27, 4.28). The diurnal cycle for biomass burning emissions is as well implemented for the three-dimensional addition of biomass burning fluxes. Table 4.4 illustrates an overview over the routines implemented for the addition of fluxes depending on the namelist options.



### 3. module\_greenhouse\_gases.F

module\_greenhouse\_gases.F is the most important module of the new established modules in WRF-GHG. The main routine is called from chem\_driver.F in WRF-Chem (cf. Fig. 3.3). It contains the code for the online calculation of all biospheric CO<sub>2</sub> and CH<sub>4</sub> fluxes described in Sec. 4.1. The different possibilities of offline or online calculation of fluxes are set in the namelist.input file (cf. Table 4.4). The routine calls in module\_add\_emissions.F and module\_plumerise\_ghg.F are located in this module.

Variable	Value	Description	Add. Routine
co2_anthro	0	No anthropogenic emissions	–
	1	Daily flux inventories	emisanthro
	2	Hourly flux inventories	co2add
wetland_type	0	No CH <sub>4</sub> wetland emissions	–
	1	Floodplain and peatland CH <sub>4</sub> wetland emissions (Kaplan)	co2add
	2	Only floodplain CH <sub>4</sub> wetland emissions (Kaplan)	co2add
	3	Only peatland CH <sub>4</sub> wetland emissions (Kaplan)	co2add
	4	External CH <sub>4</sub> wetland emissions (Walter)	co2add
term_id	0	No termite emissions	–
	1	Only CH <sub>4</sub> termite emissions	co2add
	2	CH <sub>4</sub> and CO <sub>2</sub> termite emissions	co2add
	3	Only CO <sub>2</sub> termite emissions	co2add
	4	External CH <sub>4</sub> termite emissions	co2add
bb_opt_ghg	0	No biomass burning emissions	–
	2	Biomass burning emissions (CO <sub>2</sub> , CH <sub>4</sub> and CO) with plumerise module and diurnal cycle	emisburn
	3	Biomass burning emissions without plumerise module and diurnal cycle	co2add
	4	Biomass burning emissions without plumerise module but with diurnal cycle	co2ad2
soil_id	0	No calculation of soil uptake fluxes	–
	1	Calculation of soil uptake fluxes	co2add
	2	External soil uptake dataset	co2add
veg_id	0	No calculation of CH <sub>4</sub> emissions from vegetation	–
	1	Calculation of CH <sub>4</sub> emissions from vegetation	co2add
	2	External CH <sub>4</sub> emissions from vegetation	co2add
oce_id	0	No CO <sub>2</sub> ocean fluxes	–
	1	External CO <sub>2</sub> ocean fluxes (hourly time step)	co2add

Table 4.4: WRF-GHG options in the namelist.input file. The first column describes the defined namelist.input variable, the second the possible options. A description of each option is given in column three. Column four describes the routine used for the addition of the fluxes to the corresponding atmospheric mixing ratios. The following acronyms are used: co2add: co2\_surface\_source\_add; co2ad2: co2\_surface\_source\_ad2; emisanthro: add\_emis\_anthro\_ghg; emisburn: add\_emis\_burn\_ghg.

### 4. module\_plumerise\_ghg.F

If the plumerise option is chosen, an one dimensional model calculates the injection height of the biomass burning plume depending on heat fluxes, temperature, and wind speed [Freitas et al., 2006, Grell et al., 2010]. It determines which fraction of the biomass burning emissions is released at the injection height and at the ground. The plumerise mechanism is part of the official

Variable	Value	Description
vprm_class	8	Number of VPRM classes
vprm_par_file	"VPRM_param_CERES2005.txt"	VPRM parameter file
co2_st_time	360	Starting time for tracer transport in [min]
file_term	"CH4_termite_NW.txt"	Termite parameters for America, Australia
	"CH4_termite_OW.txt"	Termite parameters for Europe, Asia, Africa
plume_frq_ghg	180	plumerise fire frequency

Table 4.5: Further namelist options required for WRF-GHG as defined in the `registry.ghg` file.

WRF-Chem release. In WRF-GHG a new module called `module_plumerise_ghg.F` was established omitting all species used with the WRF-Chem model except  $\text{CO}_2$ ,  $\text{CH}_4$ , and  $\text{CO}$ . This plumerise module calls exactly the same subroutines as the plumerise module in the original WRF-Chem code (`module_plumerise1.F`) does.

### 4.3 Initial and boundary conditions

Simulations are performed for a 30 h run time period with 6 h spin-up for the meteorology from 18 UTC to 24 UTC of the previous day and a 24 hour simulation period of the “actual” simulation day for the tracer transport. For the meteorology (including soil initialization fields), initial and boundary conditions are taken from the European Centre for Medium-Range Weather Forecasts (ECMWF) operational archive. These data is 6 h analysis data of atmospheric model version 1 on 91 hybrid levels with a horizontal resolution of  $\sim 25$  km. As initial and boundary conditions for  $\text{CO}_2$ ,  $\text{CH}_4$ , and  $\text{CO}$ , three-dimensional fields from global atmospheric inversions are utilized. They are thought to describe the distribution of the corresponding greenhouse gas tracer in the atmosphere more realistic than the standard WRF-Chem profiles. These are the TM3 model for  $\text{CO}_2$  [Rödenbeck et al., 2003], the TM5 model for  $\text{CH}_4$  [Bergamaschi et al., 2007, 2009] and the Monitoring Atmospheric Composition and Climate (MACC) or Global and regional Earth-system (Atmosphere) Monitoring using Satellite and in-situ data (GEMS) re-analysis or near-realtime data for  $\text{CO}$  (see [http://data-portal.ecmwf.int/data/d/gems\\_reanalysis/levtype=pl/](http://data-portal.ecmwf.int/data/d/gems_reanalysis/levtype=pl/) for re-analysis data and [http://data-portal.ecmwf.int/data/d/gems\\_nrealtime/levtype=pl/](http://data-portal.ecmwf.int/data/d/gems_nrealtime/levtype=pl/) for the near-realtime product). Table 4.6 summarizes the characteristics of the global models used for tracer initialization. These global fields serve as initial condition of the total  $\text{CO}_2$ ,  $\text{CH}_4$ , and  $\text{CO}$  atmospheric mixing ratios (namely the tracer variables  $\text{CO2}_I$ ,  $\text{CH4}_I$ , and  $\text{COT}_I$ ). For the lateral boundary conditions, the values of the lateral boundary are gradually applied over 5 grid cells in a relaxation zone [Ahmadov et al., 2007]. In WRF-Chem only one layer without relaxation zone is used.

The initial and boundary conditions for tracers are deployed in the following manner: On the first day of the simulation period the tracer fields  $\text{CO2}_I$ ,  $\text{CH4}_I$ , and  $\text{COT}_I$  are initialized once with the values of the global fields of the corresponding day and time, when the tracer transport starts. For the other time steps of this simulation day only lateral boundary conditions are applied. For the second day of the simulation period the application of meteorological and tracer initial and boundary conditions differs for the initial conditions, but not for the lateral boundary conditions. The meteorology is initialized with ECMWF fields every day. The initialization of the tracer

Model	Horizontal resolution	No. of vertical levels	Time interval
TM3	$\sim 4^\circ \times 5^\circ$	19	6 h
TM5	$6^\circ \times 4^\circ$	25	Daily
MACC	$1.125^\circ \times 1.125^\circ$	60	6 h

Table 4.6: *Main characteristics of the global models that are used as initial and lateral boundary conditions for greenhouse gas tracers in WRF-GHG.*

variables is taken from the final output of the WRF-GHG simulation at 24 UTC the previous day to ensure continuity. The motivation for re-initializing the meteorology each day is a better data constraint of the WRF meteorological fields.

Which tracers are initialized depends on the region for which the simulations are performed. Since the WRF-Chem code does not allow any tracer with negative mixing ratios, advected tracer fields “disappear” in case the mixing ratios become negative. This occurs even though the positive definite advection scheme is used if very strong gradients in the fluxes evolve. It is avoided by initializing all tracer with the global fields or an offset (and force them with lateral boundary conditions). The offset or the global background, which can be transported inside the WRF-GHG model as a separate tracer, is later subtracted. Special care has to be taken for the tracers *CO2\_2* and *CH4\_6*—atmospheric mixing ratios from VPRM and soil uptake fluxes. Their corresponding fluxes can become negative. In case they are not initialized with the global fields they have to be set to a constant offset (0.0002 for *CO2\_2* and  $10^{-7}$  for *CH4\_6*, respectively) to avoid problems in WRF-GHG with negative atmospheric mixing ratio values.

#### 4.4 WRF-GHG in official WRF-Chem release

The WRF-GHG code described in the previous section was modified to fulfill the requirements for a distribution within the official WRF-Chem release from version 3.4 onwards. This work was accomplished in collaboration with Ravan Ahmadov at the NOAA Earth System Research Laboratory, Boulder, Colorado, USA. The differences to the standard WRF-GHG model are described in this section.

According to WRF-Chem conventions, the flux variables described in Table 4.3 are grouped into anthropogenic fluxes (*emis\_ant*), biogenic fluxes (*eghg\_bio*), and biomass burning fluxes (*ebu*). The existing anthropogenic and biomass burning flux arrays in WRF-Chem were augmented for the addition of the required greenhouse gas flux variables. A biogenic flux array was newly introduced. Table 4.7 illustrates the new distribution of the flux variables. A test flux for all three species was included and the dimension of the anthropogenic fluxes is chosen in the *namelist.input* file by the *kemit* option. With this option the injection level of the anthropogenic emissions can be explicitly specified.

The tracers (now in units of [ppm]) are defined according to their emission origin. They are added up to the total contribution of the atmospheric mixing ratio in a post-processing step. Table 4.8 illustrates the different tracers of the Greenhouse Gas model as defined in the official WRF-Chem release. The chemistry option previously defined as *chem\_opt* = 98 is moved to the package *co2\_tracer* with *chem\_opt* = 16 including  $\text{CO}_2$  and anthropogenic CO and the package *ghg\_tracer* with *chem\_opt* = 17 includes all tracers of *chem\_opt* = 16 and additionally the complete  $\text{CH}_4$  tracers and the biomass burning tracers for  $\text{CO}_2$ ,  $\text{CH}_4$ , and CO.

The biomass burning emissions are now fully compatible with the previously established biomass burning option in the WRF-Chem code and are activated by setting `biomass_burn_opt = 5` in the `namelist.input` file. The code was made accessible for the MODIS landuse data set (a different set of landuse data that can be chosen within WRF compared to the standard data set from the U. S. Geological Survey).

Flux variable [mol km <sup>-2</sup> h <sup>-1</sup> ]	Assigned Array	Dimension [Space]	Description
<code>ebio_gee</code>	<code>eghg_bio</code>	2	Biospheric CO <sub>2</sub> GEE
<code>ebio_res</code>	<code>eghg_bio</code>	2	Biospheric CO <sub>2</sub> respiration
<code>ebio_oce</code>	<code>eghg_bio</code>	2	CO <sub>2</sub> ocean
<code>ebio_ch4wet</code>	<code>eghg_bio</code>	2	CH <sub>4</sub> wetland
<code>ebio_ch4soil</code>	<code>eghg_bio</code>	2	CH <sub>4</sub> soil uptake
<code>ebio_ch4term</code>	<code>eghg_bio</code>	2	CH <sub>4</sub> termite
<code>e_co2</code>	<code>emis_ant</code>	2–3	CO <sub>2</sub> anthropogenic
<code>e_co</code>	<code>emis_ant</code>	2–3	CO anthropogenic
<code>e_ch4</code>	<code>emis_ant</code>	2–3	CH <sub>4</sub> anthropogenic
<code>e_co2tst</code>	<code>emis_ant</code>	2–3	CO <sub>2</sub> test flux
<code>e_cotst</code>	<code>emis_ant</code>	2–3	CO test flux
<code>e_ch4tst</code>	<code>emis_ant</code>	2–3	CH <sub>4</sub> test flux
<code>ebu_co2</code>	<code>ebu</code>	3	CO <sub>2</sub> biomass burning
<code>ebu_co</code>	<code>ebu</code>	3	CO biomass burning
<code>ebu_ch4</code>	<code>ebu</code>	3	CH <sub>4</sub> biomass burning

Table 4.7: Flux variables defined for the usage of the greenhouse gas module in the official WRF-Chem version 3.4.

One new file has been added to the WRF-Chem code of the official release. It is called `module_ghg_fluxes.F`. It includes the code of the VPRM model, the Kaplan wetland model, soil uptake, and termite emissions for the “online” calculation of biogenic fluxes and the addition of the anthropogenic and biogenic fluxes to the corresponding tracers. It was previously divided into two different modules (`module_greenhouse_gases.F` and `module_add_emissions.F`). The variables previously defined in `registry.ghg` are included in `registry.chem`. The fully included biomass burning option uses the already existing plumerise module in the WRF-Chem code. The number of newly introduced namelist options was reduced from 12 to 4. Table 4.9 demonstrates the new `namelist.input` options.

A general practice within the WRF-Chem community is the initialization of tracers with standardized profiles. For simplicity, all tracers listed in Table 4.8 are initialized with a constant background mixing ratio (380 ppm for CO<sub>2</sub>; 0.1 ppm for CO; 1.77 ppm for CH<sub>4</sub>) that has to be subtracted again in a post-processing step. These values are also used for the forcing at the lateral boundaries. The initialization with background mixing ratios further prevents the tracers from mass conservation problems that were observed for cases where strong gradients occur. Fig. 4.5 illustrate the online simulated biospheric CH<sub>4</sub> fluxes from WRF-ChemV3.4 and the anthropogenic and biomass burning fluxes for the South American WRF domain (cf. Table 4.7). In Fig. 4.6 the simulation of the CH<sub>4</sub> tracer distribution is illustrated (cf. Table 4.8).

Tracer variable (chem) [ppm]	Description	chem_opt
co2_ant	CO <sub>2</sub> anthropogenic mixing ratio	16,17
co2_bio	CO <sub>2</sub> biogenic mixing ratio	16,17
co2_oce	CO <sub>2</sub> oceanic mixing ratio	16,17
co2_atst	CO <sub>2</sub> test tracer mixing ratio	16,17
co2_bbu	CO <sub>2</sub> biomass burning mixing ratio	17
co2_bck	CO <sub>2</sub> background mixing ratio	16,17
co_ant	CO anthropogenic mixing ratio	16,17
co_tst	CO test tracer mixing ratio	17
co_bbu	CO biomass burning mixing ratio	17
co_bck	CO background mixing ratio	16,17
ch4_ant	CH <sub>4</sub> anthropogenic mixing ratio	17
ch4_bio	CH <sub>4</sub> biogenic mixing ratio	17
ch4_tst	CH <sub>4</sub> test tracer mixing ratio	17
ch4_bbu	CH <sub>4</sub> biomass burning mixing ratio	17
ch4_bck	CH <sub>4</sub> background mixing ratio	17

Table 4.8: Overview over all tracer variables corresponding to the two chemistry options 16 and 17 for the transport of greenhouse gases.

Variable	Value	Description
vprm_opt	"VPRM_param_US" "VPRM_param_EUROPE" "VPRM_param_TROPICS"	VPRM parameters for North America VPRM parameters for Europe VPRM parameters for tropical regions
term_opt	"CH4_termite_NW" "CH4_termite_OW"	Termite parameters for the American continent and Australia Termite parameters for Europe, Asia, and Africa
wpeat	0.05	Scaling factor peatland wetland emissions
wflood	0.19	Scaling factor floodplain wetland emissions

Table 4.9: Options in the `namelist.input` for the new established chemistry options 16 and 17 in the official WRF-Chem release.

## 4.5 Conclusions

The development of the WRF-GHG model enables high-resolution tracer transport of greenhouse gases such as CO<sub>2</sub> and CH<sub>4</sub>. Biospheric flux models are integrated in the WRF-Chem code for online calculation of CO<sub>2</sub> fluxes using the VPRM model and CH<sub>4</sub> fluxes using the Kaplan wetland model, termite emissions, and atmospheric soil uptake. External flux fields for the description of anthropogenic and biomass burning emissions and other external biospheric emissions, e.g. from the Walter wetland model can be used within WRF-GHG. Different namelist options allow the usage of WRF-GHG in different configurations. A modified version of WRF-GHG is part of the official WRF-Chem V3.4 release in spring 2012. The application of WRF-GHG in the Amazon basin is described in Ch. 6.



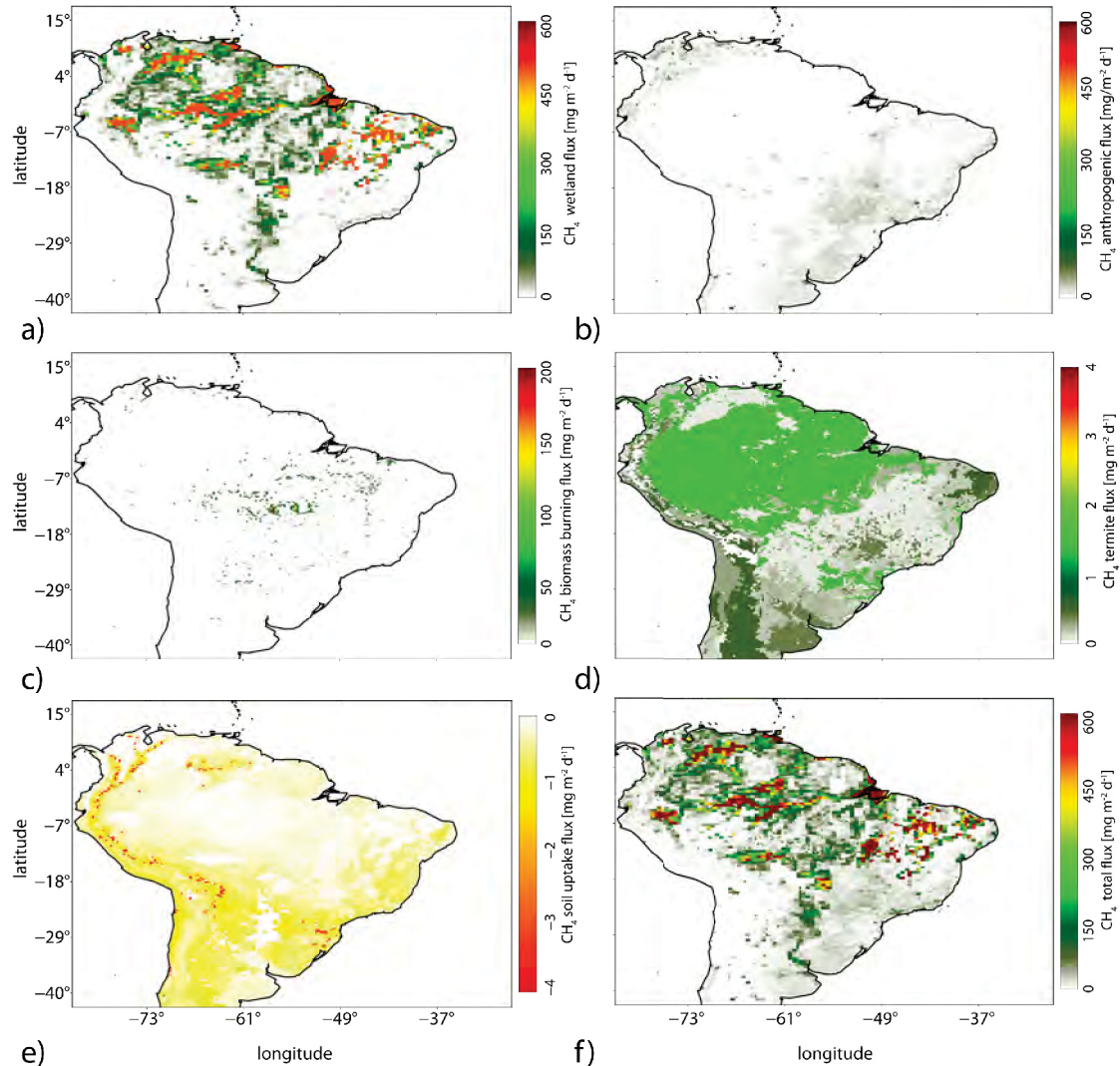


Figure 4.5: Illustration of the  $\text{CH}_4$  flux of the different source component as calculated online (code from the official WRF-ChemV3.4 release) or by the above described preprocessors for 4<sup>th</sup> August 2009 and the South American WRF domain. (a) demonstrates the online calculated  $\text{CH}_4$  wetland flux by the Kaplan wetland inventory, (b) shows the anthropogenic  $\text{CH}_4$  emissions from EDGAR, (c) the biomass burning emissions from Prep\_chem\_sources. In (d) the online calculated termite emissions are demonstrated. (e) illustrates the online calculated soil uptake flux. The total  $\text{CH}_4$  flux is shown in (f).

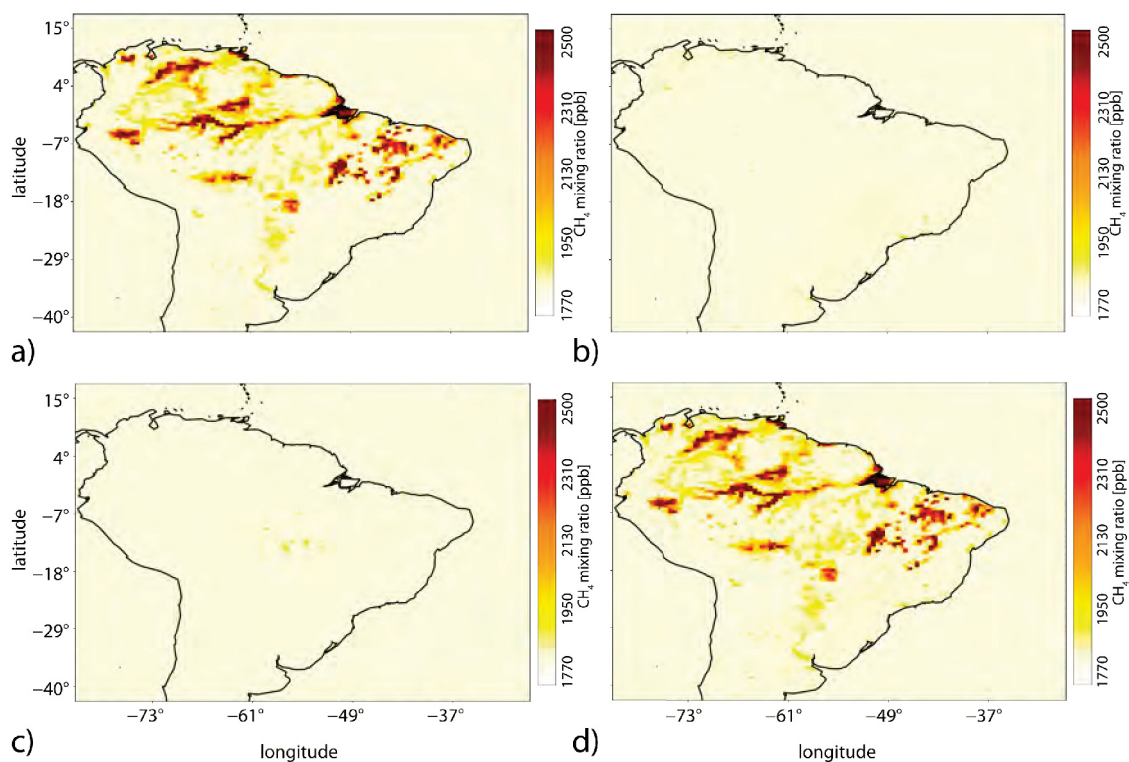


Figure 4.6: Methane atmospheric mixing ratio distribution simulated by WRF-ChemV3.4 for 4<sup>th</sup> August 2009. A constant background atmospheric mixing ratio of 1770 ppb is assumed and added to each tracer. (a) illustrates the tracer distribution for biogenic CH<sub>4</sub> sources, (b) the tracer distribution of anthropogenic CH<sub>4</sub> sources, and (c) the tracer distribution of biomass burning CH<sub>4</sub> sources. In (d) the total CH<sub>4</sub> atmospheric mixing ratio is shown.





## Chapter 5

# Data analysis and comparison to global models

An extensive set of CH<sub>4</sub> airborne data was collected during the two BARCA campaigns in November 2008 and May 2009. For the first time in the Amazon basin, continuous measurements of CH<sub>4</sub> onboard an aircraft were conducted using an analyzer based on the cavity ring-down spectroscopy (CRDS) technique (second campaign only). Flask samples were taken and analyzed for CH<sub>4</sub> during both campaigns. The continuous measurements provided the opportunity to capture a better picture of the CH<sub>4</sub> distribution in the PBL and lower free troposphere (FT) in the Amazon basin. Analysis of  $\delta^{13}\text{CH}_4$  and  $\delta\text{D}$  isotopes and CO mixing ratios as additional tracer enabled the attribution of observed CH<sub>4</sub> mixing ratios to different CH<sub>4</sub> source processes. Five different CH<sub>4</sub> inversions all based on the TM5 model [Krol et al., 2005], with two of them using additional observational constraints from SCIAMACHY, are compared to BARCA CH<sub>4</sub> observations. They are evaluated for November 2008 and May 2009 in five different sampling regions of the Amazon basin. Influence regions of the sampling regions were derived from a LPDM. The monthly budget of the influence regions is compared to the mismatch of modeled and observed CH<sub>4</sub> mixing ratios. From this evaluation, flux estimates for the Amazon lowland region are obtained that correct for the model-data mismatch.

Main parts of this chapter are published in:

*Beck, V., H. Chen, C. Gerbig, P. Bergamaschi, L. Bruhwiler, S. Houweling, T. Röckmann, O. Kolle, J. Steinbach, T. Koch, C. J. Sapart, C. van der Veen, C. Frankenberg, M. O. Andreae, P. Artaxo, K. M. Longo, S. C. Wofsy, 2012: Methane airborne measurements and comparison to global models during BARCA, J. Geophys. Res., 117, D25, doi:10.1029/2011JD017345.*

### 5.1 Data collection during the two BARCA campaigns

Two airborne measurement campaigns were conducted within the BARCA project using the Bandeirante research aircraft from the National Institute for Space Research (INPE) in Brazil. One at the end of the dry season in November 2008 (BARCA-A) and the other at the end of the wet season in May 2009 (BARCA-B). The aim of these two measurement campaigns was to obtain a set of greenhouse gas and aerosol measurements across the whole Amazon basin. Vertical cross-sections through the PBL and FT between altitudes of 500 m and 4000 m were flown. In total, data

from over 150 vertical profiles were collected on 27 flights, nearly covering the full Amazon basin (Fig. 5.1), during both campaigns. Table 5.1 shows an overview over all flights.

A total of 174 and 206 flask samples were collected during BARCA-A and BARCA-B, respectively, which were subsequently analyzed for a set of various trace gases in the Jena Gaslab (including CH<sub>4</sub>, CO, and sulphur hexafluoride, SF<sub>6</sub>). For CH<sub>4</sub> analysis, the NOAA04 scale was applied [Dlugokencky et al., 2005]. Selected flask samples from both campaigns were sent to the Institute for Marine and Atmospheric Research Utrecht for CH<sub>4</sub> isotope analysis using an analytical system described in Brass and Röckmann [2010]. Isotope ratios are reported in the conventional notation as  $\delta^{13}\text{CH}_4 = [^{13}\text{R}_{SA}/^{13}\text{R}_{ST} - 1]$  and  $\delta\text{D} = [^2\text{R}_{SA}/^2\text{R}_{ST} - 1]$ . The international standards are Vienna Pee Dee belemnite for  $\delta^{13}\text{CH}_4$  measurements and Vienna Standard Mean Ocean Water for  $\delta\text{D}$  measurements (cf. Ch. 2, Sec. 2.1.1).

During the second campaign (BARCA-B), an analyzer based on the cavity ring-down spectroscopy (CRDS) technique (Model G1301-m, Picarro Inc., CA, USA) was deployed onboard the aircraft for continuous measurements of CH<sub>4</sub>, CO<sub>2</sub>, and H<sub>2</sub>O [Chen et al., 2010] in addition to flask sampling. The CRDS analyzer reported the mixing ratios of CH<sub>4</sub> at time intervals of 3 s with a precision better than 1 ppb [Chen et al., 2010]. Comparisons of continuous measurements against flask analysis results indicate that the accuracy of CH<sub>4</sub> measurements by the CRDS analyzer is better than 2 ppb [Chen, 2010].

CO was measured at 2 s time resolution by UV resonance fluorescence, using a Fast-CO-Monitor (Model AL 5002, Aerolaser GmbH, Germany). The precision of the 0.5 Hz data was 0.6%, based on the variability of the measurements of the standard gas within each 3 s calibration period. In flight, zero and span calibrations were made every 10 min to account for instrumental drift associated with varying pressure and temperature. Further details can be found in the publication of Andreae et al. [2012].

## 5.2 Methane data analysis

Seasonal differences between the two campaigns that took place at the end of the dry season (BARCA-A) and at the end of the wet season (BARCA-B) are examined. The measured CH<sub>4</sub> mixing ratios obtained during both BARCA campaigns are discussed in relation to the CH<sub>4</sub> mixing ratios observed at the NOAA background stations east and north-east of the South American continent (location see Fig. 3.2 and Fig. 5.1a) within the same time period [Dlugokencky et al., 2010]. In a second step, CO as an additional tracer and the isotopic composition of CH<sub>4</sub> is used to distinguish between different sources of CH<sub>4</sub>, such as CH<sub>4</sub> emissions from anaerobic production by microbes in wetlands, biomass burning, and other anthropogenic sources.

### 5.2.1 BARCA-A vs. BARCA-B

To obtain an overview over the seasonal differences, the BARCA CH<sub>4</sub> observations are illustrated as function of latitude and longitude in Fig. 5.2. During BARCA-A (Fig. 5.2a1) the CH<sub>4</sub> atmospheric mixing ratios decay from southern to northern latitudes. This is contrary to the global latitudinal CH<sub>4</sub> distribution with higher CH<sub>4</sub> atmospheric mixing ratios in the northern hemisphere compared to the southern hemisphere (cf. Fig. 2.2). It can be explained by extensive biomass burning activity in the southern part of the Amazon basin in November 2008, which led to an enhancement of the CH<sub>4</sub> mixing ratio in that region. The longitudinal CH<sub>4</sub> distribution of

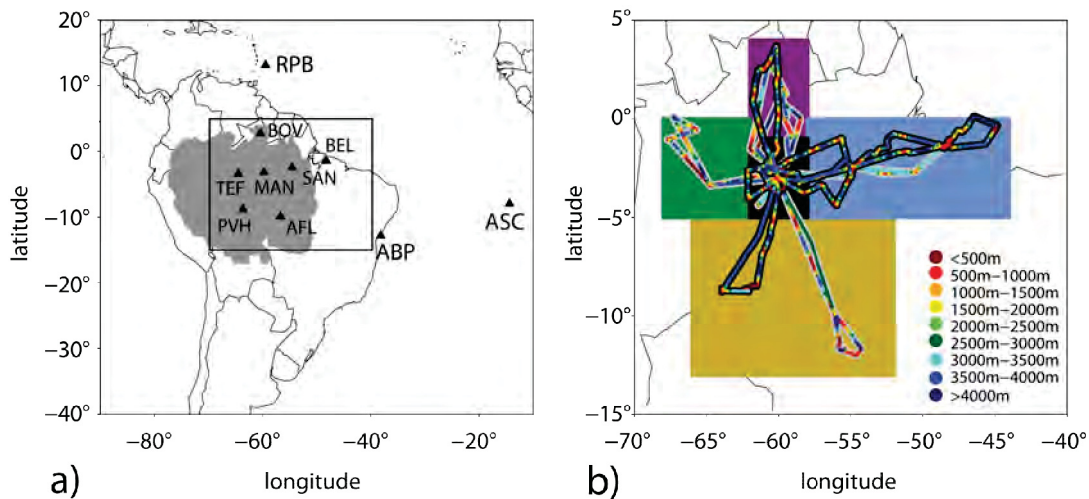


Figure 5.1: (a) Location of the NOAA-ESRL background stations Ragged Point Barbados (RBP), Ascension Island (ASC), and Arembepe (ABP) and the main cities in the Amazon basin: Manaus (MAN), Santarém (SAN), Belém (BEL), Boa Vista (BOV), Tefé (TEF), Porto Velho (PVH), and Alta Floresta (AFL). The gray shaded area depicts the Amazon lowland region (< 500 m) as described in Melack et al. [2004]. (b) illustrates the zoom into the black rectangular in (a) and shows the flight tracks of BARCA-A (gray-shaded) and BARCA-B (black-shaded). Altitudes are denoted by different colors. The solid boxes illustrate the separation of the BARCA observations into five different sampling regions of the Amazon basin: north (violet): latitude  $> -1.0^\circ$  & longitude  $> -62.0^\circ$ ; west (green): latitude  $> -5.0^\circ$  & longitude  $< -62.0^\circ$ ; center (black): latitude  $> -5.0^\circ$  & latitude  $< -1.0^\circ$  & longitude  $> -62.0^\circ$  & longitude  $< -58.0^\circ$ ; east (blue): latitude  $> -5.0^\circ$  & latitude  $< 0.0^\circ$  & longitude  $> -58.0^\circ$ ; south (yellow): latitude  $< -5.0^\circ$  (cf. Fig. 5.4 and Fig. 5.8).

the BARCA-A flasks (Fig. 5.2a2) demonstrates a gradual decrease in the atmospheric  $\text{CH}_4$  mixing ratio from the western to the eastern part of the Amazon basin. A possible explanation is the larger inundated wetland area in the western part of the Amazon basin resulting in total higher  $\text{CH}_4$  emissions from wetlands (cf. Ch. 6). In both cases the  $\text{CH}_4$  atmospheric mixing ratio is higher in the PBL (altitude < 1250 m; green) compared to the FT (altitude > 1250 m; yellow). The BARCA-B flasks (Fig. 5.2b1) for the FT show higher  $\text{CH}_4$  atmospheric mixing ratios when moving towards the northern hemisphere. This is in accordance to the global latitudinal  $\text{CH}_4$  distribution (cf. Fig. 2.2). The flask observations in the PBL show a contrary picture. It is likely induced by high  $\text{CH}_4$  atmospheric mixing ratios in the Manaus area. The longitudinal distribution of the BARCA-B flasks (Fig. 5.2b2) draws a similar picture as for the BARCA-A flasks. The latitudinal dependence of the BARCA-B continuous observations (Fig. 5.2c1) is similar to the flask observations with increasing  $\text{CH}_4$  atmospheric mixing ratios towards the northern hemisphere in the FT. The longitudinal distribution of BARCA-B continuous observations differs in the FT compared to the BARCA-B flask observations. A possible reason is the additional number of high  $\text{CH}_4$  mixing ratios observed around  $-55^\circ$  longitude in the continuous observations, which cannot be found in the BARCA-B flasks. They are responsible for the trend of higher  $\text{CH}_4$  atmospheric mixing ratios towards the eastern part of the Amazon basin in the continuous observations. This indicates that the flask observations are in general representative for the atmospheric  $\text{CH}_4$  distribution in the

	Flt.num	Date	Direction	No. Profiles	No. Flasks
BARCA-A	2	2008-11-16	around Manaus	4	-
	3	2008-11-18	Manaus-Santarém	4	13
	4	2008-11-18	Santarém-Belém	4	17
	5	2008-11-19	Belém-Santarém	6	17
	6	2008-11-19	Santarém-Manaus	4	12
	7	2008-11-22	around Manaus (north)	8	26
	8	2008-11-23	Manaus-Boa Vista	8	14
	9	2008-11-23	Boa Vista-Manaus	4	14
	10	2008-11-25	Manaus-Alta Floresta	6	15
	11	2008-11-26	around Alta Floresta	8	14
	12	2008-11-27	Alta Floresta-Manaus	2	3
	13	2008-11-29	Manaus-Tefé	4	12
	14	2008-11-30	around Tefé (northwest)	8	17
	BARCA-B	2	2009-05-17	around Manaus (west)	6
3		2009-05-17	around Manaus (west)	10	16
4		2009-05-19	Manaus-Boa Vista	10	18
5		2009-05-19	Boa Vista-Manaus	6	12
6		2009-05-21	Manaus-Santarém	8	14
7		2009-05-21	Santarém-Belém	6	16
8		2009-05-22	Belém offshore	4	15
9		2009-05-23	Belém-Santarém	5	13
10		2009-05-23	Santarém-Manaus	2	9
11		2009-05-26	Manaus-Santarém	8	14
12		2009-05-26	Santarém-Manaus	8	15
13		2009-05-27	Manaus-Porto Velho	8	13
14		2009-05-27	Porto Velho-Manaus	2	10
15		2009-05-28	around Manaus (city)	2	13

Table 5.1: Overview over all flights conducted during BARCA-A and BARCA-B indicated with their flight number (*Flt.num*), the date of each flight (*Date*), the flight origin and destination (*direction*), the number of vertical profiles flown (*No. Profiles*), and the number of flasks sampled during each flight (*No. Flasks*).

Amazon basin. However, continuous observations enable to obtain additional information on the  $\text{CH}_4$  distribution.

To derive an estimate of the magnitude of  $\text{CH}_4$  emitted from the Amazon basin, the  $\text{CH}_4$  results from flask samples for BARCA-A and BARCA-B are compared to NOAA-ESRL measurements at the background stations Ascension Island (ASC,  $7.92^\circ\text{S}$ ,  $14.42^\circ\text{W}$ ) representing southern hemisphere air, Ragged Point Barbados (RPB,  $13.17^\circ\text{N}$ ,  $59.43^\circ\text{W}$ ) representing northern hemisphere air, and Arembepe (ABP,  $12.77^\circ\text{S}$ ,  $38.17^\circ\text{W}$ ) at the Brazilian coast (cf. Fig. 3.2 and Fig. 5.1). Flasks sampled at the three background stations during the time periods of the two BARCA campaigns are utilized for the comparison. Depending on the station, 4 to 12 flask samples are used. Note that the NOAA flasks are usually sampled for baseline conditions, i.e. in case of ABP only for onshore winds. To assess the role of interhemispheric mixing,  $\text{CH}_4$  mixing ratios are plotted as a function of  $\text{SF}_6$  mixing ratios (Fig. 5.3a–b; cf. Miller et al. [2007]).  $\text{SF}_6$  is a purely anthropogenic gas, and serves as an excellent hemispheric tracer since almost all  $\text{SF}_6$  is emitted in the

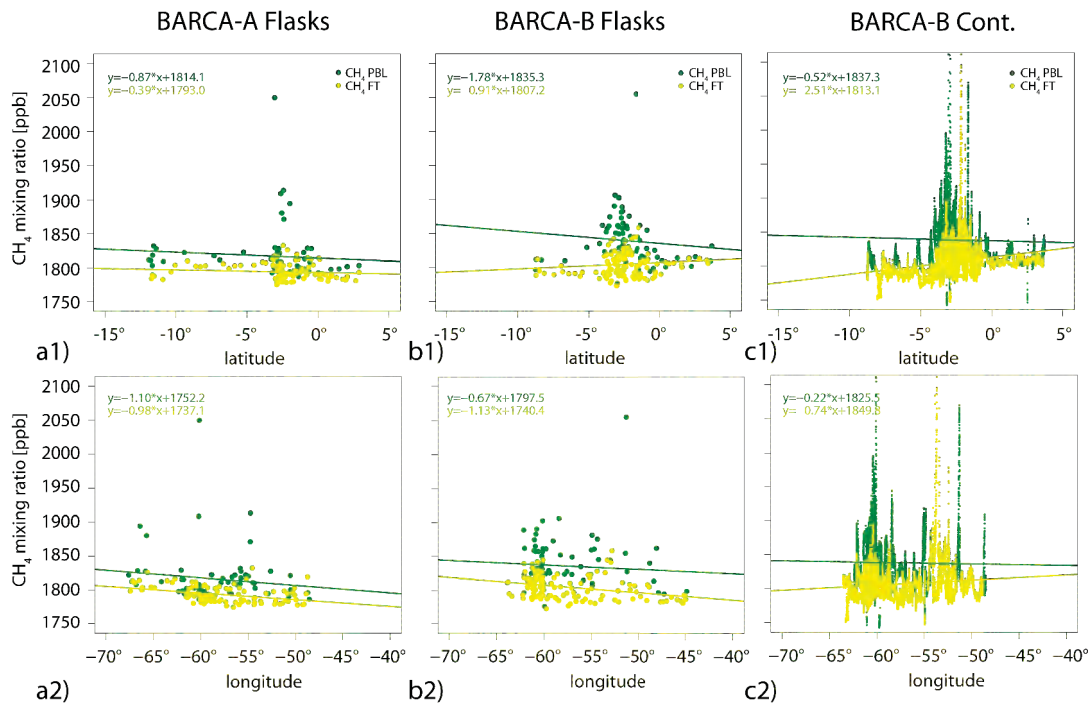


Figure 5.2: (a) shows BARCA-A  $\text{CH}_4$  flask observations as function of latitude (a1) and longitude (a2). (b1–b2) and (c1–c2) illustrate the same for the BARCA-B flask and continuous observations. The observations in the PBL (<1250 m) are colored in green. Those in the FT (>1250 m) are colored in yellow. The continuous lines are the result from a linear regression of the corresponding observations.

northern hemisphere [Olivier et al., 1999]. Mixing of northern hemispheric air, with high  $\text{CH}_4$  mixing ratios, into the southern hemisphere should proceed along the mixing lines between the two end members in the  $\text{CH}_4$ – $\text{SF}_6$  space, as indicated in Fig. 5.3. Almost all flask results show  $\text{CH}_4$  values higher than this mixing line, which clearly indicates a  $\text{CH}_4$  source in the Amazon basin.

The measured  $\text{CH}_4$  atmospheric mixing ratios are separated into those sampled in the PBL (altitudes < 1250 m; green) and in the FT (altitudes 1250 m–4500 m; yellow). For BARCA-A (Fig. 5.3a), the mean  $\text{SF}_6$  mixing ratio was  $6.49 \pm 0.03$  ppt (1-sigma standard deviation) for the PBL and  $6.49 \pm 0.04$  ppt for the FT. This clearly indicates that most of the background air sampled in the Amazon in November 2008 comes from the southern hemisphere (ASC:  $6.45 \pm 0.06$  ppt). Only a few flasks sampled in the FT have  $\text{SF}_6$  atmospheric mixing ratios closer to the  $\text{SF}_6$  atmospheric mixing ratio measured at RPB ( $6.68 \pm 0.08$  ppt). The flasks with the highest  $\text{SF}_6$  mixing ratios show  $\text{CH}_4$  mixing ratios that follow the expected mixing line. On average, the value of the  $\text{CH}_4$  atmospheric mixing ratio during BARCA-A is  $1817 \pm 39$  ppb in the PBL and  $1794 \pm 12$  ppb in the FT, which indicates an enhancement of  $\sim 45$  ppb and  $\sim 25$  ppb, respectively, compared to the mixing line between the NOAA-ESRL surface stations ASC ( $1755 \pm 4$  ppb) and RPB ( $1824 \pm 9$  ppb).

In contrast, for BARCA-B the airflow into the Amazon basin was a mixture of both hemispheres. The measured  $\text{SF}_6$  atmospheric mixing ratios cover the entire range between the two end members (Fig. 5.3b). Similar to BARCA-A, the mean  $\text{CH}_4$  atmospheric mixing ratio observed in the



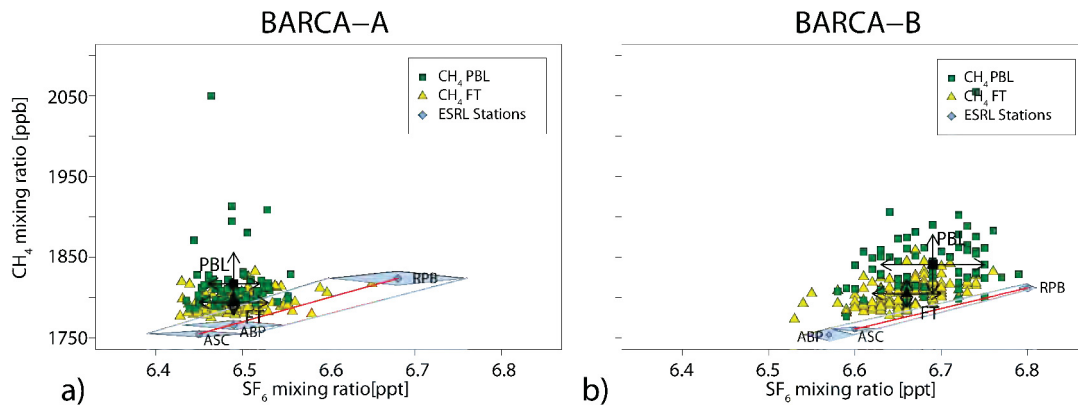


Figure 5.3: Methane atmospheric mixing ratios as function of SF<sub>6</sub> atmospheric mixing ratios for all flasks collected during BARCA-A (a) and BARCA-B (b). The CH<sub>4</sub> and SF<sub>6</sub> atmospheric mixing ratios from the NOAA-ESRL surface stations (CH<sub>4</sub> and SF<sub>6</sub> data courtesy of E. Dlugokencky, NOAA-ESRL Global Monitoring Division GMD) at Ragged Point Barbados (RPB)—representing northern hemispheric air, Ascension Island (ASC)—representing southern hemispheric air, and Arembepe (ABP) at the Brazilian coast during the duration of the two campaigns are shown. The red lines indicate the mixing line between northern and southern hemispheric air. The black squares illustrate the mean values of CH<sub>4</sub> and SF<sub>6</sub> for the PBL (altitude < 1250 m) and the FT (altitude > 1250 m). The black and blue error bars show the 1-sigma standard deviation.

PBL ( $1841 \pm 37$  ppb) and the FT ( $1806 \pm 38$  ppb) are enhanced by  $\sim 60$  ppb and  $\sim 25$  ppb, respectively, compared to the mixing line between the background stations ASC ( $1761 \pm 3$  ppb) and RPB ( $1812 \pm 5$  ppb). During BARCA-B, continuous measurements using the CRDS analyzer are also available, and they show similar mean values as the flask measurements ( $1839 \pm 37$  ppb for the PBL and  $1805 \pm 17$  ppb for the free troposphere). From the observations it is concluded that the Amazon basin is a strong source of CH<sub>4</sub> during both seasons.

For a comparison of the vertical structure of atmospheric CH<sub>4</sub> between BARCA-A and BARCA-B in different regions of the Amazon basin (north, west, east, south and center—for a definition of the regions see Fig. 5.1b), vertical profiles of the CH<sub>4</sub> mixing ratios were binned into 500 m intervals. Flask measurements were used to calculate the vertical profiles for BARCA-A, while for BARCA-B the continuous data from the CRDS analyzer were aggregated into 500 m binned profiles except for flights no. 8–10 (Table 5.1), where no continuous data were available due to instrument failure. For these flights, flask data were taken to calculate the profiles.

As already illustrated in Fig. 5.3, the mean values of CH<sub>4</sub> in the PBL are on average 23 ppb lower for BARCA-A (1817 ppb) than for BARCA-B (1839 ppb). The difference between the mean CH<sub>4</sub> mixing ratios in the FT during BARCA-A (1794 ppb) and BARCA-B (1806 ppb) is smaller (12 ppb) than for the PBL. This is also seen in the total campaign averaged vertical profile and the vertical profiles for the different regions for BARCA-A and BARCA-B (Fig. 5.4a). The mean vertical profiles for the different regions (Fig. 5.4b–f) denote an increase in the CH<sub>4</sub> atmospheric mixing ratio at altitudes between 500 m and 1000 m during BARCA-B, especially for the western and the center part, while in the southern and eastern part during BARCA-A the mixing ratio at 500–1000 m was higher than for BARCA-B. The increase in the CH<sub>4</sub> mixing ratio in the southern part during BARCA-A may be explained by more intensive biomass burning activity along the



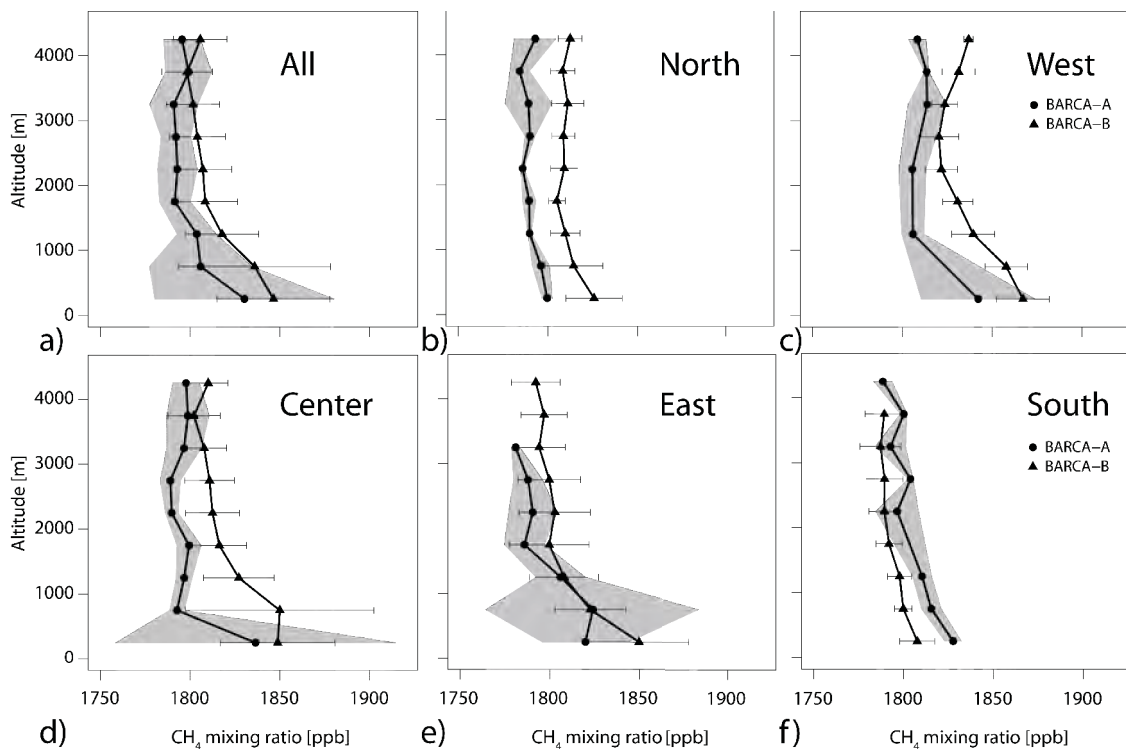


Figure 5.4: 500 m binned vertical profiles for the observed CH<sub>4</sub> mixing ratios for (a) the total campaign average and (b-f) different regions of the Amazon basin. The mean vertical profiles are shown for BARCA-A and BARCA-B. The 1-sigma standard deviation of the observations is denoted as gray shaded area for BARCA-A and as error bars for BARCA-B. The Amazon basin is divided into northern, western, center, eastern and southern part as described in Fig. 5.1b.

southern and eastern margins of the Amazon Basin in November 2008 compared to May 2009 (cf. longitudinal distribution Fig. 5.2). This was demonstrated for CO and aerosol particle number concentrations by Andreae et al. [2012], where maps of the distributions of fires during the BARCA campaigns are shown. Notable is the higher 1-sigma standard deviation of the vertical profiles in the eastern part for both campaigns due to higher oceanic influence. The higher 1-sigma standard deviation in the PBL in the center part originates from several observed high CH<sub>4</sub> mixing ratios while ascending and descending to Manaus airport. In the western, center and northern part of the Amazon basin, CH<sub>4</sub> is higher at all altitudes during BARCA-B than during BARCA-A (21 ppb on average), which might be due to the expected enhanced CH<sub>4</sub> emissions from wetlands in May (end of wet season) compared to November (end of dry season) [Devol et al., 1990].

### 5.2.2 Methane source identification

To identify and distinguish the different main sources of CH<sub>4</sub> in the Amazon basin (wetlands, biomass burning, and other anthropogenic emissions), two techniques, i.e. CO as a tracer for biomass burning and analysis of the isotopic composition of CH<sub>4</sub> are used.

During BARCA-A extensive biomass burning occurred in the Amazon basin between Santarém and Belém, in the north-east region of Brazil, and along the southern edge of the Amazon basin.

Fig. 5.5a shows the distribution of the  $\text{CH}_4$  atmospheric mixing ratios as a function of CO atmospheric mixing ratios during BARCA-A. The observations indicate that a large fraction of the flask samples contain a biomass burning signature, as identified by the high CO values. The slopes of the lines in Fig. 5.5a correspond to the expected  $\Delta\text{CH}_4/\Delta\text{CO}$  emission ratios for savanna, tropical forest, and biofuel burning after Andreae and Merlet [2001] (cf. Sec. 2.1.3). Some samples, especially flask J1420, collected on FLT 5 from Belém to Santarém ( $1.495^\circ\text{S}$ ,  $48.728^\circ\text{W}$ ) at 2104 m altitude, fall on this trend. It is an evidence that biomass burning is the dominant source of the small  $\text{CH}_4$  increase seen in this sample. The emission ratio in this sample relative to the regional background values measured on the same flight (flask J1416,  $\text{CO} = 176$  ppb,  $\text{CH}_4 = 1786$  ppb) is  $\Delta\text{CH}_4/\Delta\text{CO} = 0.095$ . A bivariate regression [Cantrell, 2008] of the  $\text{CH}_4$  vs. the CO atmospheric mixing ratios from BARCA-A (excluding sample J1420 and the samples with  $\text{CH}_4$  values  $> 1850$  ppb) yields a slope of 0.134, again consistent with the average emission ratio of  $0.114 \pm 0.020$  of Andreae and Merlet [2001] for tropical forest burning. The low explained variability,  $r^2 = 0.18$ , indicates, that only a minor fraction of the variance of  $\text{CH}_4$  is explained by the contribution from biomass burning.

During the end of the wet season (BARCA-B), a biomass burning event was sampled on FLT 5 from Boa Vista to Manaus (Fig. 5.5b) with a calculated emission ratio of  $\Delta\text{CH}_4/\Delta\text{CO} = 0.112$  for the continuous data. In addition, the emission ratio of the flask sample J1429  $\Delta\text{CH}_4/\Delta\text{CO} = 0.102$ , collected while flying through this biomass burning plume, is consistent with the emission ratio derived from the continuous data and the values proposed in the literature for tropical forest burning.

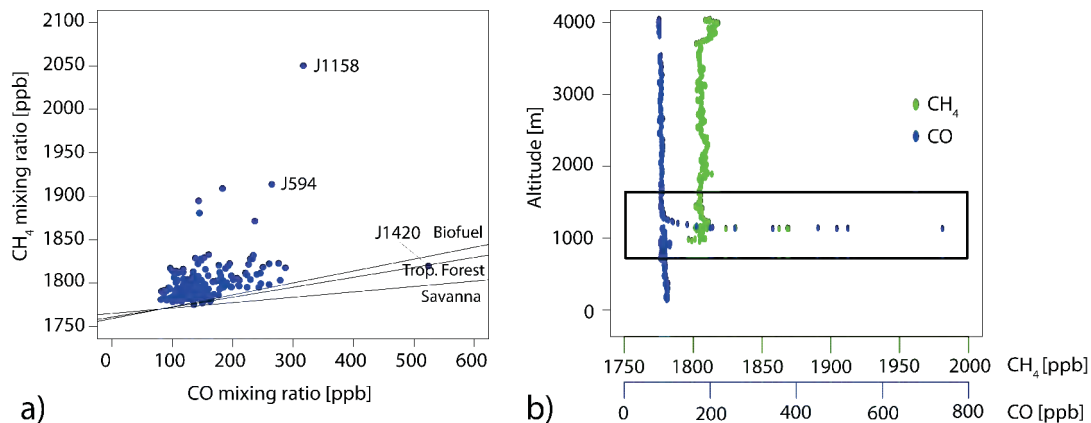


Figure 5.5: Comparison of  $\text{CH}_4$  atmospheric mixing ratio as function of the CO atmospheric mixing ratio for all flasks collected during BARCA-A (a). The emission ratios for biofuel burning ( $\Delta\text{CH}_4/\Delta\text{CO} = 0.1369$ ), tropical forest burning (0.1144), and savannah burning (0.0619) are represented by the slopes of the straight lines. (b) shows the vertical profiles for  $\text{CH}_4$  and CO on the flight from Boa Vista to Manaus (Flt 5; BARCA-B) crossing a biomass burning plume (black box). In the  $\text{CH}_4$  profile, a  $\sim 70$  ppb enhancement is notable, while for CO the enhancement is much higher ( $\sim 650$  ppb).

It is evident from Fig. 5.5, that in most of the samples the observed  $\text{CH}_4$  elevations are far stronger than what is expected from biomass burning. They are well above the straight lines in Fig. 5.5a that indicate the predicted composition of samples resulting from the addition of biomass smoke to the air entering the Amazon basin (ca. 1770 ppb  $\text{CH}_4$  and 80 ppb CO). Although most

of the flasks sampled during BARCA-A contain a biomass burning signature, this has only a minor influence on the observed CH<sub>4</sub> enhancements. In particular, all flasks with CH<sub>4</sub> mixing ratios > 1850 ppb could be identified to have excess CH<sub>4</sub> of biogenic origin by isotope analysis. Fig. 5.6a–b show the results of the isotope measurements in a Keeling plot. The values are plotted as a function of the inverse of the mixing ratio. The isotope mixing lines that would result from contributions from single potentially important CH<sub>4</sub> sources (continuous line: biogenic CH<sub>4</sub> emissions, e.g. from wetlands, dotted line: thermogenic CH<sub>4</sub> emissions like natural gas or coal mining, dashed line: CH<sub>4</sub> emissions from biomass burning) are illustrated. The y-axis intercepts of  $\delta^{13}\text{CH}_4 = -58.8\text{‰}$  for BARCA-B (Fig. 5.6a) and  $\delta\text{D} = -312\text{‰}$  for BARCA-A (Fig. 5.6b) are in excellent agreement with what is expected from biogenic sources. Most of the flasks sampled during BARCA-B with CH<sub>4</sub> atmospheric mixing ratios >1850 ppb had been collected over wetland areas, for which calculated backward trajectories do not show urban influence. For example, flask J1719 was collected at 270 m altitude over an extensive wetland area (1.67°S, 51.32°W) (Fig. 5.6b) and shows a measured CH<sub>4</sub> atmospheric mixing ratio of 2055 ppb and a  $\delta^{13}\text{CH}_4$  signature of -49.1‰, in agreement with biogenic CH<sub>4</sub> emissions. It is clear that the majority of the isotopic measurements, both for BARCA-A and for BARCA-B, agree very well with biogenic methane being the dominant source responsible for the CH<sub>4</sub> elevations in the analyzed samples. The biogenic methane can be mainly attributed to CH<sub>4</sub> emissions from wetlands as the dominant biogenic source [Bustamante et al., 2010].

As described above, the  $\Delta\text{CH}_4/\Delta\text{CO}$  emission ratio for sample J1420 strongly indicates that biomass burning is the main source of the additional CH<sub>4</sub>, and this is fully confirmed by  $\delta^{13}\text{CH}_4$  analysis (Fig. 5.6b). A clear isotope enrichment is observed that can only be caused by CH<sub>4</sub> from biomass burning. This turned out to be the only sample of this type that was selected for isotope analysis. But as stated above, the CH<sub>4</sub> elevations from biomass burning are generally small, and at the present precision isotope analysis can only identify sources when the elevations caused by this source are clearly above background levels.

Surprisingly,  $\delta\text{D}$  and  $\delta^{13}\text{CH}_4$  analysis of two flask samples collected during BARCA-A near major cities (J594 - Santarém, J1158-Manaus; Fig. 5.6a) also suggests strong biogenic CH<sub>4</sub> emission sources for these samples, while the calculated backward trajectories in both cases clearly indicate urban influence. The CH<sub>4</sub> atmospheric mixing ratio is much higher than what can be explained by combustion or biomass burning processes given the concomitant CO values. Other CH<sub>4</sub> atmospheric mixing ratio enhancements in the continuous measurements close to major cities (Manaus, Santarém, and Belém) could also be attributed to urban influence using backward trajectory calculations. As one example, the CH<sub>4</sub> atmospheric mixing ratios obtained on FLT 15 during BARCA-B are presented in Fig. 5.7a–b. The three peaks of the CH<sub>4</sub> mixing ratio time series (Fig. 5.7a–green line) with maximum values of 1870 ppb, 1926 ppb and 1980 ppb, respectively, do not show corresponding increases in CO (Fig. 5.7a–blue line), except for the last peak, which could be related to thermal combustion processes. The isotope analysis from flask J0325, collected within the first peak, indicates a biogenic CH<sub>4</sub> source (cf. Fig. 5.6b). A forward calculation of the propagation of the Manaus plume (released at the beginning of the flight) using the STILT model illustrates the influence area within the PBL. Enhanced CH<sub>4</sub> atmospheric mixing ratios are observed exactly at the locations where the flight path crosses the Manaus plume. This supports the hypothesis of biogenic CH<sub>4</sub> emissions from urban areas. Methane from anthropogenically driven biological processes, such as waste decomposition or cattle holding, cannot be readily distinguished from wetland emissions by isotope analysis. Most likely such anthropogenic

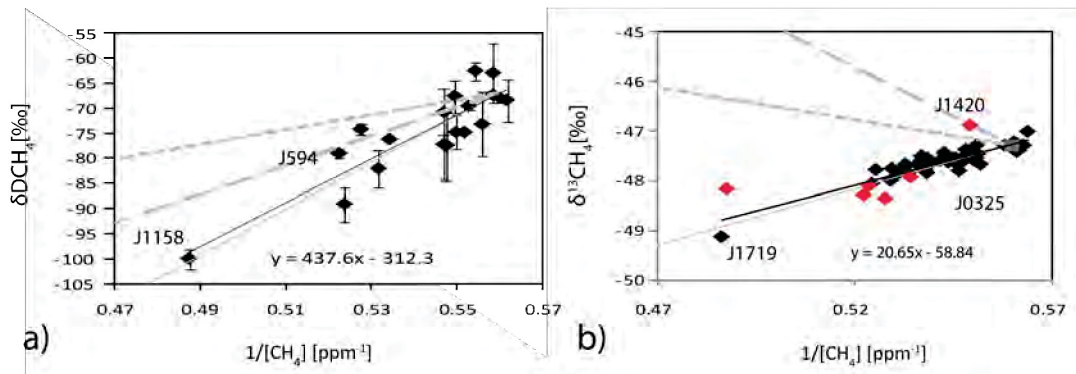


Figure 5.6: Keeling plot representation ( $\delta$  value versus inverse atmospheric mixing ratio) of the isotope measurement results obtained on selected flasks from BARCA-A and BARCA-B. (a) shows the  $\delta D$  signature for flask samples collected during BARCA-A, while (b) illustrates the  $\delta^{13}CH_4$  signature for flask samples collected during BARCA-A (red symbols) and BARCA-B (black symbols). Selected flasks include the ones with the highest mixing ratio, as well as some with the lowest and intermediate mixing ratios. Isotope mixing lines for important  $CH_4$  sources, namely biogenic  $CH_4$ , e.g. from tropical wetlands ( $\delta^{13}CH_4 \sim -60\text{‰}$ ,  $\delta D \sim -320\text{‰}$ , solid line),  $CH_4$  from thermogenic processes, e.g. natural gas and coal mining ( $\delta^{13}CH_4 \sim -40\text{‰}$ ,  $\delta D \sim -150$ , dotted line), and  $CH_4$  from biomass burning ( $\delta^{13}CH_4 \sim -25\text{‰}$ ,  $\delta D \sim -225\text{‰}$ , dashed line) are indicated as gray lines. Isotope source signatures are based on Quay et al. [1999]. The black line indicates the fit of the observation using a linear regression model. Figure courtesy of T. Röckmann.

sources, or the recently reported  $CH_4$  emissions from open sewers [Guisasola et al., 2008], could be large contributors of  $CH_4$  emissions in tropical cities. A plausible source is the decomposition of uncontrolled waste emissions into the waters of the densely populated sloughs along the Amazon river in Manaus and other urban areas. Thus, the observations suggest that the main anthropogenic  $CH_4$  emissions from the city of Manaus are of biogenic origin.

### 5.3 Comparison to global models

Model output from five different global TM5 inversions was compared to the  $CH_4$  observations of BARCA-A and BARCA-B: two versions of the model of Bergamaschi et al. [2009, 2010] (referred to as TM5-PB and TM5-PB-SCI, respectively) and two TM5 inversions from Houweling (referred to as TM5-SH and TM5-SH-SCI) - both with observational constraints from the NOAA-ESRL surface stations and the SCIAMACHY (SCI) satellite retrievals - and Carbon Tracker Methane (referred to as TM5-CT) using only NOAA-ESRL surface sites as observational constraints.

The inversion is either performed by using the 4DVAR technique (Meirink et al. [2008b]; TM5-PB, TM5-PB-SCI, TM5-SH, and TM5-SH-SCI) or Ensemble Kalman Filter (TM5-CT). Models TM5-PB and TM5-PB-SCI apply a semi-exponential probability density function (PDF) for the a-priori flux to enforce that posterior emissions remain positive, and optimize four source categories independently (wetlands, rice, biomass burning, and other emission; see Bergamaschi et al. [2010]). For TM5-SH and TM5-SH-SCI only the total  $CH_4$  flux is optimized. TM5-CT optimizes four different source categories (natural emissions, biomass burning, fossil, and one category containing rice, waste, and agriculture emissions). The number of NOAA-ESRL surface stations from

	TM5-PB-SCI	TM5-PB	TM5-SH-SCI	TM5-SH	TM5-CT
<b>A-priori fluxes</b>					
Wetlands	'JK' inventory [Bergamaschi et al., 2007]	'JK' inventory [Bergamaschi et al., 2007]	LPI-WhyME [Wania, 2007]	LPI-WhyME [Wania, 2007]	Mathews and Fung [1987]
Biomass Burning	GFEDv2 [van der Werf, 2004] average 1997–2007	GFEDv2 [van der Werf, 2004] average 1997–2007	GFEDv2 [van der Werf, 2004] 2008	GFEDv2 [van der Werf, 2004] 2008	GFEDv2 [van der Werf, 2004]
Anthropogenic Emissions	EDGARv4.0 [Olivier and Bertowski, 2001]	EDGARv4.0 [Olivier and Bertowski, 2001]	EDGARv4.0 [Olivier and Bertowski, 2001] Extrapolated using BP statistics	EDGARv4.0 [Olivier and Bertowski, 2001] Extrapolated using BP statistics	EDGAR 3 [Olivier and Bertowski, 2001]
<b>Model setup</b>					
Inversion Technique	4DVAR 32	4DVAR 32	4DVAR 46	4DVAR 46	Ensemble Kalman Filter 80
No. NOAA surface stations	IMAP v5.5 [Frankenberg et al., 2011]	-	IMAP v5.5 [Frankenberg et al., 2011]	-	-
SCIAMACHY retrieval	ECMWF ERA Interim $6^\circ \times 4^\circ$	ECMWF ERA Interim $6^\circ \times 4^\circ$	ECMWF ERA Interim $6^\circ \times 4^\circ$	ECMWF ERA Interim $6^\circ \times 4^\circ$	ECMWF Operational $6^\circ \times 4^\circ$
Meteorology	Carbon Bond Mechanism 4 (CBM-4)	Carbon Bond Mechanism 4 (CBM-4)	Carbon Bond Mechanism 4 (CBM-4)	Carbon Bond Mechanism 4 (CBM-4)	Carbon Bond Mechanism 4 (CBM-4)
Horizontal resolution	25	25	25	25	25
No. vertical levels	25	25	25	25	25
OH fields	15 months	15 months	15 months	15 months	15 months
Runtime period	01/2007–12/2009	01/2007–12/2009	01/2007–12/2009	01/2007–12/2009	01/2000–12/2009

Table 5.2: Differences between the five TM5-based global  $CH_4$  inversions used for the comparison to the BARCA observations (TM5-PB, TM5-PB-SCI, TM5-SH, TM5-SH-SCI, and TM5-CT). The source of a-priori fluxes for the most important  $CH_4$  emission sources, the number of NOAA-ESRL surface stations used for the inversion, the version of the SCIAMACHY retrievals (for TM5-PB-SCI and TM5-SH-SCI only), and additional basic information is shown.



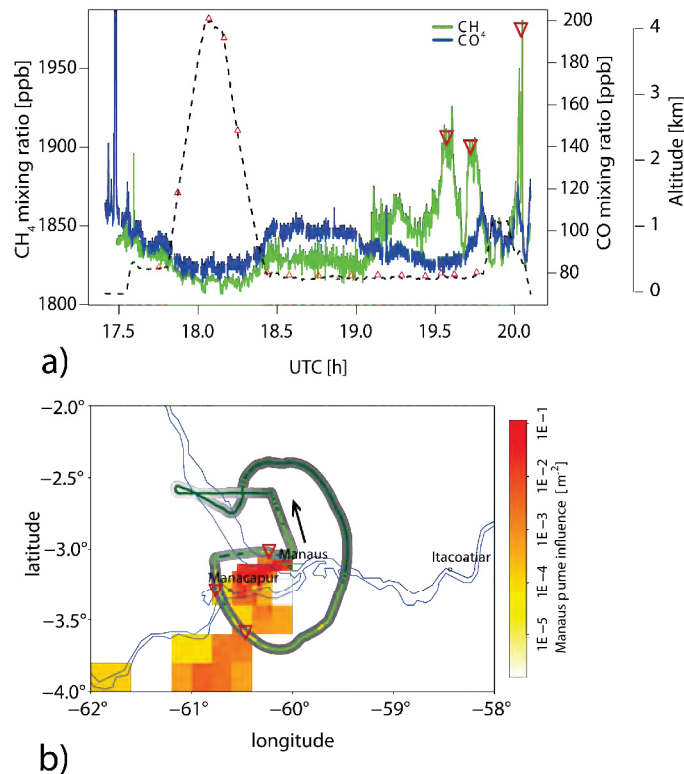


Figure 5.7: Time series of Flt 15 around Manaus city during BARCA-B (a). The black dashed line indicates the altitude of the flight track and the small red triangles show the locations at which flasks were collected. The big triangles denote the increase in the  $\text{CH}_4$  mixing ratio while crossing the Manaus plume (a,b). (b) illustrates the distribution of the Manaus plume within the PBL using a forward calculation of the STILT model and the flight track of Flt 15 around Manaus starting north (indicated by the black arrow). The gray color along the flight track indicates the altitude of the flight track (light gray—high altitude ( $\sim 3500$ – $4000$  m); dark gray—low altitude ( $\sim 500$  m)) and the overlying color denotes the magnitude of the  $\text{CH}_4$  atmospheric mixing ratio (green—low mixing ratio ( $\sim 1800$ – $1850$  ppb); orange—high mixing ratio  $>1900$  ppb).

which observations are used in the inversion ranges from 32 to 80 (cf. Table 5.2). The two inversions using SCIAMACHY observations (TM5-PB-SCI and TM5-SH-SCI) differ in their way of accounting for the bias correction of the SCIAMACHY data by fitting a 2nd order polynomial function of latitude and month (TM5-PB-SCI), and fitting a function with a uniform scaling factor for the total column and a scalar accounting for air mass dependent errors as unknowns (TM5-SH-SCI). Both TM5-PB-SCI and TM5-SH-SCI use the new IMAPv5.5 SCIAMACHY retrievals [Frankenberg et al., 2011]. They enable consistent  $\text{CH}_4$  retrievals from 2003 through 2009 despite the significant SCIAMACHY pixel degradation within the  $\text{CH}_4$   $2\nu_3$  band occurring at the end of 2005. However, these new IMAPv5.5 retrievals have systematically higher values in the tropics than the previous IMAPv5.0 retrievals available for the period 2003–2005 [Frankenberg et al., 2008, 2011]. An overview over the main characteristics of each model is found in Table 5.2.



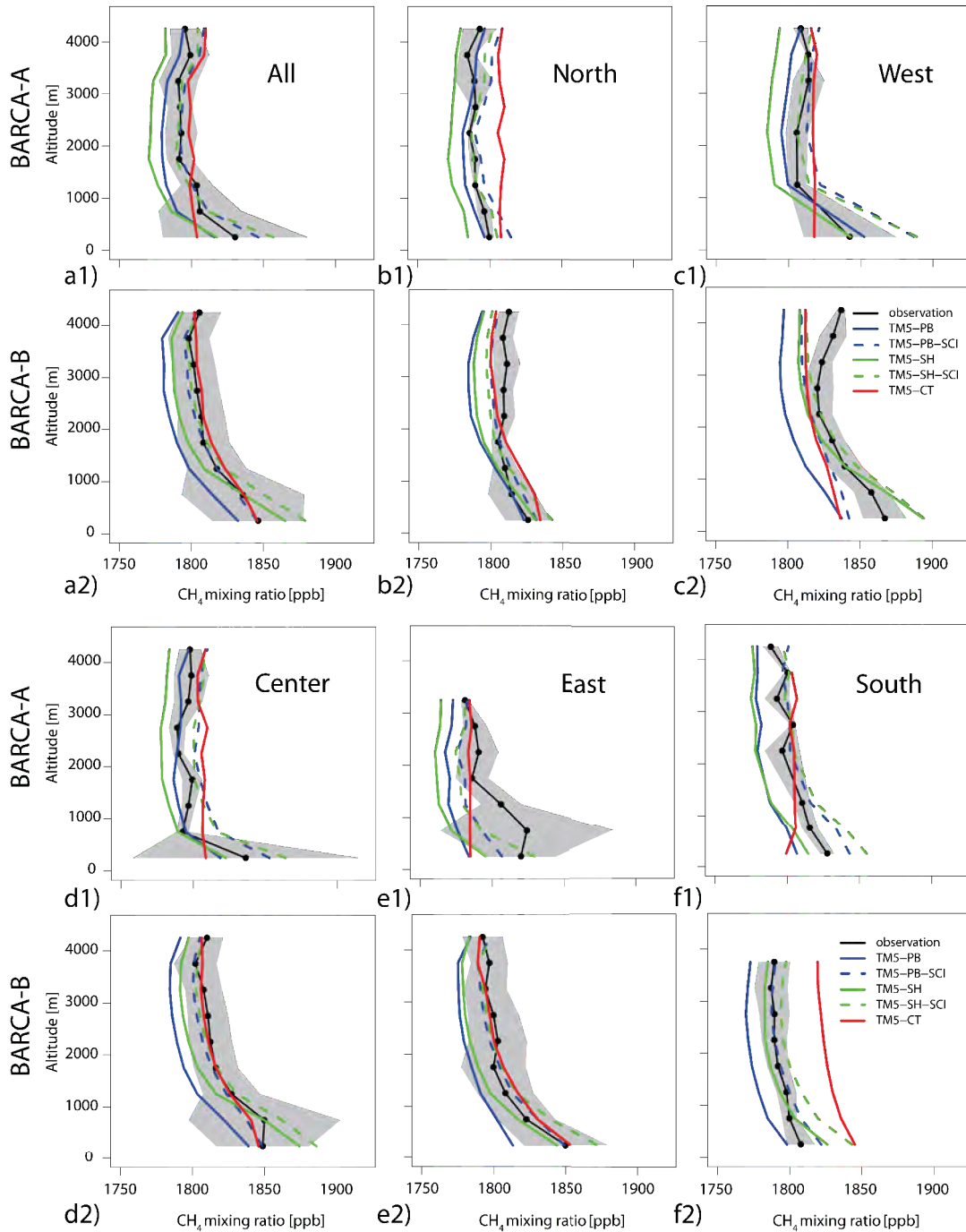


Figure 5.8: (a) 500 m binned vertical profiles for the observed modeled  $\text{CH}_4$  mixing ratios for (a) the total campaign average and (b–f) for different regions of the Amazon basin (cf. definition in Fig. 5.1b). The mean vertical profiles observed for BARCA-A (1) and BARCA-B (2) are shown in black lines and the 1-sigma standard deviation is denoted as gray shaded area.

The global models are all based on the same underlying transport model TM5, but use different a-priori input  $\text{CH}_4$  fluxes from wetlands: the Kaplan wetland inventory [Bergamaschi et al., 2007] for TM5-PB and TM5-PB-SCI, the LPJ-Wetland-hydrology Methane Emission (LPJ-WhyME) model [Wania, 2007] for TM5-SH and TM5-SH-SCI, and wetland fluxes based on Matthews and Fung [1987] for TM5-CT. Both TM5 inversions from Bergamaschi et al. [2009] use the same a-priori fluxes (referred to AP-PB from here on). The a-priori fluxes of both inversions of Houweling are denoted as AP-SH (and AP-CT for a-priori fluxes of TM5-CT). For AP-CT, the spatial distribution of the a-priori wetland  $\text{CH}_4$  fluxes is constant throughout the year and only the magnitude of the a-priori  $\text{CH}_4$  wetland emission changes in time. On the other hand, AP-PB and AP-SH have the spatial distribution of the wetland area changing in time between November 2008 and May 2009. In comparison to the a-priori wetland  $\text{CH}_4$  emissions of AP-SH, AP-PB has lower wetland a-priori emissions in the region between Manaus and Santarém and higher emissions close to the Amazon delta. The wetland a-priori fluxes of AP-CT in the northern and north-western part of the Amazon show mostly zero emissions (cf. Fig. A.1)). The biomass burning a-priori fluxes of all three models are based on the Global Fire Emission Database, Version 2 (GFEDv2) [van der Werf, 2004], but differ in their temporal resolution. AP-PB and AP-SH use monthly averages of biomass burning emissions. AP-PB utilizes here for the averages of fire emissions from the years 1997–2007. AP-SH takes the monthly averages of the year 2008 also for the year 2009. AP-CT uses daily fire emissions interpolated from monthly averages of the corresponding years 2008 and 2009. For May 2009, a comparison of the a-priori biomass burning emissions of all models does not show any significant differences in the central Amazon basin, while for November 2008 AP-SH does not capture biomass burning emissions in the eastern part of the Amazon, while the other two biomass burning a-priori fluxes do (cf. Fig. A.2). To compare the  $\text{CH}_4$  values of the global model simulations to the BARCA  $\text{CH}_4$  airborne measurements, the  $\text{CH}_4$  model values were extracted from  $6^\circ \times 4^\circ$  3 h gridded fields at the observation location (flask location for BARCA-A, measurement location every 3 s for BARCA-B) by using a three-dimensional interpolation routine and additionally temporal interpolation. The extracted values were binned into 500 m vertical intervals and separated for different regions of the Amazon basin as already described for the observations in Sec. 5.2.1.

For BARCA-A (Fig. 5.8a1–f1), the vertical profiles of the model simulations from inversions using SCIAMACHY observations show clearly higher atmospheric mixing ratios than the inversions using only observations from NOAA-ESRL surface stations (except for TM5-CT in the free troposphere). Both profiles (TM5-PB-SCI and TM5-SH-SCI) agree well with each other and overestimate the observations by  $\sim 10$  ppb except for the eastern part (cf. Fig. 5.8e1). In the eastern part, their disagreement with the observations in the PBL is highest. SCIAMACHY observations are rather insensitive to biomass burning, because the  $\text{CH}_4/\text{CO}_2$  ratio used in the retrievals is similar for background air and biomass burning (cf. Petersen et al. [2010]). This fact could be a plausible explanation for the lower  $\text{CH}_4$  mixing ratios of both models using SCIAMACHY observations in the eastern part. Surprisingly, TM5-SH-SCI shows higher atmospheric mixing ratios in the PBL even though the a-priori biomass burning emissions depict almost no emission in that region. Higher wetland a-priori emissions of AP-SH as compared to AP-PB between Manaus and Santarém could be a reasonable explanation for this. The deviation from the observed vertical profiles for all simulations is highest in the eastern part during BARCA-A. It could be due to underestimated wetland emissions and biomass burning activity of all models in that region. For BARCA-A, the vertical profiles of the simulations using observations only from NOAA-ESRL

surface stations for their inversion system have the tendency to underestimate the observed atmospheric mixing ratios, TM5-SH more than TM5-PB and TM5-CT. In the FT TM5-CT is closest to the observations and surprisingly overestimates the observations (except for the eastern part) on average by 7 ppb, but underestimates the observations especially in the PBL. One reason lies in much lower a-posteriori fluxes of TM5-CT compared to all other models (cf. Fig. A.3). For BARCA-A, the comparison clearly illustrates the benefit of using SCIAMACHY observations in the inversion as those fit the observations better on average (5–6 ppb overall bias for TM5-PB-SCI and TM5-SH-SCI compared to 11–17 ppb bias for TM5-PB, TM5-SH, and TM5-CT) as demonstrated in Fig. 5.8a1.

For BARCA-B (Fig. 5.8a2–f2), the situation is more complex: In contrast to BARCA-A, the simulations of the SCIAMACHY based inversions do not always show higher atmospheric mixing ratios throughout the total vertical profile for all regions when compared to simulations of the same models using constraints from NOAA-ESRL surface stations only in the inversion. In the FT (except for the western part), the simulations of SCIAMACHY based inversions TM5-PB-SCI and TM5-SH-SCI fit the observed atmospheric mixing ratios well (bias < 10 ppb). This applies also for TM5-CT (except for the southern part), which is constrained only by NOAA-ESRL surface stations. TM5-SH-SCI and TM5-SH have the highest atmospheric mixing ratios in the PBL, contrary to the results for BARCA-A, where the SCIAMACHY based inversions TM5-PB-SCI and TM5-SH-SCI always show the highest CH<sub>4</sub> atmospheric mixing ratios. The atmospheric mixing ratios of TM5-PB-SCI and TM5-PB in the PBL are significantly lower (western, center, and eastern part) in comparison to atmospheric mixing ratios of TM5-SH and TM5-SH-SCI during BARCA-B. This suggests that the distribution of the wetland a-priori emission patterns has a stronger impact on the simulated atmospheric mixing ratios in the PBL for BARCA-B than for BARCA-A, even though differences in the weight of the a-priori flux between the different models could be a possible reason. Interestingly, the CH<sub>4</sub> atmospheric mixing ratios in the western part (and partially in the northern part) at altitudes between 3000 m and 4000 m are enhanced compared to the other regions of the Amazon basin, which is not captured well by any of the models. This points to a larger source from a greater distance. Indeed, calculations of backward trajectories for these days at the corresponding altitudes indicate contributions from the north-western part of South America, a region where SCIAMACHY suggests high CH<sub>4</sub> mixing ratios [Frankenberg et al., 2005, 2011]. This proposes that the atmospheric region influencing the Amazon basin is considerably larger than the Amazon basin itself.

The differences between each model and the observations for the different sampling regions are likely related to differing a-posteriori flux distributions. To assess this, a closer look was taken at the a-posteriori fluxes within the surface area influencing the respective sampling regions. In order to obtain the influence regions of the Amazon basin during BARCA-A and BARCA-B, footprint calculations, describing the sensitivity of atmospheric mixing ratio observations to upstream surface fluxes within the PBL, were carried out using the STILT model for each flask observation during BARCA-A and roughly four observations per flown vertical profile during BARCA-B. They were calculated 10 days backward in time and temporally integrated for each sampling region (cf. Fig. A.5 and Fig. A.6). 3 h ECMWF meteorological fields were used for the calculation and it was performed on a 6°×4° horizontal grid (same as the grid of the posterior fluxes) to minimize the differences in the representation of the atmospheric transport between STILT and TM5. Fig. 5.9a–b illustrates the monthly budgets for BARCA-A (a) and BARCA-B (b) as function of the mean bias of the vertical profiles as illustrated in Fig. 5.8. The CH<sub>4</sub> flux for

each sampling region  $k = 1, \dots, 5$  for the total land fraction of the STILT domain (cf. Fig. A.5 and Fig. A.6), is weighted by the relative influence from integrated footprints per sampling region using the following formula:

$$Bud_{mo,k} = \sum_{n=1}^{n_k} \sum_{[i,j]_{land}} \frac{f[i,j] \times FP_k^{[n]}[i,j]}{TFP} \quad (5.1)$$

Here,  $Bud_{mo,k}$  indicates the derived monthly budget for the corresponding sampling region  $k$  as illustrated in Fig. 5.9a–b.  $f[i,j]$  is the  $CH_4$  a-posteriori flux of the TM5 simulations of each land grid cell  $[i,j]$ .  $FP$  indicates the value of each single footprint with receptor location in the sampling region  $k$  (sum over the total number of  $n_k$  footprints with receptor location in the corresponding sampling region). The value of the total integrated campaign footprint  $TFP$  is calculated as follows:

$$TFP = \sum_{k=1}^5 \sum_{n=1}^{n_k} \sum_{[i,j]_{land}} FP_k^{[n]}[i,j]. \quad (5.2)$$

The obtained relationship between monthly  $CH_4$  budget and bias of the vertical profile indicates an almost linear relation between the model-observation mismatch and the calculated monthly  $CH_4$  budget of the influence region. However, TM5-CT clearly does not fall on the trend. Possible reasons that influence the bias are the above described differences in the  $CH_4$  fluxes over land, differences in the atmospheric background mixing ratio upstream of the continent, and differences in the vertical distribution. For TM5-CT, differences of 18 ppb (BARCA-A) to 36 ppb (BARCA-B) were found in the background  $CH_4$  mixing ratio upstream of the South American continent compared to the other four inversions, which show a maximum difference of 3 ppb among themselves. Besides potential differences in the vertical distribution, which cannot be excluded, this might be an explanation why TM5-CT does not fall on the trend. Therefore, TM5-CT is not included in the calculations of the linear regression. The correlation coefficients of the linear regression range from  $r = 0.72$  (north) to 0.95 (east) for BARCA-A (a) and from  $r = 0.70$  (west) to 0.96 (center) for BARCA-B (b). The slope of the lines in Fig. 5.9a-b increases with increased relative influence of the footprints or higher budget of the corresponding influence region (cf. Eq. 5.1). For BARCA-A, the southern and center parts show the highest slopes. Due to the high number of observations in the center part, the relative influence of the footprint is higher compared to other regions (also true for BARCA-B). The influence region of the southern region during BARCA-A is mainly located over the South American continent leading to higher budget number in comparison to other regions. In the northern part the budget numbers are very low for both campaigns, because most of the surface influence area is located over the ocean. For BARCA-A (except for the northern part), the inversions using SCIAMACHY observations show in general a more positive bias in the model-observation mismatch of the vertical profile. They have higher monthly  $CH_4$  budgets compared to inversions using only observations from NOAA surface stations, which is not clearly seen for BARCA-B, as already discussed above. The lower panels of Fig. 5.9 demonstrate the total monthly budget (sum over the monthly emissions of all land grid cells of the STILT domain - not weighted) as function of the mean weighted model-observation mismatch for all five TM5-based inversion systems during BARCA-A (c) and BARCA-B (d). Weighting of the mean model-observation mismatch from all five sampling regions  $k$  ( $d_{mean(TM5,obs)}$ ) was calculated

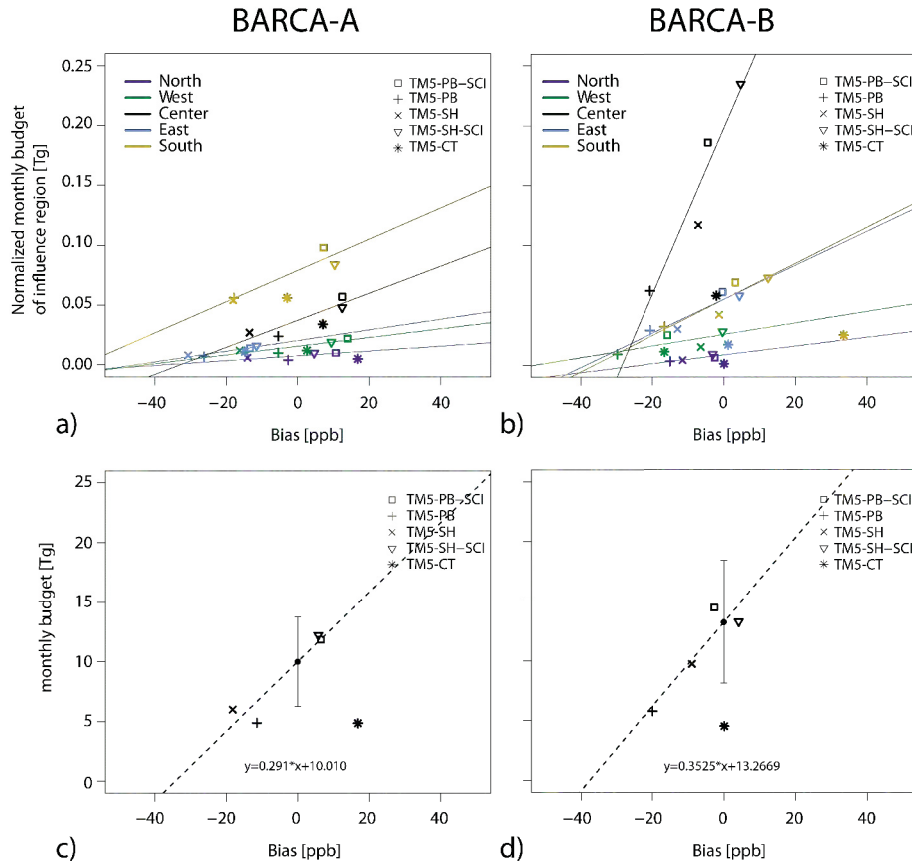


Figure 5.9: (a) and (b) illustrate the monthly budget for each of the five TM5-based global  $\text{CH}_4$  inversions, determined for the influence regions (cf. Fig. A.5 and Fig. A.6) derived from the STILT model, as function of the model-observation mismatch (bias) of the vertical profiles for each of the five different sampling regions. The points are colored accordingly to the corresponding sampling regions (yellow–south, green–west, violet–north, blue–east, black–center; cf. Fig. 5.1b). Colored lines correspond to linear regressions within each region with correlation coefficients ranging from 0.72 to 0.96. Note that TM5-CT was not included in the calculation of the linear regressions. The monthly budget of the land fraction of the STILT domain (cf. Fig. A.5 and Fig. A.6) is depicted as function of the mean weighted bias (weighting accordingly to the fraction of the influence region) for November 2008 (c) and May 2009 (d) for each of the five models. The black dot denotes the “best budget estimate” obtained for bias=0 and the error bars illustrate the 95% confidence interval (CT also not included here). The resulting linear regression is shown as the black dashed line.

according to:

$$d_{\text{mean}(TM5,obs)} = \sum_{k=1}^5 \frac{d_{TM5,obs}[k] \times \sum_{n=1}^{n_k} FP_k^{[n]}}{TFP} \quad (5.3)$$

with  $d_{TM5,obs}$  being the model-observation mismatch of the corresponding sampling region  $k$ . From the linear fit illustrated in Fig. 5.9c–d (note that CT is also not included in the linear fit), the monthly  $\text{CH}_4$  budget for the total land fraction of the STILT domain for  $d_{TM5,obs} = 0$  is

obtained at 10.5 Tg for November 2008 and at 13.3 Tg for May 2009 with a 95% confidence interval of the linear fit ranging from 6.8 Tg to 13.3 Tg for November 2008 and 8.1 Tg to 18.4 Tg for May 2009. The fraction emitted by the Amazon lowland region (<500 m) as described in Melack et al. [2004] (cf. gray shaded area in Fig. 5.1) is calculated to  $0.57 \pm 0.14$  (1-sigma standard deviation resulting from differences in the spatial flux patterns between models) for BARCA-A, and to  $0.51 \pm 0.17$  for BARCA-B. By multiplication of this fraction with the obtained monthly  $\text{CH}_4$  budgets for  $\text{bias} = 0$  in Fig. 5.9c–d and division by the area of the Amazon lowland region, the  $\text{CH}_4$  flux strength of the Amazon lowland region is estimated to  $36 \pm 12 \text{ mg m}^{-2} \text{ d}^{-1}$  for BARCA-A and  $43 \pm 18 \text{ mg m}^{-2} \text{ d}^{-1}$  for BARCA-B using quadratic error propagation ( $29 \pm 12 \text{ mg m}^{-2} \text{ d}^{-1}$  for BARCA-A and  $34 \pm 19 \text{ mg m}^{-2} \text{ d}^{-1}$  for BARCA-B if TM5-CT is included in the calculations). The flux estimates derived for the Amazon lowland region agree well with the numbers found by Miller et al. [2007] who proposed  $35 \text{ mg m}^{-2} \text{ d}^{-1}$  as multi-annual averaged  $\text{CH}_4$  flux estimates for the Santarém area and  $20 \text{ mg m}^{-2} \text{ d}^{-1}$  for the Manaus area.

The obtained annual  $\text{CH}_4$  budget of 2008 and 2009 for the Amazon lowland region for the different model simulations ranges from 33 Tg to 42 Tg for TM5-PB, TM5-PB-SCI, TM5-SH and TM5-SH-SCI and 17–18 Tg for TM5-CT. Compared to Melack et al. [2004] who suggested a number of 29.3 Tg for the annual  $\text{CH}_4$  wetland emissions in the Amazon lowland region, the TM5-based global inversions (except for TM5-CT) have the tendency to estimate up to 7 Tg higher  $\text{CH}_4$  wetland fluxes under the assumption that 80-90% of the total fluxes are originating from wetlands (calculated from the optimized a-posteriori fluxes of TM5-PB-SCI, TM5-PB, and TM5-CT) throughout the complete year. No linear relationship between the calculated annual budget numbers of all five TM5-based inversions, both for 2008 and 2009, and the model data mismatch of the two BARCA campaigns could be found. This emphasizes that it is very difficult to obtain a reliable estimate of an annual  $\text{CH}_4$  budget number of the Amazon basin based on the model-observation mismatch with only two months data coverage per year. A plausible reason is the different seasonal variation of the a-posteriori fluxes of the five global TM5-based  $\text{CH}_4$  inversions.



## 5.4 Conclusions

The dataset presented here, with over 150 vertical profiles from 27 flights across the Amazon basin during two time periods at the end of the dry season in November 2008 and the end of the wet season in May 2009, gives an impressive overview over the CH<sub>4</sub> distribution in the lower troposphere in the Amazon basin. The observations can be used to validate and evaluate models.

Using SF<sub>6</sub> as hemispheric tracer allowed to trace the incoming air into the Amazon basin back to be dominantly of southern hemispheric origin during BARCA-A and a mixture of both hemispheres during BARCA-B. With the help of isotope analysis it was confirmed that the dominant part of the CH<sub>4</sub> emissions can be attributed to biogenic origin. Methane emissions of major cities were found to have a major contribution from biogenic origin, e.g. sewage gas. During BARCA-A, a minor part of the CH<sub>4</sub> emissions could be identified to originate from biomass burning using CO as an additional tracer.

By comparing the observations to five TM5-based global CH<sub>4</sub> inversions, it was found that the inversions using SCIAMACHY satellite retrievals match the observations best during both campaigns. Except for the western part of the Amazon basin, TM5-PB-SCI was found to be very consistent with the observations during BARCA-B. Comparing the monthly CH<sub>4</sub> budgets of the land influence regions of the Amazon basin to the observed model-observation mismatch, the source strength of the Amazon lowland basin was estimated to  $36 \pm 12 \text{ mg m}^{-2} \text{ d}^{-1}$  during BARCA-A and  $43 \pm 18 \text{ mg m}^{-2} \text{ d}^{-1}$  during BARCA-B. In this case the model-observation mismatch could be attributed to the monthly CH<sub>4</sub> budget of the corresponding simulation, but not to the annual budget. For obtaining a robust and reliable annual CH<sub>4</sub> budget for the Amazon basin, conducting such aircraft campaigns, at regular time intervals during the entire year is essential.



## Chapter 6

# WRF-GHG simulations in the Amazon basin

The set up of WRF-GHG (cf. Ch. 4) is utilized to simulate CH<sub>4</sub> atmospheric mixing ratios over the Amazon basin during the two one-month time periods of the two BARCA campaigns (November 2008 and May 2009). The performance of WRF-GHG is evaluated against the BARCA CH<sub>4</sub> observations. Four simulations with combinations of two different wetland models [Kaplan, 2002, Walter et al., 2001a] and three wetland inundation maps of different horizontal resolution [Bergamaschi et al., 2007, Hess et al., 2003, Prigent et al., 2007] are carried out. The WRF-Chem meteorology at 10 km horizontal grid resolution is evaluated against observations of meteorological variables during the airborne campaigns, precipitation observations, and radiosondes (November 2008 only). The impact on the simulated CH<sub>4</sub> distribution over the Amazon basin is discussed. Monthly budgets for the Amazon lowland region are derived from the WRF-GHG simulations.

Main parts of this chapter were published in:

Beck, V., C. Gerbig, T. Koch, M. M. Bela, K. M. Longo, S. R. Freitas, C. Prigent, J. O. Kaplan, P. Bergamaschi, M. Heimann, (2012): *WRF-Chem simulations in the Amazon region during wet and dry season transitions: evaluation of methane models and wetland inundation maps*, *Atmos. Chem. Phys. Discuss.*, 12, 22835-22890.

WRF-GHG simulations of CO, which were conducted in similar manner as for CH<sub>4</sub> are published in:

Andreae, M. O., P. Artaxo, V. Beck, M. Bela, S. Freitas, C. Gerbig, K. Longo, J. W. Munger, K. T. Wiedemann, and S. C. Wofsy, (2012): *Carbon monoxide and related trace gases and aerosols over the Amazon Basin during the wet and dry seasons*, *Atmos. Chem. Phys. Discuss.*, 12, 8107–8168.

## 6.1 Modeling framework description

Simulations of CH<sub>4</sub> atmospheric mixing ratios over the Amazon basin are accomplished with the WRF Greenhouse Gas Module (WRF-GHG, cf. Ch. 4). Compared to simulations in northern hemispheric mid-latitudes (e.g. Ahmadov et al. [2009], Pillai et al. [2010, 2011]), the WRF-Chem model had to be adapted to the tropics by replacing the standard WRF land-surface data with updated maps for the Amazon basin. The wetland inundation maps utilized for the WRF-GHG CH<sub>4</sub> simulations are described.

### 6.1.1 WRF model and meteorology set up for the Amazon basin

For the WRF-GHG simulations over the Amazon, a coarse domain (“d01”) covering most of South America with a horizontal grid distance of 30 km and a total area of 6600 km × 6000 km was set up. It contains a two-way nested inner domain (“d02”), which includes the BARCA flight area and most of the Amazon basin with a horizontal grid distance of 10 km and a total area of 2280 km × 2760 km (cf. Fig. 6.1). The simulations use 41 vertical levels. 35 of them are identical to those used in the Brazilian developments on the Regional Atmospheric Modeling System (BRAMS) [Freitas et al., 2009]. Additional six levels were added in the PBL for increased resolution. In order to account for the effects of recent changes in landuse, e.g. from deforestation, updated maps of land-surface data at higher resolution replace those of the standard WRF-Chem version. This affects in particular albedo and greenness fraction. Observation from MODIS with 30 s resolution from the years 1992–1993 are used. The updated vegetation map includes 1 km LANDSAT data from the years 1999–2000 [M. Bela, pers. communication, 2010]. As initial and lateral boundary conditions for all meteorological fields and sea surface temperature (SST) ECMWF 6 h analysis data with a horizontal resolution of about 35 km are utilized. The ECMWF soil moisture was replaced by the GPNR soil moisture product [Gevaerd and Freitas, 2006], a hybrid product combining estimates from the Global Precipitation Climatology Project (GPCP) and the Tropical Rainfall Measuring Mission (TRMM). The runtime period ranges from 3<sup>rd</sup>–30<sup>th</sup> November 2008 (BARCA-A) and 3<sup>rd</sup>–30<sup>th</sup> May 2009 (BARCA-B). Simulations are conducted for 30 h periods starting with 6 h meteorological spin-up at 18 UTC the previous day. Because of the short simulation periods (~4 weeks) effects on the CH<sub>4</sub> atmospheric mixing ratio from OH destruction in the atmosphere are neglected. An overview over the different configurations and physics options used for the WRF-GHG simulations are found in Table 6.1. Simulations with different PBL schemes, microphysics schemes, and convective schemes were carried out and are compared against radiosondes and TRMM observations in Sec. 6.2.1.

### 6.1.2 Methane tracers and fluxes for WRF-GHG in the Amazon basin

In order to distinguish between different CH<sub>4</sub> source processes, in total eight different CH<sub>4</sub> tracers are implemented in the WRF-GHG model for simulations over the Amazon basin. Beside the total CH<sub>4</sub> atmospheric mixing ratio, CH<sub>4</sub> contributions from wetlands, anthropogenic sources (except for biomass burning), biomass burning, termites, uptake of CH<sub>4</sub> from the atmosphere by soil, and CH<sub>4</sub> emissions from plants are defined as separate tracers. The last tracer contains the atmospheric background mixing ratio, which serves as initial atmospheric mixing ratio for all eight tracers. It is obtained from the global atmospheric CH<sub>4</sub> inversion using the TM5 model [Bergamaschi et al., 2009, 2010] (cf. Sec. 4.3).

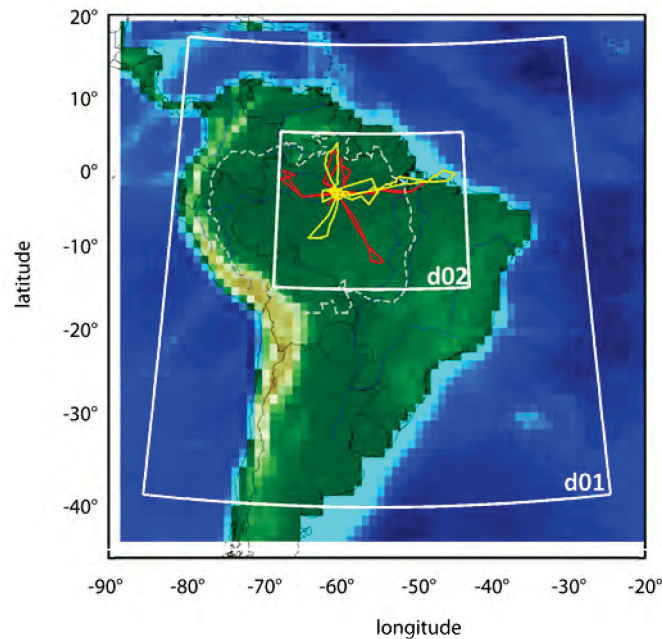


Figure 6.1: Topographic map illustrating the position of the coarse domain ( $d01$ –30 km horizontal resolution) and the nested domain ( $d02$ –10 km horizontal resolution).  $d02$  covers the flight area of all flights conducted during BARCA-A and BARCA-B. The total flight track of BARCA-A is depicted in red and the total flight track of BARCA-B in yellow. The Amazon lowland region is framed by a white dashed line.

For the calculation of  $\text{CH}_4$  emissions from wetlands, two different process-based bottom-up models are utilized for the WRF-GHG simulations over the Amazon basin: the Kaplan wetland inventory [Kaplan, 2002, Kaplan et al., 2006, Drevet, 2008] - online integrated into the WRF-GHG code (called “KWI”) and the Walter wetland model (“WWK”) [Walter et al., 1996, Walter and Heimann, 2000, Walter et al., 2001a,b] in offline modus driven by WRF-Chem meteorology. Biomass burning emissions are calculated with the 3BEM model [Longo et al., 2010]. As anthropogenic emission inventory for  $\text{CH}_4$  emissions, the EDGARV4.1 database is utilized with an update for South American cities as proposed by Alonso et al. [2010]. Methane emissions from termites follow Sanderson [1996] and uptake of atmospheric  $\text{CH}_4$  by soils is based on Ridgwell et al. [1999]. For hypothesis testing, a potential flux for  $\text{CH}_4$  emissions from vegetation based on Keppler et al. [2006] is implemented. A detailed description of all flux models is found in Sec. 4.1.

### 6.1.3 Wetland inundation maps

A wetland inundation map indicating the fraction of inundation per grid cell (i.e. the percentage of the grid cell that is covered by wetland area) is multiplied by the  $\text{CH}_4$  wetland emissions for each grid cell from one of the two wetland flux models to derive the total amount of wetland  $\text{CH}_4$  emissions per grid cell. For this study,  $\text{CH}_4$  wetland emissions were simulated using the Walter wetland model in combination with three different wetland inundation maps. The Kaplan wetland inventory is only used in combination with the Kaplan wetland inundation map. The potential wet-

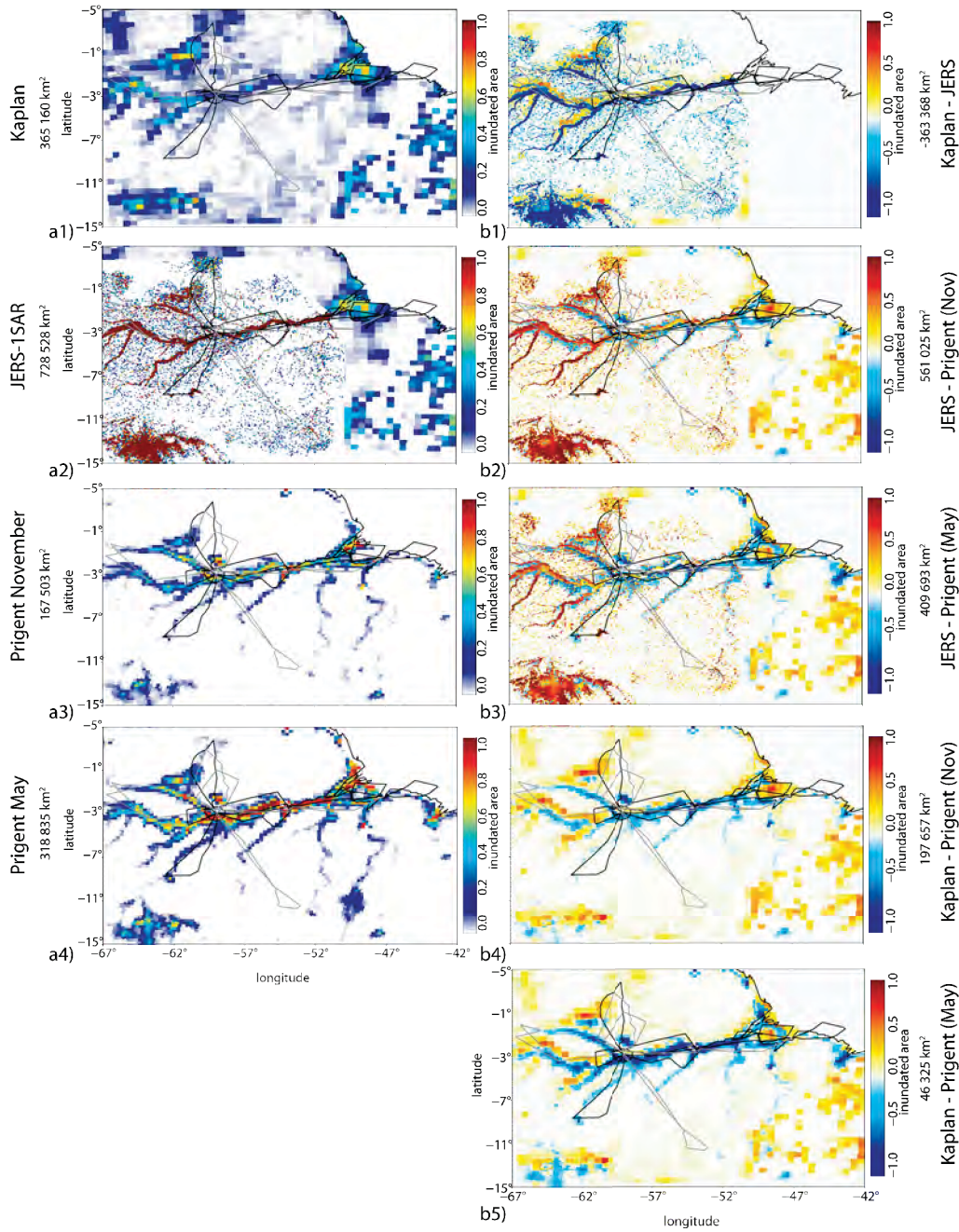


Figure 6.2: Three different wetland inundation maps (a) and the differences between these three wetland inundation maps (b) are illustrated. The wetland inundation maps indicate the fraction of inundated area per grid cell ranging from 0 to 1. They are projected on the WRF d02 nested grid (10 km horizontal grid distance). The BARCA flight tracks are overlaid (BARCA-A—gray, BARCA-B—black). The numbers illustrate the total inundated wetland area or difference in the inundated wetland area for the d02 domain.



Category	Configuration option
Vertical coordinates	Terrain-following hydrostatic pressure vertical coordinate
Basic equations	Nonhydrostatic, compressible
Grid type	Arakawa C-grid
Time integration	3 <sup>rd</sup> order Rung-Kutta split-explicit
Spatial integration	3 <sup>rd</sup> and 5 <sup>th</sup> order differencing for vertical and horizontal advection, respectively; both for momentum and scalars
Advection option	Positive definite
Domain configuration	2 domains with resolution 30 km and 10 km for outer and inner domain, respectively; 41 vertical layers up to 20 km altitude (cors in mb)
Time step	180 s outer domain, 60 s inner domain
Physics schemes	Microphysics: WSM 5-class scheme; radiation: new version of the Rapid Radiative Transfer Model (RRTMG) for long- and shortwave radiation; convection: Grell-Dévényi and Grell 3 for outer and inner domain, respectively; surface layer: Monin-Obukhov; land-surface: NOAH-LSM; PBL: MYJ; cumulus-radiation feedback turned on shallow convection option turned off
Updated surface maps	Vegetation Map: USGS + PROVEG (INPE) Amazonia 1 km Landsat 1999–2000; Greenness Fraction: MODIS NDVI 30 s 1992–1993; Albedo: MODIS NDVI 30 s 1992–1993; Soil moisture: GPNR 0.25° × 0.25° daily

Table 6.1: *Overview over WRF configuration, physics options, and updated land-surface maps used for the WRF-GHG simulations in the Amazon basin.*

land inundation map of Kaplan [Bergamaschi et al., 2007] has a horizontal resolution of  $0.5^\circ \times 0.5^\circ$  and global coverage. The wetland inundation map of Hess et al. [2009] (“JERS-1SAR” wetland inundation map) covers the area of maximum inundation for the Amazon lowland region ( $< 500$  m) with a horizontal resolution of approx. 100 m. It is based on the Japanese Earth Resources Satellite 1 Synthetic Aperture Radar (JERS-1SAR). In both wetland inundation maps the wetland area does not depend on the season and is constant in time. As the JERS-1SAR wetland inundation map does not cover the entire simulation domain, it is completed with the Kaplan wetland inundation map. Furthermore, the wetland inundation map of Prigent et al. [2001a, 2007] with  $0.25^\circ \times 0.25^\circ$  horizontal resolution is used. It relies on a combined product of visible and near-infrared reflectance, the Normalized Difference Vegetation Index (NDVI) from AVHRR, passive microwave Special Sensor Microwave/Imager (SSM/I) measurements between 19 and 85 GHz, and active microwave backscattering coefficients at 5.25 GHz from a scatterometer of the European Remote Sensing (ERS) satellite. The inundated area of the Prigent et al. [2007] wetland inundation map changes in time with monthly resolution. It accounts for less inundated areas during the dry season. For this study a monthly multi-annual average of the years 1997–2003 [Prigent et al., 2012] is utilized. Fig. 6.2 illustrates the three wetland inundation maps and the differences between those together with the BARCA flight tracks.

## 6.2 Results and discussion

The evaluation of three different meteorological set ups of WRF-Chem against radiosondes and precipitation observations is described (Sec. 6.2.1). The simulated  $\text{CH}_4$  fluxes from two wetland models (KWI and WWM) are compared to each other for the two simulation periods and to literature values in Sec. 6.2.2. The WRF-GHG  $\text{CH}_4$  simulations are compared to BARCA  $\text{CH}_4$  observations in Sec. 6.2.3. A comparison of two single flights in the eastern part of the Amazon basin is accomplished. An evaluation of the performance of WRF-GHG under “good” and “bad” weather conditions (i.e., days with little and much convective activity) is presented. The adjustment of the  $\text{CH}_4$  wetland emissions is described in detail. A comparison of vertical profiles of the lower 4 km of the atmosphere in five different regions in the Amazon is illustrated. Budget calculations of the Amazon basin for the two one-month periods in Sec. 6.2.4 conclude the section.

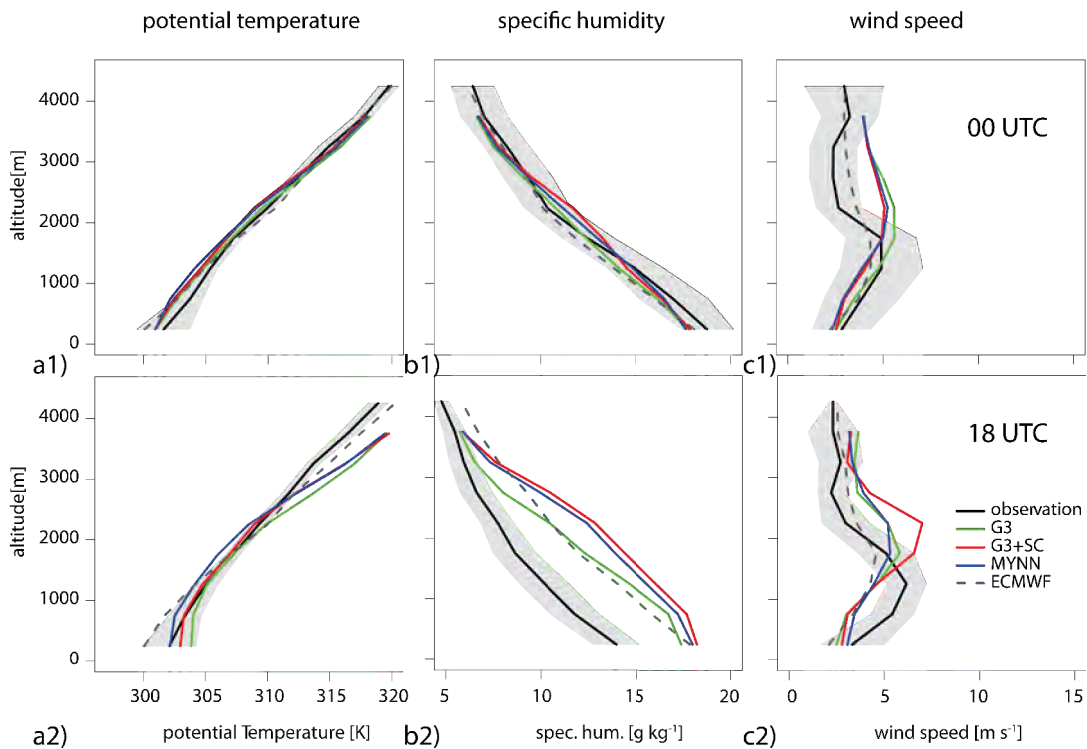


Figure 6.3: Comparison of the meteorological variables potential temperature, specific humidity, and wind speed from different WRF meteorologies (green–G3, red–G3+SC, blue–MYNN) and from ECMWF (gray dashed) with observed radiosonde profiles for Manaus. The average for the period of 18<sup>th</sup>–29<sup>th</sup> November 2008 during BARCA-A at 00 UTC (upper panel) and 18 UTC (lower panel) is shown. The gray shaded area indicates the 1-sigma standard deviation of the radiosonde observations.

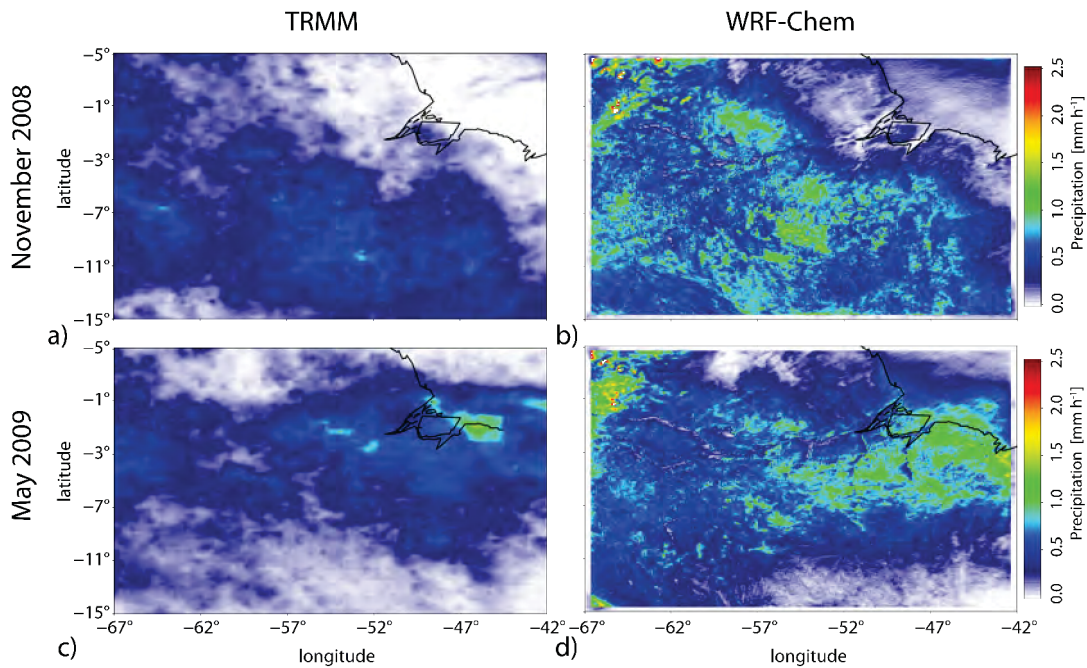


Figure 6.4: Daily averaged precipitation [ $\text{mm h}^{-1}$ ] from the TRMM 3B42 product (a,c) and the WRF simulations using the G3 convection option without shallow convection (b,d) for the WRF-GHG d02 domain. (a,b) illustrate the daily averaged precipitation for the period of 4<sup>th</sup>–29<sup>th</sup> November 2008 (BARCA-A) and (c,d) for the period 4<sup>th</sup>–29<sup>th</sup> May 2009 (BARCA-B).

### 6.2.1 Meteorology

Simulating atmospheric methane distributions requires an adequate representation of the main transport processes. To assess the impact of the choice of PBL and convective parameterizations, three different WRF-Chem meteorological set ups are compared to independent observations from radiosondes in Manaus, Santarém, and Belém (during BARCA-A only). The set up called “G3” is described in Table 6.1. Set up “G3+SC” additionally uses the shallow convection option. For the “MYNN” set up the PBL scheme is changed from the MYJ to MYNN, the shallow convection option was turned on, and the microphysics scheme changed from WSM-5 class to WSM-6 class scheme compared to G3. Fig. 6.3 demonstrates the comparison of the three different meteorological WRF set ups as well as of the ECMWF data (used as meteorological initial and boundary conditions) to observations from radiosondes for Manaus averaged over the time period of 18<sup>th</sup>–29<sup>th</sup> November 2008. The lowest 4 km, the altitudes where the BARCA airborne data were collected, are illustrated.

At 00 UTC corresponding to 20:00 local time (Fig. 6.3, upper panel), the potential temperature and the specific humidity of all three set ups are in good agreement with the observations (bias = -0.17–0.51 K for the potential temperature, bias = -0.04–0.46 g kg<sup>-1</sup> for the specific humidity). Only the wind speed is overestimated by the WRF-Chem model (throughout all different meteorologies) in altitudes between 2000 m and 4000 m (bias = 1.8–2.1 m s<sup>-1</sup>), which is less notable in the ECMWF data (bias = 0.61 m s<sup>-1</sup>). In contrast, at 18 UTC (14:00 local time) all meteorologies overestimate the potential temperature close to the ground. For altitudes of 2500 m and more, it results in total biases of 0.30–1.42 K. Even more obvious is the deviation of the specific humidity

from the ground up to 4000 m altitude (bias = 2.68–4.12 g kg<sup>-1</sup>). The simulations using the shallow convection scheme (G3+SC and MYNN) denote even higher deviations from the radiosondes observations (4.12 and 3.75 g kg<sup>-1</sup> vs. 2.68 g kg<sup>-1</sup>). The positive deviations of the specific humidity at 18 UTC are already notable in the ECMWF fields (bias = 2.96 g kg<sup>-1</sup>) as the forcing meteorology. This points to problems in the representation of the convective transport in both, the WRF-Chem and the ECMWF model. Comparisons at higher altitudes show a problem with the implementation of the shallow convection scheme in WRF-Chem that leads to the unexpected low simulated specific humidity values [S. Freitas, pers. communication, 2011]. A test simulation with the G3 set up using only the coarse d01 domain without nesting did not improve the results of the comparison.

Compared to northern mid-latitudes, where the WRF-Chem model is able to capture the well-mixed afternoon PBL and shows more problems in capturing the stable nocturnal boundary layer [Ahmadov et al., 2007], the situation is different in the tropics. The convective activity is not dominated by synoptic events, but rather by small scale and local effects such as convective cells (cf. Sec. 2.2.1). They are more difficult to represent by the model. As a measure for the performance of the convective transport in WRF-Chem, WRF-Chem convective precipitation is compared to TRMM precipitation observations. The TRMM observations have a horizontal resolution of 0.25° × 0.25° and a temporal resolution of 3 h. The WRF-Chem simulations overestimate daily averaged mean precipitation (Fig. 6.4). During November 2008 WRF-Chem precipitation averages 0.50 mm d<sup>-1</sup> compared to 0.24 mm d<sup>-1</sup> as observed by TRMM. In May 2009 a similar overestimation (0.47 mm d<sup>-1</sup> for WRF-Chem and 0.26 mm d<sup>-1</sup> for TRMM) is seen. The amplitude of the diurnal cycle for precipitation for different regions of the nested domain is overestimated and the phasing is not always correct (cf. Figs. A.10 and A.11).

As the representation of the convective transport is crucial for an adequate representation of the atmospheric transport in the tropics, the G3 meteorological set up was selected as “standard” meteorological set up for the WRF-GHG CH<sub>4</sub> simulations. This selection was based on two criteria: (1) the comparison of the specific humidity to radiosondes observations, and (2) the mean average precipitation rate. The G3 set up compares best to the radiosondes observations of the specific humidity and it has a similar mean daily average precipitation rate as the MYNN meteorological set up (both 0.50 mm d<sup>-1</sup> compared to 0.57 mm d<sup>-1</sup> for G3+SC for November 2008 and 0.44 mm d<sup>-1</sup> (G3) 0.44 mm d<sup>-1</sup> (MYNN), and 0.51 mm d<sup>-1</sup> (G3+SC) for May 2009). A simulation without daily re-initialization of the meteorological fields did not improve the results.

### 6.2.2 Wetland fluxes

The KWI and the WWM, are both driven by the same WRF-Chem meteorological set up (G3). KWI depends on the soil moisture and soil temperature obtained from WRF-Chem, while WWM uses soil temperature, ground heat fluxes, solar radiation, and precipitation from WRF-Chem. The offline simulations of WWM provide CH<sub>4</sub> emissions as daily mean values. The KWI methane fluxes are calculated online in WRF-GHG and output is available on an hourly basis. The amplitude of the KWI CH<sub>4</sub> flux diurnal cycle can reach values up to 90 mg m<sup>-2</sup> d<sup>-1</sup> in extreme cases. An average value of 4 mg m<sup>-2</sup> d<sup>-1</sup> was found. This corresponds to ~25% of the total daily flux on average for both months, November 2008 and May 2009. Large impacts from neglecting the diurnal cycle of the CH<sub>4</sub> wetland emissions calculated by WWM, especially for comparisons of WRF-GHG to airborne observations, are not expected. Fig. 6.5 illustrates the monthly mean CH<sub>4</sub>



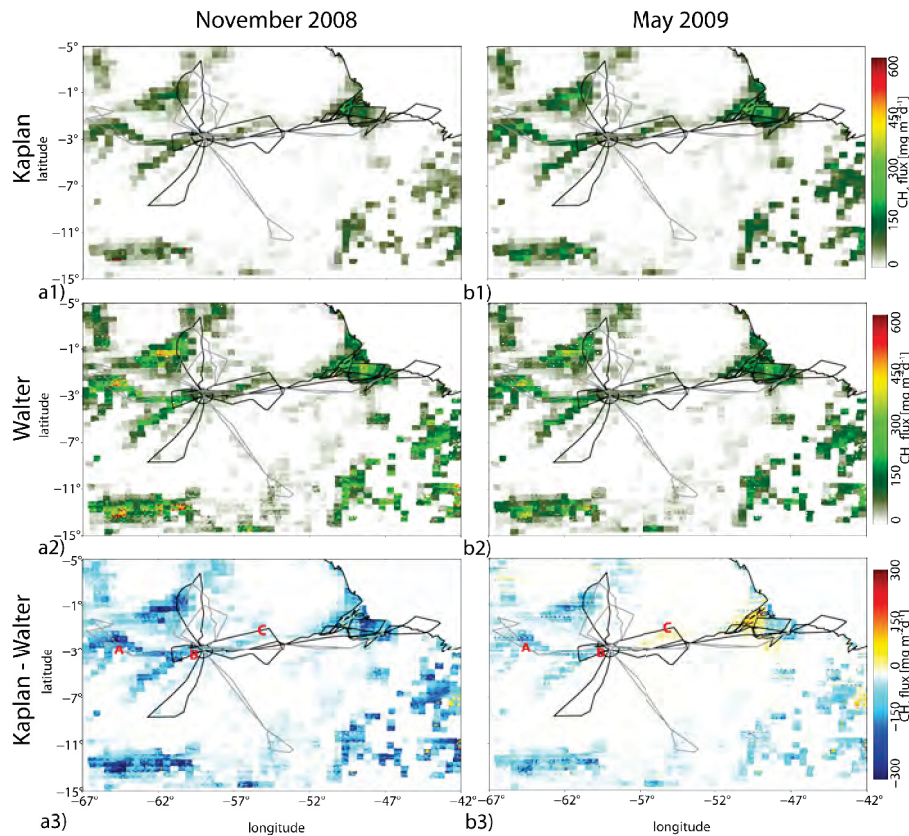


Figure 6.5: Monthly mean  $\text{CH}_4$  fluxes of the Kaplan wetland inventory (KWI) and the Walter wetland model (WWM) for the “d02” domain, both using the Kaplan wetland inundation map for November 2008 (a1–a2) and May 2009 (b1–b2). The flux fields were adjusted according to the description in Sec. 6.2.3. The figures on the lower panel illustrate the difference in the  $\text{CH}_4$  flux between the KWI and WWM for November 2008 (a3) and May 2009 (b3). The locations of the grid cells with different wetlands types as further explained in Table 6.2 and Sec. 6.2.2 are illustrated in (a3) and (b3) with red letters (A–Manirana; B–Cabalina; C–Curuái). The flight track of the two BARCA campaigns are illustrated in gray (BARCA-A) and black (BARCA-B).

flux of KWI and WWM both using the Kaplan wetland inundation map for November 2008 (a) and May 2009 (b). The KWI emissions have been reduced by 76% for November 2008 and May 2009 compared to the original KWI. The adjustment of the wetland  $\text{CH}_4$  fluxes accounts for different meteorological drivers and wetland inundation maps compared to the original models. For WWM the emissions are increased by 9% for both simulation periods. The adjustment of the wetland emissions from all models was chosen in a way that averaged observed mean  $\text{CH}_4$  atmospheric mixing ratios for flights with a good representation of the atmospheric transport in the model during BARCA-B matches the corresponding atmospheric mixing ratio of the WRF-GHG  $\text{CH}_4$  simulation when extracted at the observation sampling location along the flight track (see Sec. 6.2.3 for details).

The differences in the  $\text{CH}_4$  flux of both models are illustrated in Fig. 6.5a3–b3 for November 2008 and May 2009, respectively. For November 2008,  $\text{CH}_4$  emissions of WWM show higher values especially in the western part of the Amazon basin and the upper Rio Negro. Along the

Amazon river between Manaus and Belém WWM shows only slightly higher  $\text{CH}_4$  emissions compared to KWI. In May 2009, KWI has higher emissions compared to WWM along the Amazon river between Manaus and Belém and along the Amazon delta. WWM denotes higher emissions in the western part of the Amazon similar to November 2008.

As WWM is sensitive to different wetland types through the plant-mediated transport mechanism that depends on the vegetation type [Walter et al., 2001a] (cf. Sec. 4.1), locations with three different wetland types as described in Fig. 8 in Hess et al. [2003] were selected. The  $\text{CH}_4$  wetland flux from both models was compared at these location. The locations are Manirana near Tefé–flooded forest (A), Cabalina close to Manacapuru–mixture between flooded forest and open water (B), and Curuaí close to Obidos–mainly open water (C) indicated in Fig. 6.5a3–b3 by red letters. Table 6.2 illustrates the detailed comparison of both models at the prescribed locations and a comparison to literature values for different wetland types. The general agreement with the available observations of  $\text{CH}_4$  fluxes suggests that both models are able to simulate the  $\text{CH}_4$  wetland flux for the Amazon basin in the right order of magnitude.

The nested domain averaged  $\text{CH}_4$  flux for all wetland grid points for KWI is  $22 \text{ mg m}^{-2} \text{ d}^{-1}$  for May 2009 and  $13 \text{ mg m}^{-2} \text{ d}^{-1}$  for November 2008 compared to  $30 \text{ mg m}^{-2} \text{ d}^{-1}$  and  $37 \text{ mg m}^{-2} \text{ d}^{-1}$ , respectively for WWM. This indicates that both models simulate roughly a similar magnitude of  $\text{CH}_4$  emissions. In addition, WWM allows for a separation of the contributions of the different pathways of  $\text{CH}_4$  to the atmosphere, such as diffusion, ebullition, and plant-mediated transport. The mean contribution of the three different pathways for the whole d02 domain for WWM in November 2008 results in 30% plant-mediated transport, 47% ebullition, and 23% diffusion. For May 2009, the ratio is slightly different (34% plant-mediated transport, 44% ebullition, and 22% diffusion). Compared to Bartlett et al. [1988] who estimated the ebullitive flux to account for 48% in open water and 54% in flooded forest areas, the ebullitive contribution of WWM to the  $\text{CH}_4$  transport to the atmosphere is in the same order of magnitude. However, Crill et al. [1988] estimated 70% contribution of ebullition. Up to this study WWM has only been validated against observations from a swamp region in Panama in the tropics [Walter and Heimann, 2000]. Due to the agreement with the observations as indicated above, the WWM is considered suitable for the Amazon basin.

### 6.2.3 Comparison to BARCA observations

In total four WRF-GHG simulations using the G3 meteorological set-up (Table 6.1 and Sec. 6.2.1) with different combinations of wetland models and wetland inundation maps (named WKK, WWK, WWJ, and WWP in the following - the second letters indicates the wetland model “K” for KWI and “W” for “WWM”, while the third letter stands for the choice of wetland inundation map “K” for Kaplan, “J” for JERS-1SAR, and “P” for Prigent) have been carried out (see Table 6.3). In this section, a comparison of two selected flights under different weather conditions is presented first. It illustrates the impact of the quality of the representation of the atmospheric transport on the simulated tracer distribution. An evaluation of the simulations of the  $\text{CH}_4$  mixing ratio distribution is presented for weather conditions that are better represented in WRF vs. those that are not well represented. The  $\text{CH}_4$  wetland contribution is adjusted taking only flights with a good representation of the atmospheric transport during BARCA-A. The comparison of the adjusted WRF-GHG simulations to vertical profiles of the BARCA  $\text{CH}_4$  observations in five different regions of the Amazon is shown.



	Kaplan (KWI)	Walter (WWM)	Literature references
<b>Flooded forest (A)</b> <i>Manirana (Tefé)</i> 2.93°S, 64.93°W November 2008 May 2009	57 mg m <sup>-2</sup> d <sup>-1</sup> 96 mg m <sup>-2</sup> d <sup>-1</sup>	165 mg m <sup>-2</sup> d <sup>-1</sup> 161 mg m <sup>-2</sup> d <sup>-1</sup>	126 mg m <sup>-2</sup> d <sup>-1</sup> [Bartlett et al., 1988] 150 mg m <sup>-2</sup> d <sup>-1</sup> [Devol et al., 1990]
<b>Mixed flooded forest/ open water (B)</b> <i>Cabalina (Manacapuru)</i> 3.43°S, 60.78°W November 2008 May 2009	37 mg m <sup>-2</sup> d <sup>-1</sup> 58 mg m <sup>-2</sup> d <sup>-1</sup>	115 mg m <sup>-2</sup> d <sup>-1</sup> 146 mg m <sup>-2</sup> d <sup>-1</sup>	
<b>Open water (C)</b> <i>Curuaí (Obidos)</i> 1.95°S, 55.78°W November 2008 May 2009	43 mg m <sup>-2</sup> d <sup>-1</sup> 67 mg m <sup>-2</sup> d <sup>-1</sup>	37 mg m <sup>-2</sup> d <sup>-1</sup> 37 mg m <sup>-2</sup> d <sup>-1</sup>	74 mg m <sup>-2</sup> d <sup>-1</sup> [Bartlett et al., 1988] 44 mg m <sup>-2</sup> d <sup>-1</sup> [Devol et al., 1990]

Table 6.2: Comparison of the CH<sub>4</sub> flux from the Kaplan wetland model (KWI) and the Walter wetland model (WWM) for grid cells specific for different wetland types (flooded forest, mixed flooded forest/open water, open water; cf. Hess et al. [2003] Fig. 8). The locations of the three different grid cells are illustrated as (A), (B), and (C) in Fig. 6.5a3–b3. In addition, literature values for the specific wetland types are denoted.

WRF simulation	Wetland model	Wetland inundation map	Horizontal resolution wetland map	Wetland grid points in d02 domain	Wetland adjustment factor
WKK	Kaplan (KWI)	Kaplan	0.5° × 0.5°	30670	-76%
WWK	Walter (WWM)	Kaplan	0.5° × 0.5°	30670	+9%
WWJ	Walter (WWM)	JERS-1SAR	ca. 100 m	28081	-27%
WWP	Walter (WWM)	Prigent	0.25° × 0.25°	15006/15826	-55%

Table 6.3: Overview of the four WRF-GHG CH<sub>4</sub> simulations using different configurations for wetland models and wetland inundation maps. All simulations use the G3 convective scheme without the shallow convection options, the plumerise mechanism for biomass burning emissions, and initial and lateral boundary conditions for CH<sub>4</sub> from TM5. The number of wetland grid points shows the values for November and May for the Prigent map. Adjustment factors are chosen to match the mean atmospheric CH<sub>4</sub> observations of flights with a good representation of the atmospheric transport in the model in May 2009 (BARCA-B).

To compare the WRF-GHG simulations to the BARCA airborne observations, the WRF-GHG simulations have been extracted at the grid cell closest to the location of each observation point. For BARCA-A, the location of the flask observations is used as extracting point while for BARCA-B the locations of the 3 s continuous observations are utilized except for the flights 8–10 where no continuous observations are available due to instrument failure. For these flights, the locations of the flask observations are taken to extract the model values. Bias is calculated as the mean of the residuals originating from the model - observation difference of each observation point.

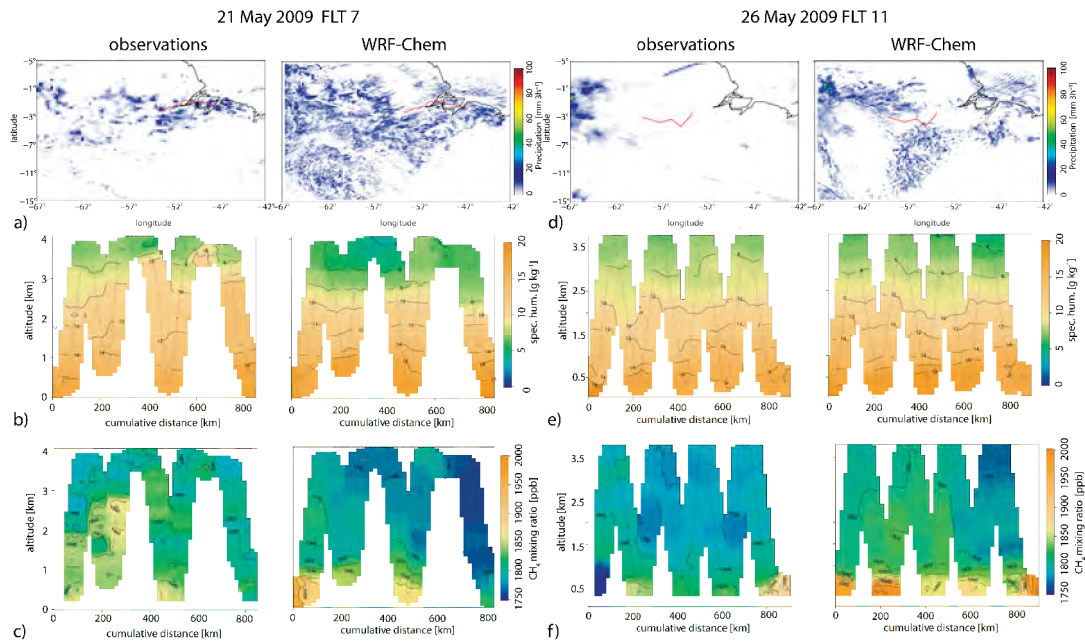


Figure 6.6: Comparison between observations and WRF-GHG model output for two case studies during BARCA-B (FLT 7 from Santarém to Belém on 21-05-2009 18:00–21:00 UTC–left panel and FLT 11 from Manaus to Santarém on 26-05-2009 13:00–16:00 UTC–right panel). On the left side of each panel the observations (TRMM for precipitation (a,d), specific humidity and CH<sub>4</sub> from airborne observations (b,c,e,f)) are illustrated. On the right panel the WRF-GHG simulation output of WWP using the Walter wetland model and the Prigent wetland inundation map is presented.

### Comparison for two selected flights during BARCA-B

To illustrate the importance of the representation of the atmospheric transport in the model, two flights in the eastern part of the Amazon basin during BARCA-B with different quality of representation in the model are selected as examples for a case study: one flight where WRF-GHG shows problems in the representation of the atmospheric transport (FLT 7, 21-05-2009, 18:00–21:00 UTC, left panel Fig. 6.6a–c) and one flight where the atmospheric transport is reproduced better by WRF-Chem (FLT 11, 26-05-2009, 13:00–16:00 UTC, right panel Fig. 6.6d–f) during the 3 h time period of the flight. For both flights, WRF-GHG simulations of WWP are utilized.

For FLT 7, the TRMM observations indicate convective events (precipitation is used as a proxy for convective events during the 3 h flight period here) along the flight path (a) while WRF-Chem produces more convective events (or precipitation) compared to the TRMM observations for this time period, but almost no convective event along the flight track. This is illustrated in the comparison of the specific humidity (b). WRF-Chem simulations show a much more stratified distribution of the specific humidity than what was observed with the aircraft ( $r^2 = 0.895$ , bias = 0.632 K). The modeled CH<sub>4</sub> atmospheric mixing ratio of WRF-GHG does therefore not represent well the observed CH<sub>4</sub> mixing ratio for this flight ( $r^2 = 0.30$ , bias = -22 ppb). To evaluate the ability WRF-GHG to simulate convective transport during time periods with much convective activity, simulations with in total four different convective schemes have been carried out for the time pe-

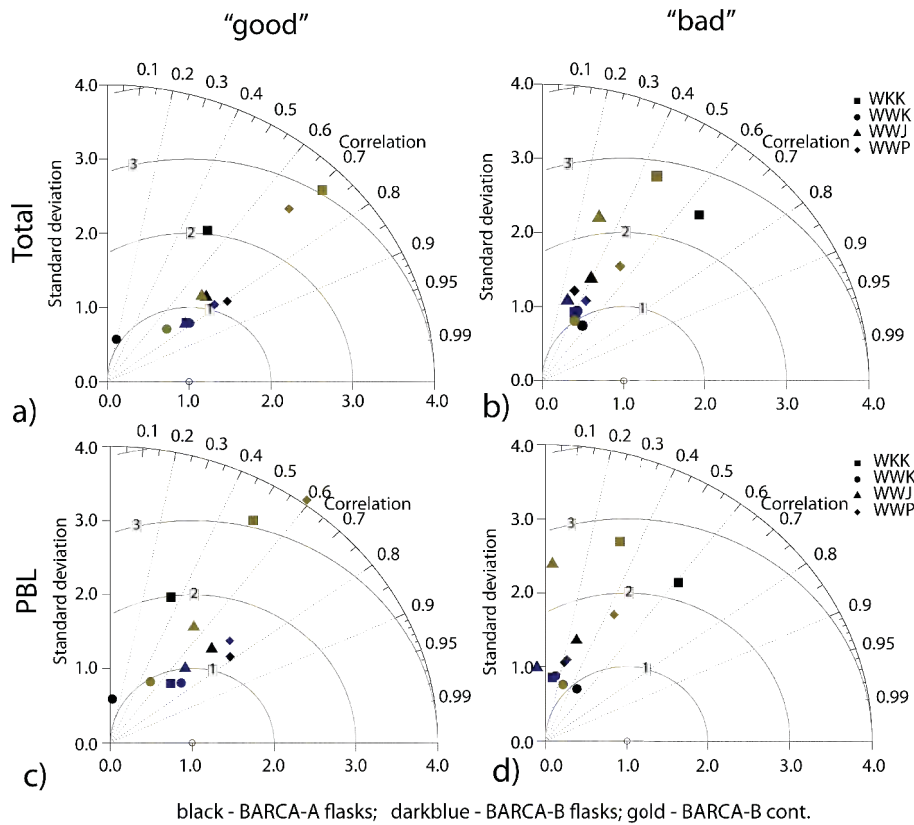


Figure 6.7: Taylor diagram illustrating the normalized standard deviation and the Pearson's correlation coefficient for the comparison of the total  $\text{CH}_4$  atmospheric mixing ratio of the different WRF simulations (BARCA-A flasks—black; BARCA-B flasks—darkblue; BARCA-B cont. observations—gold). They are divided into flights with good weather conditions (a,c) and bad weather conditions (b,d). Additionally, they are separated in observations at all altitudes (a,b) and observations in the PBL (altitudes  $< 1250$  m) only (c,d).

riod of 19<sup>th</sup>–21<sup>th</sup> May 2009. None of the simulations was able to capture the convective transport properly as comparisons against TRMM precipitation patterns demonstrate.

The situation is different for FLT 11 (right panel, Fig. 6.6d–f). Again the WRF-Chem model simulates more convective events compared to the TRMM observations. This time almost no precipitation is found along the flight track in the 3 h time period during the flight neither in the TRMM observations nor in the WRF-Chem simulations (d). The observed and the modeled specific humidity demonstrates in both, the observations and the modeled specific humidity, more stratified layers (e) and a higher r-squared value ( $r^2 = 0.944$ , bias = 0.194 K). The modeled  $\text{CH}_4$  atmospheric mixing ratio is much closer to the observed  $\text{CH}_4$  atmospheric mixing ratio for this flight ( $r^2 = 0.62$ , bias = 28 ppb). This clearly indicates the higher ability of the model for the representation of the observations under more stable conditions with less convective events.

It supports the assumptions that the representation of convective events in the model along the flight track during the time of the flight has an important impact on the representation of the  $\text{CH}_4$  atmospheric mixing ratio in the model.

Another difference between those two flights is the time of the day during which the flight took place. FLT 7 was conducted in the afternoon hours (18:00–21:00 UTC, 14:00–17:00 local time). FLT 11 took place in the morning hours (13:00–16:00 UTC, 9:00–12:00 local time). Modeled and observed CH<sub>4</sub> atmospheric mixing ratio and specific humidity of six flights on three different flight days during BARCA-B with one morning and one afternoon flight (excluding one flight because of strong convective events along the flight track) are compared. On each flight at least six vertical profiles were flown. This comparison illustrates that WRF-GHG shows a better representation of morning flights compared to afternoon flights. The explained variance for the specific humidity as well as for the CH<sub>4</sub> atmospheric mixing ratio is on averaged higher for the three morning flights ( $r_{spec.hum}^2 = 0.94$  and  $r_{CH_4}^2 = 0.52$ ) compared to the afternoon flights ( $r_{spec.hum}^2 = 0.90$  and  $r_{CH_4}^2 = 0.33$ ) for WWP simulations. The other WRF-GHG simulations draw a similar picture.

### WRF-GHG methane simulations under different weather conditions

To assess the impact of the atmospheric transport on the representation of the CH<sub>4</sub> atmospheric tracer mixing ratios in the model for all flights, the WRF-GHG simulations are separated in flights with good representation of the convective transport by the WRF-Chem model and those with a poorer representation. They are evaluated separately against the observations. To distinguish between “good” and “bad” flights, accumulated WRF-Chem precipitation was compared against TRMM precipitation. The precipitation pattern of TRMM was compared to that of WRF-Chem for 48 h upstream of the flight track (obtained from footprint calculations using the STILT model). A flight was rated as “good” flight when the accumulated precipitation pattern for the 48 h time-period in the upstream region of the flight track showed a similar pattern as the corresponding TRMM observations and if additionally no convective event in the TRMM observations in the vicinity of the flight track was found during the 3 h time period of the flight. The corresponding TRMM and WRF-Chem precipitation patterns are found in Fig. A.14–A.17. For BARCA-A, the flights 3,4,5,9 and for BARCA-B the flights 2,9,10,11,12,15 were rated as “good” flights. Table 6.4 demonstrates an overview of flight destination, flight origin, and rating of each single flight during BARCA-A and BARCA-B.

Fig. 6.7 presents a normalized Taylor diagram [Taylor, 2001] that separates between “good” (Fig. 6.7a,c) and “bad” (Fig. 6.7b,d) flights of both campaigns (BARCA-A flasks–black symbols, BARCA-B flasks–darkblue symbols, and BARCA-B continuous observations–gold symbols). For each case the comparison is separately evaluated at all flight altitudes (a,b) and in the PBL (c,d).

Considering the correlations of the model output with the observations at all altitudes of all three datasets (BARCA-A flasks, BARCA-B flasks, BARCA-B continuous observations) for the “good” and the “bad” flights (Fig. 6.7a–b), especially for BARCA-B, a significant higher correlation  $r$  is notable for the “good” flights ( $r = 0.77–0.79$  for flasks and  $r = 0.69–0.72$  for continuous observations) compared to the “bad” flights ( $r = 0.28–0.44$  for flasks and  $r = 0.30–0.53$  for continuous observations). At first glance the difference in the ability of the WRF-GHG model in capturing the variances of the observed CH<sub>4</sub> atmospheric mixing ratios seems not to be dependent on the quality of the representation of the atmospheric transport for BARCA-A. For WWJ and WWP the variability explained by the model for the “good” rated flights is significantly higher compared to the “bad” rated flights ( $r = 0.73$  and  $0.80$  compared to  $r = 0.40$  and  $0.31$ , respectively). This is not the case for the two WRF-GHG simulations using the Kaplan wetland inundation map. Exploring the location of the four “good” rated flights during BARCA-A, it is that seen that three of them

	Flt.num	Date	Direction	No. Profiles	No. Flasks	Rating
BARCA-A	2	2008-11-16	around Manaus	4	-	-
	3	2008-11-18	Manaus-Santarém	4	13	“good”
	4	2008-11-18	Santarém-Belém	4	17	“good”
	5	2008-11-19	Belém-Santarém	6	17	“good”
	6	2008-11-19	Santarém-Manaus	4	12	“bad”
	7	2008-11-22	around Manaus (north)	8	26	“bad”
	8	2008-11-23	Manaus-Boa Vista	8	14	“bad”
	9	2008-11-23	Boa Vista-Manaus	4	14	“good”
	10	2008-11-25	Manaus-Alta Floresta	6	15	“bad”
	11	2008-11-26	around Alta Floresta	8	14	“bad”
	12	2008-11-27	Alta Floresta-Manaus	2	3	“bad”
	13	2008-11-29	Manaus-Tefé	4	12	“bad”
	14	2008-11-30	around Tefé (northwest)	8	17	“bad”
	BARCA-B	2	2009-05-17	around Manaus (west)	6	14
3		2009-05-17	around Manaus (west)	10	16	“bad”
4		2009-05-19	Manaus-Boa Vista	10	18	“bad”
5		2009-05-19	Boa Vista-Manaus	6	12	“bad”
6		2009-05-21	Manaus-Santarém	8	14	“bad”
7		2009-05-21	Santarém-Belém	6	16	“bad”
8		2009-05-22	Belém offshore	4	15	“good”
9		2009-05-23	Belém-Santarém	5	13	“bad”
10		2009-05-23	Santarém-Manaus	2	9	“good”
11		2009-05-26	Manaus-Santarém	8	14	“good”
12		2009-05-26	Santarém-Manaus	8	15	“good”
13		2009-05-27	Manaus-Porto Velho	8	13	“bad”
14		2009-05-27	Porto Velho-Manaus	2	10	“bad”
15		2009-05-28	around Manaus (city)	2	13	“good”

Table 6.4: All flights conducted during BARCA-A and BARCA-B indicated with their flight number (Flt.num), the date of each flight (Date), the flight origin and destination (direction), the number of vertical profiles flown (No. Profiles), the number of flasks sampled (No. Flasks) and rating as “good” or “bad” flights (Rating) (cf. Table 5.1).

(Flights 3,4,5) took place in the eastern part of the Amazon basin (cf. Table 6.4). This leads to the assumption that the Kaplan wetland inundation might not represent the inundated area in the eastern part of the Amazon basin properly (see also Sec. 6.2.3). The correlation taking model output at all altitudes into account is higher than considering the PBL only for all three observation types. This indicates that the model more easily captures the gradient in the CH<sub>4</sub> atmospheric mixing ratio between the PBL and the FT than the spatial and temporal patterns within the PBL.

This leads to the conclusion that during both, BARCA-A and BARCA-B, the representation of the variances depends on the weather conditions. Both the weather conditions during a 48 h time period upstream of the flight track and during the 3 h time period of the flight itself have an impact on the simulation tracer distribution. The WRF-GHG model has a greater ability to capture variances in the CH<sub>4</sub> atmospheric mixing ratio, if the convective transport is represented properly.



### Adjustment of wetland fluxes

As the calculated  $\text{CH}_4$  emissions from the bottom-up models (here: KWI and WWM) depend on the driving meteorology and the choice of wetland inundation map, the  $\text{CH}_4$  emissions from wetlands have been adjusted for all four WRF-GHG simulations for the Amazon basin. As reference period for the adjustment, the simulation period of May 2009 was selected. Due to almost no biomass burning activity during that time period and given that emissions from anthropogenic and other smaller sources are rather constant throughout the year, the only varying source component are  $\text{CH}_4$  emissions from wetlands. To reduce the impact of a not proper representation of the atmospheric transport on the simulated tracer distribution, only those flights with a “good” rating during BARCA-B (cf. Table 6.4) were included in the adjustment. FLT 8 was not included as the flight track is mainly located over the Atlantic Ocean. The tagged tracer analysis of the four WRF-GHG simulations for all other “good” rated flights results in a mean wetland contribution of 91%. To calculate the adjustment factor for the  $\text{CH}_4$  emissions from wetlands, the model simulations of the corresponding flights were sampled at the time and location of the BARCA-B observations for all  $\text{CH}_4$  tagged tracers in WRF-GHG. The sum of the mean values of all tagged tracers (including background tracer and excluding the wetland tagged tracer) was subtracted from the observation mean value. The mean of the wetland tagged tracer was adjusted to match this difference. The adjustment includes both observations of the PBL and the FT. All observations are equally weighted. However, the tendency of the scaling factors is mainly driven by the values in the PBL. The adjustment is considered to be representative for most of the BARCA-B flights as the western, center, and eastern regions have been fully covered. As the same scaling factors for each wetland  $\text{CH}_4$  emission model were also applied to the BARCA-A simulations during November 2008, the model skills to describe seasonal changes can be assessed.

In the first simulation (WKK), the  $\text{CH}_4$  wetland emissions have been calculated online using KWI in combination with the Kaplan wetland inundation map. The  $\text{CH}_4$  wetland emissions calculated by KWI have been reduced by 76% for November 2008 and May 2009. The second simulation (WWK) uses WWM together with the Kaplan wetland inundation map to allow for a direct comparison of the two wetland models. For WWK, the  $\text{CH}_4$  wetland emissions are increased by 9% for both months. In WWJ, WWM in combination with the JERS-1SAR wetland inundation map is utilized with reduced  $\text{CH}_4$  wetland emissions of 27%. Finally, in the fourth simulation (WWP) WWM in combination with the Prigent wetland inundation map was selected. The  $\text{CH}_4$  wetland emissions of WWP have been reduced by 55%. Table 6.3 summarizes all details.

An evaluation of the separate  $\text{CH}_4$  tracers for all different flux components within the WRF-GHG simulations demonstrates that the contributions of  $\text{CH}_4$  emissions from termites,  $\text{CH}_4$  uptake by soils, and  $\text{CH}_4$  emissions from plants are negligible compared to the three main sources, namely as  $\text{CH}_4$  emissions from wetlands, biomass burning, and other anthropogenic sources (not shown). Methane emissions from plants were found to be several orders of magnitude lower than  $\text{CH}_4$  emissions of termites. This is in better agreement with Querino et al. [2011], who could not identify aerobic  $\text{CH}_4$  emissions from plants in the Amazon basin, and with Dueck et al. [2007] and Nisbet et al. [2009], who pointed out experimental artifacts of the work of Keppler et al. [2006].



### Comparison to BARCA methane observations with adjusted wetland fluxes

Fig. 6.8 illustrates vertical profiles of the observations (black) and the four WRF-GHG simulations (WKK–blue, WWK–green, WWJ–red, and WWP–blueviolet) during both campaigns for all observations of the BARCA-A and BARCA-B campaigns, and separated into five different sampling regions. The profiles are binned into 500 m vertical intervals. The  $r^2$  value is calculated prior to binning into 500 m vertical intervals for all observations and model values in that sampling region. For both campaigns,  $r^2$  values of the comparison between flask observations and the corresponding model values are given, while for BARCA-B also the  $r^2$  values of the comparison to the continuous observations (not including flights 8–10) are calculated as well.

During BARCA-A, the comparison of the campaign averaged vertical profile of the four different WRF-GHG simulations with the observations (Fig. 6.8a1) illustrates that all combinations of different wetland models and wetland inundation maps are able to reproduce the vertical structure of the campaign averaged profile of the observations. This is indicated by a fairly constant bias between model simulations and observations for the total profile (6–18 ppb), which does not change significantly when calculating the bias separately for the PBL (4–24 ppb) and the FT (7–16 ppb). The situation changes for BARCA-B (Fig. 6.8a2). Here all simulations have difficulties in reproducing the vertical structure of the campaign averaged profile. It results in a smaller overall bias compared to BARCA-A (-6 to -11 ppb) due to the binning into 500 m height intervals. However, when splitting the bias calculation into a PBL and a FT part (-2 to 8 ppb vs. -12 to -16 ppb), it is clear that the models are not able to capture the vertical structure of the observations, but have especially a high bias in the FT.

As next step the WRF-GHG simulations are evaluated against observations in five different regions of the Amazon basin separately for BARCA-A and BARCA-B starting with BARCA-A.

In the northern and center part during BARCA-A (Fig. 6.8b1), all simulations denote a constant bias of the total vertical profile compared to the observations (7–19 ppb). The structure of the vertical profile of the observations in the western part during BARCA-A (Fig. 6.8c1) is captured well, however most of the models tend to overestimate the observations in the PBL (-9 to 42 ppb). In the eastern part (Fig. 6.8e1), the model simulations show a slight overestimation in the FT (8–16 ppb) and a range of -11 to 15 ppb in the PBL. In the southern part, all models overestimate the observations of the total vertical profile during BARCA-A by 13–32 ppb (Fig. 6.8f1). This can be partially traced back to too high  $\text{CH}_4$  emissions from biomass burning as the tagged tracers indicate that emissions from biomass burning are either the dominating source of  $\text{CH}_4$  (WWP) or of the same magnitude as the wetland emissions in that region (WKK, WWK, and WWJ). Given that a comparison of simulated with observed CO during the same campaign indicates close agreement and suggests that biomass burning emissions of CO are fully consistent with the atmospheric constraint [Andreae et al., 2012], this might point to an overestimation of emission factors for  $\text{CH}_4$ . For the WWP simulations, a reduction of the biomass burning emissions by a factor two would be required to match the observations.

For BARCA-B, similar to the total vertical profile, the simulations tend to underestimate the observations in the FT (-13 to -36 ppb) and to overestimate the observations in the PBL (-10 to 32 ppb) in the northern, center, and western part. Interestingly, the observations in the western part during BARCA-B show high values up to 1850 ppb at 4000 m altitude, which haven't been observed in other regions of the Amazon basin. Backward calculations using the STILT model indicate that most of the air at 3000–4000 m altitude in that region originates from the north-western part of

the Amazon. For this region also observations from SCIAMACHY suggest high  $\text{CH}_4$  emissions [Frankenberg et al., 2005, 2011]. This potential source region might not be properly represented in the flux distribution of the outer domain (d01), leading to an additional underestimation of the observations in the FT besides vertical mixing. The structure of the vertical profile of the observations in the eastern part during BARCA-B (Fig. 6.8e2) is reproduced well by all of the models with slight underestimation of the total vertical profile, resulting in biases of -6 to -13 ppb. The observations in the southern part during BARCA-B (Fig. 6.8f2) show a bias of -10 to 12 ppb on the total vertical profile.

As last step the differences between the four model simulations (WKK, WWK, WWJ, and WWP) are discussed for the five different regions of the Amazon basin. If not explicitly stated, we use the continuous observations for BARCA-B for the comparison (in addition the flask samples for BARCA-A).

For BARCA-A and BARCA-B WKK and WWK seem to capture the variances better in the northern sampling region ( $r^2 = 0.39\text{--}0.47$  (BARCA-A) and  $r^2 = 0.18\text{--}0.26$  (BARCA-B), Fig. 6.8b1-b2) compared to WWJ and WWP ( $r^2 = 0.02\text{--}0.14$  (BARCA-A) vs.  $r^2 = 0.08\text{--}0.09$  (BARCA-B)). This is also true for the center region during BARCA-A. In Fig. 6.2b4-b5, the Kaplan wetland inundation map shows higher values in the northern part of the nested domain compared to the Prigent wetland inundation map for both months, while the JERS-1SAR wetland inundation map also denotes high fraction of inundation values for the northern part (Fig. 6.2b1). However, calculated backward trajectories from the STILT model also indicate contributions of the north-western part of South America for the northern part of the Amazon region, an area where the Kaplan wetland inundation map depicts a wider spread area with a higher fraction of inundation (cf. Fig. A.12). This leads to the conclusion that the Kaplan wetland map represents the inundated area in the northern and center part of the Amazon basin and the South American continent better than the other two wetland inundation maps.

Considering the western part, the variances of the observations are captured well by all WRF-GHG simulations ( $r^2$  between 0.57 and 0.77) for both campaigns (Fig. 6.8c1-c2). For BARCA-A, WKK, WWK, and WWJ overestimate the observations in the PBL between 19 and 42 ppb. Only WWP slightly underestimates the observations (bias of the total vertical profile -8 ppb). Compared to the other wetland inundation maps, the Prigent wetland inundation map shows lower inundated area right beneath the flight track for the western Amazon flights (cf. Fig. 6.2a1-a3). For BARCA-B, the relatively high  $r^2$  of 0.52–0.56 for all four model simulations should not hide the fact that the representation of the vertical structure of the observations for all simulations is worst in this region compared to all other regions as discussed above. The global TM5 inversions on  $6^\circ \times 4^\circ$  horizontal resolution (cf. Ch. 5) using additional constraints on the a-posteriori fluxes from SCIAMACHY observations, are able to represent the structure of the vertical profile better compared to the WRF-GHG simulations (cf. Fig. A.18).

In the eastern part, during BARCA-A the WRF-GHG simulations of WWJ and WWP seem to capture the variances better compared to WKK and WWK (Fig. 6.8e1;  $r^2 = 0.49\text{--}0.62$  vs.  $r^2 = 0.05\text{--}0.17$ , respectively), which points to an underestimation of the inundated area in the Kaplan wetland inundation map in that region (cf. Fig. 6.2a1-a3). In contrast to TM5 inversions (cf. Ch. 5), the high resolution WRF-GHG simulations were able to capture the higher  $\text{CH}_4$  mixing ratios in that regions during BARCA-A. During BARCA-B (Fig. 6.8e2), all WRF-GHG simulations show low  $r^2$  values ( $r^2 = 0.27\text{--}0.29$ ), which could be partially explained by strong convective events that took place in this area during the flight days.

During BARCA-B, all WRF-GHG simulations in the southern part except for WWJ show high  $r^2$  especially compared to the flask observations ( $r^2$  ranging from 0.56 to 0.73 and  $r^2=0.09$  for WWJ). WWJ denotes too high  $\text{CH}_4$  mixing ratio in the PBL in that sampling region. A closer look on the wetland inundation map in Fig. 6.2a2 and b1-b3 indicates that the JERS-1SAR wetland inundation map shows a greater inundated area around  $60^\circ\text{W}$  and  $9^\circ\text{S}$ , which cannot be found in the other wetland maps. A comparison of different cross-sections depicts high emissions on about 70% of the total flown distance of that flight, coinciding very well with the location of the inundated area described above.

In general, the  $r^2$  values when using only the flask observations are higher than using continuous observations during BARCA-B (cf. Fig. 6.7, Fig. 6.8). This is due to the fact that the flask samples are already collected in a way (one/two samples in the PBL and one/two samples in the FT per flown profile) that they favor the explanation of the variances by the model more than the continuous observations which report a data point each three seconds [Chen et al., 2010].

From the comparison of the four WRF-GHG simulations utilizing two different wetland models and three different wetland inundation maps, it is stated that the Kaplan wetland inundation map represents the wetland area in the northern part of the Amazon basin and around the Manaus area during both months November and May best, while the Prigent wetland inundation map has the best representation in the western and eastern part of the Amazon basin during BARCA-A. This favors at least for those regions a wetland inundation map with inundated area changing in time during the dry season. Further, it can be concluded that the choice of the wetland model producing the  $\text{CH}_4$  emissions is less important than the choice of the wetland inundation map that defines the distribution of the inundated area for comparisons with aircraft observations.

The explained variability ( $r^2$ ) of the high-resolution WRF-GHG simulations compared to the global TM5-based  $\text{CH}_4$  inversions (cf. Ch. 5) was found to be significantly larger only for the western and eastern region during BARCA-A. This underlines the importance of a proper representation of the atmospheric transport in regional atmospheric transport models when they are applied in tropical regions. It further emphasizes the need for a wetland inundation map at high horizontal and monthly temporal resolution that adequately represents the inundated wetland area throughout the complete Amazon basin as the monthly temporal resolution of the inundated wetland area is e.g., already implicitly included in the global TM5 inversions. With these two requirements additional benefits from the usage of regional atmospheric transport models can be achieved.

#### 6.2.4 Amazon basin budget calculations

After the evaluation of the WRF-GHG simulations against the BARCA observations, the derived  $\text{CH}_4$  budgets for these forward simulations with an already adjusted wetland flux component are presented. The budgets are determined for the 5.19 million square kilometer area of the Amazon lowland region and the 1.77 million square kilometer area of the Amazon mainstream from  $-8^\circ\text{S}$  to  $0^\circ$  and  $-72^\circ\text{W}$  to  $-54^\circ\text{W}$  (cf. Fig. 2.10). Both regions are defined and described in Melack et al. [2004]. Table 6.5 illustrates the calculations of the monthly  $\text{CH}_4$  budgets in detail. The  $\text{CH}_4$  budgets from the WRF-GHG simulations for both regions are discussed before they are compared to literature values.

The resulting total monthly  $\text{CH}_4$  budgets from the four different WRF-GHG simulations for the Amazon lowland region range from 1.5 to 4.8 Tg for November 2008 and from 1.3 to 5.5 Tg for

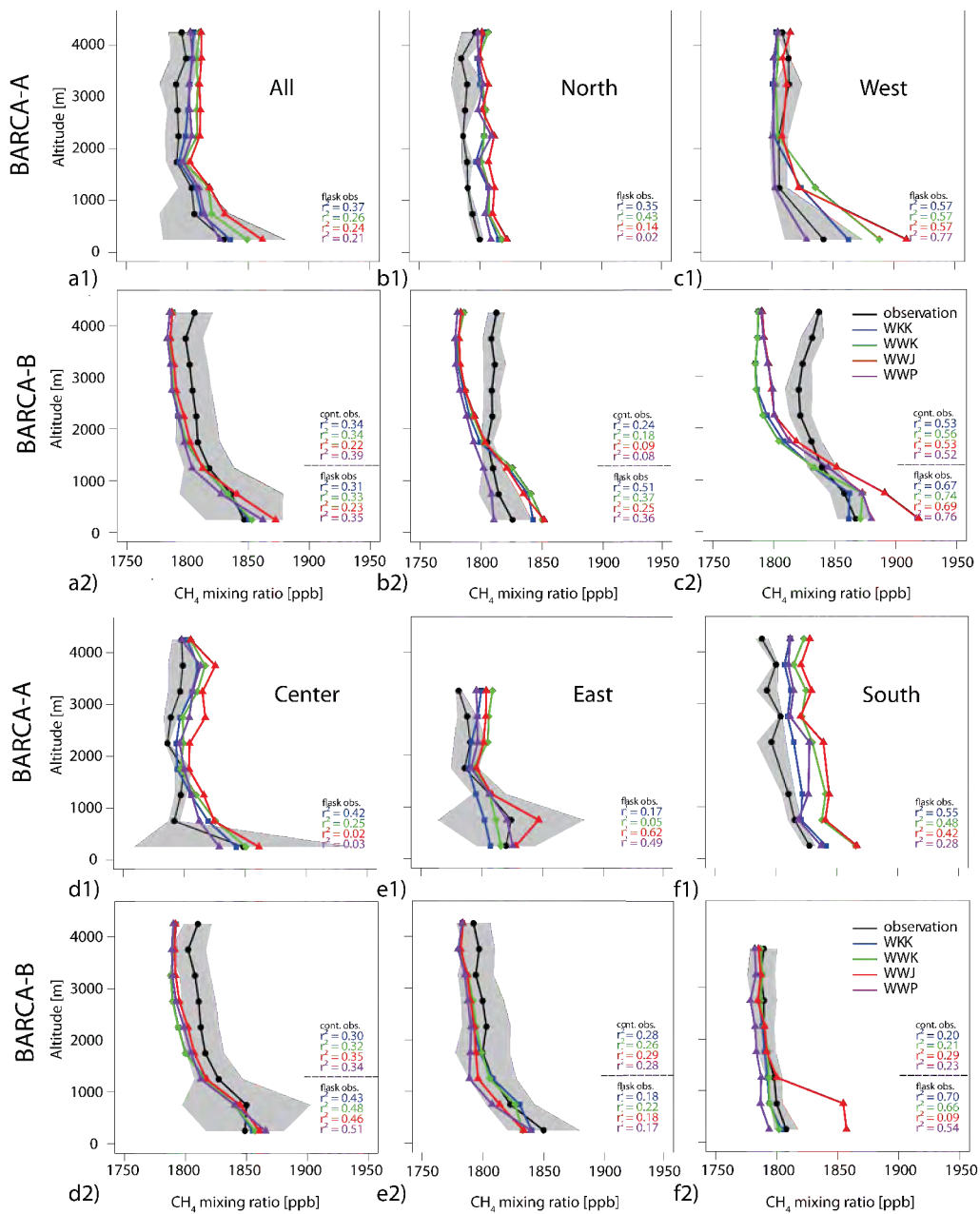


Figure 6.8: Comparison of BARCA-A (1) and BARCA-B (2) observations (black) to different WRF simulations (WKK–blue; WWK–green; WWJ–red; WWP–violet) binned in 500 m vertical profiles for five different region of the Amazon basin (for definition of the sampling regions see Fig. 5.1b).

May 2009. The  $\text{CH}_4$  emissions from wetlands are the dominating source both in November 2008 and May 2009 (cf. Table 6.5). The  $\text{CH}_4$  biomass burning flux contributes 0.27 Tg in November 2008 and 0.04 Tg in May 2009. The contribution of other anthropogenic sources is similar in both months ( $\sim 0.12$  Tg). This implies average  $\text{CH}_4$  fluxes ranging from 9 to 31  $\text{mg m}^{-2} \text{d}^{-1}$  for November 2008 and 8–36  $\text{mg m}^{-2} \text{d}^{-1}$  for May 2009. It indicates that besides the biomass burning emissions and slightly higher wetland emissions during BARCA-B (on average 2.7 Tg vs.

3.3 Tg), no significant change in the source contributions between November 2008 and May 2009 is notable. Even though the wetland source was adjusted to match the mean of the observation for selected flights with a good representation of the atmospheric transport in the model during BARCA-B for all four WRF-GHG simulations, the wetland contributions for the total Amazon lowland region draw a highly variable picture. For this region, the combination of the Walter wetland model and the Prigent wetland inundation map led to the lowest wetland emissions (0.9 Tg for both month). Using the same wetland model but the JERS-1SAR wetland inundation map instead produced the highest wetland emissions (4.2 Tg for November 2008 and 5.2 Tg for May 2009). WWK is the only simulation that shows a significant higher wetland contribution in November 2008 (4.2 Tg) compared to May 2009 (3.1 Tg). All other simulations have either similar or smaller wetland contributions in November 2008 compared to May 2009 (cf. Table 6.5). As also two other simulations utilizing the same wetland model WWM as the WWK simulation (WWJ and WWP) have a higher wetland contribution in May 2009 compared to November 2008, the explanation has to be traced back to differences in the wetland inundation maps. The Kaplan wetland inundation map utilized for the WWK simulations contains significantly more wetland grid points in the north-western Amazon compared to the JERS-1SAR and Prigent wetland inundation map. In this area WWM calculates a considerable higher  $\text{CH}_4$  flux for November 2008 compared to KWI.

This indicates that the method of comparison is not sensitive to different regions. The results might change by adding information of the bias for the different regions as it could be conducted e.g., by a regional inversion with spatial flexibility in adjusting fluxes and flux patterns. It further clearly demonstrates that the BARCA observations do not allow an observational constraint for the complete Amazon lowland region, especially not for the western part.

To focus more on an area that was covered to a higher percentage by the BARCA flights, the  $\text{CH}_4$  budget numbers for the reference area of the Amazon mainstream were evaluated. The calculated budget numbers range from 0.8–1.8 Tg for November 2008 to 0.8–2.1 Tg for May 2009. The average total calculated  $\text{CH}_4$  flux to the atmosphere is higher compared to the Amazon lowland region. For this region the simulation using the Prigent wetland inundation map has the lowest budget number compared to the other simulations (e.g. 0.8 Tg vs. to 1.4–2.1 Tg for May 2009). This leads to the assumption that even though the Prigent wetland inundation map performed very well in capturing the variability along the flight path, it might underestimate the wetland area, e.g. in flooded forest areas further away from the open waters of the Amazon river (cf. number of wetland grid points in the d02 domain in Table 6.3 and Fig. A.12).

The average of the calculated budgets of the four WRF-GHG simulations of the Amazon lowland region is lower ( $3.3 \pm 0.8$  Tg for November 2008 and  $3.3 \pm 0.9$  Tg for May 2009) compared to the budget estimates obtained from the comparison of TM5-based global  $\text{CH}_4$  inversions and the BARCA observations ( $5.7 \pm 0.7$  Tg for November 2008 and  $6.9 \pm 1.1$  Tg for May 2009) as described in Ch. 5. Neglecting the simulation using the Prigent wetland inundation map (WWP), the average of the calculated WRF-GHG budgets is significantly higher ( $3.9 \pm 0.8$  Tg for November 2008 and  $4.0 \pm 0.8$  Tg for May 2009) and closer to the budget numbers derived in Ch. 5. The calculated monthly  $\text{CH}_4$  budgets for November 2008 and May 2009 show similar numbers. However, when taking into account the constant bias of the vertical profile during BARCA-A (12–15 ppb), the budget that would match the observations perfectly for November 2008 would be lower, which would be more in accordance with the expected higher wetland emissions in May compared to November [Devol et al., 1990].



	Amazon lowland region			Amazon mainstream area		
	Total monthly budget [Tg]	Monthly wetland contribution [Tg]	Average total flux [ $\text{mg m}^{-2} \text{d}^{-1}$ ]	Total monthly budget [Tg]	Monthly wetland contribution [Tg]	Average total flux [ $\text{mg m}^{-2} \text{d}^{-1}$ ]
BARCA-A						
WKK	2.2	1.6	14	0.9	0.8	17
WWK	4.8	4.2	31	1.8	1.7	34
WWJ	4.8	4.2	31	1.8	1.7	34
WWP	1.5	0.9	9	0.8	0.8	15
BARCA-B						
WKK	3.0	2.6	19	1.4	1.3	26
WWK	3.5	3.1	22	1.4	1.3	26
WWJ	5.5	5.1	36	2.1	2.0	39
WWP	1.3	0.9	8	0.6	0.7	13

Table 6.5: Calculation of the total  $\text{CH}_4$  budget numbers [ $\text{Tg mo}^{-1}$ ] and the wetland contributions of the four different WRF-GHG simulations for the Amazon lowland region and Amazon mainstream area (definition see text and Fig. 2.10).

Melack et al. [2004] estimated the yearly contribution of wetland  $\text{CH}_4$  emissions in the Amazon lowland region to 29.3 Tg, corresponding to a monthly average of 2.4 Tg. The monthly wetland contribution of WWP for November 2008 and May 2009 is approx. 50% of that estimated by Melack et al. [2004]. The wetland contribution of almost all other simulations is significantly higher than 2.4 Tg for both months, November 2008 and May 2009. For the Amazon mainstream area, Melack et al. [2004] estimated the yearly  $\text{CH}_4$  contributions from wetlands to be 9.0 Tg (corresponding to  $0.75 \text{ Tg mo}^{-1}$  assuming an equal distribution over the complete year). The estimate of Bloom et al. [2010] with 20.0 Tg for the Amazon basin is even lower. In this region, all WRF-GHG simulations show a higher monthly  $\text{CH}_4$  wetland contribution ranging from 0.6–2.1 Tg.

Miller et al. [2007] calculated flux estimates for the Amazon basin based on the difference in the atmospheric mixing ratios between the NOAA-ESRL background stations in Ragged Point Barbados (BDS) and Ascension Island (UK) and vertical airborne profiles over Manaus and Santarém. They estimated a  $\text{CH}_4$  flux of  $35 \text{ mg m}^{-2} \text{d}^{-1}$  for the Santarém area and  $20 \text{ mg m}^{-2} \text{d}^{-1}$  for the Manaus area. The obtained flux estimates from the WRF-GHG simulations ( $15\text{--}34 \text{ mg m}^{-2} \text{d}^{-1}$  for November 2008 and  $13\text{--}39 \text{ mg m}^{-2} \text{d}^{-1}$  for May 2009) for the Amazon mainstream area are in good agreement with what has been observed by Miller et al. [2007].

Summarizing the comparison of the WRF-GHG  $\text{CH}_4$  budgets to previous budget estimates for the Amazon basin, it can be concluded that  $\text{CH}_4$  budget estimates using the top-down approach (this Chapter, Ch. 5, Miller et al. [2007]) up to now lead to a higher  $\text{CH}_4$  budget of the Amazon basin compared to the bottom-up estimate as described in Melack et al. [2004] or the GRACE based approach by Bloom et al. [2010].



### 6.3 Conclusions

The evaluation demonstrated that choice of the wetland inundation map for simulating CH<sub>4</sub> transport of the Amazon basin is of high impact, much more than the choice of the model for the calculation of the CH<sub>4</sub> emissions from anaerobic production in wetlands itself. However, before scaling the wetland emission, the covered range of the different wetland models was about 30% higher compared to the range of the different wetland inundation maps. When emissions are scaled to match the atmospheric observations, both wetland models were found to represent the CH<sub>4</sub> flux from anaerobic production by microbes in wetlands according to the literature values. For the northern part of the Amazon and the Manaus area, the CH<sub>4</sub> emissions using the Kaplan wetland inundation map showed the best agreement to the observations. During BARCA-A only, the wetland inundation map of Prigent was found to have the best agreement to the observations in the western and eastern part. This favours (except for the northern part) the assumption that a wetland inundation map with inundated area changing in time could improve the agreement with the observations. A regional inversion with spatial flexibility in adjusting fluxes and flux patterns could lead to significant improvements here. Additional observations in the western part of the Amazon basin are essential for improved constraints on the wetland emissions in the complete Amazon basin.

It was demonstrated that the WRF-Chem model represents the observations better during days with less convection during the 48 h before the flight in the upstream area. The significant decrease in model performance for flights with stronger convective activity (about half of the total number of flights) suggests that vertical transport by convection has a major impact on the distribution of atmospheric methane in the Amazon, and that current generation transport models inadequately represent this process. Improvements in representing the challenging meteorological conditions and thus of atmospheric transport models are required, in order to constrain flux estimates properly and obtain more stable budget numbers. This is regarded as an essential step that needs to be taken before using such transport models for regional scale inverse estimates.



## Chapter 7

# Annual methane budget of the Amazon basin

A regional CH<sub>4</sub> inversion for the year 2009 is conducted with the Jena two-step inversion scheme TM3-STILT (cf. Sec. 3.4) to estimate the annual CH<sub>4</sub> budget of the Amazon basin. The TT34 tower observations serve as observational constraints for the inversion system. The impact of different meteorological forcing for the Walter wetland model and the usage of different regional atmospheric transport models on the simulated CH<sub>4</sub> mixing ratios of the TT34 tower is evaluated. The regional inversion is carried out with three different a-priori flux distributions. The STILT simulations with the optimized a-posteriori flux distributions are evaluated against independent airborne observations from the BARCA-B airborne campaign (cf. Ch. 5) and monthly stationary profiles close to the city of Santarém conducted by NOAA-ESRL as described in Miller et al. [2007]. Annual CH<sub>4</sub> budget estimates for the Amazon lowland region and the Amazon main-stream area with calculated uncertainties are derived from the regional inversion study.

### 7.1 Two-step regional inversion set up

For the first time, a regional CH<sub>4</sub> inversion study is conducted for the Amazon basin using the Jena two-step inversion scheme. The regional inversion is carried out for the complete year 2009. As first step, a global CH<sub>4</sub> inversion with the global atmospheric transport model TM3 (cf. Sec. 3.3.2) for the years 2005–2010 was conducted. The a-priori CH<sub>4</sub> fluxes of the global CH<sub>4</sub> inversion are identical to those of the TM5 global CH<sub>4</sub> inversion from Bergamaschi et al. [2010] described in Table 5.2. The horizontal resolution of the TM3 is 5° × ~4° (fine grid) whereas the horizontal resolution of the TM5 grid is 6° × 4°. Observations from 32 surface stations were utilized to constrain the a-posteriori flux field, which were described in Bergamaschi et al. [2009]. Detailed information on the observations from surface stations and their locations is given in Table A.1 and Fig. A.19. The settings for conducting the global CH<sub>4</sub> TM3-based atmospheric inversion were provided by U. Karstens.

Based on the above described global TM3 inversion the intermediate step for the Domain of Interest (DoI) (see Sec. 3.4 and Fig. 3.4) was carried out to obtain the atmospheric background mixing ratio  $C_{\text{mod,back}}$  before proceeding with the regional inversion. The DoI for the regional inversion is defined as 220 × 200 grid cells with a horizontal resolution of 0.25° × 0.25°. It is located

between  $-85^{\circ}\text{W}$  to  $-30^{\circ}\text{W}$  and  $-35^{\circ}\text{S}$  to  $15^{\circ}\text{N}$  and covers almost whole South America (cf. Fig. 7.4 and Fig. 7.8). The domain was selected to have main overlap with the coarse “d01” domain of the WRF-GHG simulations described in Ch. 6 (cf. Fig. 6.1).

The atmospheric transport model utilized for the regional inversion is the Lagrangian Transport model STILT (details in Sec. 3.3.3). It is driven by 3 h meteorological fields from the ECMWF operational archive on  $0.25^{\circ} \times 0.25^{\circ}$  horizontal resolution. The meteorological fields undergo a preprocessing step which ensures mass conservation of the wind fields. The first 61 vertical levels (starting from the ground) of the 91 available vertical levels from the ECMWF operational archive are taken as vertical resolution.

The STILT model calculates the atmospheric  $\text{CH}_4$  mixing ratio by multiplying the footprint function with the corresponding flux field (cf. Eq. (3.20)). The footprints describing the sensitivity to upstream surface fluxes are calculated for hourly TT34 tower observations throughout the year 2009. 100 particles were released at the TT34 tower location ( $-60.21^{\circ}\text{W}$ ,  $-2.61^{\circ}\text{S}$ ) at 35 m above ground for each hourly observation. The footprints were calculated 10 days backward in time. Winderlich [2011] showed for the northern latitudes that a footprint calculation for 10 days backward already includes 99% of the overall footprint of a tower for a domain of similar size.

The  $\text{CH}_4$  TT34 tower observations (called “TT34 tower observations”) are a combined time series of two different continuous measurements. It ranges from end of November 2008 to April 2010. The measurements from November 2008 until May 2009 were conducted by the Institute for Marine and Atmospheric Research Utrecht (IMAU), Netherlands, using a Los Gatos methane analyzer. Those measurements were obtained at the K34 tower ( $-60.21^{\circ}\text{W}$ ,  $-2.61^{\circ}\text{S}$ ) approx. 60 km north-west of Manaus at 55 m height. The TT34 tower with a height of 35 m is located in close vicinity ( $\sim 1.5$  km) to the K34 tower. At the TT34 tower the Picarro CRDS analyzer was successfully installed after the second flight campaign BARCA-B (cf. Ch. 5). The  $\text{CH}_4$  observations from June 2009 to April 2010 were obtained from the CRDS instrument. The observations of both time series were corrected for drift of the instruments and merged to obtain a continuous time series from November 2008 to April 2010. For this chapter, the focus of the observations is on the complete year 2009.

The observations of the TT34 tower used in the inversion system to constrain the a-posteriori flux distribution are pre-selected to minimize transport model errors. Afternoon observations in a well-mixed PBL were found to be better represented by the regional atmospheric transport models compared to night-time observations, where the models have problems in representing the night-time PBL height [Geels et al., 2007, Ahmadov et al., 2007]. 18 UTC TT34 observations were selected for the regional (and global) inversion. This is in accordance with the highest observed PBL heights around 17 UTC as described in Table 2.2.

Through the implemented data density weighting in the Jena inversion scheme continuous observations from surface stations have the same weight as a weekly sampled flask observation [Rödenbeck, 2005]. Airborne observations are not utilized in the  $\text{CH}_4$  regional inversion system as observations on irregular time intervals would lead to a disturbance of the inversion mechanism causing potential artificial artifacts in the a-posteriori flux distribution [P. Bergamaschi, pers. communication, 2011].

In Sec. 3.1 the different uncertainty components of the top-down approach were described. For the two-step regional inversion scheme, it includes the atmospheric transport model uncertainty, the uncertainty of the TT34 observations, and the representation error. The measurement uncertainty is estimated to  $\sigma_{obs} = 0.4$  ppb [U. Karstens, pers. communication, 2011]. The model un-

certainty includes both, the uncertainty in representing the atmospheric transport by the regional atmospheric transport model and the representation error (cf. Sec. 3.4). It is dependent on the location of the tower station (background or continental site). For the TT34 tower, a continental surface station, it is defined to  $\sigma_{mod} = 1.5$  ppb [U. Karstens, pers. communication, 2011]. The off-diagonal elements of the error covariance matrix  $\mathbf{Q}_c$  are set to zero (only one single station). The uncertainty of the a-priori flux distribution is defined as the standard deviation of the a-priori flux field  $\sigma_f$  normalized by the sigma target of  $0.316 \text{ Tmol a}^{-1}$  for the  $\text{CH}_4$  land flux. The  $\text{CH}_4$  land and the  $\text{CH}_4$  ocean flux are optimized separately.

### 7.1.1 A-priori flux distribution

In addition to the information obtained from the TT34 observations, information is added by a-priori  $\text{CH}_4$  flux fields. The different source components are compared to the  $\text{CH}_4$  flux fields used for the WRF-GHG simulations in Ch. 6 to ensure continuity of the flux distributions. Special focus is given to the evaluation of the Walter wetland model with different meteorological forcing.

For the optimization of the oceanic component, the same a-priori flux distribution as for the global TM3  $\text{CH}_4$  inversion is utilized [Lambert and Schmidt, 1993]. For the  $\text{CH}_4$  land flux, new a-priori flux distributions at higher spatial and temporal resolution compared to the global TM3 inversion are used. The  $\text{CH}_4$  land flux consists of the three main  $\text{CH}_4$  source components in the Amazon basin wetlands, biomass burning, and anthropogenic sources. The contribution from minor sources and sinks such as termites or soil uptakes was found to be negligible (cf. Sec. 6.2.3).

The anthropogenic  $\text{CH}_4$  flux and the  $\text{CH}_4$  flux from biomass burning were calculated as described for the WRF-GHG simulations (cf. Sec. 4.1.2). For the WRF-GHG simulations a diurnal cycle for biomass burning and anthropogenic emissions was implemented. The a-priori flux distribution of the Jena two-step regional inversion usually does not account for diurnal cycles in the emissions. To estimate the impact of the diurnal cycle of anthropogenic and biomass burning fluxes on the TT34 tower observations, two different WRF-GHG simulations were conducted. The set up of the WRF-GHG simulations is identical to the WWP simulation described in Table 6.3. The simulations are conducted for the time period of August 2009. The time period of August 2009 was chosen to obtain additional information on the representation of the atmospheric transport during the dry season with less expected convective activity as completion to the WRF-GHG simulations in May 2009 and November 2008. In the second WRF-GHG simulation the  $\text{CH}_4$  fluxes for biomass burning and anthropogenic emissions are included as daily constant values. The comparison of the monthly time series with reduced wetland component (reduced by -40% according to the description in Sec. 6.2.3) of the simulation with a diurnal cycle in the anthropogenic and biomass burning emission and the simulation with daily constant fluxes show no impact on the explained variability of the TT34 tower observations (same  $r^2$  value for both simulations). Calculating the bias of the two WRF-GHG simulations and the TT34 tower observations yields a difference of  $<3$  ppb between both WRF-GHG simulations. From this, it can be concluded that the effect of diurnal variation in the a-priori fluxes will not have an important impact on the constraint of the a-posteriori flux distribution.

In Ch. 5 and 6 the importance of  $\text{CH}_4$  emissions from wetlands as the dominant source process in the Amazon basin was discussed. A reasonable choice of wetland model and wetland inundation map as a-priori  $\text{CH}_4$  wetland flux distribution is important for a proper representation of the  $\text{CH}_4$  atmospheric mixing ratio in the Amazon basin required for the regional inversion.

To determine the “best” wetland inundation map, the conducted WRF-GHG simulations of Ch. 6 with three different wetland inundation maps are evaluated against the TT34 tower observations for May 2009. Fig. 7.1a illustrates a comparison of the mean diurnal cycle of the TT34 tower observations (black) and the four WRF-GHG simulations described in Table 6.3. Note that the CH<sub>4</sub> wetland fluxes have already been adjusted to account for the differences in the wetland inundation maps as described in Table 6.3. The two WRF-GHG simulations using the Walter wetland model in combination with the JERS-1SAR wetland inundation map and the Prigent inundation map have the highest explained variability ( $r^2 = 0.36$ – $0.37$  vs.  $r^2 = 0.03$ – $0.04$ ) and the lowest bias (28.2–30.2 ppb vs. 131.6–338.2 ppb) compared to the WKK and WWK simulations. Reasons for this deviation are found in the distribution of the wetland area around the TT34 tower. Fig. 7.1b–d illustrates the distribution of the inundated wetland area in a radius of  $\sim 130$  km around the TT34 tower. The Kaplan wetland inundation map (Fig. 7.1b) shows inundated area right at the TT34 tower grid cell (1.3% inundated area). Both the JERS-1SAR and the Prigent wetland inundation map do not contain any wetland area in the grid cell in which the TT34 tower is located. The closest inundated area grid cell of these two wetland inundation maps is at least 10 km away. Footprint analysis in the surroundings of the TT34 tower demonstrates that most of the contribution originates from the grid cell in which the TT34 tower is located and the two neighboring grid cells in eastern direction. This explains why the WRF-GHG simulations using the Kaplan wetland inundation map shows such high simulated CH<sub>4</sub> atmospheric mixing ratios at the TT34 tower.

For the calculated CH<sub>4</sub> wetland fluxes in Ch. 6, the meteorological forcing of the WRF-Chem model was used. Now CH<sub>4</sub> wetland fluxes need to be calculated for the complete year 2009. To force a wetland model with WRF-Chem meteorology would require to perform WRF-Chem simulations for the entire year 2009. Because of demanding disk space and runtime requirements of the WRF-Chem model, it would be too cost extensive. Instead the CH<sub>4</sub> wetland fluxes are calculated offline using ERA-Interim meteorological forcing. The Walter wetland model was chosen as preferred wetland model. It has the advantage to account for enhanced CH<sub>4</sub> emissions from falling water table [Walter et al., 2001a] compared to the pure soil moisture and soil temperature based Kaplan wetland inventory. For the calculation of the CH<sub>4</sub> wetland fluxes, 6 h ERA-Interim meteorological data were obtained from ECMWF (<http://www.ecmwf.int/products/data/archive/descriptions/ei/index.html>). In detail, soil temperature level 1–4, 2 m temperature, total precipitation, surface solar radiation, and surface thermal radiation are the meteorological input variables from ERA-interim for the Walter wetland model. Other static parameters, e.g. for the calculation of the root depths, are still obtained from the WRF-Chem model and regridded to the STILT domain.

The impacts of the different meteorological forcing on the CH<sub>4</sub> wetland fluxes are evaluated. The integrated daily CH<sub>4</sub> flux of the Amazon mainstream area for the complete year 2009 from the ERA-Interim forced CH<sub>4</sub> wetland flux (WWP-ERA–dashed line) is compared to the WRF-Chem forced CH<sub>4</sub> wetland flux (WWP–continuous line) for the months May and August 2009 (Fig. 7.2a). The CH<sub>4</sub> wetland flux as the main source dominates the variability in this comparison. The CH<sub>4</sub> fluxes of November 2008 from the WRF-Chem simulations are also included in the comparison, even though they are compared to CH<sub>4</sub> fluxes of November 2009. The WRF-Chem forced fluxes were not adjusted for this comparison.

The comparison in Fig. 7.2a demonstrates that the magnitude of the CH<sub>4</sub> fluxes calculated with ERA-Interim and WRF-Chem meteorology is very similar for May and August 2009. Calculating the mean CH<sub>4</sub> flux for the Amazon mainstream area for both months yields a difference of



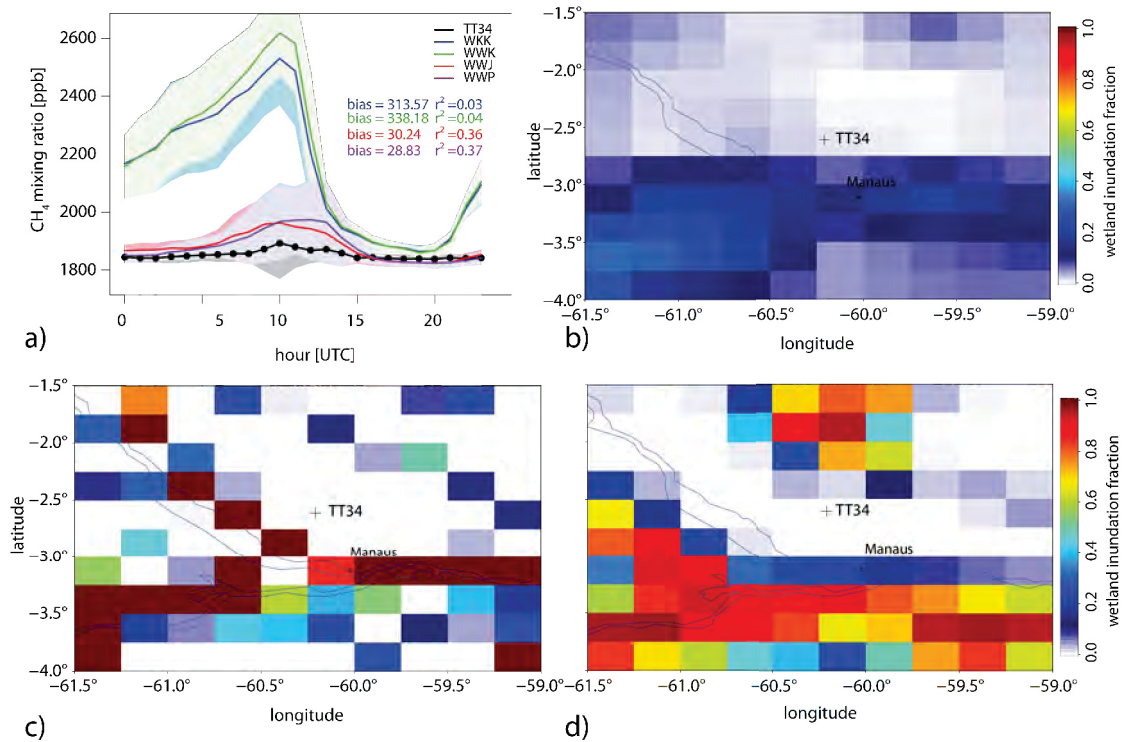


Figure 7.1: (a) Comparison of the four WRF-GHG simulations as described in Ch. 6 to TT34 tower observations (black). The mean diurnal cycle of the four simulations and the observations for the time period 15<sup>th</sup>–31<sup>th</sup> May 2009 is illustrated. (b) distribution of wetland area around the TT34 tower as given from the Kaplan wetland inundation map, (c) the JERS-1SAR wetland inundation map, and (d) the Prigent wetland inundation map for May 2009. The color scale of (c) and (d) is identical.

$\sim 2 \text{ mg m}^{-2} \text{ d}^{-1}$ . The difference in the mean  $\text{CH}_4$  flux between the ERA-Interim forced  $\text{CH}_4$  fluxes for November 2009 and the WRF-Chem calculated  $\text{CH}_4$  fluxes for November 2008 is slightly higher ( $\sim 4 \text{ mg m}^{-2} \text{ d}^{-1}$ ). It is difficult to compare those two months as the meteorological conditions between November 2008 and November 2009 were different. As illustrated in Fig. 2.7 and Fig. 2.8 November 2008 was assigned a “La Niña” month with more than average rainfall. November 2009 was found to be an “El Niño” month with significantly less than average rainfall.

Even though the mean monthly average  $\text{CH}_4$  flux for the Amazon mainstream region is very similar for calculations from the two different meteorological forcing, the variability is different. According to the sensitivity studies of the Walter wetland model presented in Walter and Heimann [2000], a reduction in the water table of 10 cm can decrease the  $\text{CH}_4$  flux by 20%. A change in the soil temperature of 1 K is described to have an impact of 20% on the  $\text{CH}_4$  flux. Other parameters that are described in the sensitivity tests in Walter and Heimann [2000] were kept constant for both cases.

No significant differences in the water table position ( $< 2 \text{ cm}$ ) could be found between the water table calculated by the ERA-Interim and WRF-Chem meteorology, e.g. for August 2009. The variations of the soil temperature in the ERA-Interim meteorology coincides well with the varia-

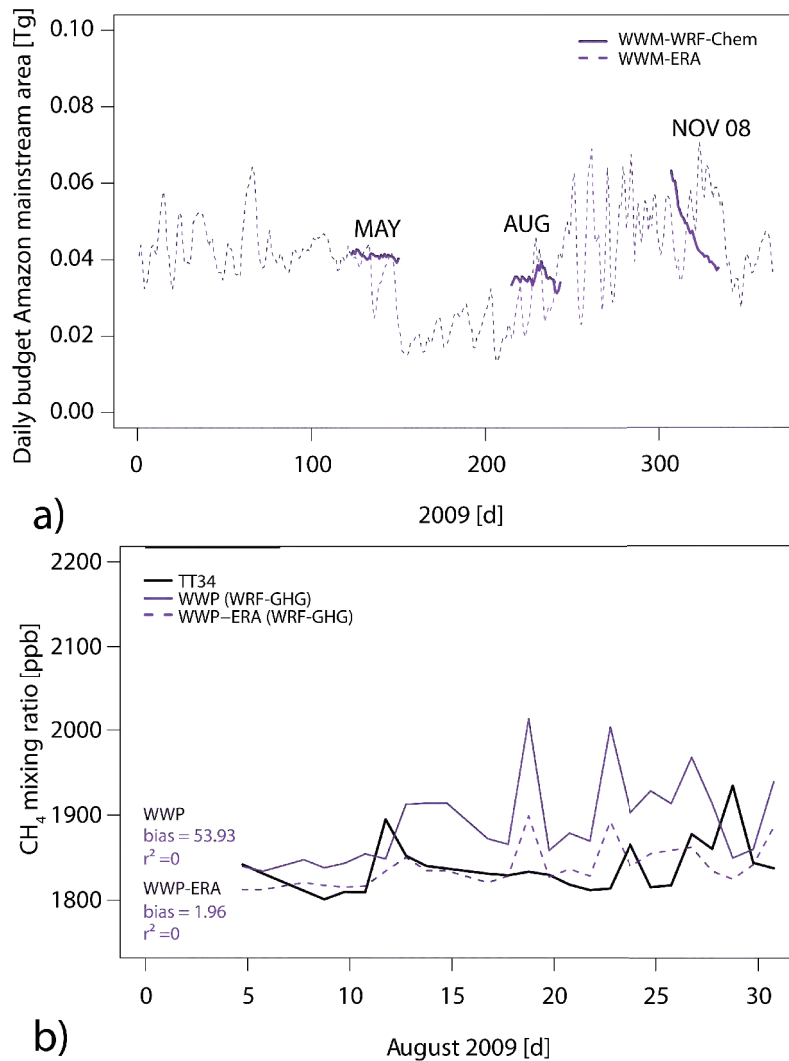


Figure 7.2: (a) Daily averaged  $\text{CH}_4$  budgets for the Amazon mainstream area of  $\text{CH}_4$  wetland fluxes calculated with ERA-Interim meteorology (WWM-ERA—dashed line) for the entire year 2009 and WRF-Chem meteorology (WWM-WRF-Chem—continuous line) for the months May and August 2009 and November 2008. (b) Comparison of 18 UTC TT34 observations to 18 UTC  $\text{CH}_4$  atmospheric mixing ratio from WRF-GHG simulations using wetland  $\text{CH}_4$  fluxes forced by ERA-Interim meteorology (WWP-ERA—dashed line) and WRF-Chem meteorology (WWP—continuous line) for August 2009. In both cases the combination of Walter wetland model and Prigent wetland inundation map was utilized.

tions of the  $\text{CH}_4$  flux as seen in the daily budget of the Amazon mainstream region (cf. Fig. 7.2a). Similar to the ERA-Interim meteorology, also for the WRF-Chem meteorology the fluctuation in the calculated  $\text{CH}_4$  fluxes can be explained by variations in the first layer soil temperature. In Fig. 7.2b a comparison of two WRF-GHG simulations with  $\text{CH}_4$  fluxes from ERA-interim (WWP-ERA—dashed line) and WRF-Chem (WWP—continuous line) meteorology to 18 UTC TT34 tower observations for August 2009 is presented. Noticeable here is the difference in the bias ( $\sim 50$  ppb), when comparing both simulations to TT34 18 UTC tower observations. Comparing the mean

maximum soil temperature of the ERA-Interim and the WRF-Chem meteorology in the surroundings of the TT34 tower, yields an approx. 2 K difference. This could explain the higher observed atmospheric CH<sub>4</sub> mixing ratios of the WWP simulation compared to the WWP-ERA simulation. From these results, one can conclude that the first layer soil temperature is the main meteorological driver causing the variations of the CH<sub>4</sub> wetland fluxes in the Amazon basin as modeled by the Walter wetland model. The comparison demonstrates that the differences in the CH<sub>4</sub> fluxes originating from different forcing meteorological fields do not have a very large impact on the overall CH<sub>4</sub> budget. For specific locations, the impact on the simulated atmospheric CH<sub>4</sub> mixing ratio from differences in the soil temperature between the two meteorological forcing might be larger.

### 7.1.2 Atmospheric transport

The representation of the atmospheric transport has an important impact on the budget estimate in the regional inversion scheme. Misrepresentation of simulated atmospheric CH<sub>4</sub> mixing ratios at the TT34 tower originating from errors in the atmospheric transport can have an influence on the optimized a-posteriori flux distribution, as the inversion scheme assumes a perfect transport (except for what was accounted in the transport model uncertainty  $\sigma_{mod}$ ).

For the comparison to the BARCA airborne observations in Ch. 6, the Eulerian regional atmospheric transport model WRF-Chem was utilized. The Jena two-step inversion scheme is implemented using the Lagrangian Transport model STILT. Pillai et al. [2012] already showed that the STILT model can be used as an adjoint transport model of the WRF-Chem model. In that work, the STILT model was driven by meteorological output fields from WRF-Chem. For the Amazon basin, the meteorological configuration is different to that used in northern mid-latitudes. For the convective parametrization in WRF-Chem the Grell3 (G3) convection scheme is used for the Amazon basin (cf. Table 6.1). For simulations of the WRF-Chem meteorology with the G3 convection scheme no hourly averaged meteorological fields could be produced as meteorological input for the STILT model due to partially not proper defined variables.

For an estimation of the difference in the representation of the atmospheric transport between the WRF-Chem model and the STILT model driven by ECMWF meteorology, both are compared to CH<sub>4</sub> observations at the TT34 tower during August 2009. For both simulations (WRF-GHG and STILT) the previously described a-priori CH<sub>4</sub> fluxes including wetland fluxes calculated by the Walter wetland model with ERA-Interim meteorology and the Prigent wetland inundation map are used.

Fig. 7.3a illustrates the comparison of the hourly monthly time series for WRF-GHG simulated atmospheric mixing ratios (WWP-ERA–blue), STILT simulated atmospheric CH<sub>4</sub> mixing ratios (STILT-ERA–green), and TT34 tower observations (black). Noticeable is the difference in the mean bias between the WWP-ERA simulation and TT34 tower observations (-3.58 ppb) and the STILT-ERA simulation to TT34 tower observations (-28.04 ppb). Considering the mean background contribution of the both simulations, a difference of 25.8 ppb is calculated. Correcting the STILT-ERA CH<sub>4</sub> atmospheric background mixing ratio for 25.8 ppb yields an overall total bias of -2.24 ppb. This indicates that the choice of the atmospheric background mixing ratio (here TM3 vs. TM5 global atmospheric mixing ratio distribution) can have an important impact on the simulated atmospheric mixing ratio distribution of the regional atmospheric transport model.

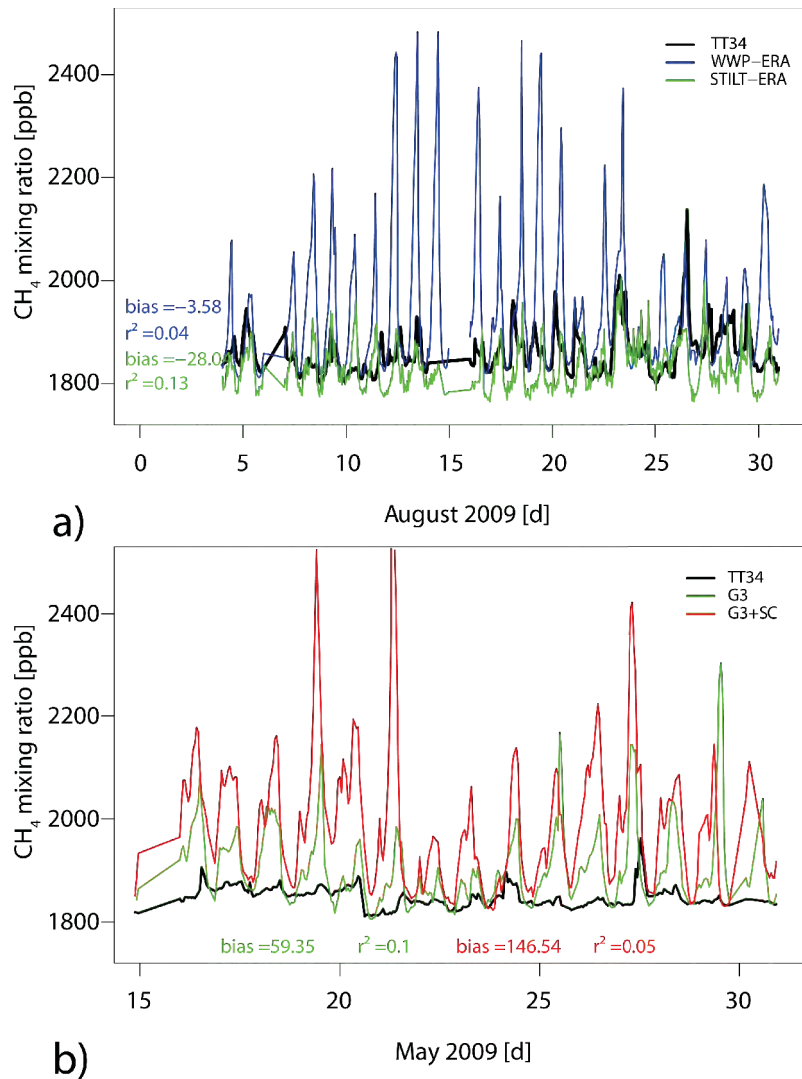


Figure 7.3: (a) Comparison of simulated CH<sub>4</sub> atmospheric mixing ratio of the WRF-GHG model (blue) and the STILT model (green) to TT34 tower observations (black) for August 2009. For both simulations identical CH<sub>4</sub> flux fields based on ERA-Interim meteorology, Walter wetland model, and Prigent wetland inundation map are used. (b) Comparison of two WRF-GHG simulations with two different convective schemes (G3–green and G3+SC–red) to TT34 observations (black) for May 2009. Due to lack of observations only the period of 15<sup>th</sup>–31<sup>st</sup> May 2009 is shown. The CH<sub>4</sub> wetland fluxes are calculated as combination of the Walter wetland model and the JERS-1SAR wetland inundation map.

Correcting for the atmospheric background mixing ratio in the STILT-ERA simulations does not yet lead to a reasonable match of the WWP-ERA and the STILT-ERA simulated atmospheric mixing ratio as it was found for simulations carried out in Europe (cf. Pillai et al. [2012]). Fig. 7.3b illustrates the comparison of two different WRF-GHG simulations to TT34 observations (black) in May 2009 using the G3 (green) and G3+SC (red) meteorological set up as described in Sec. 6.2.1. G3 was utilized for the WWP-ERA simulations in Fig. 7.3a. Due to a lack in observations the

comparison is only carried out for the second half of May 2009. The simulations were performed with the WWJ set up using the Walter wetland model and the JERS-1SAR wetland inundation map. It demonstrates that the differences between simulations using the same atmospheric transport model but different convective parametrization can be larger than the differences between two different atmospheric transport models using the same meteorological forcing fields. It shows that another convective parametrization can lead to even worse results compared to the default G3 meteorological set up when comparing to TT34 tower observations. This underlines the importance of the proper representation of the convective transport in atmospheric transport models when comparing to tower observations in tropical regions.

In addition, differences in PBL height that affect the vertical transport of the tracer distribution [Gerbig et al., 2009] were found for the STILT-ERA and the WWP-ERA simulations. The WRF-GHG simulations using the MYNN PBL scheme (cf. Sec. 6.1) show very low PBL heights ( $<10$  m) at the TT34 tower location during the night. Compared to the observed PBL heights for 200 m by Nobre et al. [1996] over tropical forest, the PBL heights from the WRF-GHG simulation seem unrealistic low during the night. The very low PBL heights in the model lead to an accumulation of the  $\text{CH}_4$  in the first model layer that results in the high  $\text{CH}_4$  atmospheric mixing ratio peaks in the WRF-GHG simulation at the TT34 tower location (cf. Fig. 7.3a). This effect was already reported by Kretschmer et al. [2012] for the comparison of WRF-VPRM simulations using the MYJ PBL scheme to observations from surface stations in Europe. The STILT model has higher minimum values for the PBL during the night ( $\sim 50$ – $70$  m) that prohibits the model from a strong accumulation of  $\text{CH}_4$  close to the ground during night times and results in lower  $\text{CH}_4$  atmospheric mixing ratios. The difference in the maximum of the PBL height, which is presumably achieved during afternoon hours and from which the TT34 tower observations are taken as constraint for the inversion system is significant. The maximum ranges from 1000 to 2000 m for WRF-Chem simulations. The PBL height in STILT is on average considerably higher (2700–4500 m) leading to lower simulated atmospheric  $\text{CH}_4$  mixing ratios at the TT34 tower. The maximum value of the PBL height from the WRF-Chem model is closer to the PBL height of 1250 m observed by Nobre et al. [1996] over tropical forest in the afternoon hours. A further difference beside the  $\text{CH}_4$  background mixing ratio, meteorological forcing, convective parametrization, and PBL height could lie in differences in the representation of the advection in both models as mentioned by Pillai et al. [2012].

This comparison points out that the choice of the atmospheric transport model in inversion systems can decide about upscaling or downscaling of a-posteriori flux distributions. It gives an explanation why  $\text{CH}_4$  wetland fluxes with simulations of the WRF-GHG model have to be scaled down and on the other hand TM5-based inversions suggest an upscaling of the  $\text{CH}_4$  wetland fluxes when using identical  $\text{CH}_4$  wetland models [Bergamaschi et al., 2007].

### 7.1.3 Conducted regional inversions

The regional inversion is performed for the complete year 2009. For the land  $\text{CH}_4$  fluxes, inversions with two different a-priori wetland fluxes are carried out. One using the combination of the Walter wetland model and the Prigent wetland inundation map (called “WP” from hereon) and one using the Walter wetland model and the JERS-1SAR wetland map (“WJ”). An inversion with a constant  $\text{CH}_4$  land flux for all land grid cells (called “FLAT” from hereon) is conducted. This inversion gives information on how the spatial distribution of the  $\text{CH}_4$  land flux is seen by the



TT34 tower observations. As average flux strength the mean of the land flux from the WP a-priori flux distribution was utilized resulting in a constant  $\text{CH}_4$  flux of  $13 \text{ mg m}^{-2}\text{d}^{-1}$ .

Three regional inversions for each land flux type (WP, WJ, and FLAT) were conducted with different temporal  $G_{tcor}$  and spatial correlation length  $G_{xycor}$ . These correlation lengths are a measure of the correlation of the a-priori flux uncertainty within a certain time interval and spatially distributed region (cf. Sec. 3.4). The spatial correlation length was shortened both by a factor 4 and 20 compared to the standard set up. The temporal correlation length was reduced by a factor 4. Table 7.1 illustrates an overview over the conducted regional inversions and the corresponding temporal and spatial correlation lengths.

The weighting of the a-priori flux for the optimization of the cost function (cf. Eq. (3.32)) is described through the factor  $\mu$ . Forward simulations with the optimized a-posteriori fluxes for values of  $\mu = 0.06, 0.25, 1.0, 4.0,$  and  $16.0$  were carried out for the a-priori distributions of WP, WJ, and FLAT.

## 7.2 Results and discussion

The different set ups are compared to TT34 tower observations in order to determine the best regional inversion set up. For validation of the TM3-STILT regional inversion, the Santarém airborne profiles and the BARCA-B flask observations are utilized. Yearly and monthly  $\text{CH}_4$  budget estimates for the Amazon basin are presented with their corresponding uncertainty brackets.

### 7.2.1 TT34 observations

Fig. 7.4a demonstrates the daily averages of the TT34 observations for the year 2009. Data gaps in the first quarter of 2009 result from instrument failure. The mean monthly  $\text{CH}_4$  atmospheric mixing ratios at TT34 are continuously increasing from January to August 2009 (1827 ppb to 1857 ppb). Only July 2009 does not follow the trend (1843 ppb). The two months August and September show the highest  $\text{CH}_4$  atmospheric mixing ratios (1857 ppb and 1859 ppb, respectively). The lowest  $\text{CH}_4$  atmospheric mixing ratios are observed in November and December 2009 (1813 ppb and 1824 ppb, respectively). The observed seasonal cycle is well in accordance with the description of Devol et al. [1990]. With the beginning of the wet season in December or January, the wetlands are flooded, anoxic conditions can establish, and  $\text{CH}_4$  production starts. This explains the increase of the  $\text{CH}_4$  atmospheric mixing ratios from January to August. The high  $\text{CH}_4$  atmospheric mixing ratios in August, September, and October are traced back to the enhanced  $\text{CH}_4$  wetland emissions from falling water table during the dry season from August to December 2009 as altimetry data from satellite observations demonstrate ([http://www.legos.obs-mip.fr/soa/hydrologie/hydroweb/StationsVirtuelles/Amazon\\_Amazon\\_Env\\_tablo3.html](http://www.legos.obs-mip.fr/soa/hydrologie/hydroweb/StationsVirtuelles/Amazon_Amazon_Env_tablo3.html)).

In Fig. 7.4b the stationary vertical profiles located close to the city of Santarém ( $-54.9^\circ\text{W}, -2.5^\circ\text{S}$ ) are shown. The flights were conducted by NOAA-ESRL and the flasks analyzed in the gas lab of the Instituto de Pesquisas Energeticas Nucleares (IPEN), Pinheiros, Brazil. Except for July, one to two profiles per months binned into 500 m vertical intervals are illustrated. The profiles show high  $\text{CH}_4$  atmospheric mixing ratios in the PBL ( $<1250 \text{ m}$ ) for the months August, September, and October (1857–1870 ppb). This is in accordance with the high  $\text{CH}_4$  atmospheric mixing ratios observed at the TT34 tower. The observed  $\text{CH}_4$  atmospheric mixing ratios in the FT



Name	Acronym	Temporal correlation	Temporal correlation length	Spatial correlation	Spatial correlation length
PRIGENT_STANDARD	WP-Std	Standard	One month	Standard	~640 km
PRIGENT_FAST4x_SHORT4x	WP-F4-S4	FAST4x	One week	SHORT4x	~160 km
PRIGENT_FAST4x_SHORT20x	WP-F4-S20	FAST4x	One week	SHORT20x	~32 km
JERS_STANDARD	WJ-Std	Standard	One month	Standard	~640 km
JERS_FAST4x_SHORT4x	WJ-F4-S4	FAST4x	One week	SHORT4x	~160 km
JERS_FAST4x_SHORT20x	WJ-F4-S20	FAST4x	One week	SHORT20x	~32 km
FLAT_STANDARD	FLAT-Std	Standard	One month	Standard	~640 km
FLAT_FAST4x_SHORT4x	FLAT-F4-S4	FAST4x	One week	SHORT4x	~160 km
FLAT_FAST4x_SHORT20x	FLAT-F4-S20	FAST4x	One week	SHORT20x	~32 km

Table 7.1: Characteristics of the different regional TM3-STILT inversions. Different a-priori  $CH_4$  wetland fluxes, temporal, and spatial correlation lengths are denoted.

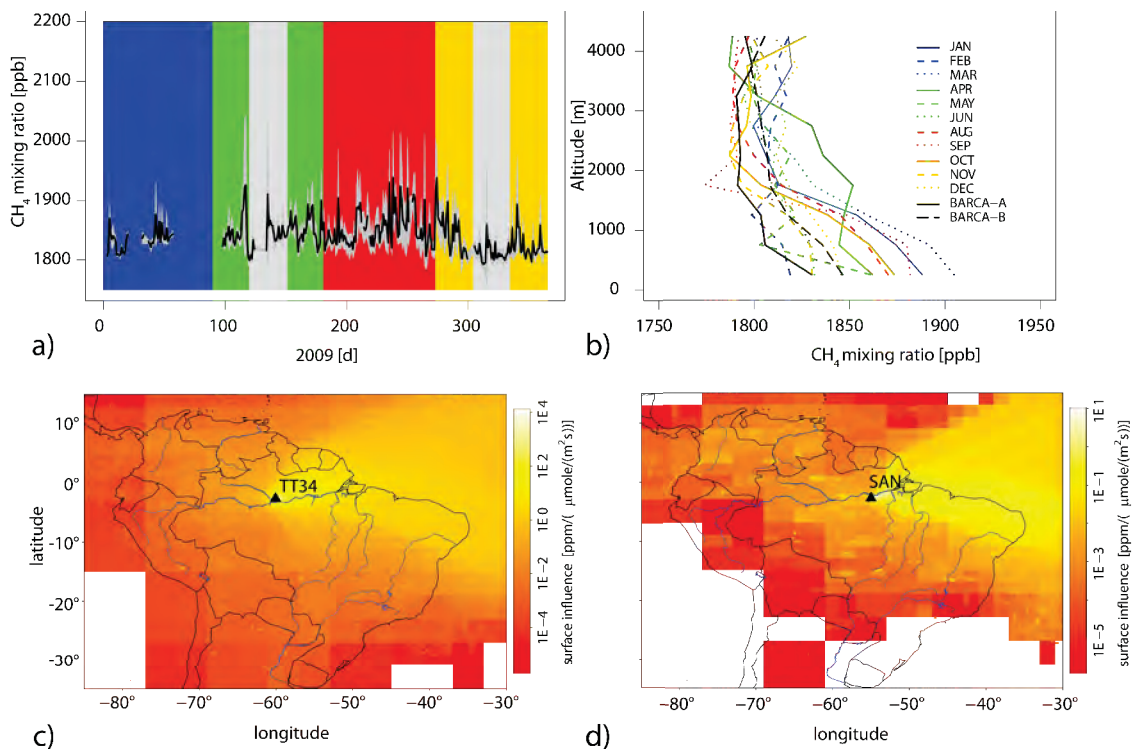


Figure 7.4: (a) Daily averaged TT34 CH<sub>4</sub> observations for 2009 (black line). The gray shaded area around the TT34 observations illustrate the 1-sigma standard deviation of the daily averages. The different colors indicate the different seasons (blue: JAN, FEB, MAR; green: APR, MAY, JUN; red: JUL, AUG, SEP; yellow: OCT, NOV, DEC). The seasons of the two BARCA campaigns in May and November are marked as light gray area. (b) Monthly stationary vertical airborne CH<sub>4</sub> profiles over Santarém as described in Miller et al. [2007] and the total averaged aircraft profiles from the two BARCA campaigns. (c) total yearly integrated footprint of the TT34 tower in 2009. (d) total integrated footprint of the stationary airborne observations at Santarém. Note that the color scale for (c) and (d) is logarithmic.

for May 2009 and November 2008 are very close to the values from the averaged vertical profile of the two BARCA campaigns (difference in the FT vertical profile < 1 ppb). This indicates that the observed CH<sub>4</sub> atmospheric mixing ratios in the FT from both aircraft observations show a consistent seasonality.

Fig. 7.4c–d illustrate the yearly integrated footprints (a measure for the upstream surface sensitivity cf. Sec. 3.3.3) calculated from the STILT model. Monthly integrated footprints of the TT34 tower are found in Fig. A.20 and Fig. A.21. In (d) the longitude, latitude, and height information of the provided data set of the Santarém data (SAN) was utilized for the footprint calculation. Both footprints demonstrate that the upstream influence area is located towards the east. Footprint analysis indicates that 50% of the upstream influence of the TT34 tower is located in the first ~550 km east of the TT34 tower. It is comparable with the size of a tower footprint of 10<sup>6</sup> km<sup>2</sup> as estimated by Gloor et al. [2001a]. The footprint influence area was determined by a cross-section of the integrated footprint at -2.5°S in Fig. 7.4c.

### 7.2.2 Global TM3 inversion

In Fig. 7.5 the comparison of global atmospheric CH<sub>4</sub> inversions to TT34 observations for the year 2009 is demonstrated. Fig. 7.5a illustrates the comparison of the above described TM3 Jena inversion (TM3–violet) and the TM5-based global atmospheric CH<sub>4</sub> inversions from Bergamaschi et al. [2010] (TM5-PB–blue continuous line: constraints only from NOAA surface stations; TM5-PB-SCI blue dashed line: additional constraints from SCIAMACHY observations). Daily averaged CH<sub>4</sub> atmospheric mixing ratios are utilized for this comparison. All three global models are not able to explain the variability of the TT34 observations properly. The differences in the global inversions are larger when considering the bias between observations and model simulations. The TM5-based inversion from Bergamaschi et al. [2010] using only observations from NOAA surface stations as constraint (TM5-PB) has a bias of 0.4 ppb, while the inversion additionally using SCIAMACHY observations (TM5-PB-SCI) has a bias of 4.8 ppb compared to TT34 tower observations. The bias of the TM3-based global inversion is by far higher (54.5 ppb). Using the same a-priori fluxes, three main reasons are identified for the difference between the TM3 and the TM5-based inversions: (1) the more advanced inversion algorithm used by Bergamaschi et al. [2010]; (2) differences in the choice of meteorological forcing fields, ECMWF for TM5 and NCEP for TM3; (3) the different horizontal resolution ( $\sim 4^\circ \times 5^\circ$  for TM3 vs.  $6^\circ \times 4^\circ$  for TM5) does have a significant impact on the simulated atmospheric CH<sub>4</sub> mixing ratios for TT34. Through the different horizontal resolution, the spatial distribution of the maxima of the CH<sub>4</sub> a-priori flux distribution slightly changes. The TT34 grid cell of the TM5 a-priori CH<sub>4</sub> flux distribution is surrounded by grid cells with significant higher CH<sub>4</sub> flux distribution. In the TM3 a-priori flux distribution, it is more equally distributed. Hence the TM3 a-priori flux distribution at the TT34 tower grid cell is on average more than three times higher (yearly 2009 average:  $21.6 \text{ mg m}^{-2} \text{ d}^{-1}$ ) compared to the TM5 a-priori flux distribution ( $6.2 \text{ mg m}^{-2} \text{ d}^{-1}$ ).

Both the TM5 and the TM3 based global CH<sub>4</sub> inversion contain their maximum simulated CH<sub>4</sub> atmospheric mixing ratios in January to March. The minimum is obtained in August and September (TM5) or October (TM3). The temporal distribution of the minima and maxima coincides with a corresponding a-priori flux distribution. This is contradictory to the seasonal cycle of the TT34 tower observations.

Fig. 7.5b illustrates the comparison of a-priori simulated atmospheric mixing ratios with the TM3 model (turquoise–TM3-P), to optimized a-posteriori fluxes as described above (violet–TM3), and to the TM3 global CH<sub>4</sub> inversion using 18 UTC TT34 tower observations as additional constraint (gold–TM3-TT34). The difference between the TM3 simulation using a-priori CH<sub>4</sub> fluxes (TM3-P) and the optimized fluxes (TM3) is small ( $r^2 = 0$  for both simulations; bias = 43.3 ppb for TM3-P and bias = 54.5 ppb for TM3). This is explained by the lack of observational constraints from surface stations on the South American continent in the tropics (cf. Fig. A.19) and different inversion algorithms of TM3 compared to TM5-PB and TM5-PB-SCI. TM5-PB and TM5-PB-SCI, e.g. remove observations with a bias larger than three sigma (standard deviation of the model-observation atmospheric mixing ratio mismatch) in an additional iteration of the inversion system from the observational constraint. Using observations within the Amazon basin (TM3-TT34) clearly shows the impact on the simulated CH<sub>4</sub> atmospheric mixing ratios at the TT34 tower (bias 1.3 ppb). The explained variability is still low ( $r^2 = 0.16$ ). This might originate from the difficulties in representing the atmospheric transport in tropical regions (cf. Sec. 6.2.3). Not properly represented subgrid scale variability of global atmospheric transport models is a further

possible reason [Pillai et al., 2010].

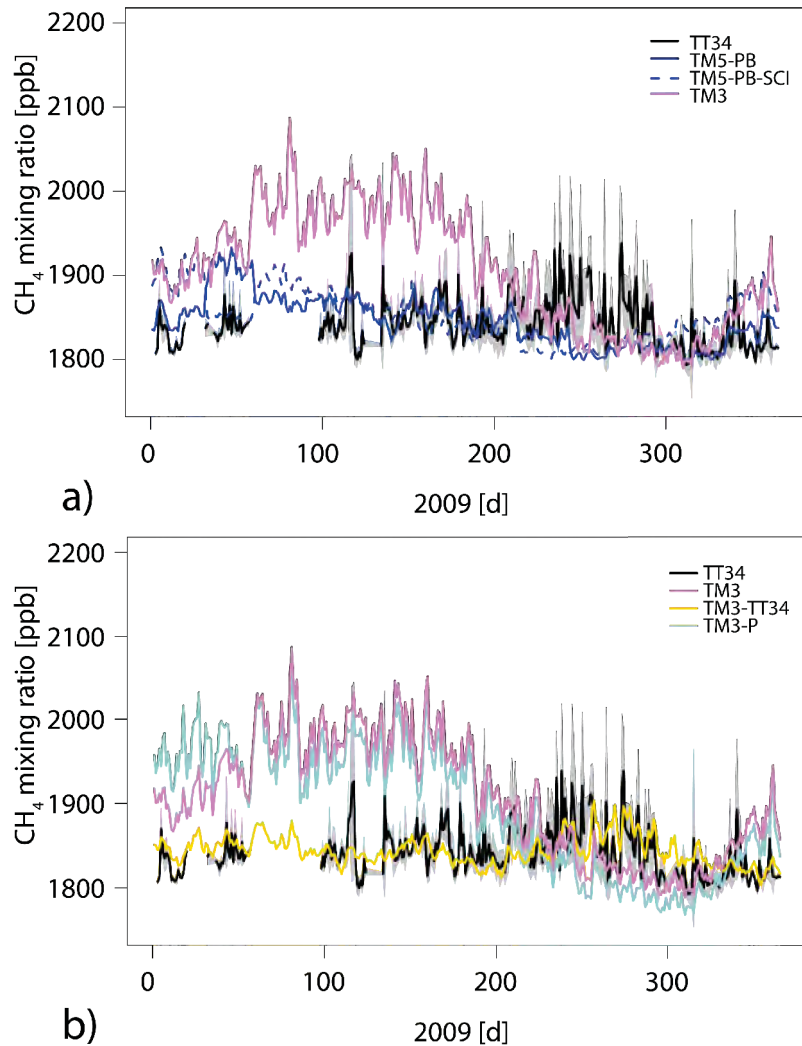


Figure 7.5: (a) Comparison of daily averages of TM5 (blue; cf. Ch. 5) and TM3 (violet) based global  $\text{CH}_4$  inversions to TT34 observations for 2009. The gray shaded area denotes the 1-sigma standard deviation of the daily averages from the TT34 tower observations. (b) illustrates the comparison of TM3 simulations using a-priori fluxes (TM3-P–light green), a-posteriori fluxes (TM3–violet), and a-posteriori fluxes that were constrained by TT34 observations (TM3-TT34–yellow).

### 7.2.3 Regional TM3-STILT inversion

#### Comparison to TT34 observations

In Fig. 7.6a the comparison of TT34 observations to simulations of the different TM3-STILT regional inversions described in Table 7.1 is summarized in a Taylor diagram. The simulated  $\text{CH}_4$  atmospheric mixing ratios from the three different a-priori fluxes (WP–dark violet, WJ–red, and FLAT–orange) have a significantly higher standard deviation (except for the a-priori flux of the

FLAT inversion) compared to the CH<sub>4</sub> atmospheric mixing ratios obtained from simulations using the a-posteriori flux distribution. The mean bias is reduced from -30 ppb for the WP inversions using the a-priori fluxes to 10 ppb for the WP a-posteriori fluxes. The reduction is even stronger for the WJ a-priori and a-posteriori fluxes (bias = -49 ppb compared to 4 ppb). For the FLAT prior inversion, the bias between simulations using a-priori and a-posteriori fluxes does not change much (both  $\sim 18$  ppb). This is mainly due to the fact that the simulations of WP and WJ with their a-priori fluxes partially show very high CH<sub>4</sub> atmospheric mixing ratios of  $>2100$  ppb (cf. Fig. 7.7a–b). This is removed by the TM3-STILT inversion mechanism and does not occur for the a-posteriori flux fields. For the FLAT prior inversion, these spikes are not notable in the simulated CH<sub>4</sub> atmospheric mixing ratios using the FLAT a-priori flux distribution. This explains the very small reduction in the bias of the simulation using the a-posteriori flux distribution of the FLAT inversion. The correlation coefficient  $r$  increases slightly for the FLAT inversion when using shorter temporal and spatial correlation lengths ( $r = 0.19$  for a-priori simulation to  $r = 0.28$  for FLAT-F4-S4). This effect is stronger for inversions with WP and WJ a-priori flux distributions.  $r$  increases for WP-based inversions from 0.04 (WP a-priori simulation) to 0.28 (WP-F4-S20). It is similar for the WJ a-priori flux distribution ( $r = 0.09$ – $0.27$ ). Through the short temporal and spatial correlation length, the number of degrees of freedom of the inversion to fit the observations increases. This allows a better fit to the observations.

The simulation of atmospheric mixing ratios using both, a-priori and a-posteriori flux distribution and different temporal and spatial correlation length are compared to independent stationary airborne profiles close to Santarém (cf. Fig. A.22). The comparison yields that the regional inversion set up with one week temporal and  $\sim 160$  km spatial correlation length (FAST4x\_SHORT4x) is the most suitable. An inversion with a higher spatial correlation length (FAST20x) does not improve results in the comparison to airborne observations compared to the FAST4x\_SHORT4x set up (Fig. A.23). This set up is used as standard set up in the following if not noted differently. When using the acronyms WP, WJ, and FLAT in the following, regional inversions with the WP, WJ, and FLAT a-priori flux distributions are conducted, if not stated differently.

Another option to improve the correlation and reduce the standard deviation of the bias between the TT34 tower observations and the simulated CH<sub>4</sub> atmospheric mixing ratios is the variation of the impact of the a-priori flux distribution on the fit to the observations by the factor  $\mu$  (cf. Sec. 3.4). A value of  $\mu = 1$  implies that the a-priori distribution has an uncertainty of one sigma normalized by the sigma target of  $0.316 \text{ Tmol a}^{-1}$ . For a factor of  $\mu = 0.25$ , the a-priori uncertainty is multiplied by a factor of 2. The relation between the standard deviation of the a-priori flux field  $\sigma_f$  and the factor  $\mu$  is described as  $\sigma_f = \frac{1}{\sqrt{\mu}}$ . Fig. 7.6b illustrates the Taylor plot of the WP-F4-S4 (dark violet), WJ-F4-S4 (red), and FLAT-F4-S4 (orange) inversions using different values of  $\mu$ . The highest correlation with the observations in all cases is obtained for  $\mu = 0.06$  ( $r = 0.38$ – $0.39$ ).

In summary, the optimized regional inversion set up is obtained by shorting the temporal and spatial correlation length to one week and  $\sim 160$  km, respectively and given the a-priori flux distribution less weight ( $\mu = 0.06$ ).

Fig. 7.7a–c demonstrates the comparison of TT34 observed CH<sub>4</sub> atmospheric mixing ratios and simulated CH<sub>4</sub> atmospheric mixing ratios for inversions with the three different a-priori flux distributions. Simulations with the a-priori flux distributions are denoted with WP-P (a), WJ-P (b), FLAT-P (c). The simulations using the optimized a-posteriori flux fields are noted in accordance to the optimized regional inversion set up as WP-F4-S4 (a), WJ-F4-S4 (b), and FLAT-F4-S4 (c). All inversions were conducted with the above described optimized set up. As already described

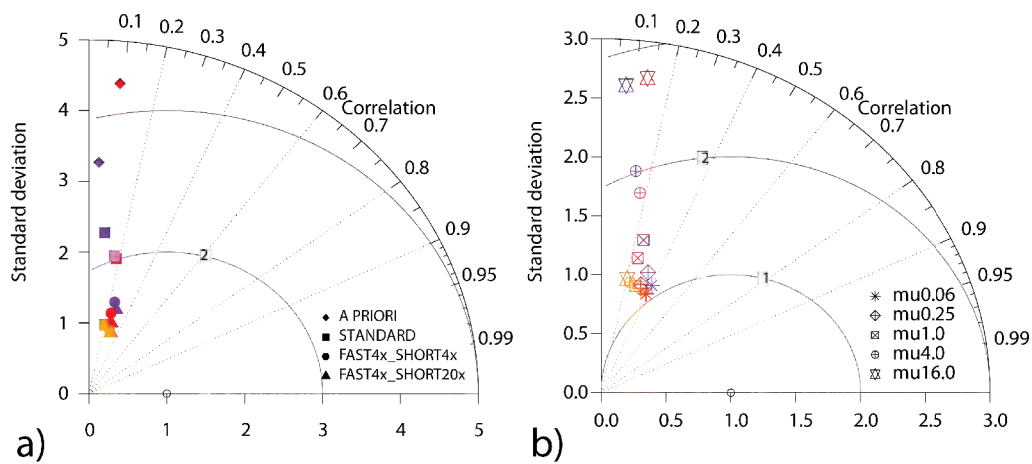


Figure 7.6: (a) Taylor plot illustrating the results of TM3-STILT forward simulations (atmospheric  $\text{CH}_4$  mixing ratios of simulations using the a-posteriori flux distribution) with TT34 observations using different temporal and spatial correlation length. The choice of the a-priori flux is indicated by different colors (dark violet–WP; red–WJ; orange–FLAT). The result of the global TM3 inversion is indicated in violet. For all results  $\mu = 1.0$  was used. (b) demonstrates the results for the three regional inversions with different a-priori fluxes using the FAST4x\_SHORT4x set up when changing the weight of the a-priori flux for minimization of the cost function (colors are the same as in (a)).

above, the bias is significantly reduced for the simulations with the a-posteriori distribution of WP and WJ. In all three cases the explained variability of the observations increases from  $r^2 = 0.0$ – $0.007$  to  $r^2 = 0.24$ – $0.26$ . Considering the representation of the seasonal cycle in the simulated  $\text{CH}_4$  atmospheric mixing ratio, differences between simulations using the a-priori and the a-posteriori flux distributions occur for all three inversions. The simulations with the a-priori flux distributions show the maximum of the simulated  $\text{CH}_4$  atmospheric mixing ratios in October and November 2009. The minimum occurs during June and August, similar to the results of the TM5-based  $\text{CH}_4$  global atmospheric inversions (cf. Sec. 7.2.2). This is in contrast to the TT34 observations.

The seasonality of the TT34 tower observations is represented better by the simulations using the optimized a-posteriori flux distribution. In all three simulations the monthly mean minimum  $\text{CH}_4$  atmospheric mixing ratio is found in November. The maximum of the simulated  $\text{CH}_4$  atmospheric mixing ratio is shifted to April to June for the simulations with the a-posteriori flux distributions. It can be stated that the inversion system is capable in reproducing the temporal correct minimum of the  $\text{CH}_4$  observed atmospheric mixing ratios at TT34. The maximum is shifted to April to June. It is an improvement compared to the a-priori simulations that predict the maximum at the times when the minimum should occur.

### A-posteriori flux distribution

The resulting a-posteriori fluxes are constrained by TT34 observations for the year 2009. Fig. 7.8 illustrates the mean a-priori (1) and a-posteriori (2)  $\text{CH}_4$  flux distribution for May 2009. The different a-priori fluxes (a–WP, b–WJ, and c–FLAT) are demonstrated. In the third column, the difference between the a-priori and a-posteriori flux distribution of the corresponding a-priori fluxes



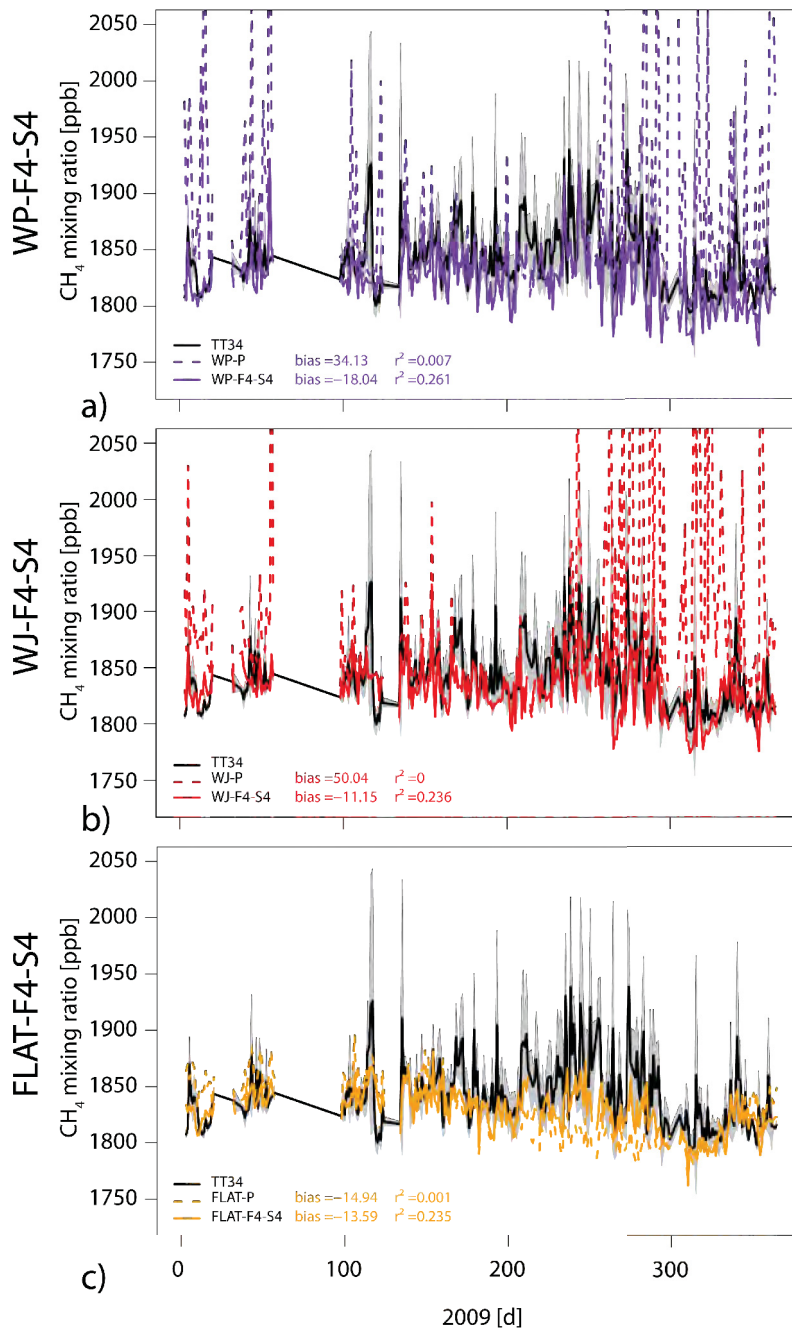


Figure 7.7: (a) Illustration of the daily averaged time series of  $\text{CH}_4$  atmospheric mixing ratios of TT34 tower observations (black line) and a-priori (dashed dark violet line) and a-posteriori (continuous dark violet line) flux simulations with STILT using the WP a-priori flux distribution for 2009. (b) Same comparison with the inversion using the WJ a-priori flux distribution. (c) Comparison of the TT34 tower observations to inversion results with the FLAT a-priori flux distribution.  $\mu = 0.06$  was utilized in all three cases and the gray shaded area denotes the 1-sigma standard deviation of the daily averaged TT34 tower observations.

is shown. The distribution of the a-priori–a-posteriori difference for WP-F4-S4 (a3) and WJ-F4-S4 (b3) draws a very similar picture. The a-posteriori flux in the surroundings of the TT34 tower and further downstream of the Amazon mainstream river close to the city of Santarém was decreased by the inversion system. An increase in the a-posteriori  $\text{CH}_4$  flux further to the Atlantic coast is notable. The a-priori–a-posteriori difference of the FLAT-F4-S4 inversions has a different structure. Only in the northern and north-western surroundings of the TT34 tower the a-posteriori flux is decreased by the regional inversion. It is almost doubled east of the TT34 tower. The increase in  $\text{CH}_4$  emissions in the a-posteriori flux is explained by the low constant flux of  $13 \text{ mg m}^{-2} \text{ d}^{-1}$  throughout the whole domain compared to  $\text{CH}_4$  fluxes  $>200 \text{ mg m}^{-2} \text{ d}^{-1}$  in the surroundings of the TT34 tower of the WP and WJ a-priori flux distributions. The area in which the a-posteriori flux is increased coincides well with the main influence area of the calculated footprint of the TT34 tower for the month May 2009 (cf. Fig. A.20).

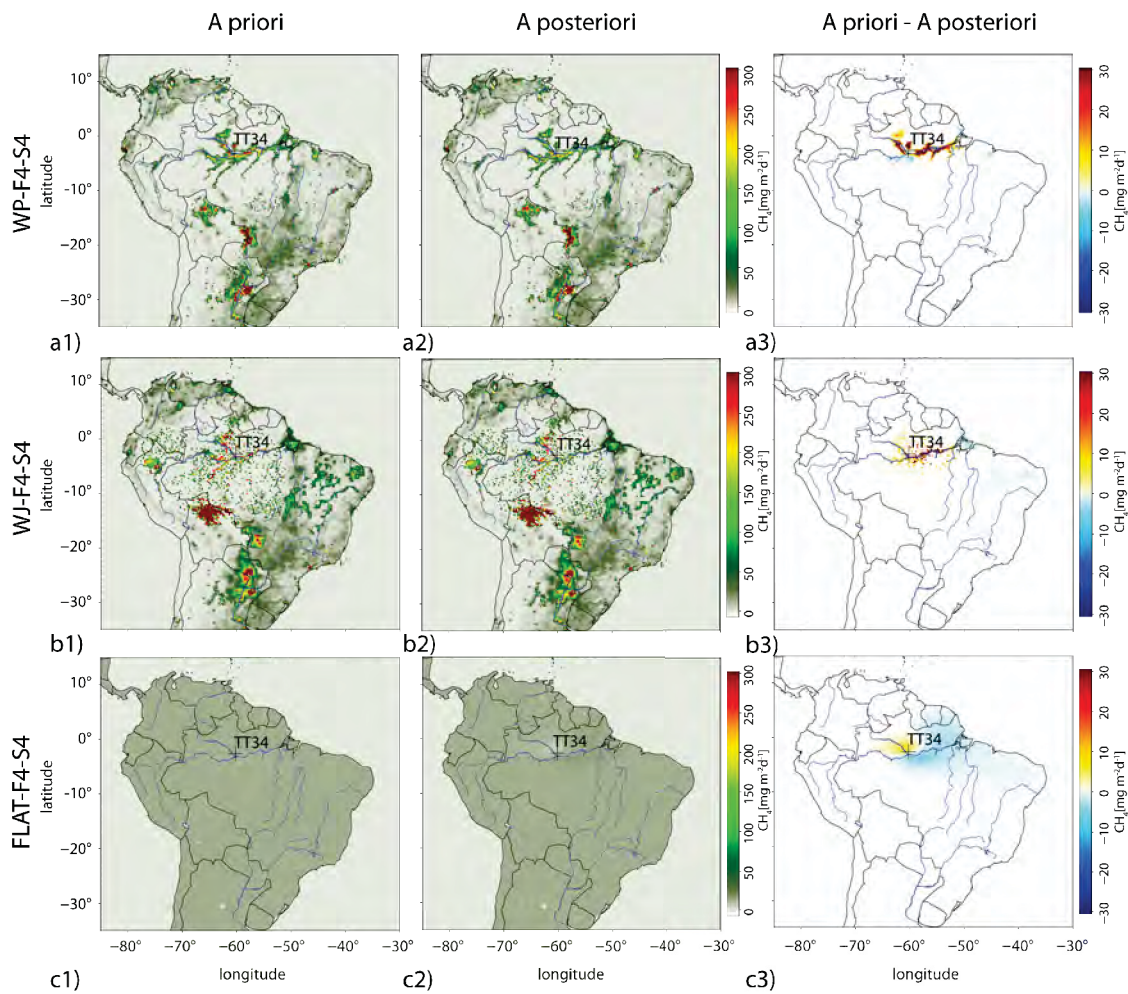


Figure 7.8: (a1–a3) a-priori (a1), a-posteriori (a2), and difference between a-priori and a-posteriori flux distribution (a3) using the inversion with the WP a-priori flux distribution for May 2009. (b1–b3) illustrates the same flux distributions for the inversion with the WJ a-priori flux distribution. In (c1–c3) the fluxes of the inversion using the FLAT a-priori flux distribution are illustrated.

Considering the impact of the TT34 observations on the a-posteriori flux distribution throughout the complete year 2009, a similar picture as discussed above for May 2009 is notable for the months January to May 2009 and November to December 2009 (Fig. A.26 and Fig. A.27). The a-posteriori flux in the surroundings of the TT34 tower and until 1000 km east of the TT34 tower is decreased and the CH<sub>4</sub> a-posteriori flux further east is slightly increased. This obtained structure with smaller CH<sub>4</sub> emissions in the Amazon mainstream area between Manaus and Santarém as estimated by the regional inversion system is similar to the obtained a-posteriori flux distribution of the TM5-based global CH<sub>4</sub> inversions TM5-PB and TM5-PB-SCI (cf. Fig. A.3a1–a2 and b1–b2). The calculated CH<sub>4</sub> fluxes of Miller et al. [2007] of 35 mg m<sup>-2</sup> d<sup>-1</sup> for the Santarém area and the 20 mg m<sup>-2</sup> d<sup>-1</sup> around Manaus support the results from the regional inversion with lower CH<sub>4</sub> fluxes in the Manaus area and higher CH<sub>4</sub> fluxes towards the Amazon delta. In the months June, July, and August 2009 the a-posteriori flux of all three a-priori flux distributions is increased eastwards of the TT34 tower and only reduced in the north and north-western surroundings of the TT34 tower (cf. Fig. A.26 and Fig. A.27). This effect is less intensive during the month September and October. The a-posteriori WP and WJ flux distribution during June–October mirrors how the inversion mechanism tries to account for a proper representation of the seasonal cycle even though the seasonality of the a-priori flux distribution was not correct. The CH<sub>4</sub> flux in the surroundings (~150 km) of the TT34 tower was too high during these months, the CH<sub>4</sub> flux in the influence area east (~600–1000 km and even further east) of the TT34 tower was increased for a proper representation of the seasonal cycle.

### Validation of regional inversion

A method to prove the robustness and proper optimization of the a-posteriori fluxes by the regional inversion system is to assess latitudinal and longitudinal gradients of resulting simulated atmospheric CH<sub>4</sub> mixing ratios against independent aircraft observations. For this purpose, the BARCA-B flask observations (cf. Fig. 5.1) were compared to the simulated CH<sub>4</sub> atmospheric mixing ratios of the a-posteriori and a-priori fluxes of three different regional inversions (Fig. 7.9). Similar to Fig. 5.2, the BARCA-B flasks and the simulated CH<sub>4</sub> atmospheric mixing ratios were plotted as function of latitude and longitude. The evaluation was separately done for the PBL (a,c) and the FT (b,d). Except for the latitudinal gradient of the FT, the direction of the gradient is produced well by simulations with the optimized a-posteriori flux distributions. Compared to the simulations with the a-priori flux distribution an improvement in the representation of the gradient with the a-posteriori flux distribution is notable (converging of the slope from the linear fit to the slope from the linear fit of the observations). The misfit in the latitudinal gradient for the FT is explained by the low simulated CH<sub>4</sub> atmospheric mixing ratios for latitudes > 0°. Free troposphere air masses in this area originate from the north-western part of the South American continent, where no constraint from the TT34 tower observations can be expected. This indicates that the inversion system optimizes the a-posteriori flux distribution in a consistent way with independent aircraft observations. It is concluded from the comparison that the correction of the inversion system on the a-posteriori flux distribution is no artifact of the inversion system.

After the evaluation of the robustness of the inversion system, the results are compared to additional independent airborne profiles from Santarém (cf. Fig. 7.4b). The location of the stationary airborne profiles is denoted as “SAN” in Fig. 7.4d. The monthly observed vertical profiles are illustrated as black line (binned into 500 m vertical intervals) in Fig. 7.10. For comparison to

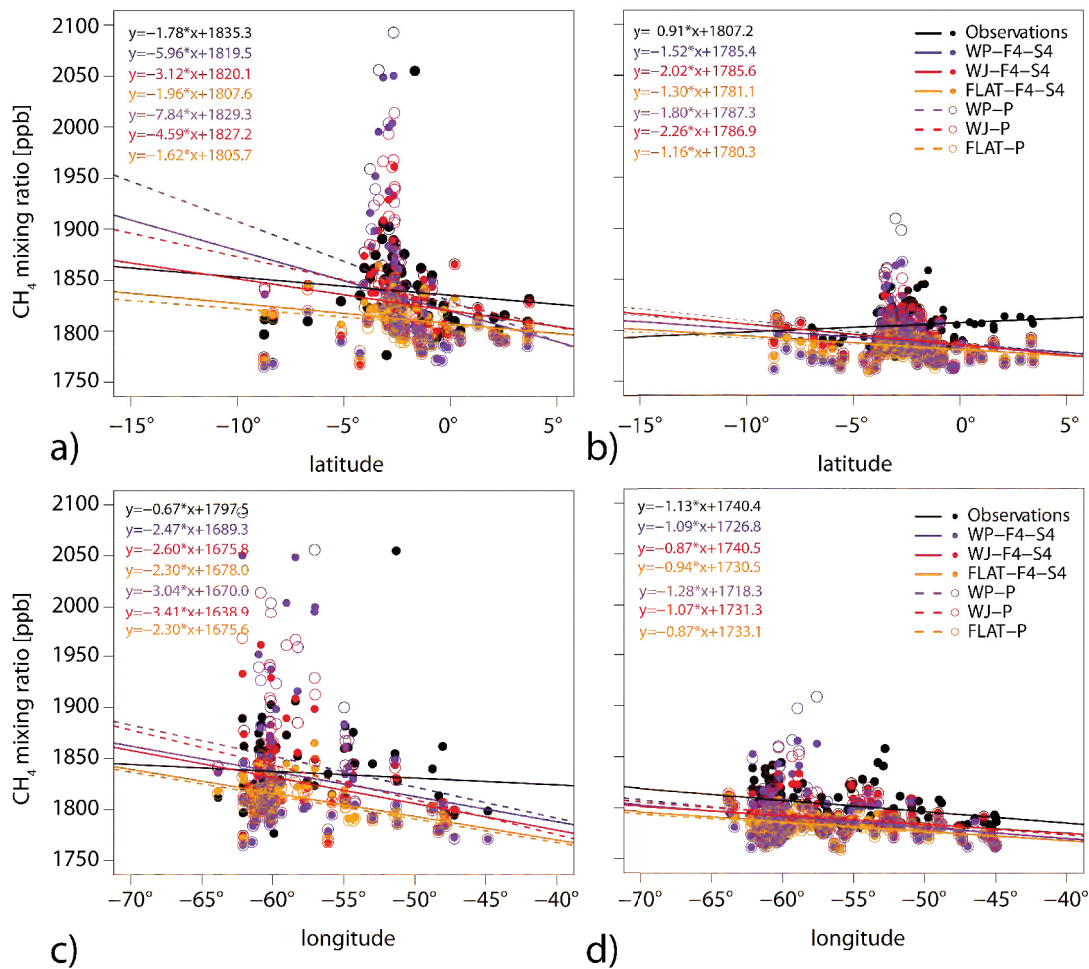


Figure 7.9: Comparison of CH<sub>4</sub> atmospheric mixing ratios from BARCA-B flask observations and STILT simulations with three different a-priori and a-posteriori fluxes for May 2009. In (a), the latitudinal gradient of all flasks in the PBL are illustrated. The latitudinal gradient for the FT flasks is found in (b). (c) and (d) demonstrate the same for the longitudinal gradient of the observed and simulated atmospheric CH<sub>4</sub> mixing ratio. The order of the linear equation of the straight line obtained from the linear regression is identical with the order of the legend in (b) and (d).

simulated STILT CH<sub>4</sub> atmospheric mixing ratios, each flask observation was taken as receptor point for the STILT simulations. The CH<sub>4</sub> atmospheric mixing ratio were calculated from simulations using both, the a-priori and the optimized a-posteriori flux distribution. The observations were compared to simulations with the three different a-priori flux distributions (WP, WJ, FLAT). The resulting simulated CH<sub>4</sub> atmospheric mixing ratios were binned into 500 m vertical intervals similar to the observations.

In the comparison to the Santarém airborne observations the difference in the simulations using a-priori or a-posteriori is rather small (max. 6 ppb difference on the total vertical profile). No difference or very small difference (<1 ppb) in the bias of the vertical profile between a-priori and a-posteriori fluxes is found in the months February to April. This is explained by less or no



availability of TT34 observations during those months (cf. Fig. 7.4a). It affects all three inversions with different a-priori flux distributions in the same manner. Larger differences in the simulations using the a-priori and the a-posteriori flux distribution are found for the months August to November. In those months differences are highest in the PBL and can reach values of 15 ppb. From this evaluation, it is concluded that the impact of the TT34 observations on the optimized a-posteriori fluxes is not very high. This results from the fact that the spatial correlation length was chosen to be  $\sim 160$  km, while the distance between the TT34 tower and the Santarém stationary airborne profiles is  $\sim 600$  km.

Compared to the airborne observations, still a considerable mismatch of simulated and observed atmospheric  $\text{CH}_4$  mixing ratios is found. Two main reasons are possible: Problems in the representation of the atmospheric transport or the representation of the near-field flux distribution. ECMWF operational archive precipitation patterns were compared to TRMM observations for both the 3 h period of the vertical profile measurement and the 48 h upstream footprint area similar to Sec. 6.2.3 to eliminate periods of not good representation of the atmospheric transport in the model. As result only for the months May, August, September, October, and December a proper representation of the atmospheric transport by the model can be assumed. An improvement in the  $r^2$  value for comparisons with a good representation in the atmospheric transport is not found. This leads to the conclusion that the near-field flux distribution (cf. low influence area in the PBL) must be the main reason for the deviation of the simulated to the observed atmospheric  $\text{CH}_4$  mixing ratios.

The simulation observation mismatch with respect to the 48 h footprint and the a-priori and a-posteriori flux distribution was evaluated. According to the analysis of the 48 hr footprint of the Santarém stationary airborne profiles (cf. Fig. A.24 and Fig. A.25) and the two different wetland inundation maps (Prigent and JERS-1SAR), certain characteristics could be identified for the comparison of the simulations to the observations.

In months of low data constraints through instrument failure as, e.g. in March and April 2009, the difference in the simulated atmospheric mixing ratios between simulations with an a-priori and a-posteriori flux distribution is negligible for the location of the Santarém stationary profiles. The lowest bias ( $< 10$  ppb) to the observations is found for months (February and May 2009) in which the main footprint influence area of the Santarém airborne observations is not located over extensive inundated wetland area. The largest deviation between the simulated atmospheric mixing ratios of the two different a-posteriori flux distributions WP and WJ occurs in April and June 2009 (overestimation of the WP simulations and underestimation of WJ simulations compared to the Santarém airborne profiles). The different behavior can be explained by differences in the inundated wetland area east of Santarém between the Prigent and JERS-1SAR wetland inundation map. August and September 2009 draw a relative similar picture. In both month the main influence area is found in the Amazon delta and south of the Amazon mainstream east of Santarém. The inversion system tried to increase the a-posteriori flux distribution in this area (cf. Fig. A.27). The increase originating from the TT34 tower observations was not strong enough. This still leads to a strong underestimation of the observed atmospheric mixing ratio especially in the PBL. The situation is similar for the months October-December. Due to the wrong seasonal cycle in the a-priori flux distribution the bias between simulated and observed atmospheric mixing ratio in the PBL changes from underestimation in October to overestimation of WP and WJ based simulations in December 2009.

From this comparison one can conclude that the regional inversion is capable of constraining the a-posteriori flux in the “right direction”. In the months of the main  $\text{CH}_4$  fluxes (August–September) the constraint of a 35 m tower located  $\sim 600$  km away is not powerful enough. The WP based regional inversion explains the variability of the observations on average better than the WJ based regional inversions. This is consistent with the results found in Ch. 6. The months April and June are an exception. The influence area from the footprint analysis in these two months is located close to the Santarém area. One can suggest that the JERS-1SAR wetland inundation map has advantages in the representation of the inundated wetland area in the direct neighborhood of Santarém. The lowest bias to the airborne profiles is obtained, when the footprint influence area is not located over extensive wetland area. The vertical profiles of the global TM3 inversion do not show improvements compared to the results of the regional inversions.

#### 7.2.4 Budget estimates

From the performed regional inversions as described in Table 7.1, the annual  $\text{CH}_4$  budget was calculated for the Amazon mainstream area and the Amazon lowland region as defined by Melack et al. [2004].

Fig. 7.11a–b illustrates the daily calculated budgets for the Amazon mainstream area (a) and the Amazon lowland region (b). A difference between the a-priori calculated daily  $\text{CH}_4$  budgets (dashed lines) and the calculated budgets of the optimized a-posteriori distribution (continuous line) is notable for the Amazon mainstream area. The largest differences in the daily calculated budget (monthly mean difference) occur for the inversion using the WJ a-priori flux distribution (0.04 Tg), followed by the inversion with the WP a-priori flux distribution (0.02 Tg). The maximum differences for both were found in November 2009. The minimum differences in the monthly mean budget are found in the months June–August, (difference of 0.001 Tg for WP a-priori flux distribution in July and August and 0.0032 Tg for the WJ a-priori flux distribution in July). The differences in the inversion using the FLAT a-priori flux distribution are much smaller. The highest monthly mean difference of 0.006 Tg is found in September 2009, when the optimized a-posteriori flux distribution is higher than the a-priori flux distribution. Considering the daily budget calculation of the Amazon lowland region, no difference between the a-priori and the a-posteriori flux distribution is found. Two effects cause this negligible difference. Most parts of the Amazon lowland area are not located within the main influence area of the TT34 tower, thus no observational constraint on the a-posteriori flux distribution in that regions is obtained. The decrease in the budget originating from the decrease in the Amazon mainstream area is compensated by an increase in the eastern and south-eastern part of the Amazon lowland region.

In Table 7.2 the annual  $\text{CH}_4$  budget of the year 2009 for the Amazon lowland region and the Amazon mainstream area is denoted for the different regional inversion set ups as described in Table 7.1. For the purpose of comparison also the monthly budgets for May 2009 are given. The annual 2009  $\text{CH}_4$  budget of the global  $\text{CH}_4$  inversions described in Sec. 7.2.2 is calculated for both regions. The largest difference in the comparison of the annual  $\text{CH}_4$  budget of the WP and WJ a-priori simulations with the corresponding a-posteriori simulations is found for the standard set up with the largest temporal and spatial correlation length. The shorter the temporal and spatial correlation length, the less effect on the annual budget is notable. For the standard (Std) regional inversion set up it is assumed that the TT34 observations are able to constrain a much larger area than it was obtained from footprint analysis. This results in an unrealistic large change in the



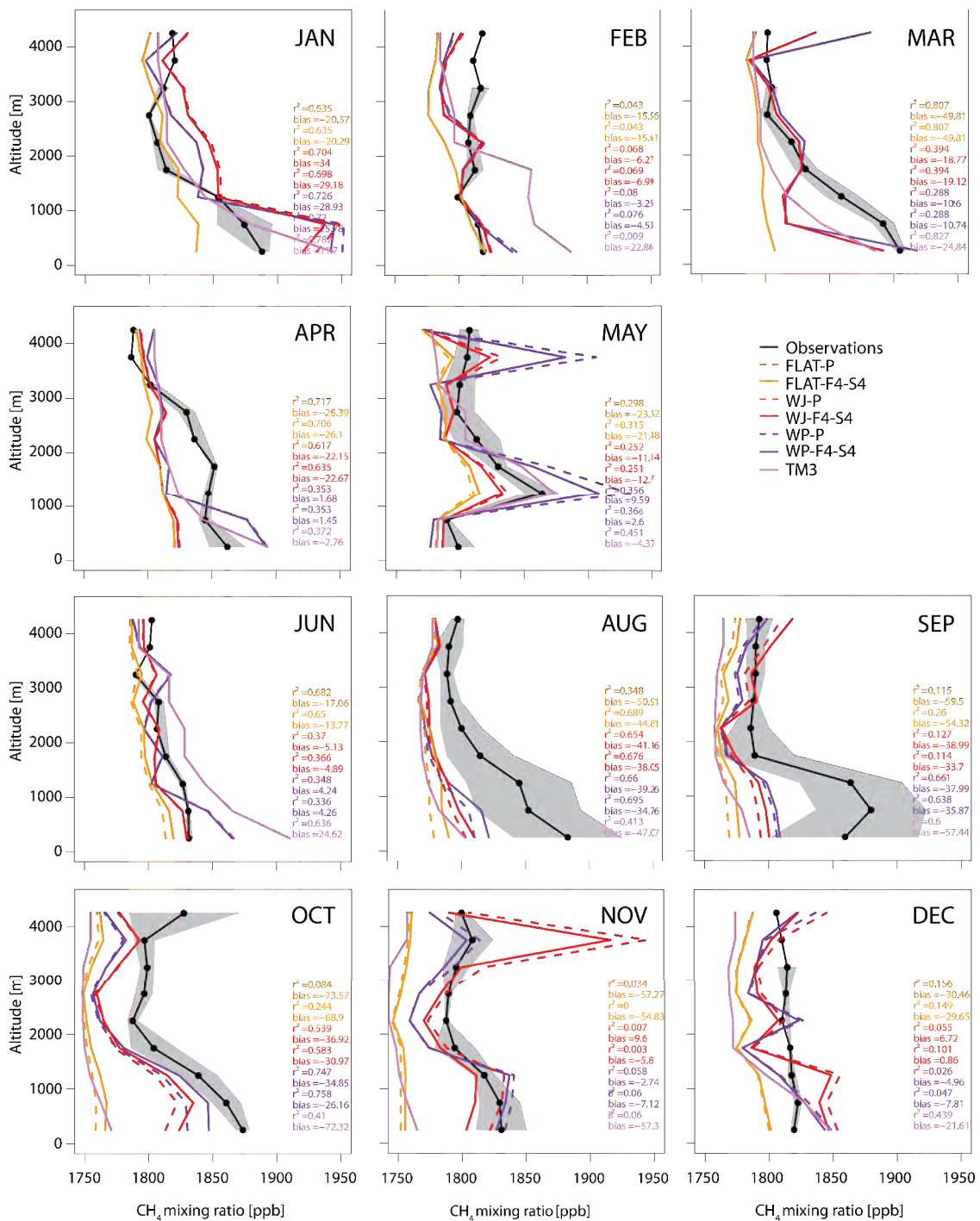


Figure 7.10: Comparison of monthly airborne profiles (black) obtained close to the city of Santarém ( $-54.9^\circ\text{W}$ ,  $-2.5^\circ\text{S}$ ) to simulated  $\text{CH}_4$  atmospheric mixing ratios from the regional TM3-STILT inversion during the year 2009. Simulated  $\text{CH}_4$  mixing ratios using the WP a-priori distribution are depicted in dark violet and those using the WJ a-priori flux distribution in red. The results of the FLAT prior inversion are illustrated in orange. The results of the global TM3 inversion are shown in violet. The simulations using the a-priori flux distribution are shown as dashed lines. The gray-shaded area denotes the 1-sigma standard deviation of the airborne observations. The bias and  $r^2$  values correspond to all observations of the one to two profiles within the corresponding month. The order of bias and  $r^2$  for the different simulations is identical to the order of the legend.

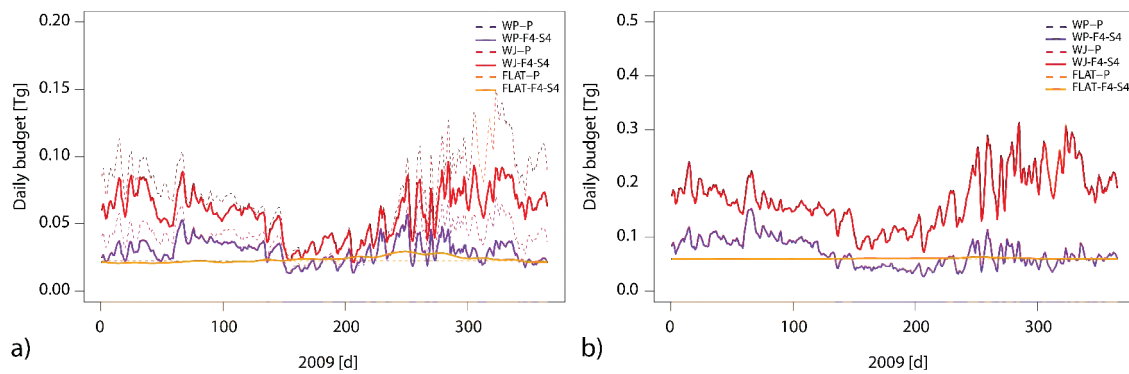


Figure 7.11: (a) Time series of daily budgets for the Amazon mainstream area (cf. yellow rectangle in Fig. 2.10) for a-priori (P) and optimized  $\text{CH}_4$  fluxes from three different a-priori flux distributions (WP, WJ, FLAT) using the FAST4x\_SHORT4x regional inversion set up. (b) Similar time series for the Amazon lowland region as defined in Melack et al. [2004]. The dashed and the continuous lines are identical in this case.

annual  $\text{CH}_4$  budget which is even larger when performing inversions with larger temporal and spatial correlation length.

The differences in the annual  $\text{CH}_4$  budget between the regional inversions using different a-priori fluxes are large. The calculated annual  $\text{CH}_4$  budget of the WJ-F4-S4 regional inversion is more than double the amount compared to the annual budget of the WP-F4-S4 inversion (62.78 Tg vs. 25.74 Tg) for the Amazon lowland region. The situation is somewhat better for the Amazon mainstream area. The annual budget of the WJ-F4-S4 regional inversion (21.30 Tg) is only slightly less than double the amount of the annual budget of the WP-F4-S4 regional inversion (10.87 Tg). This shows that it is not possible to constrain a region from the size of the Amazon lowland region (or the even the Amazon mainstream area) sufficient enough with one single surface observation tower. From the improvement within the Amazon mainstream area, it can be concluded that a higher density of observations will lead to a more robust annual  $\text{CH}_4$  budget estimate independent of the choice of the a-priori flux distribution.

The uncertainties of the annual budget estimate for the Amazon lowland region and the Amazon mainstream area were derived in the following way. Due to the large difference in the budget estimates of the inversions using the WP and WJ a-priori flux distribution, the uncertainty was calculated separately for the WP and WJ a-priori flux distribution. The uncertainty estimate of the a-posteriori flux was calculated as the standard error of the mean annual  $\text{CH}_4$  budget. All conducted regional inversions using the same a-priori flux WP or WJ, different spatial and temporal correlation length, and different weighting of the a-priori flux distribution  $\mu$  were included in the statistical ensemble. The uncertainty is estimated to  $\pm 0.5$  Tg for the WP inversions for the Amazon lowland region and the Amazon mainstream area and  $\pm 0.8$  Tg and  $\pm 0.9$  Tg for the WJ a-priori flux distribution, respectively. The mean annual  $\text{CH}_4$  budget for the Amazon lowland region using the Prigent wetland inundation map is derived to  $24.9 \pm 0.5$  Tg. For the Amazon mainstream area it yields  $12.0 \pm 0.5$  Tg. For the regional inversion using the JERS-1SAR wetland inundation map, the annual  $\text{CH}_4$  budget estimates are calculated to  $61.2 \pm 0.8$  Tg for the Amazon lowland region and  $22.4 \pm 0.9$  Tg for the Amazon mainstream area. This clearly illustrates the impact of the distribution of the wetland inundated area on the calculation of the regional  $\text{CH}_4$  budget.

Inversion set up	Amazon lowland region annual budget [Tg]	Amazon mainstream area annual budget [Tg]	Amazon lowland region May 2009 [Tg]	Amazon mainstream area May 2009 [Tg]
WP-Std	19.56	6.49	1.58	0.70
WP-F4-S4	25.74	10.87	1.92	0.95
WP-F4-S20	25.86	12.47	1.92	1.07
WP-P	25.85	14.32	1.96	1.14
WJ-Std	56.74	13.41	4.12	1.38
WJ-F4-S4	62.78	21.30	4.30	1.58
WJ-F4-S20	63.15	23.59	4.30	1.60
WJ-P	63.17	26.39	4.39	1.71
FLAT-Std	21.98	8.07	1.78	0.64
FLAT-F4-S4	22.06	8.63	1.87	0.71
FLAT-F4-S20	21.96	8.84	1.92	0.72
FLAT-P	21.83	8.17	1.91	0.69
TM3	24.04	8.50	2.51	0.93
TM3-TT34	23.68	6.64	1.81	0.51
TM5-PB	42.12	16.56	2.46	1.09
TM5-PB-SCI	35.26	11.46	1.96	0.84

Table 7.2: Calculated  $CH_4$  budgets for the Amazon lowland region and the Amazon mainstream area for the entire year 2009 and the month May 2009. The different regional inversion set ups and TM3 and TM5-based global  $CH_4$  inversions are denoted. All  $CH_4$  budget estimates from the regional inversion were calculated with  $\mu = 0.06$ . For the global TM3 inversions also  $\mu = 0.06$  was used.

The annual budget estimates of the global  $CH_4$  atmospheric inversions are within the boundaries of the regional inversions conducted with the two different a-priori flux distributions. The annual  $CH_4$  budgets obtained from the TM3 global  $CH_4$  inversions (20.4–25.9 Tg for the Amazon lowland region and 6.1–9.2 Tg for the Amazon mainstream area) are even lower than the results of the bottom-up approach derived by Melack et al. [2004] (29.3 Tg and 9 Tg, respectively). The results are more similar to the annual budget of the TM5-CT simulation (17–18 Tg annual  $CH_4$  budget for the Amazon lowland region) described in Ch. 5. The annual  $CH_4$  budgets of the other global  $CH_4$  inversions described in Ch. 5 are in the order of 33–42 Tg for the Amazon lowland region. They are still lower compared to the 61.2 Tg estimated from the regional inversion using the JERS-1SAR wetland inundation map.

The estimated  $CH_4$  budget for May 2009 of the Amazon lowland region for the WP regional inversions (1.9 Tg) is similar to the budget obtained from the WRF-GHG simulation using the Prigent wetland inundation map (WWP; 1.6 Tg). The monthly  $CH_4$  budget for the same region in May 2009 obtained from the regional inversion using the WJ set up is as well similar to the results from the WWJ WRF-GHG simulation (4.4 Tg vs. 4.9 Tg, respectively). This value is closer to the estimate from the comparison of BARCA-B observation and TM5-based global  $CH_4$  inversions (5.4 Tg) for May 2009 for the Amazon lowland region. The calculated domain average  $CH_4$  flux from the different  $CH_4$  budget estimates of the WJ regional inversion leads to values of 27–36  $mg\ m^{-2}\ d^{-1}$ . This is well in accordance with Miller et al. [2007] who estimate the flux strength to be 35  $mg\ m^{-2}\ d^{-1}$  in the Santarém area and 20  $mg\ m^{-2}\ d^{-1}$  around Manaus.

### 7.3 Conclusions

The regional inversion using the Jena two-step inversion scheme was carried out for the year 2009 for the Amazon basin using the TT34 tower observations as observational constraints. Three different a-priori flux distributions were utilized. Evaluation of the CH<sub>4</sub> wetland flux distribution with different meteorological forcing (ERA-Interim and WRF-Chem) using the Walter wetland model results in a good agreement considering spatial and temporal integrated fluxes, e.g. for one month and the Amazon mainstream area. For particular sites, differences in the wetland CH<sub>4</sub> flux were found between the two meteorological forcings, originating from differences in the first layer soil temperature. A comparison of two different regional atmospheric transport models using identical CH<sub>4</sub> fluxes (WRF-GHG and STILT) demonstrates significant differences between the models and underlines once more the importance of a proper representation of the atmospheric transport for regional inversion studies. The cause for the deviation of the two regional atmospheric transport models could be traced back to the convective parametrization, the PBL scheme, differences in the background CH<sub>4</sub> atmospheric mixing ratio, and different meteorological forcing.

Comparisons of simulated CH<sub>4</sub> mixing ratios from regional inversions with three different a-priori flux distributions and varying temporal and spatial correlations lengths to TT34 tower observations were conducted. The comparison to independent airborne observations close to Santarém demonstrates that a regional inversion using weekly temporal correlation length and a spatial correlation lengths in the order of 160 km matches the TT34 observations best and is in agreement with the influence function of the TT34 tower observations. The constraint of the inversion system is a step into the right direction. This is confirmed by the proper reproduction of the latitudinal and longitudinal gradients when comparing to BARCA-B flask observations.

The annual CH<sub>4</sub> budget for the Amazon lowland region is estimated to  $24.9 \pm 0.5$  Tg and to  $12.0 \pm 0.5$  Tg for the Amazon mainstream area using the Prigent wetland inundation map. The numbers for the CH<sub>4</sub> annual budget double for the regional inversion using the JERS-1SAR wetland inundation map. This clearly indicates that the distribution of the wetland inundated area has an important impact of the magnitude of the CH<sub>4</sub> budget estimate.

The comparison to the stationary airborne profiles in the Santarém area further demonstrates that the constraint of the a-posteriori flux distribution with one single 35 m high tower is not sufficient to constrain the flux distribution in the entire Amazon basin. A higher density of surface observation stations distributed equally in the Amazon basin could lead to significant improvements in the constraint of optimized a-posteriori flux distributions correcting as well for the wrong seasonal cycle in the a-priori flux distributions. The results also emphasize the need for improvements in the regional atmospheric transport models especially in the parametrization of the convection and the PBL scheme.

## Chapter 8

# Summary and outlook

### 8.1 Summary

During two BARCA aircraft campaigns in November 2008 (BARCA-A) and May 2009 (BARCA-B), an impressive data set of greenhouse gases and related tracers was collected from 27 research flights in the Amazon basin. The observations covered the majority of the Amazon basin in vertical cross-sections between an altitude of 500 m and 4000 m. For the first time in the Amazon basin, continuous measurements of CH<sub>4</sub> onboard an aircraft were performed during BARCA-B with a CRDS analyzer. A total of 174 and 206 flask samples, respectively, were collected during the two campaigns. The combined time series of continuous CH<sub>4</sub> tower measurements from the K34 and TT34 tower 60 km north-west of Manaus from November 2008 to April 2010 at 55 m and 35 m height, respectively, complemented the BARCA CH<sub>4</sub> airborne observations.

The main objective of this work was to perform a benchmark study that explored different pathways for the estimation of the CH<sub>4</sub> budget of the Amazon basin. The work presented here points to some new research questions concerning the CH<sub>4</sub> budget of the Amazon basin.

The WRF Greenhouse Gas model (WRF-GHG) was developed to allow for high-resolution passive tracer simulations of CH<sub>4</sub>, CO<sub>2</sub>, and CO with online coupled biospheric flux models. The model code of the process-based models for the calculation of biospheric CH<sub>4</sub> fluxes from wetlands, termites, and soil uptake was written during this work. Together with the existing VPRM code for the calculation of biospheric CO<sub>2</sub> fluxes these models are included as a separate “greenhouse gas” module in the WRF-Chem code. A fully compatible WRF-Chem version of the Greenhouse Gas model is part of the official WRF-Chem V3.4 release from spring 2012 onwards.

After comparing the flask and continuous observations obtained from the two BARCA campaigns with the background measurements made at three tower stations, it has been confirmed that the Amazon basin is a strong source of CH<sub>4</sub>. The atmospheric methane mixing ratio in the Amazon basin was found to be lower at the end of the dry season in November 2008 ( $1817 \pm 39$  ppb in the planetary boundary layer and  $1794 \pm 12$  ppb in the lower free troposphere) compared to the end of the wet season in May 2009 ( $1841 \pm 37$  ppb and  $1806 \pm 38$  ppb, respectively). Isotope analysis of  $\delta^{13}\text{C}$  and  $\delta\text{D}$  in the flask samples indicates that most of the airborne CH<sub>4</sub> in the Amazon basin is of biogenic origin. Anaerobic production by microbes in wetlands was found to be the main

source process for biogenic  $\text{CH}_4$ . Anthropogenic  $\text{CH}_4$  emissions from major cities in the Amazon basin (Manaus, Santarém) were also determined to have a biogenic origin. Methane emissions from open sewers, for example, are presumed to play a major role. During BARCA-A part of the variability in the  $\text{CH}_4$  observations could be explained by biomass burning emissions.

The evaluation of five different global atmospheric TM5-based  $\text{CH}_4$  inversions against the BARCA observations illustrates the benefit of satellite observations in inversion systems. The two inversions using SCIAMACHY observations to constrain the a-posteriori flux fields compare better to the BARCA observations than the other three inversions using only constraints from surface stations. The choice of the a-priori wetland distribution was found to have a significant impact on the  $\text{CH}_4$  budget calculations. The monthly budget estimate of  $5.7 \pm 0.7$  Tg for November 2008 and  $6.9 \pm 1.1$  Tg for May 2009 for the Amazon lowland region was derived from minimizing the model-observation mismatch. LPDM simulations indicate that the influence area of the BARCA airborne observations is considerably larger than the Amazon basin.

High resolution WRF-GHG simulations (10 km) with three wetland inundation maps at different horizontal resolutions (Kaplan:  $0.5^\circ \times 0.5^\circ$ , Prigent:  $0.25^\circ \times 0.25^\circ$ , and JERS-1SAR:  $\sim 100$  m) and two wetland models (Kaplan [2002] and Walter et al. [2001a]) were compared to the BARCA observations made in November 2008 and May 2009. The  $\text{CH}_4$  wetland emissions were scaled (mainly downwards) so that the simulated atmospheric  $\text{CH}_4$  mixing ratio matched the averaged  $\text{CH}_4$  atmospheric mixing ratio of selected flights with a good representation of the atmospheric transport in the model during BARCA-B. This was required to account for differences in the wetland inundation fractions of the corresponding wetland inundation maps. The comparison to aircraft observations indicates that the impact of the wetland area distribution on the simulated  $\text{CH}_4$  atmospheric mixing ratios is higher compared to the choice of the wetland model. The location of a particular wetland was found to be more important than its actual emission strength. None of the wetland inundation maps could properly represent the distribution of the inundated area in the Amazon basin. The Kaplan wetland inundation map had a better representation in the north of the Amazon basin and around the Manaus area compared to the other two wetland inundation maps. The Prigent wetland inundation map was found to have the best agreement during BARCA-A in the western and eastern part of the Amazon basin.

A comparison of WRF-GHG precipitation to TRMM observations made during the 3 h flight period indicates problems in the representation of the convective transport in the WRF-Chem model. The location and timing of convective cells not correctly reproduced by the atmospheric transport model were found to have a significant impact on the simulated  $\text{CH}_4$  atmospheric mixing ratio. By a comparison of simulated WRF-Chem precipitation patterns to TRMM observations in the 48 h upstream footprint influence area of the flight track and during the 3 h flight period, flights with a good representation of the atmospheric transport could be selected. They show a better correlation with BARCA observations compared to flights with a poorer representation of the atmospheric transport.



Methane budget estimates for the Amazon lowland region range between 1.5–4.8 Tg for November 2008 to 1.3–5.5 Tg for May 2009 for the four performed WRF-GHG simulations. Considering the lowest budget estimate as an outlier (more than 50% lower compared to the other estimates), the average results in  $3.9 \pm 0.8$  Tg for November 2008 and  $4.0 \pm 0.8$  Tg for May 2009. The main reason for the differences in the CH<sub>4</sub> budget estimates of the four WRF-GHG simulations was found to lie in the different distribution of the wetland area in the western part of the Amazon basin, which could not be constrained by BARCA observations.

The Jena two-step inversion scheme TM3-STILT was applied to the Amazon basin to perform a regional CH<sub>4</sub> inversion for the year 2009 with three different a-priori flux distributions. The 18 UTC TT34 tower CH<sub>4</sub> observations, mainly influenced by the eastern part of the Amazon basin, served as observational constraints. A-posteriori fluxes were found to decrease in the vicinity of the TT34 tower and increase in the eastern part of the Amazon basin. Comparison of latitudinal and longitudinal gradients of the simulated atmospheric CH<sub>4</sub> mixing ratios to independent airborne observations during BARCA-B demonstrated that the a-posteriori fluxes were optimized in accordance with the observations. The comparison to airborne profiles conducted close to the city of Santarém showed the spatial impact of a single tower based inversion and confirmed the choice of spatial correlations in the a-priori uncertainty.

Comparisons of global TM5 and TM3-based CH<sub>4</sub> inversions to TT34 tower observations indicated a seasonal cycle with opposite phase. The optimized a-posteriori flux distribution of the regional inversion demonstrated improvements in the representation of the seasonal cycle in accordance with TT34 tower observations. The a-posteriori fluxes increased in the months August–October and decreased in the beginning and end of the year 2009.

Different meteorological forcing (ERA-Interim vs. WRF-Chem) for the Walter wetland model led to similar monthly integrated CH<sub>4</sub> wetland fluxes for a set region. Differences in the variability of the CH<sub>4</sub> fluxes could be mainly traced back to differences in the first layer soil temperature. Discrepancies in the simulated CH<sub>4</sub> atmospheric mixing ratios originating from different regional atmospheric transport models were found to be significant. Main explanations for this are differences in the meteorological forcing, the background atmospheric CH<sub>4</sub> mixing ratio, convective parametrization, and the PBL height of the models.

The total annual CH<sub>4</sub> budget 2009 of the Amazon lowland region obtained from the TM3-STILT regional inversion is estimated to  $24.9 \pm 0.5$  Tg using the WP a-priori flux distribution and  $61.2 \pm 0.8$  Tg for the WJ a-priori flux distribution. This clearly indicates that the distribution of the inundated wetland area in the Amazon basin has a large influence on the derived budget numbers. The TT34 tower allows for the constraint of the CH<sub>4</sub> budget only in a limited region, namely the eastern part of the Amazon basin.

	Amazon lowland region 2009 [Tg a <sup>-1</sup> ]	Amazon lowland region May 2009 [Tg mo <sup>-1</sup> ]	Amazon mainstream area 2009 [Tg a <sup>-1</sup> ]	Chapter
TM5-BARCA	-	6.9±1.1	-	5
WRF-GHG (no WWP)	-	4.0±0.8	-	6
WRF-GHG WWP	-	1.3	-	6
WRF-GHG WWJ	-	5.5	-	6
TM3	25.9±0.5	2.5±0.0002	9.2±0.2	7
TM3-TT34	20.4±0.8	1.4±0.1	6.2±0.2	7
STILT WP	24.9±0.5	1.9±0.02	12.0±0.5	7
STILT WJ	61.2±0.8	4.4±0.01	22.4±0.9	7

Table 8.1: Comparison of CH<sub>4</sub> budget estimates derived for the Amazon lowland region and the Amazon mainstream area for the entire year 2009 and May 2009 using different methods applied within this work. For the TM5-BARCA estimate, the uncertainty of the CH<sub>4</sub> budgets is estimated using quadratic error propagation. For the WRF-GHG and for TM3 and STILT estimates, the standard error of the mean is utilized.

In summary, different methods for estimating the CH<sub>4</sub> budget were evaluated within this work. For this purpose, the WRF Greenhouse Gas model was developed, and has become a powerful tool for high-resolution greenhouse gas tracer simulations. The code is now available to the scientific community via the official WRF-Chem release V3.4. BARCA CH<sub>4</sub> observations confirmed that the Amazon basin is a strong CH<sub>4</sub> source region, mainly originating from CH<sub>4</sub> emissions in wetlands. The usage of satellite observations in global CH<sub>4</sub> inversions, in addition to observations from surface stations, demonstrated a substantial benefit in tropical regions when comparing to BARCA observations. Detailed knowledge of the inundated wetland area distribution in the Amazon basin was crucial for the comparison of CH<sub>4</sub> high-resolution transport simulations to airborne observations and obtaining reliable budget estimates. The impact of the choice of the wetland model, and the forcing meteorology of the wetland model used within this work on the budget estimate, was of minor importance. Important for robust budget estimates with reduced uncertainties was a proper representation of the atmospheric transport. Comparisons to airborne observations improved considerably when only flights with a good representation of the atmospheric transport were taken into account. With the current generation of regional atmospheric transport models and sparse availability of atmospheric CH<sub>4</sub> observations in the Amazon basin, a CH<sub>4</sub> budget estimate is still associated with high uncertainties, independent of the method used for the estimation of the CH<sub>4</sub> budget, as Table 8.1 summarizes.

## 8.2 Outlook

Future directions for scientific inquiry based on the results of this thesis are presented here, with the aim of producing a robust and reliable annual CH<sub>4</sub> budget for the Amazon basin.

Both the budget estimates from the WRF-GHG simulations and the TM3-STILT regional inversion lack observational constraints in the western part of the Amazon basin. The results of the TM3-STILT regional inversion with one surface station tower illustrated the potential for deriving a budget estimate with a correct representation of the seasonal cycle of the CH<sub>4</sub> emissions in the Amazon basin. Considering the main influence area of the TT34 tower, ~600 km to the east (which is consistent with the BARCA observations), there are two options for the derivation of a robust budget estimate. One option would be to enlarge the observational constraint with an increased number of towers. The other option would be an improved a-priori CH<sub>4</sub> wetland distribution that allows for larger spatial correlation lengths. As the latter is not available from current process-based CH<sub>4</sub> flux models, more tower observations seem the only remaining choice. Several surface towers will be required within the Amazon basin to obtain sufficient data coverage, specifically four surface towers in the west-east direction. Additional towers in the north-west and south/south-west regions would complete the surface station network. In the north-west, this would allow for more detailed knowledge of the CH<sub>4</sub> source distribution, and in the south-west, the source contribution from biomass burning and land-use change could both be further constrained. The ATTO tall tower and the additional planned surface stations within the AMAZONICA project are steps in the right direction. A denser network of observations will enable a better constraint on regional inversion studies. This would likely result in sensitivity studies with different a-priori fluxes being more likely to converge on a single estimate of the CH<sub>4</sub> budget for the Amazon basin.

In the next years satellite observations of greenhouse gases, especially CH<sub>4</sub>, at higher accuracy and spatial resolution (up to 2 km × 2 km), will become available through the CarbonSat and MERLIN projects. The possibility of using these observations in regional inversion studies should be investigated, as SCHIAMACHY data has already been shown to provide a substantial benefit for global CH<sub>4</sub> inversions, particularly in the tropics.

Exact knowledge of the inundated wetland area is another very important factor in estimating the CH<sub>4</sub> budget for the Amazon basin. Wetland inundation maps based on the SAR remote sensing technique with a monthly time resolution would be very useful. This technique is able to identify flooded forest wetland area, which contributes to nearly 70% to the total wetland extent in the Amazon mainstream area [Melack and Hess, 2011]. The fraction of flooded forest wetland area in the western part of the Amazon may be relatively high, considering the large differences in the inundated wetland area between the JERS-1SAR wetland inundation map and the Prigent wetland inundation map, which is more sensitive to open water wetland area. Up-to-date, time-dependent wetland inundation maps are important for realistic model simulations at the regional scale to account for specific climatic conditions, such as severe flooding or drought, that have a high impact on the distribution of wetland inundated area and the resulting amount of wetland CH<sub>4</sub> emissions. Together with multi-annual time series from surface stations, effects from different climatological conditions (e.g. El Niño events) on the CH<sub>4</sub> budget in the Amazon basin can be studied in detail.

Improving the representations of convective transport processes in regional atmospheric transport models is another area of future investigation. Budget estimates within small uncertainty ranges will only be possible if the uncertainties from the atmospheric transport models are significantly lower compared to the uncertainties from the flux estimates. For model-data comparisons in tropical regions, the ability of the atmospheric transport model to simulate convective processes and convective cells at the right spatial and temporal location is crucial and necessary. Also, the performance of convection and precipitation processes in Global Circulation Models (GCM) requires further investigation as they provide meteorological forcing for regional atmospheric transport models. A first step would be the quantification of the atmospheric transport model uncertainty on the tracer atmospheric mixing ratio originating from convective transport processes, as illustrated for other transport model processes by Gerbig et al. [2009].

Once the transport uncertainties of the regional atmospheric transport models in tropical regions can be assumed to be small, atmospheric observations could be used to optimize parameters of the biospheric wetland models. A system similar to the Carbon Cycle Data Assimilation System (CCDAS; [Rayner et al., 2005]) for  $\text{CO}_2$  could be established for  $\text{CH}_4$ . The  $\text{CH}_4$  atmospheric mixing ratio could then be used to calibrate the tuning parameters of the wetland models, e.g.  $R_0$  for the Walter wetland model. In a second step, the water table depths or other forcing variables of the Walter wetland model could be directly assimilated into the system, if the observations, e.g. from satellites are available.

# Appendix A

## Additional figures and tables

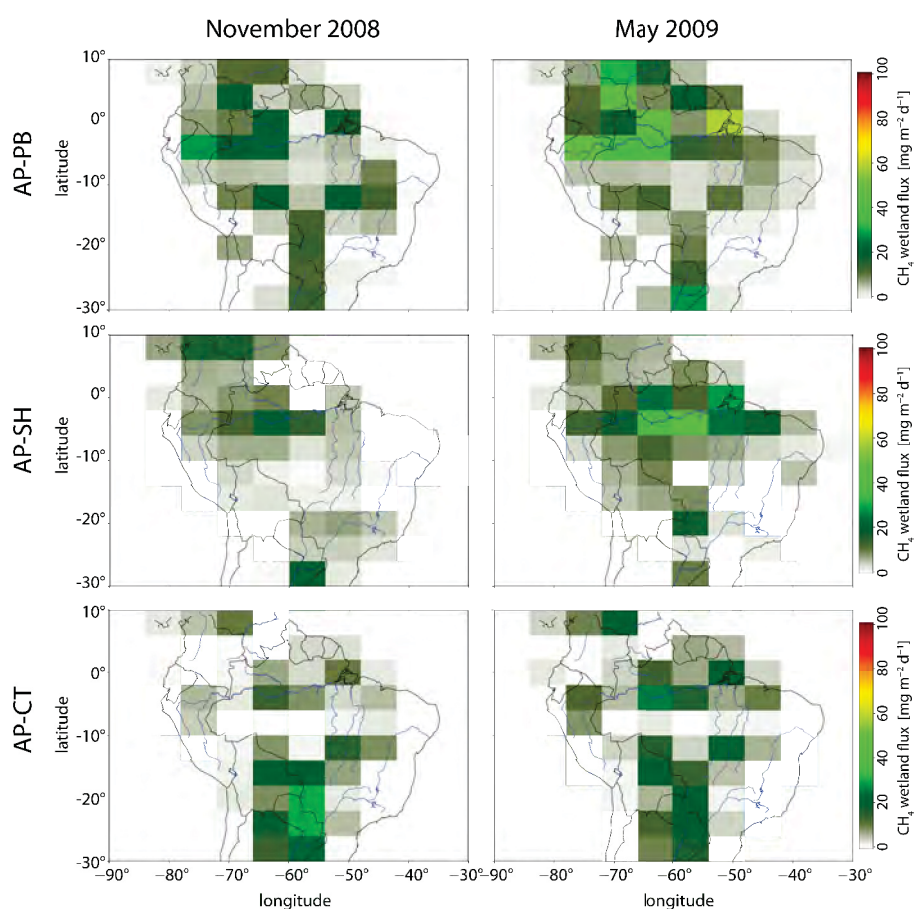


Figure A.1: Monthly a-priori wetland CH<sub>4</sub> fluxes of the different TM5 global CH<sub>4</sub> inversions for November 2008 (left panel) and May 2009 (right panel). AP-PB illustrates the a-priori wetland fluxes of P. Bergamaschi, AP-SH those of S. Houweling, and AP-CT those of Carbon-Tracker Methane.

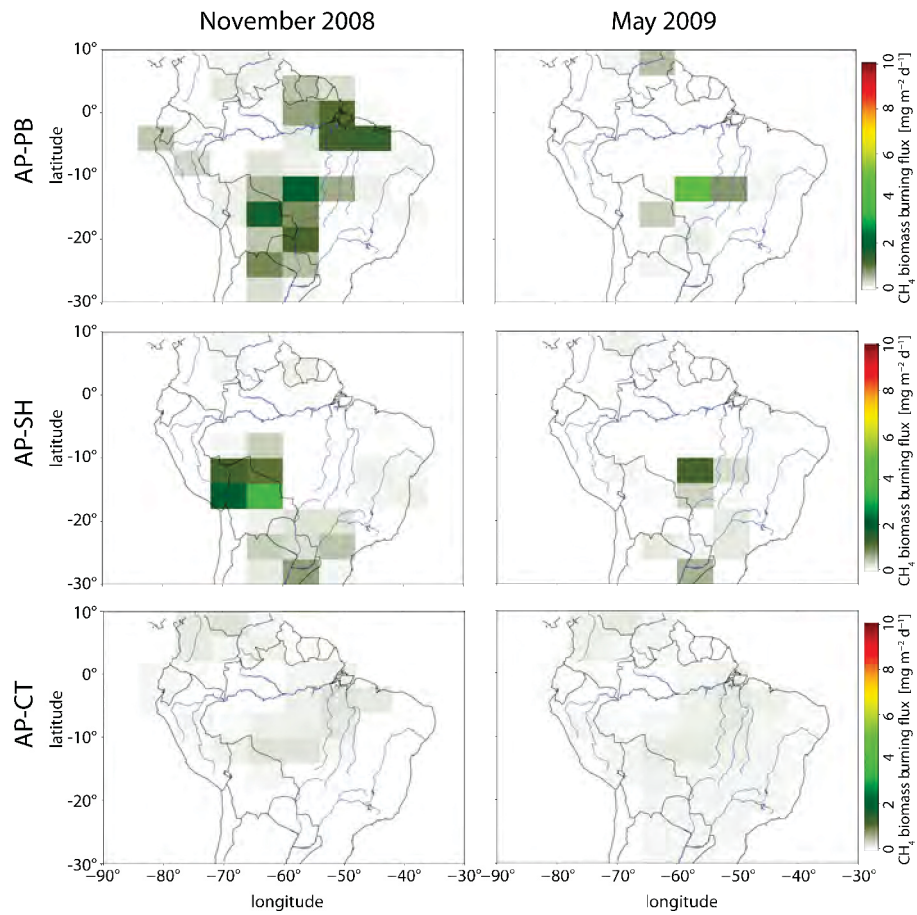


Figure A.2: Monthly a-priori biomass burning  $\text{CH}_4$  fluxes of the different TM5 global  $\text{CH}_4$  inversions, all based on GFEDV2 [van der Werf, 2004], for November 2008 (left panel) and May 2009 (right panel). P. Bergamaschi uses monthly averages of GFED from the years 1997–2007 (AP-PB). S. Houweling uses the a-priori biomass burning emissions of 2008 also for 2009 (AP-SH), while Carbon-Tracker Methane uses current a-priori biomass burning fluxes (AP-CT).



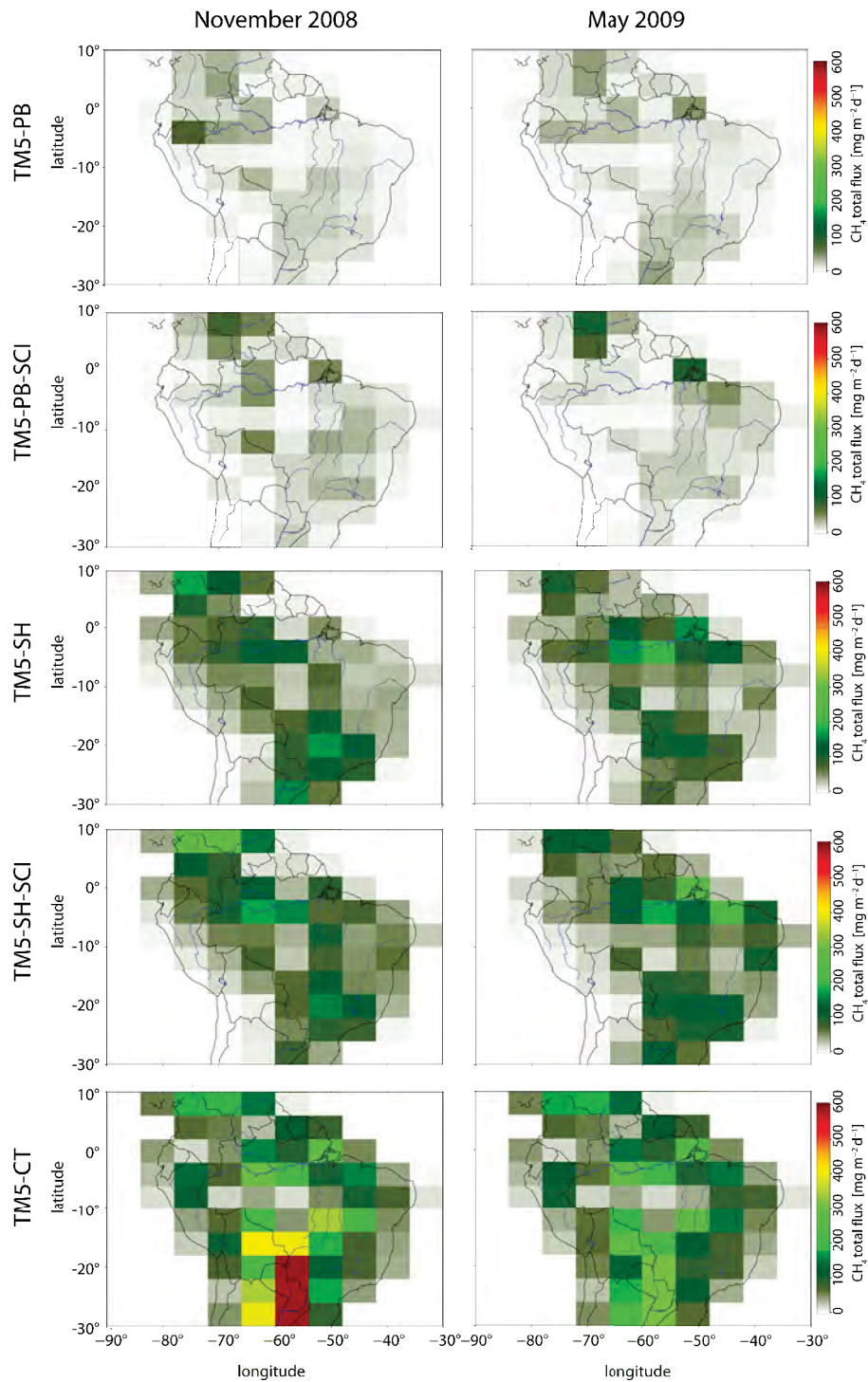


Figure A.3: Monthly a-posteriori total  $\text{CH}_4$  fluxes obtained from five different global  $\text{CH}_4$  inversions for November 2008 (left panel) and May 2009 (right panel). The configuration of the different TM5 global  $\text{CH}_4$  inversions is described in Table 5.2.

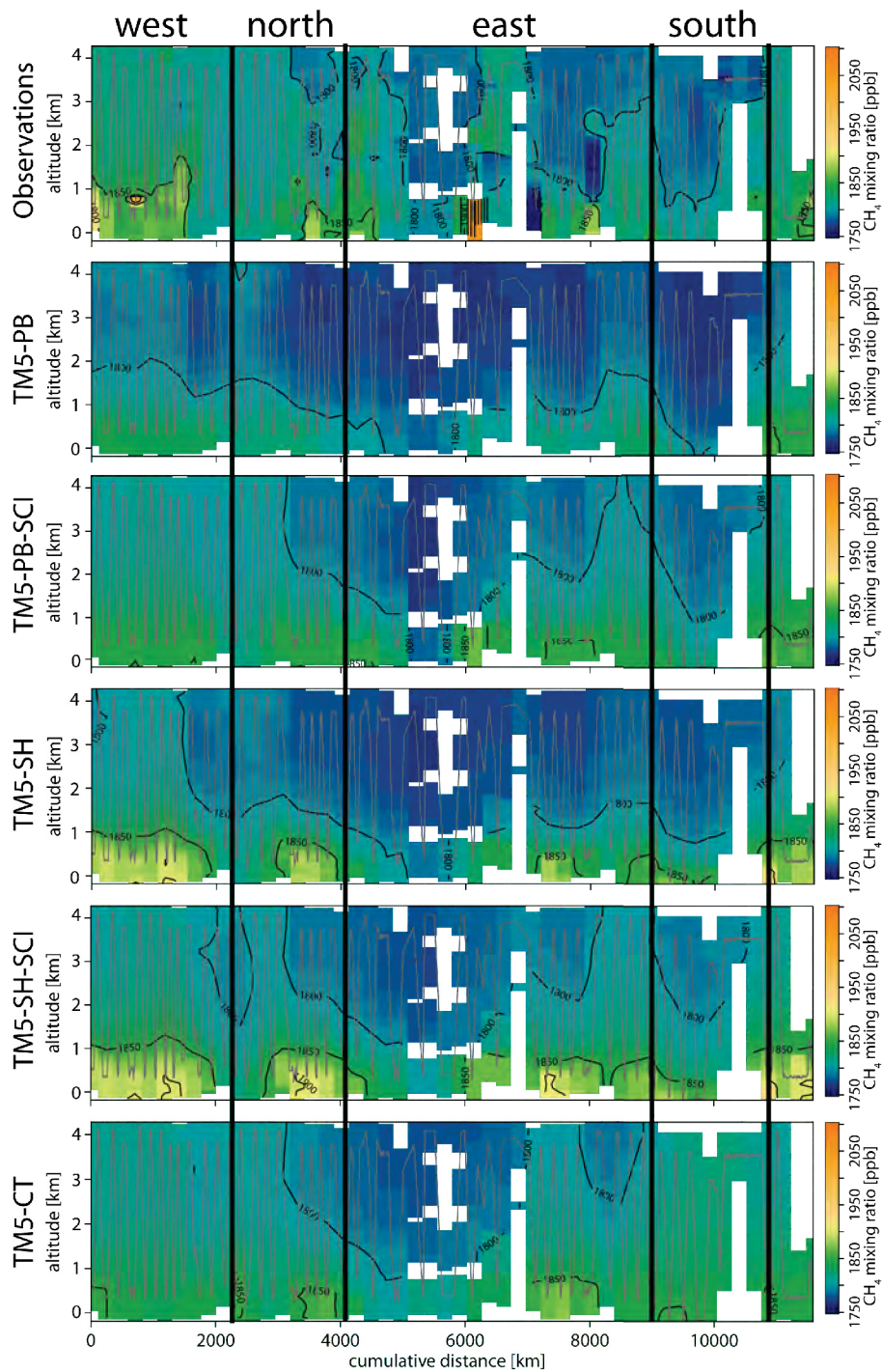


Figure A.4: Vertical cross-section of  $\text{CH}_4$  BARCA-B continuous observations and  $\text{CH}_4$  atmospheric mixing ratios for the five TM5-based  $\text{CH}_4$  inversions (TM5-PB, TM5-PB-SCI, TM5-SH, TM5-SH-SCI, and TM5-CT) as function of the cumulative distance flown by the aircraft. The model data was extracted at each observation location. For the flights 8–10 flask observations were used due to instrument failure. The geographic directions of the flights within the Amazon basin are indicated.

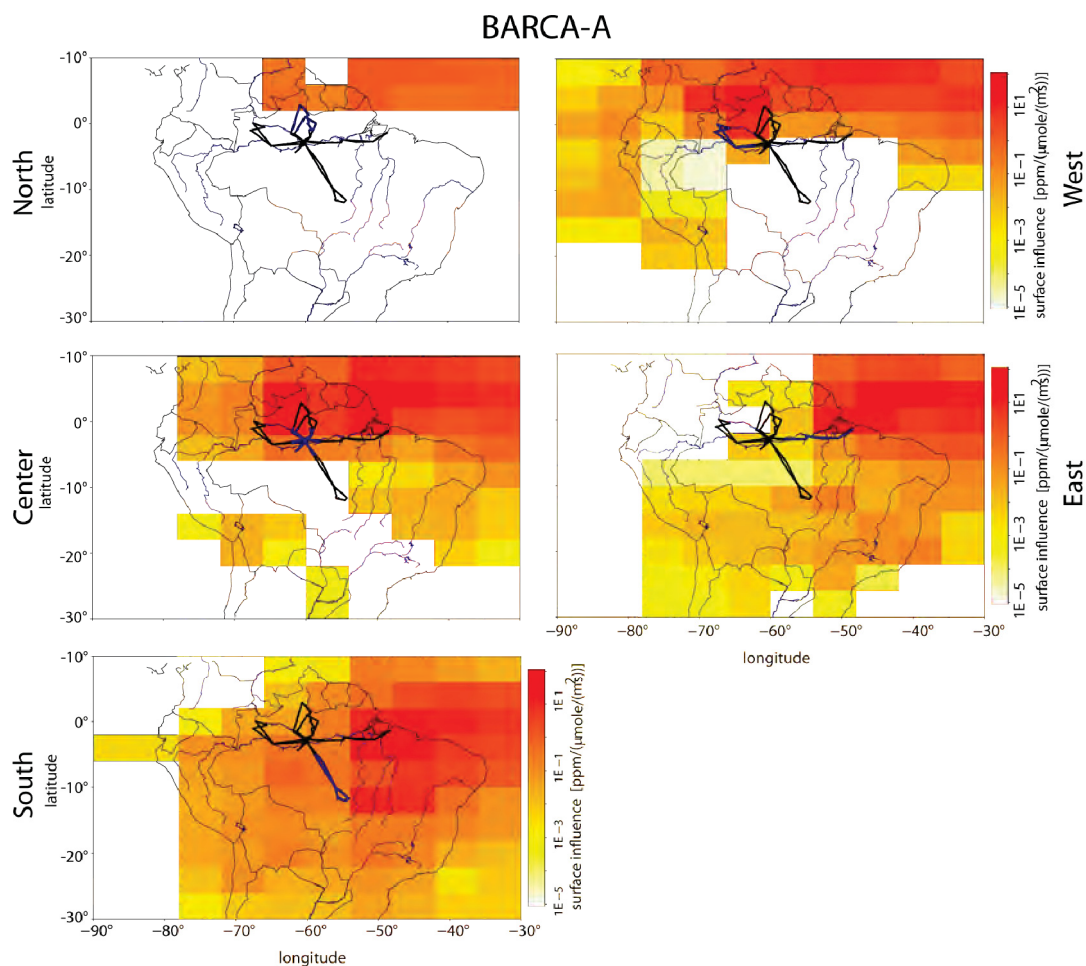


Figure A.5: *Integrated footprints (describing the sensitivity of atmospheric mixing ratio measurements to upstream surface-atmosphere fluxes) for all flask observations obtained in the corresponding sampling regions (north, west, center, east, south) (cf. Fig. 5.1b) during BARCA-A. The flight track of each airborne campaign is colored in black, while the part of the flight track that corresponds to the respective sampling region is colored in blue.*



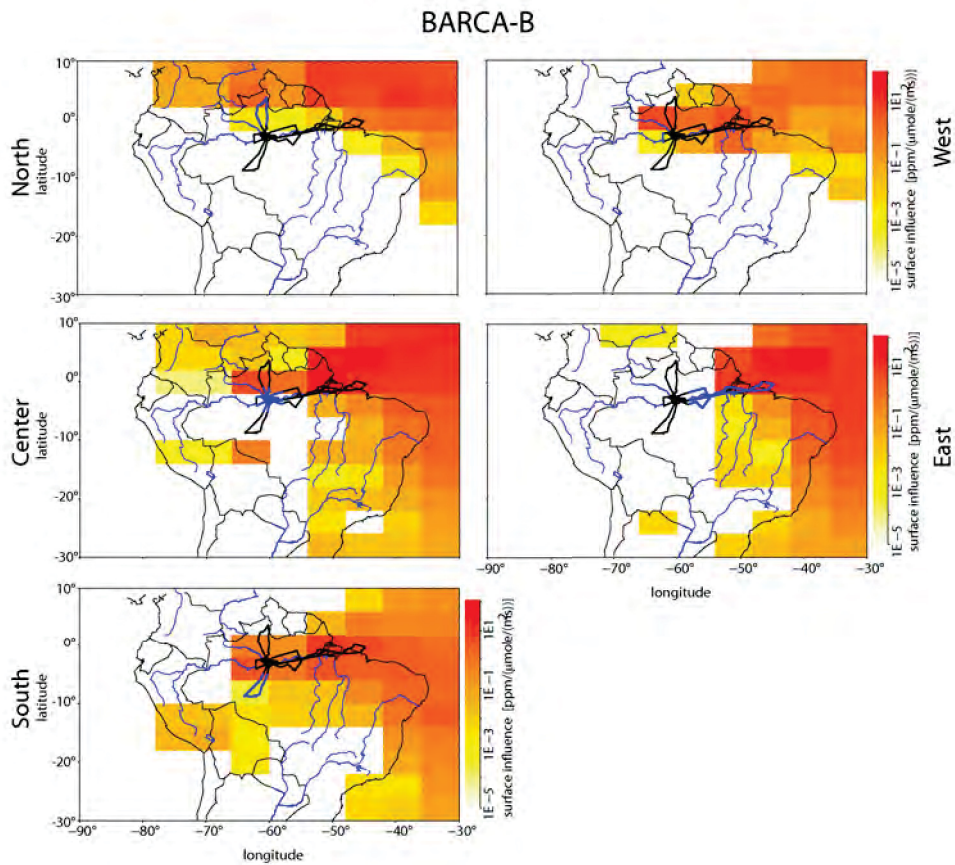


Figure A.6: *Integrated footprints (describing the sensitivity of atmospheric mixing ratio measurements to upstream surface-atmosphere fluxes) for roughly four equally distributed observation per flown vertical profile in the corresponding sampling regions (north, west, center, east, south) (cf. Fig. 5.1b) during BARCA-B. The flight track of each airborne campaign is colored in black, while the part of the flight track that corresponds to the respective sampling region is colored in blue.*

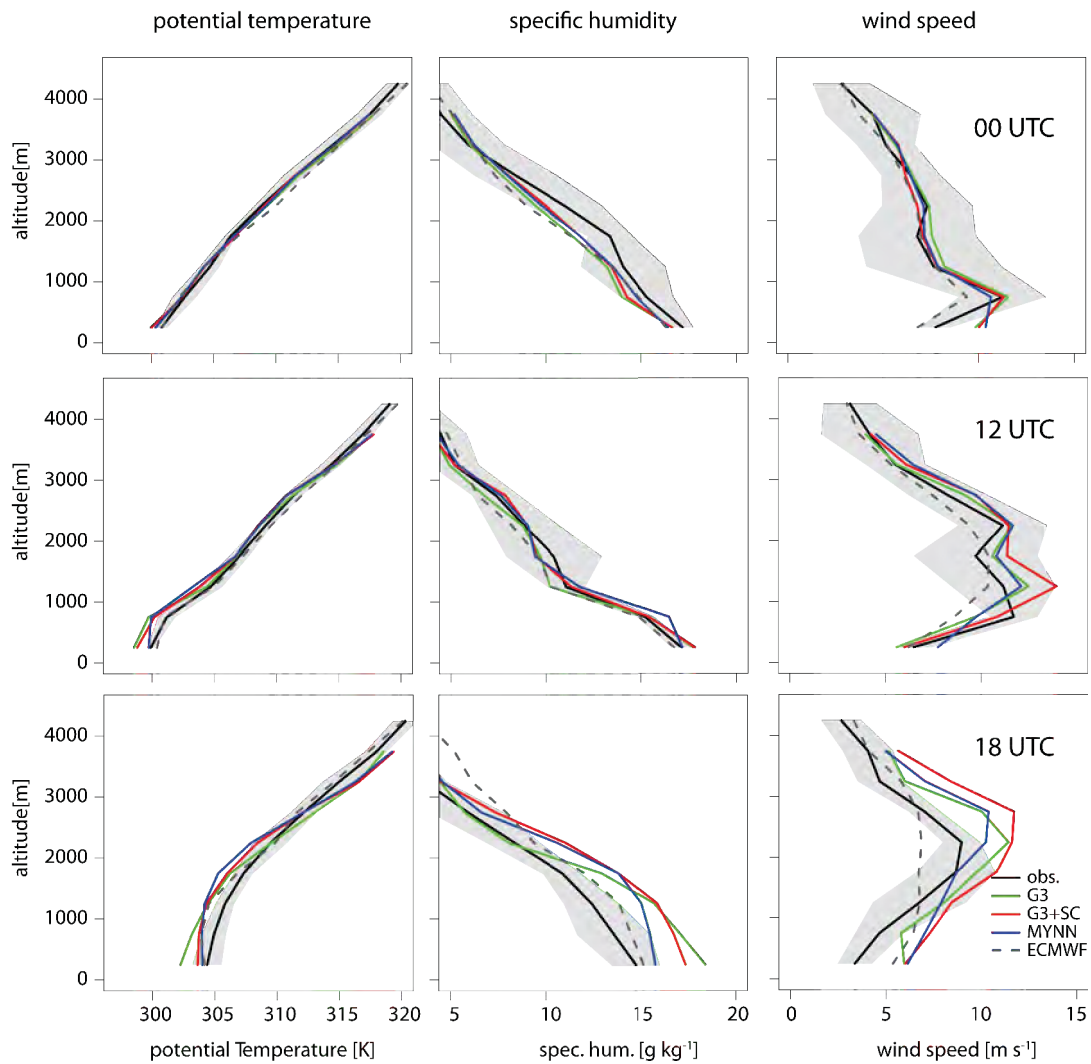


Figure A.7: Comparison of radiosonde profiles for potential temperature, specific humidity, and wind speed to WRF-Chem simulations using three different meteorological set ups as described in Sec. 6.2.1 for the city of Belém. Additionally, the ECMWF meteorology as forcing meteorology for WRF-Chem is shown. Radiosonde observations were conducted for Belém at 00, 12, 18 UTC during 21–30 November 2008.

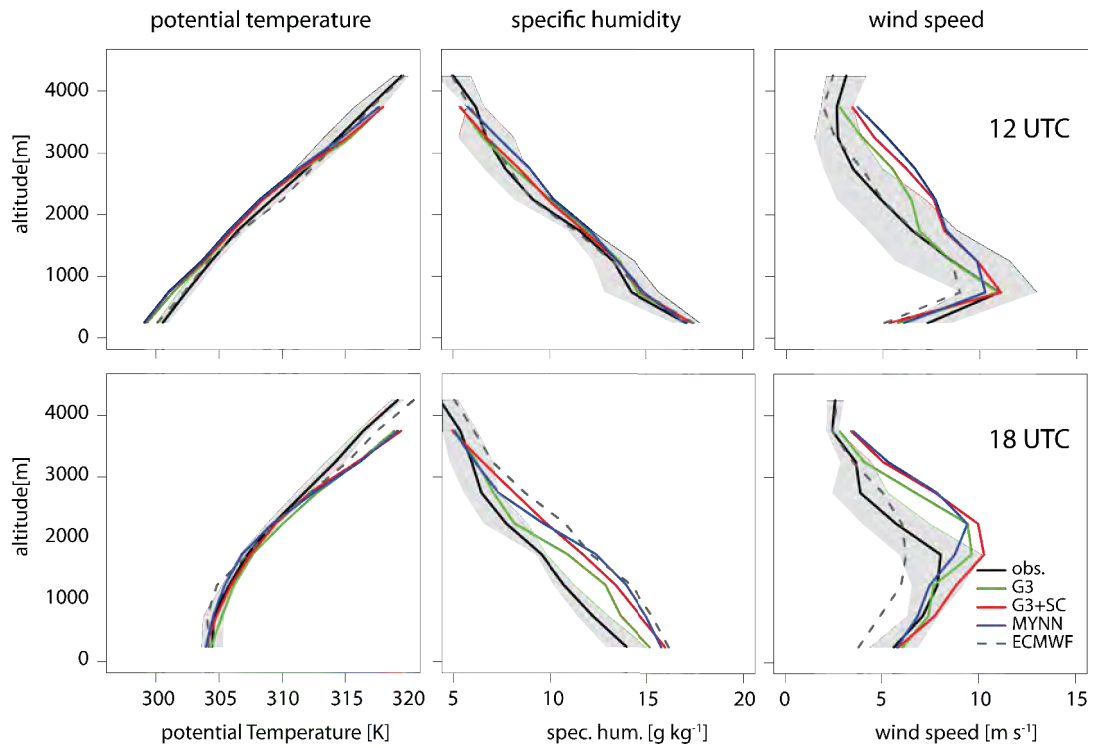


Figure A.8: Comparison of radiosonde profiles for potential temperature, specific humidity, and wind speed to WRF-Chem simulations using three different meteorological set ups as described in Sec. 6.2.1 for the city of Santarém. Additionally, the ECMWF meteorology as forcing meteorology for WRF-Chem is shown. Radiosonde observations were conducted for Santarém at 12 and 18 UTC during 21–30 November 2008.



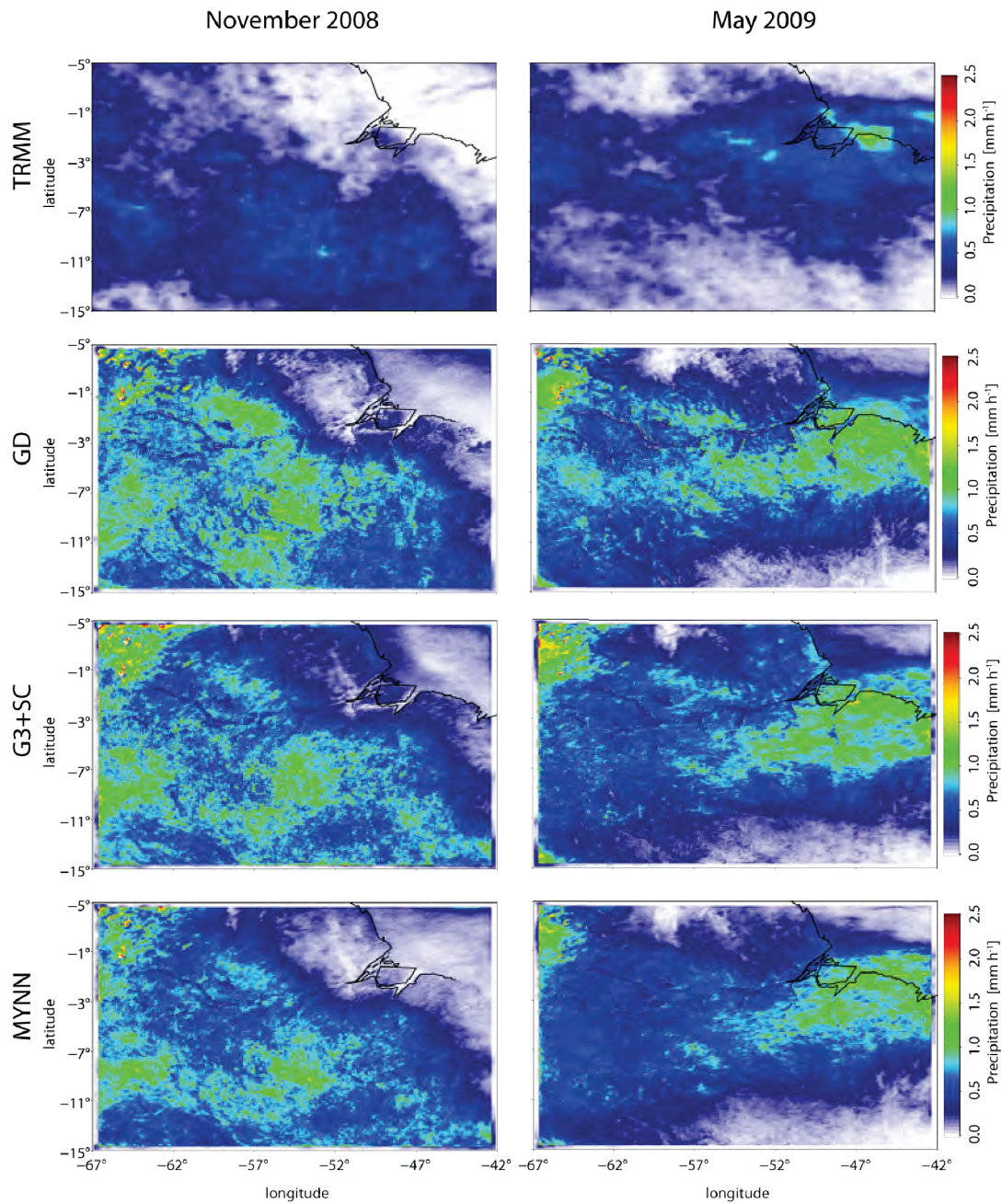


Figure A.9: (a) Monthly mean average of TRMM precipitation in the d02 WRF-GHG simulation domain for November 2008 (a1) and May 2009 (a2) in comparison the precipitation estimate of different meteorological set ups of WRF-Chem: (b) GD using the Grell-Dévényi convective scheme (c) G3+SC using the Grell3 convection scheme in combination with the shallow convection option, and (d) MYNN using G3 with a different scheme for the PBL parametrization (MYNN instead of MYJ).

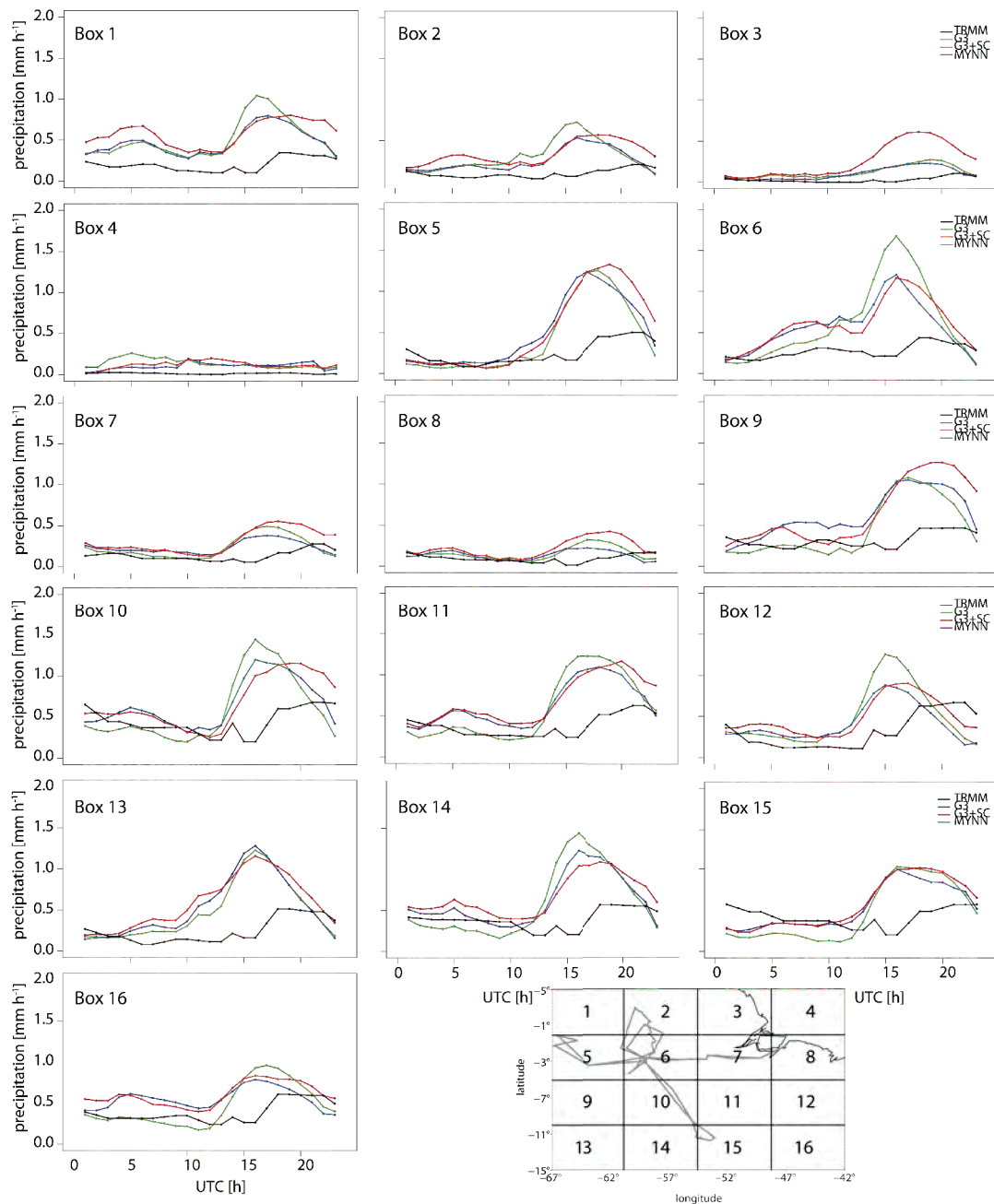


Figure A.10: Monthly averaged diurnal cycles of precipitation within the d02 WRF domain for simulations of different WRF-Chem meteorologies (green–G3, red–G3+SC, blue–MYNN) against TRMM observations (black) for November 2008. The domain was divided into 16 equally spaced boxes.

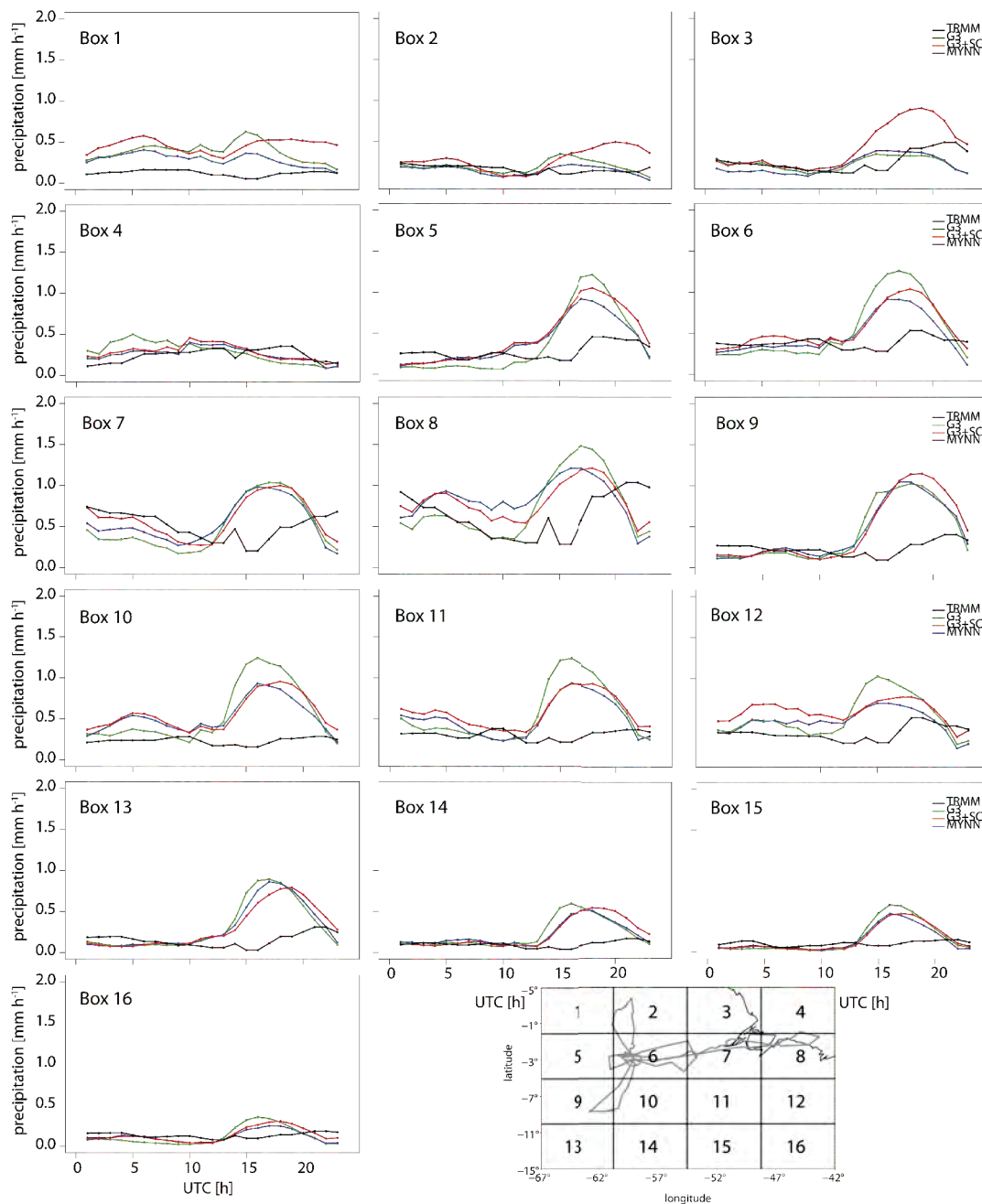


Figure A.11: Monthly averaged diurnal cycles of precipitation within the d02 WRF domain for simulations of different WRF-Chem meteorologies (green–G3, red–G3+SC, blue–MYNN) against TRMM observations (black) for May 2009. The domain was divided into 16 equally spaced boxes.

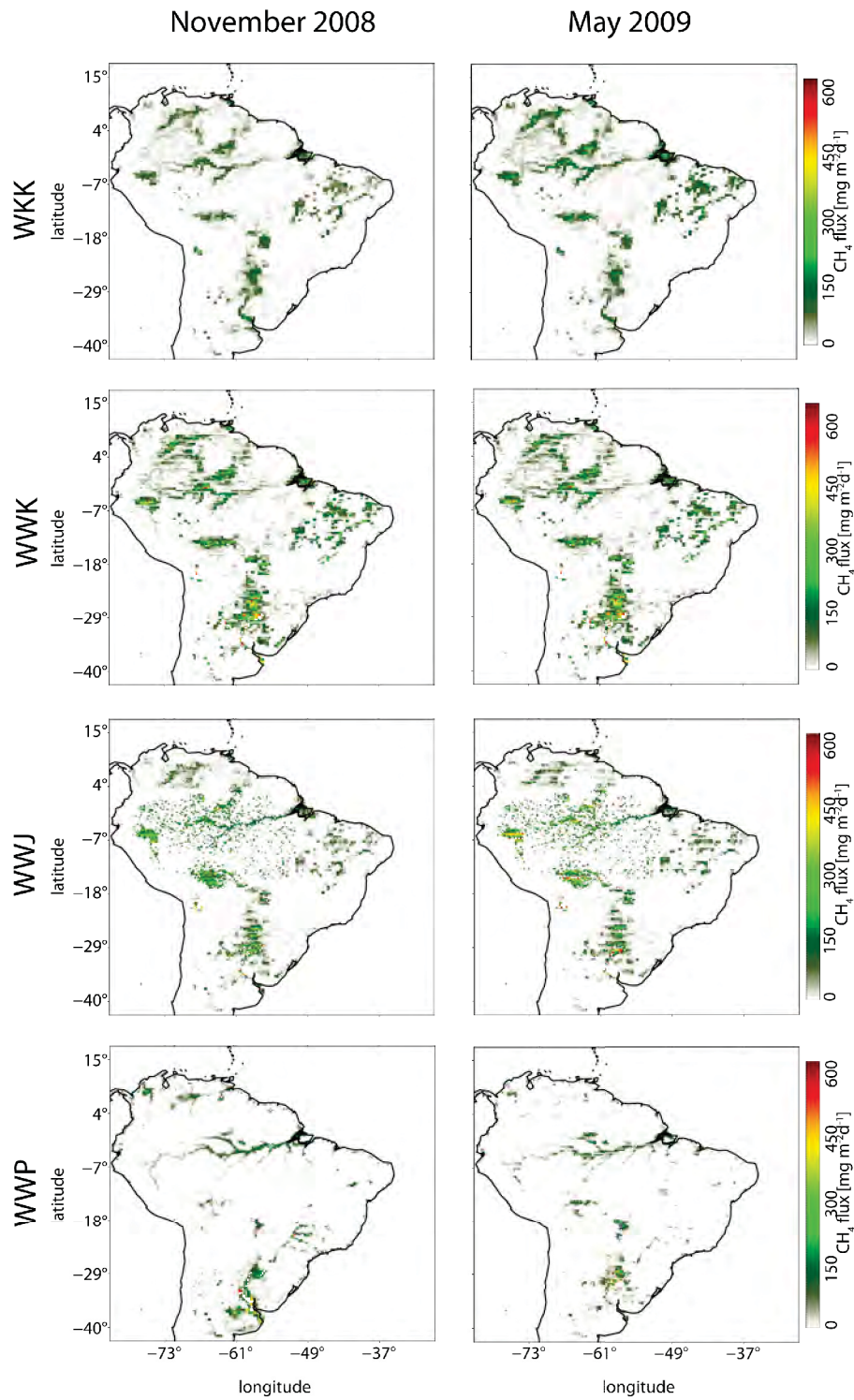


Figure A.12: Monthly mean  $\text{CH}_4$  wetland fluxes of the WRF-GHG d01 simulation domain for November 2008 (left panel) and May 2009 (right panel). The configuration of the four WRF-GHG simulations is found in Table 6.1 and Table 6.3.



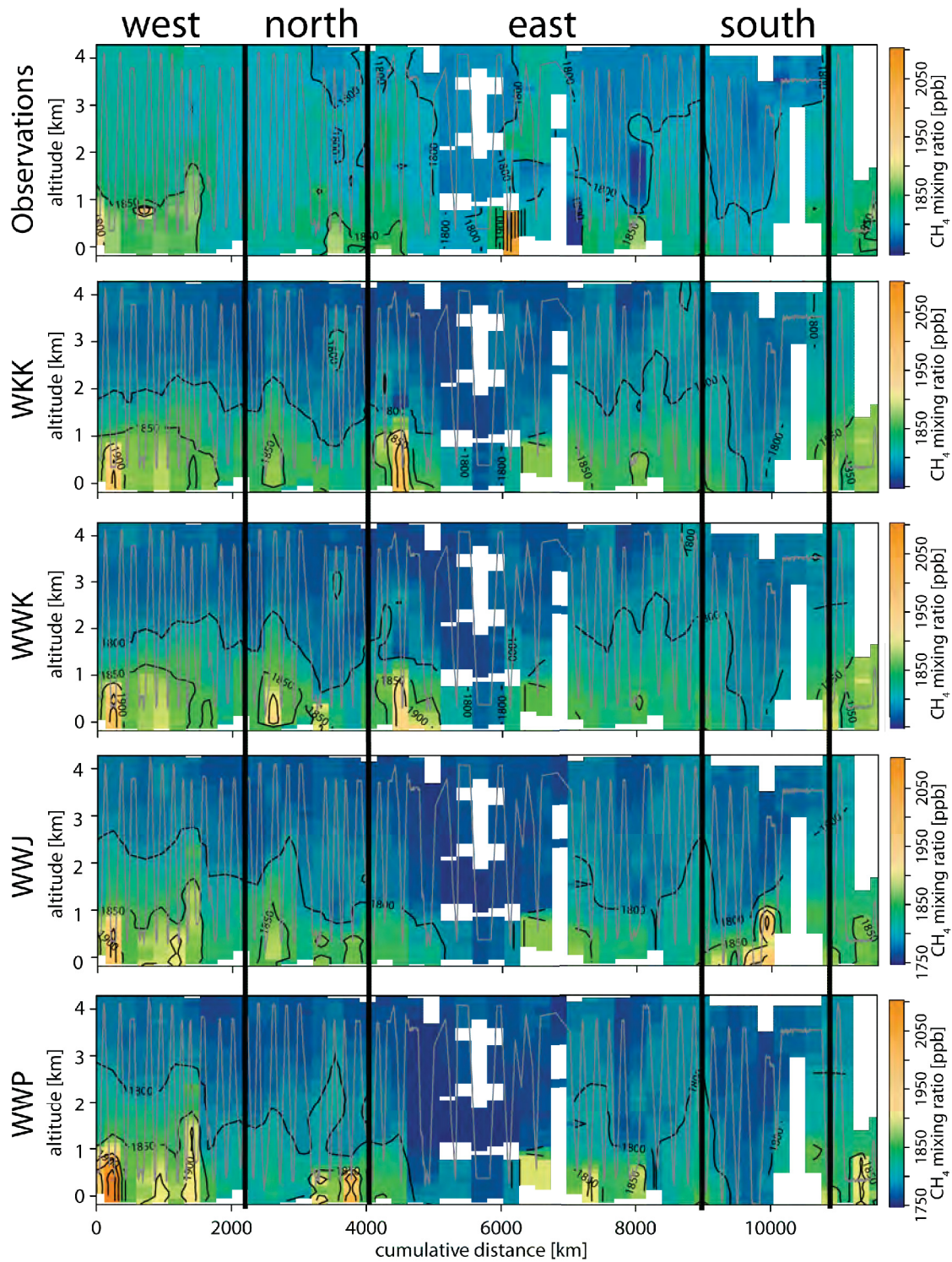


Figure A.13: Vertical cross-section of  $\text{CH}_4$  BARCA-B continuous observations and  $\text{CH}_4$  atmospheric mixing ratios for the four WRF-GHG simulations (WKK, WWK, WWJ, and WWP) as function of the cumulative distance flown by the aircraft. The model data was extracted at each observation location. For the flights 8–10 flask observations were used due to instrument failure. The geographic directions of the flights within the Amazon basin are indicated.

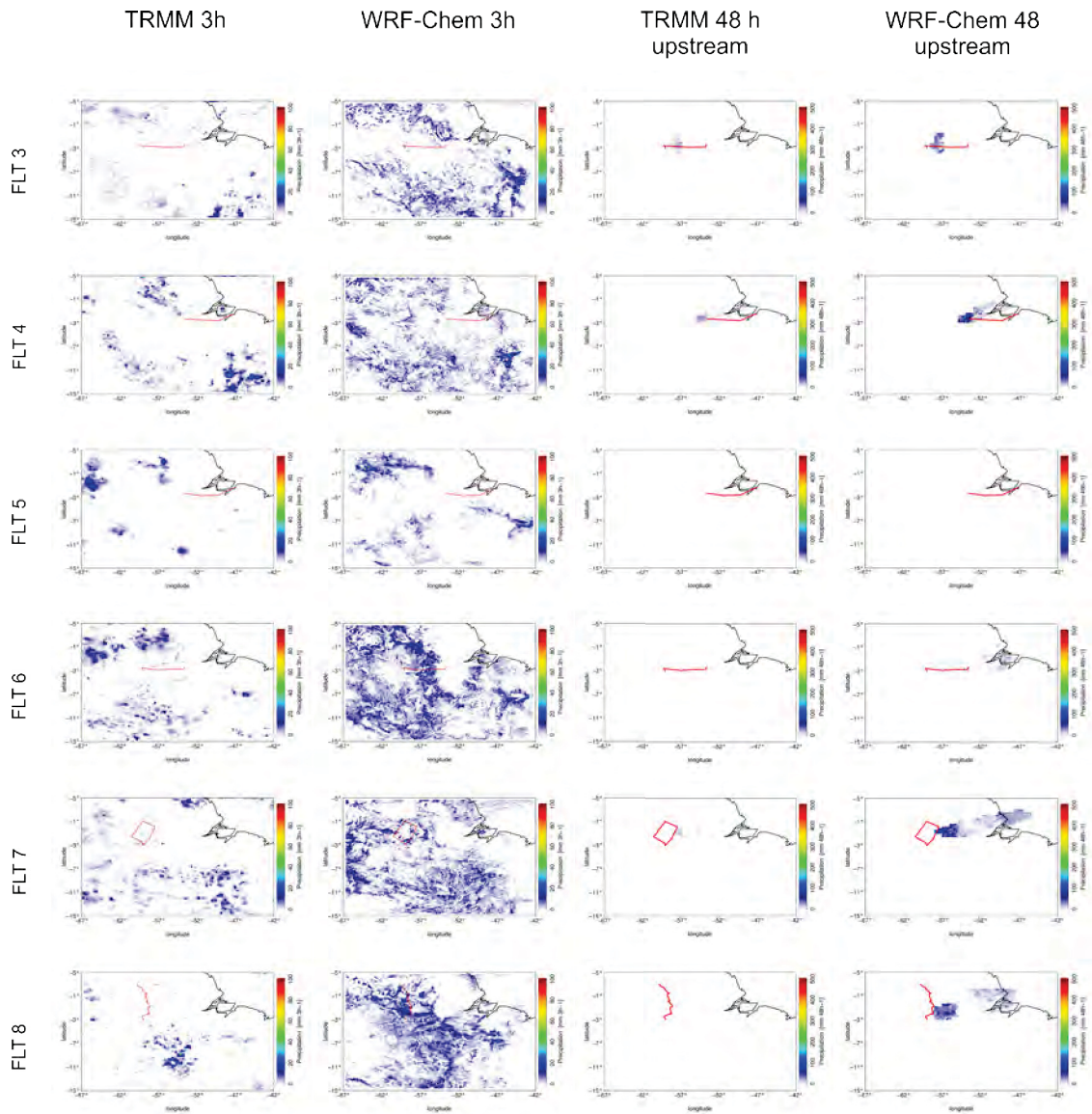


Figure A.14: Comparison of WRF-Chem and TRMM precipitation patterns during the 3 h time period of each flight and the 48 h upstream period for FLT 3 to FLT 8 during BARCA-A.



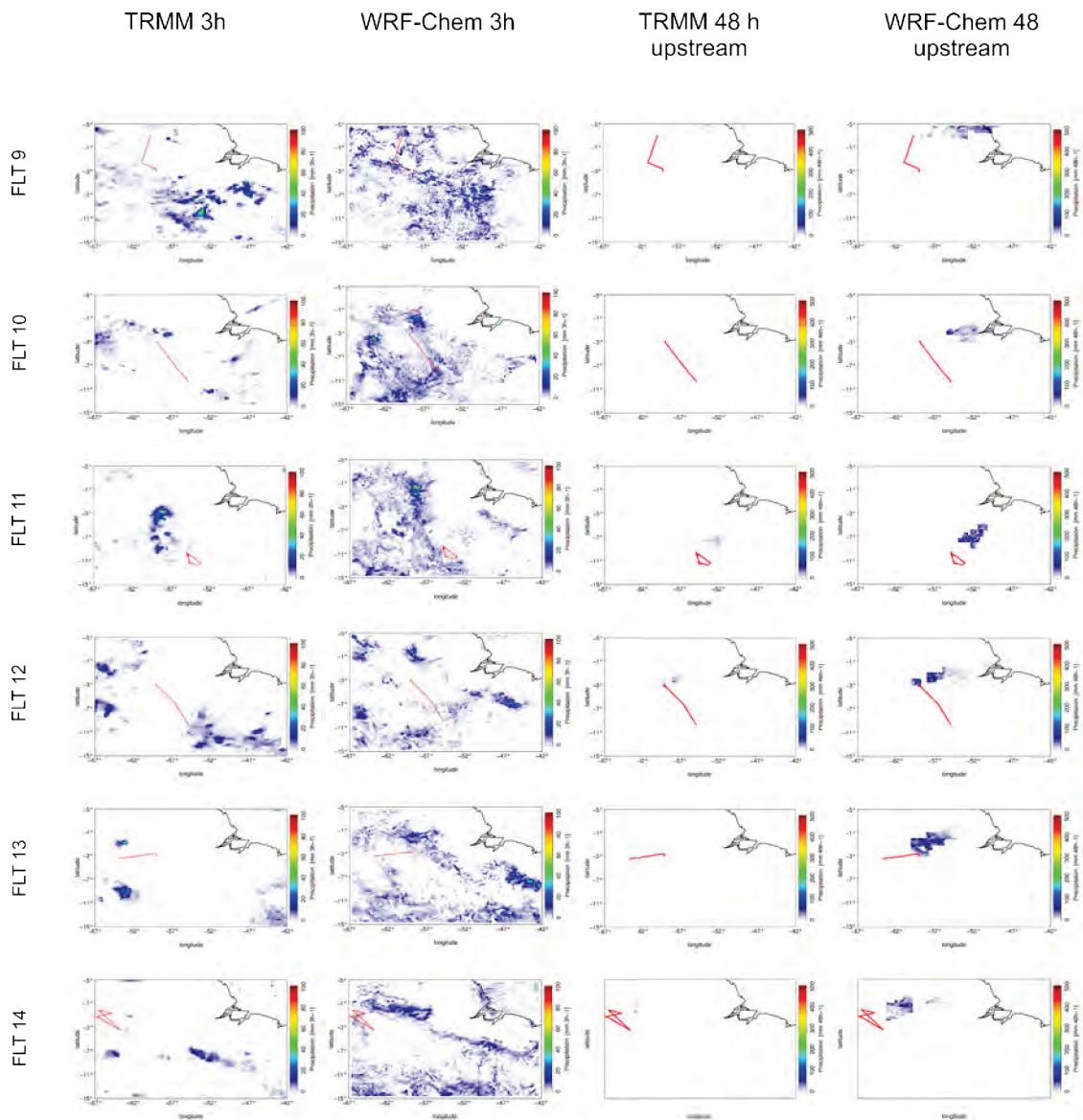


Figure A.15: Comparison of WRF-Chem and TRMM precipitation patterns during the 3 h time period of each flight and the 48 h upstream period for FLT 9 to FLT 14 during BARCA-A.

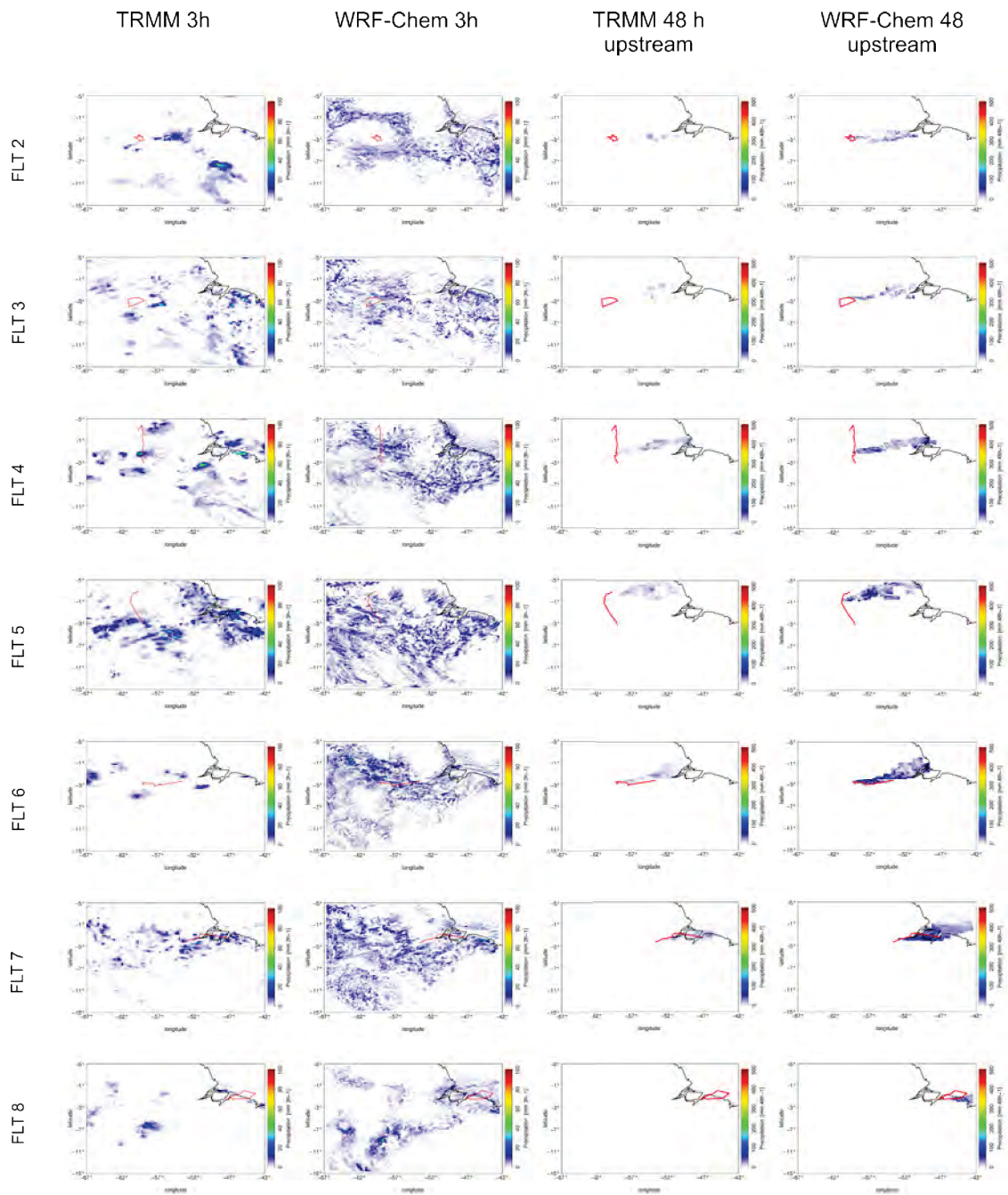


Figure A.16: Comparison of WRF-Chem and TRMM precipitation patterns during the 3 h time period of each flight and the 48 h upstream period for FLT 2 to FLT 8 during BARCA-B.

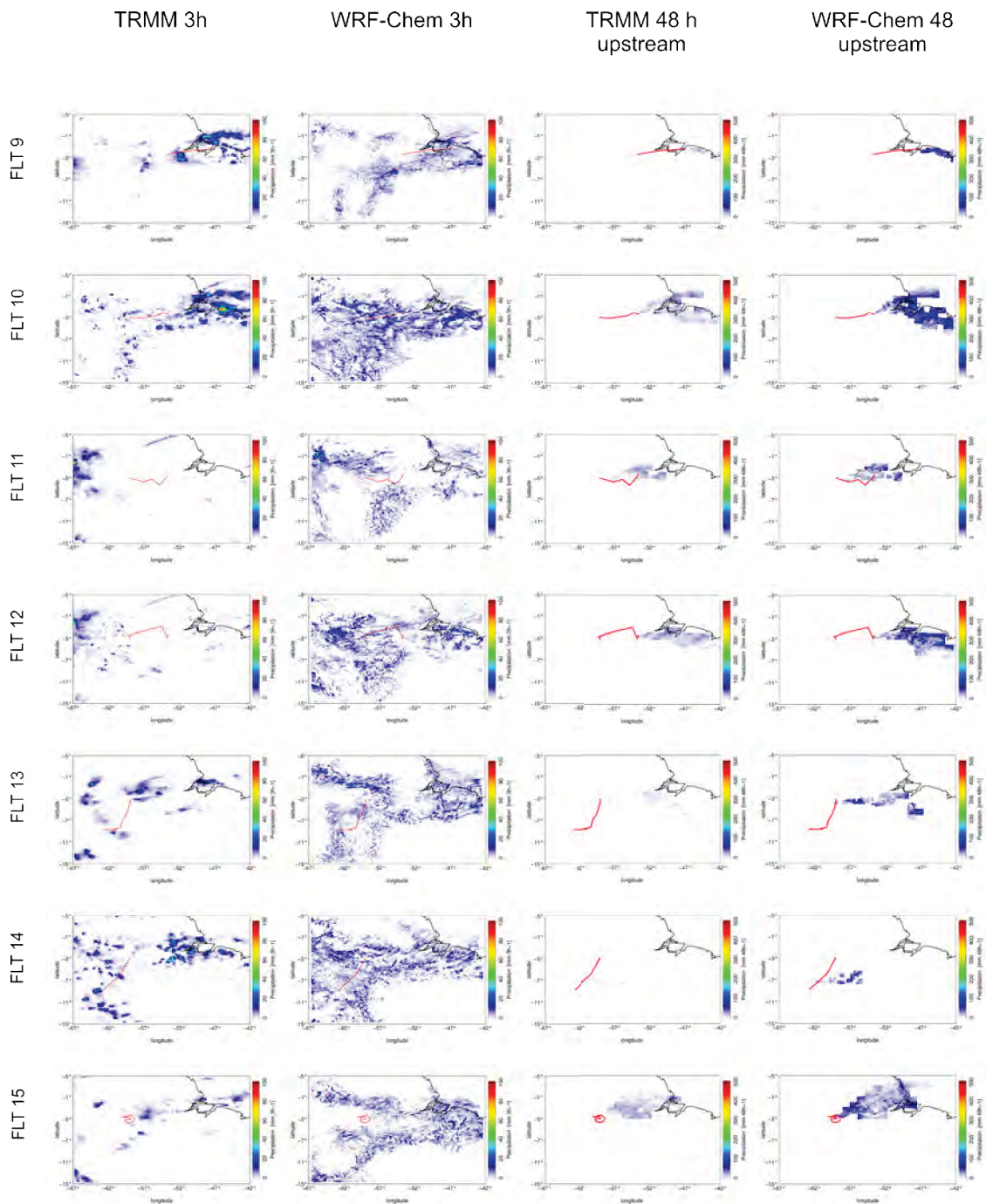


Figure A.17: Comparison of WRF-Chem and TRMM precipitation patterns during the 3 h time period of each flight and the 48 h upstream period for FLT 9 to FLT 15 during BARCA-B.



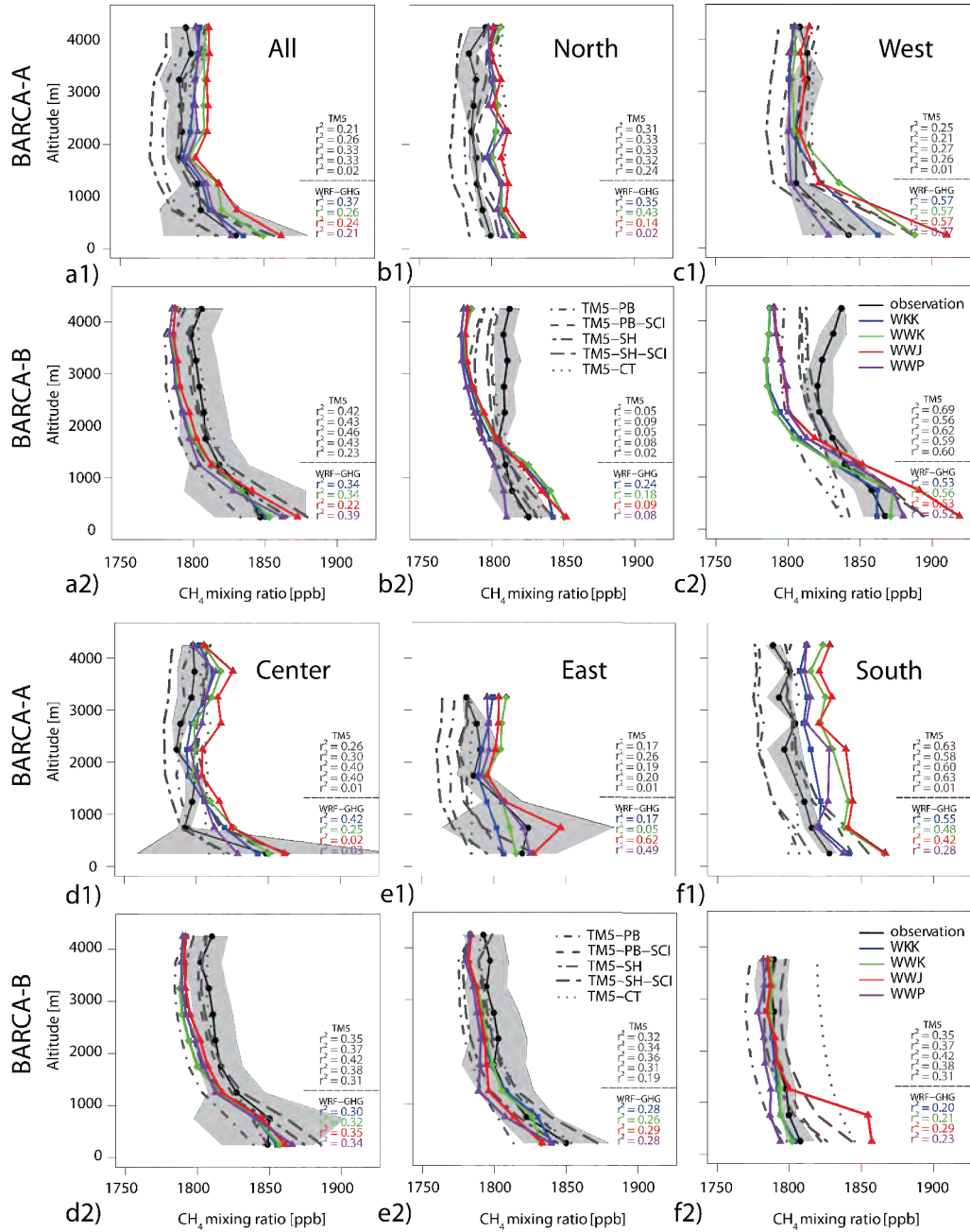


Figure A.18: Comparison of TM5 and WRF-GHG vertical profiles to BARCA observations. The  $r^2$  values were calculated with all available data for each specific region. The order of the TM5  $r^2$  values corresponds to the order of the legend.

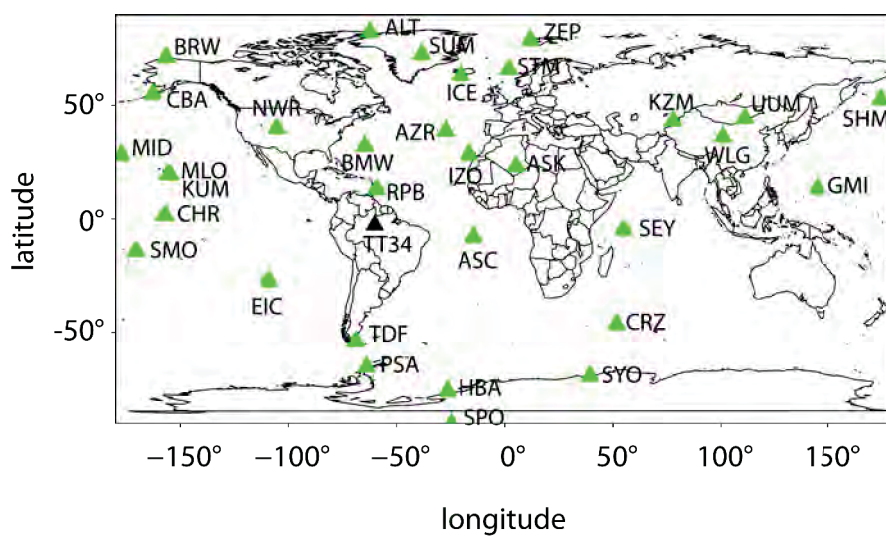


Figure A.19: Location of the  $\text{CH}_4$  surface observation stations for the usage in the TM3 global  $\text{CH}_4$  inversion (green triangles). The location of the TT34 tower is denoted as black triangle. Additional information in the measurement locations is found in Table A.1.

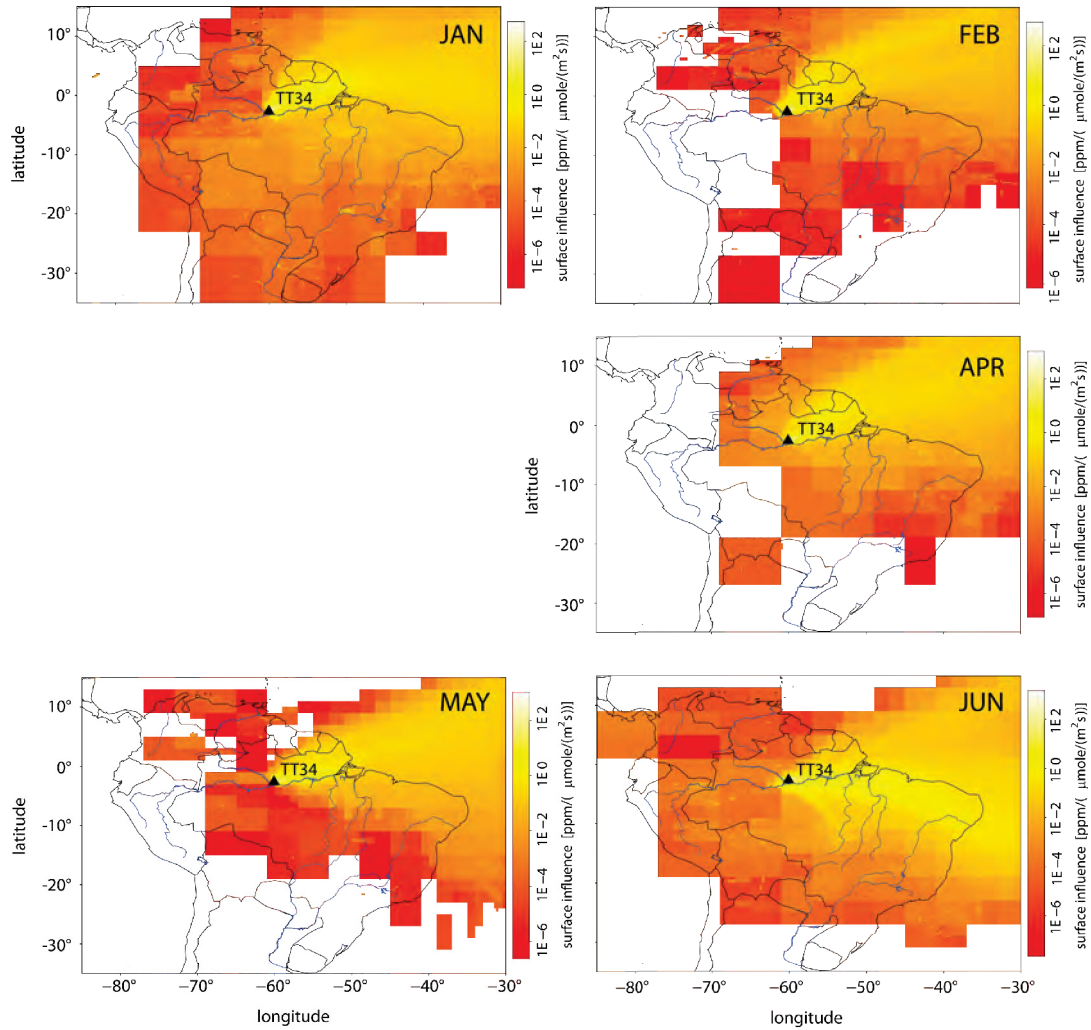


Figure A.20: Monthly integrated footprints of the TT34 tower from January 2009 to June 2009. For March 2009 no footprint is available because of no TT34 tower observations are available. Note that the scale is logarithmic.



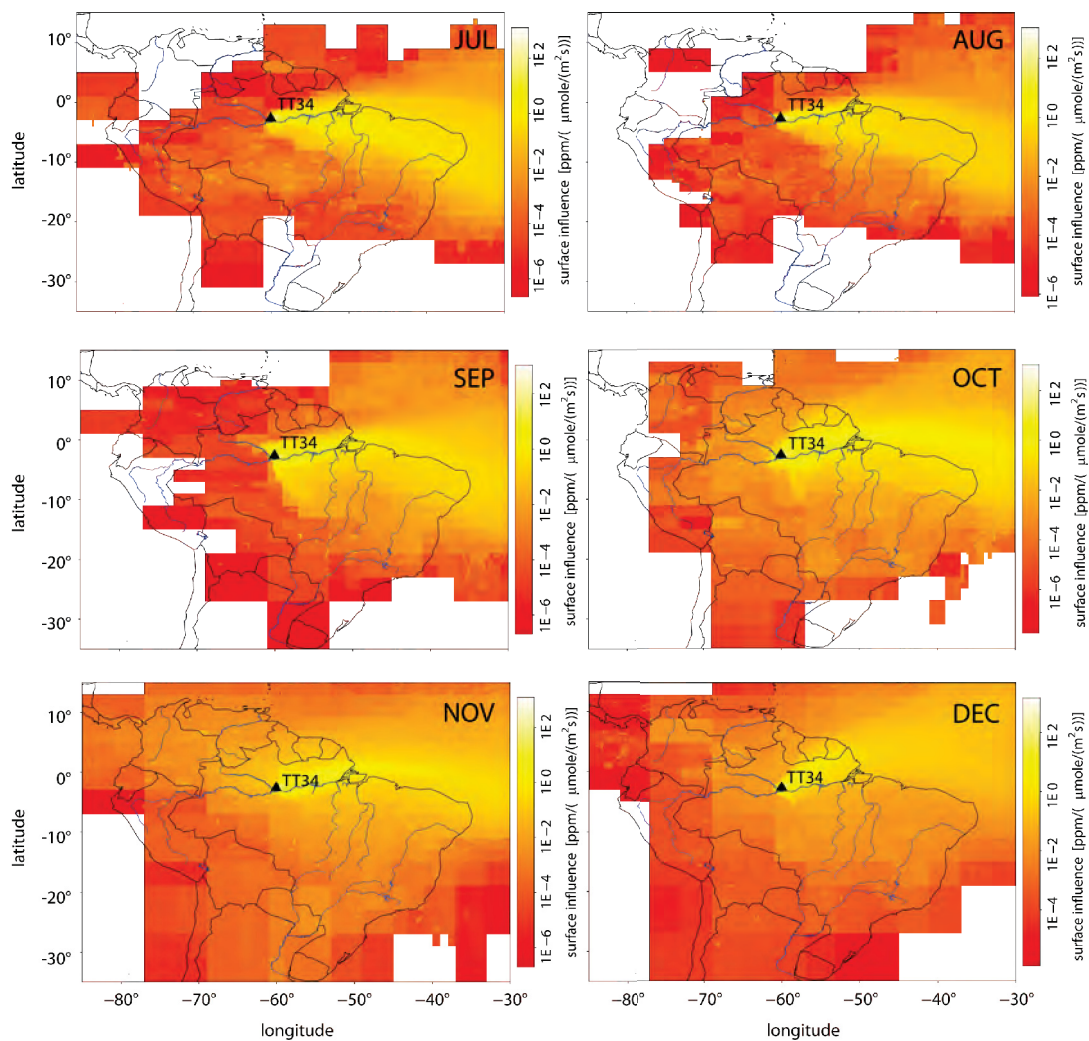


Figure A.21: Monthly integrated footprints of the TT34 tower from July 2009 to December 2009. Note that the scale is logarithmic.

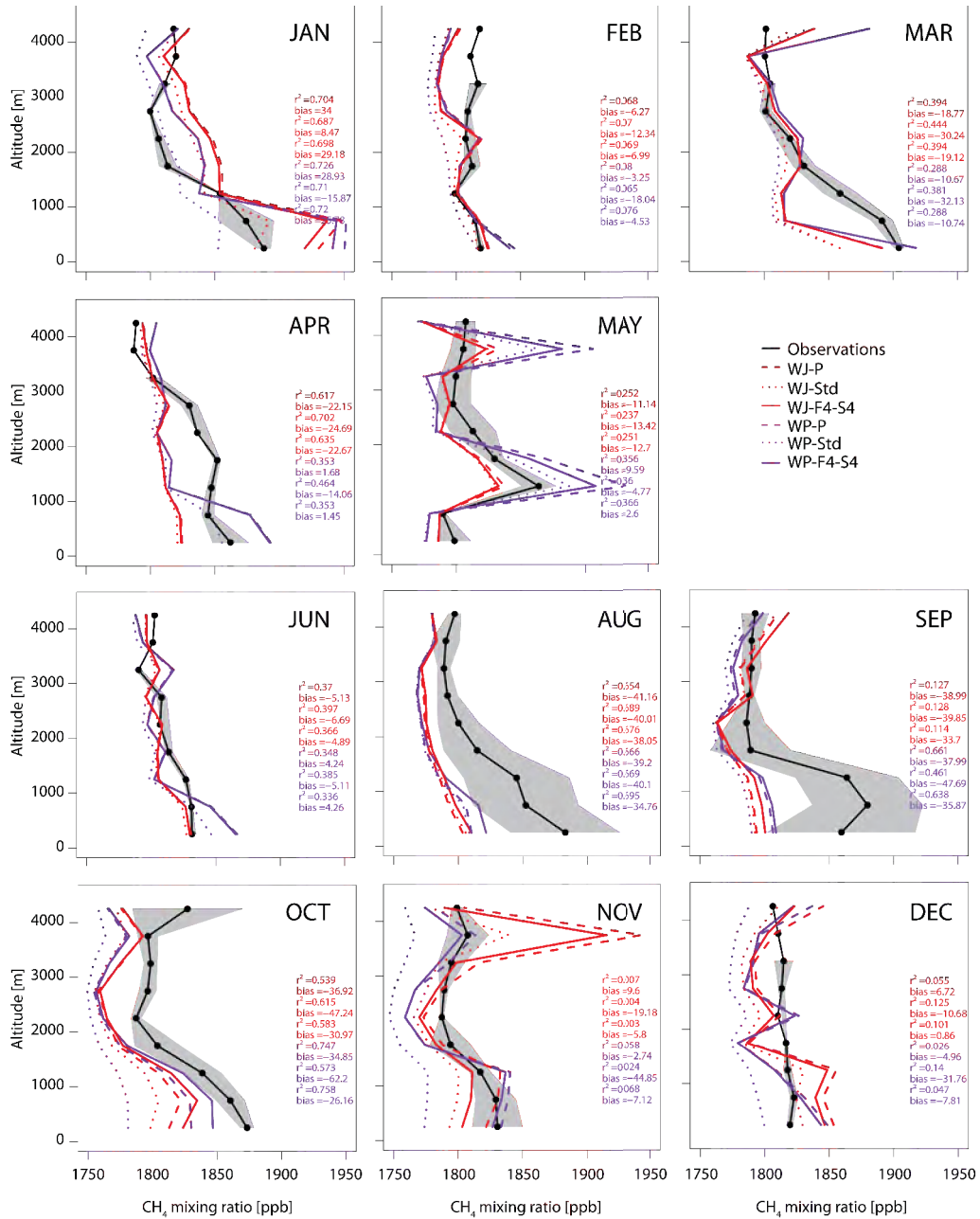


Figure A.22: Comparison of monthly airborne profiles (black) obtained close to the city of Santarém ( $-54.9^\circ\text{W}$ ,  $-2.5^\circ\text{S}$ ) during the year 2009 to simulated  $\text{CH}_4$  mixing ratios from regional TM3-STILT inversions with different temporal and spatial correlation lengths. For the two different a-priori flux distributions WP and WJ, the simulated  $\text{CH}_4$  mixing ratio of the a-priori flux (P), the a-posteriori flux with the standard inversion (Std), and the shortened temporal and spatial correlation lengths (F4-S4) are shown. The bias and  $r^2$  values correspond to all observations of the one or two profiles within the corresponding month. The order of bias and  $r^2$  for the different simulations is identical to the order of the legend.

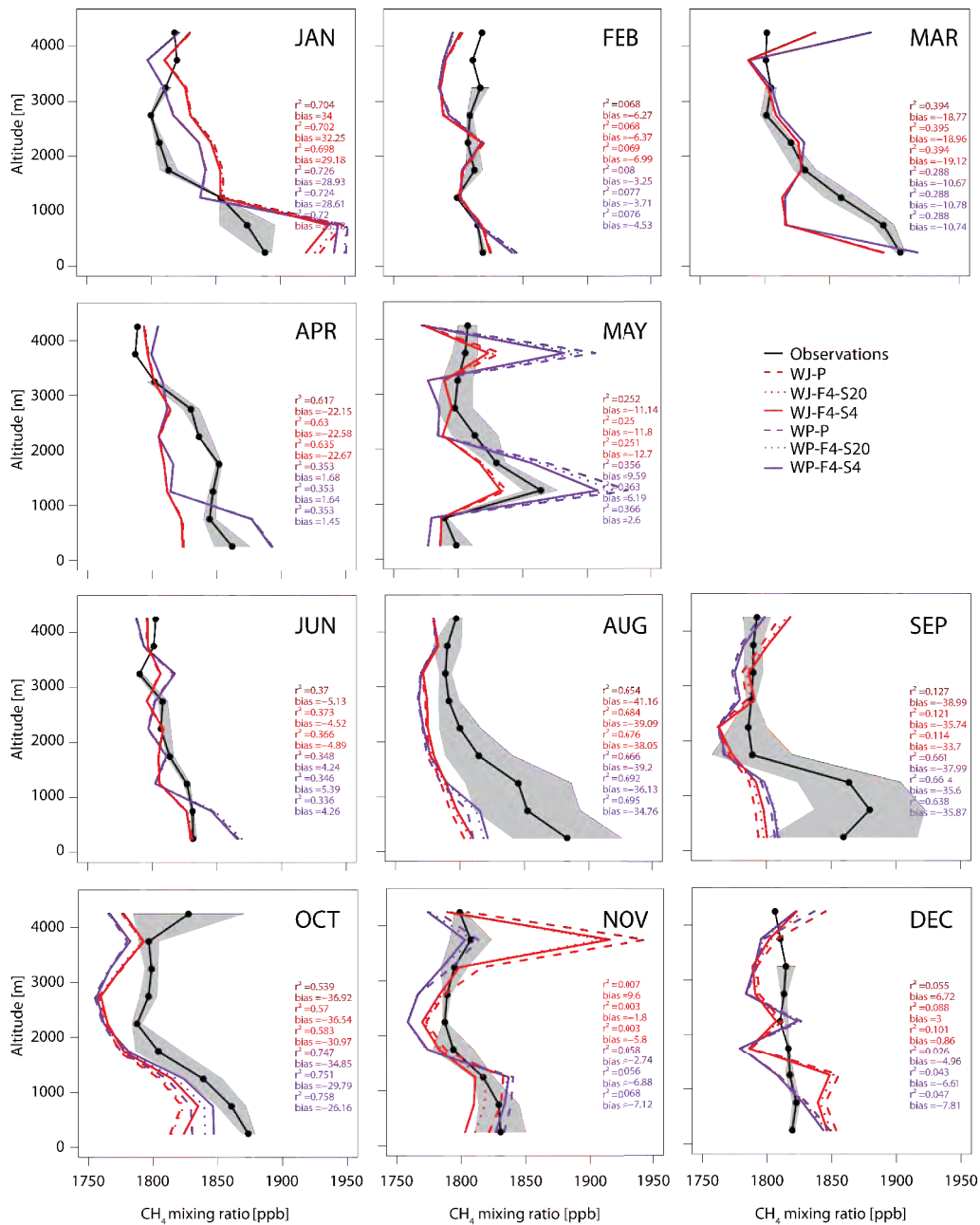


Figure A.23: Comparison of monthly airborne profiles (black) obtained close to the city of Santarém ( $-54.9^\circ\text{W}$ ,  $-2.5^\circ\text{S}$ ) during the year 2009 to simulated  $\text{CH}_4$  mixing ratios from regional TM3-STILT inversions with different temporal and spatial correlation lengths. For the two different a-priori flux distributions WP and WJ, the simulated  $\text{CH}_4$  mixing ratio of the a-priori flux (P), the a-posteriori flux with the shortened temporal and spatial correlation lengths (F4-S4), and the additionally shortened spatial correlation length (F4-S20) are shown. The bias and  $r^2$  values correspond to all observations of the one or two profiles within the corresponding month. The order of bias and  $r^2$  for the different simulations is identical to the order of the legend.

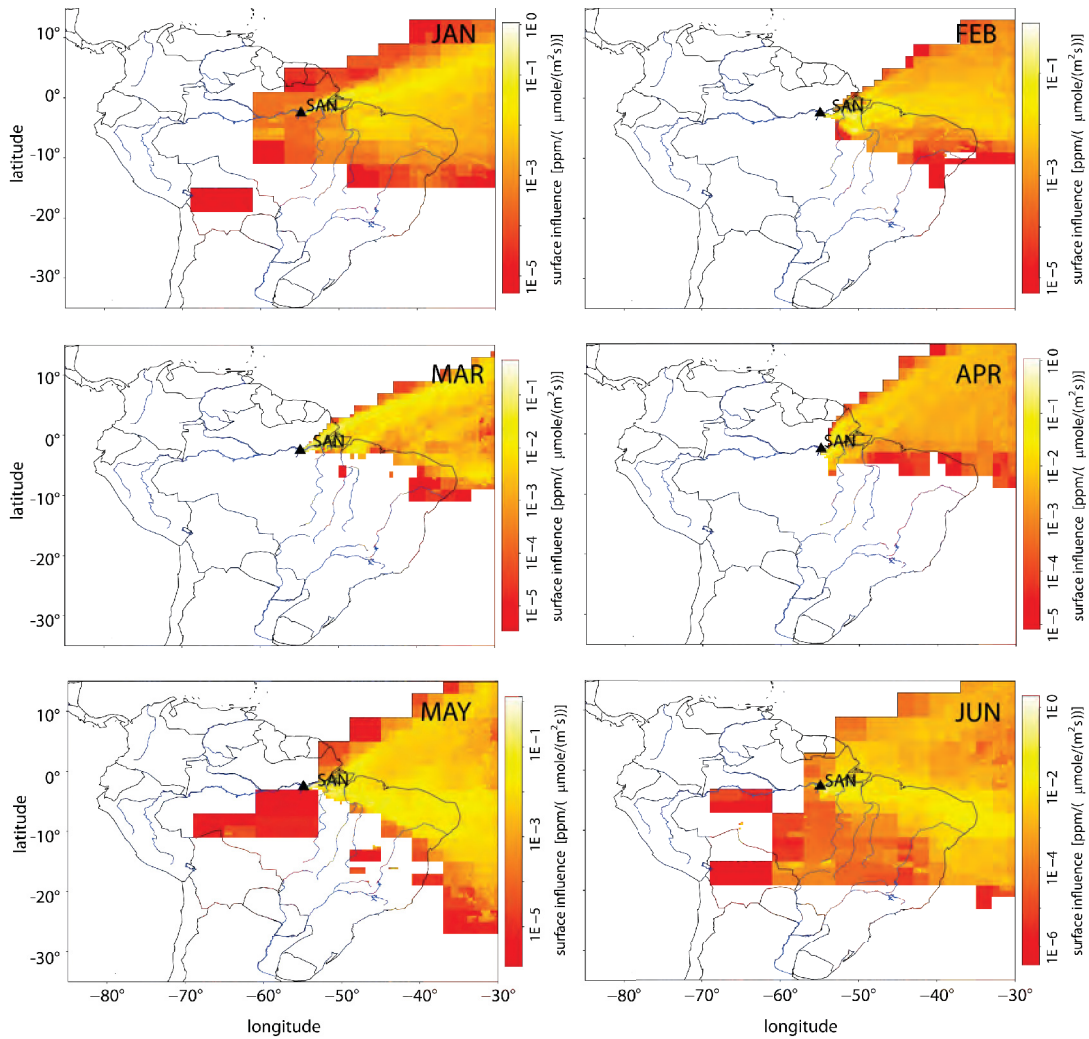


Figure A.24: Monthly integrated footprints of the Santarém airborne profiles from January 2009 to June 2009. Note that the scale is logarithmic.

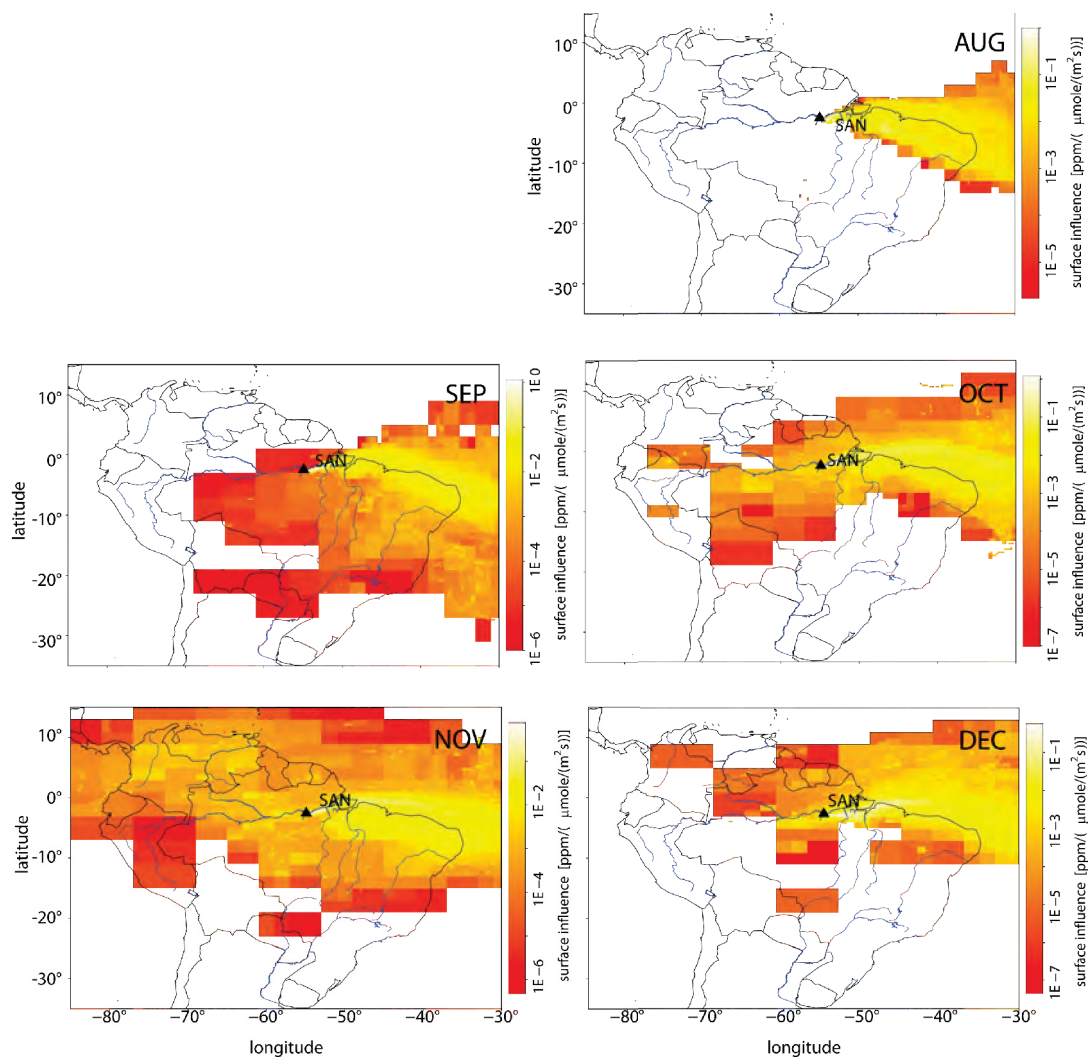


Figure A.25: Monthly integrated footprints of the Santarém airborne profiles from August 2009 to December 2009. For July 2009, no airborne profiles were conducted. Note that the scale is logarithmic.



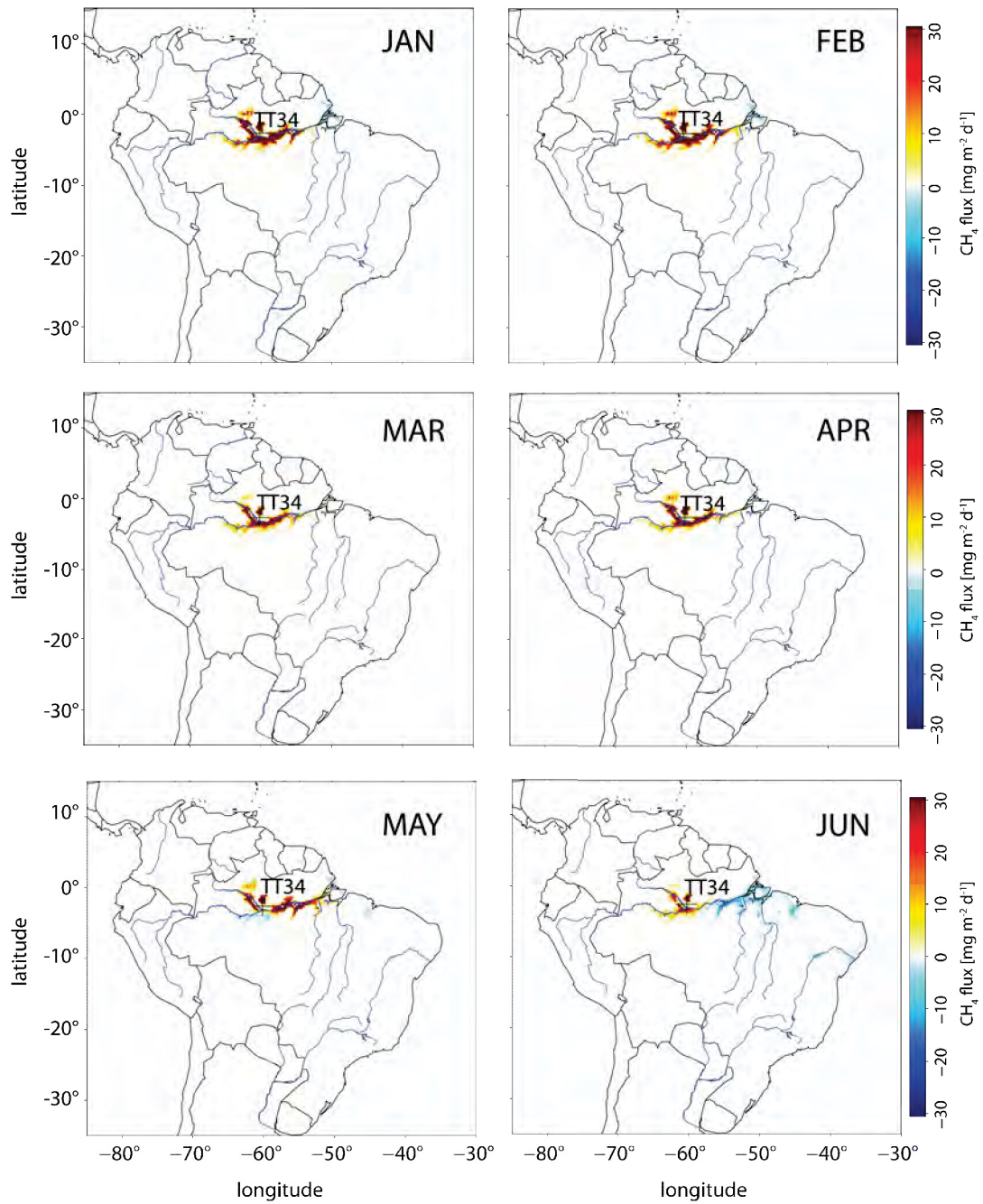


Figure A.26: Monthly difference between a-priori and a-posteriori flux distribution for the WP-F4-S4 regional inversion set up for the first half of the year 2009. For the calculation  $\mu = 0.06$  was used.

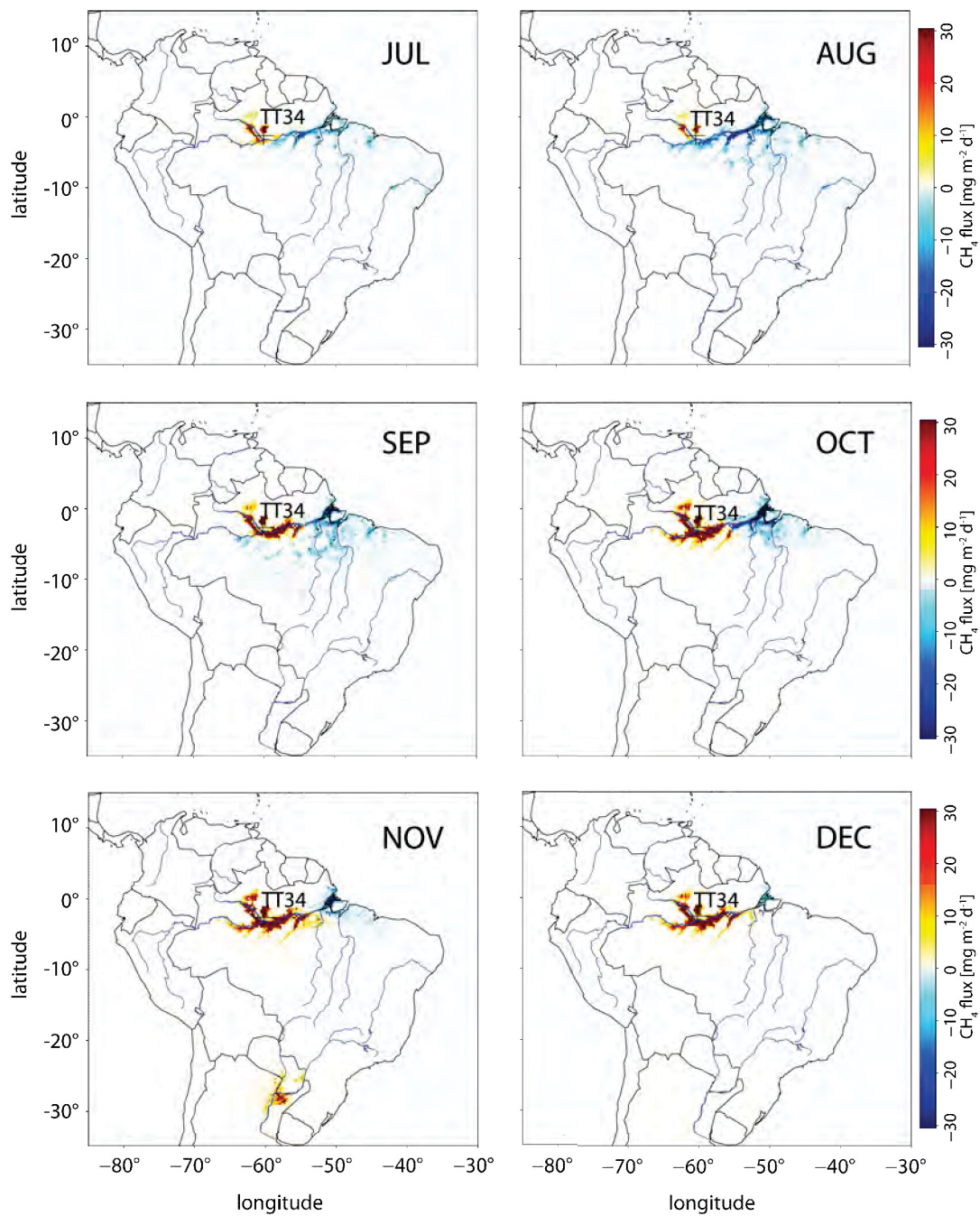


Figure A.27: Monthly difference between *a-priori* and *a-posteriori* flux distribution for the WP-F4-S4 regional inversion set up for the second half of the year 2009. For the calculation  $\mu = 0.06$  was used.

Acronym	Latitude [°]	Longitude [°]	Altitude [m a.s.l.]	Name & Country
ALT	82.45	-62.52	210	Alert, Nunavut, Canada
ASC	-7.92	-14.42	54	Ascension Island, UK
ASK	23.18	5.42	2728	Assekrem, Algeria
AZR	38.77	-27.38	40	Terceira Island, Azores, Portugal
BMW	32.27	-64.88	30	Tudor Hill, Bermuda, UK
BRW	71.32	-156.60	11	Barrow, Alaska, USA
CBA	55.20	-162.72	25	Cold Bay, Alaska, USA
CHR	1.70	-157.17	3	Christmas Island, Republic of Kiribati
CRZ	-46.45	51.85	120	Crozet Island, France
EIC	-27.15	-109.45	50	Easter Island, Chile
GMI	13.43	144.78	6	Mariana Islands, Guam
HBA	-75.58	-26.50	33	Halley Station, Antarctica, UK
ICE	63.34	-20.29	127	Heimay, Vestmannaeyjar, Iceland
IZO	28.30	-16.48	2360	Tenerife, Canary Islands, Spain
KUM	19.52	-154.82	3	Cape Kumukahi, Hawaii, USA
KZM	43.25	77.88	2519	Plateau Assy, Kazakhstan
MID	28.22	-177.37	8	Sand Island, Midway, USA
MLO	19.53	-155.58	3397	Mauna Loa, Hawaii, USA
NWR	40.05	-105.58	3526	Niwot Ridge, Colorado, USA
PSA	-64.92	-64.00	10	Palmer Station, Antarctica, USA
RPB	13.17	-59.43	45	Ragged Point, Barbados
SEY	-4.67	55.17	7	Mahe Island, Seychelles
SHM	52.72	174.10	40	Shemya Island, Alaska, USA
SMO	-14.23	-170.57	42	Tutuila, American Samoa, USA
SPO	-89.98	-24.80	2810	South Pole, Antarctica, USA
STM	66.00	2.00	5	Ocean station M, Norway
SUM	72.58	-38.48	3238	Summit, Greenland, Denmark
SYO	-69.00	39.58	14	Syowa Station, Antarctica, Japan
TDF	-54.87	-68.48	20	Isla Redonda, Tierra Del Fuego, Argentina
UUM	44.45	111.10	914	Ulaan Uul, Mongolia
WLG	36.29	100.90	3810	Mt. Waliguan, People's Republic of China
ZEP	78.90	11.88	475	Ny-Ålesund, Spitsbergen, Norway

Table A.1: Surface stations of  $CH_4$  observations used for the global TM3  $CH_4$  inversion (based on Bergamaschi et al. [2009]).

## Appendix B

# List of acronyms and symbols

### Units

Acronym	Meaning
m	Meter
km	Kilometer
cm	Centimeter
mm	Millimeter
$\mu\text{m}$	Micrometer
$\text{m}^2$	Square meter
$\text{km}^2$	Square kilometer
$\text{km}^3$	Cubic kilometer
g	Gram
kg	Kilogram
Tg	Teragram
mg	Milligram
s	Second
min	Minute
h	Hour
d	Day
mo	Month
a	Year
mole	Mole
ppm	Parts per million ( $\mu\text{mole mole}^{-1}$ )
ppb	Parts per billion ( $\text{nmole mole}^{-1}$ )
ppt	Parts per trillion ( $\text{pmole mole}^{-1}$ )
Hz	Hertz
GHz	GigaHertz
J	Joule
W	Watt
$^{\circ}\text{C}$	Degree Celsius
K	Kelvin
Gt C	Gigatons carbon

## Chemical species

Acronym	Name
CaCO <sub>3</sub>	Calcium carbonate
CH <sub>2</sub> O	Average composition of biomass material Formaldehyde
CH <sub>3</sub>	Methyl radical
CH <sub>3</sub> O	Methoxide ion
CH <sub>3</sub> O <sub>2</sub>	Methylperoxy radical
CH <sub>3</sub> O <sub>2</sub> H	Methyl hydrogen peroxide
CH <sub>3</sub> COOH	Acetic acid
CH <sub>4</sub>	Methane
<sup>13</sup> CH <sub>4</sub>	Isotopic <sup>13</sup> C carbon in CH <sub>4</sub>
<sup>14</sup> CH <sub>4</sub>	Isotopic <sup>14</sup> C carbon in CH <sub>4</sub>
Cl	Chloride
CO	Carbon monoxide
CO <sub>2</sub>	Carbon dioxide
D	Deuterium
<sup>2</sup> H	Isotopic hydrogen in CH <sub>4</sub>
H <sub>2</sub>	Molecular hydrogen
HCl	Hydrogen chloride
H <sub>2</sub> O	Water/water vapor
H <sub>2</sub> O <sub>2</sub>	Hydrogen peroxide
HO <sub>2</sub>	Radical component of H <sub>2</sub> O <sub>2</sub>
NO	Nitric oxide
NO <sub>2</sub>	Nitrogen dioxide
NO <sub>x</sub>	Nitrous oxides
O( <sup>1</sup> D)	Oxygen radical in the 1D (excited) state
O <sub>2</sub>	Molecular oxygen
O <sub>3</sub>	Ozone
OH	Hydroxyl radical
SF <sub>6</sub>	Sulphur hexafluoride
SO <sub>4</sub> <sup>2-</sup>	Sulfate



## Physical Variables

Notation	Meaning
<b>A</b>	Transport operator
$a_{fire}$	Size of burned area per fire
$a_l$	Real coefficient for pressure level calculation
$A_{xy}$	Least square estimator for linear regression model
$b_l$	Real coefficient for pressure level calculation
$B_{xy}$	Least square estimator for linear regression model
$Bud_{mo,k}$	Monthly budget of sampling region $k$
$C$	Atmospheric mixing ratio
$[C]_{biomass}$	Carbon concentration in biomass burned
$C_{ini}$	Initial atmospheric mixing ratio
$C_{mod}$	Modeled atmospheric mixing ratio
$C_{obs}$	Observed atmospheric mixing ratio
$c_p$	Specific heat of air at constant pressure
$c_v$	Specific heat of air at constant volume
$\Delta CO_2$	Difference in atmospheric mixing ratio $CO_2$
$CO_{2,b}$	Atmospheric $CO_2$ background mixing ratio
$CO_{2,obs}$	Observed atmospheric $CO_2$ mixing ratio
$Cov$	Covariance
$d_{mean(TM5,obs)}$	Mean TM5 model-BARCA observation mismatch
$d_{TM5,obs}$	TM5 model-BARCA observation mismatch
$EF_{CO_2}$	Emission factor of $CO_2$
$EF_X$	Emission factor of tracer $X$
$ER_{XCO_2}$	Emission ratio of tracer $X$ and reference tracer $CO_2$
<b>f</b>	Flux
$f_{ad}$	Adjustable flux term
$f_{fix}$	Fixed flux term
$f_{post}$	A-posteriori flux
$f_{sh}$	Shape function
$F_U, F_V, F_W, F_\Theta$	Forcing terms WRF
$FP$	Footprint
$g$	Standard gravity
$G_{tcor}$	Temporal correlation factor
$G_{xycor}$	Spatial correlation factor
$h$	Planck constant
$h_m$	Height
$I$	Influence function
$I_{conf}$	Confidence interval
$J$	Cost function

Notation	Meaning
$m_{air}$	Air mass
$M_X$	Released mass of tracer $X$ within biomass burning process
$M_C$	Released mass of carbon emitted during a biomass burning process
$MW_X$	Molecular weight of tracer $X$
$MW_{CO_2}$	Molecular weight of $CO_2$
$M_X^{fire}$	Emitted mass of tracer $X$ during fire
$N_{com}$	Different components of the total flux field
$n_k$	Number of footprints with receptor point in sampling region $k$
$N_{tot}$	Total number of released particles
$P$	Probability
$p$	Pressure
$p_0$	Reference pressure
$p_h$	Hydrostatic pressure
$p_{ht}$	Pressure at model top
<b>P<sub>inv</sub></b>	Inversion parameter set
$p_l$	Pressure at level $l$
$p_s$	Surface pressure
<b>Q<sub>c</sub></b>	Error covariance matrix
$r$	Pearson product-moment correlation coefficient
$r^2$	Squared correlation coefficient
$R_0$	Measure for amount and quality of substrate availability, tuning parameter in the Walter wetland model
$R_d$	Gas constant for dry air ( $8.314 \text{ J mol}^{-1} \text{ K}^{-1}$ )
$R_{SA}$	Isotopic composition of the sample
$R_{ST}$	Isotopic composition of the reference sample
$R(\Delta t)$	Random autocorrelation coefficient
$S$	Source term
$SE$	Standard error of the mean
$t$	Time
$t_0$	Initial time
$T_L$	Lagrangian time scale
$t_r$	Time at receptor point
$TFP$	Total integrated footprint
$u$	Wind velocity component in horizontal $x$ direction
$v$	Wind velocity component in horizontal $y$ direction
<b>v</b>	Velocity vector
<b>V = (U, V, W)</b>	Velocity vector in flux form
$Var$	Variance
$w$	Wind velocity component in vertical direction
$w'$	Fluctuations of the vertical wind velocity component
$\bar{x}$	Mean value of $x$
$x_b$	Bias
<b>x</b>	Position vector

Notation	Meaning
$\mathbf{x}_r$	Receptor point position vector
$\overline{x_W}$	Weighted mean value of $x$
$X$	Tracer variable
$\Delta X$	Difference in atmospheric mixing ratio of tracer $X$
$X_b$	Atmospheric background mixing ratio of tracer $X$
$X_{obs}$	Observed atmospheric mixing ratio of tracer $X$
$\alpha$	Inverse air density
$\alpha_{inv}$	Overall scaling factor for adjustable flux term
$\alpha_{veg}$	Available above ground biomass for burning
$\beta_{inv}$	Scaling factor for a-priori flux term
$\beta_{veg}$	Combustion fraction
$\gamma$	Ratio of heat capacity for dry air
$\delta$	$\delta$ notation for isotopes
$\partial$	Partial derivative
$\eta$	Hydro-static pressure vertical coordinate
$\theta$	Potential temperature
$\lambda$	Wavelength
$\mu$	Scaling factor for impact of a-priori distribution
$\mu_{mod}$	Mass per unit area
$\nu$	Frequency
$\Phi$	Geopotential
$\rho_{air}$	Air density
$\rho_{CH_4}$	Density of $CH_4$ atmospheric mixing ratio
$\overline{\rho_{CH_4}}$	Mean density of $CH_4$ atmospheric mixing ratio
$\rho'_{CH_4}$	Fluctuations of the density of $CH_4$ atmospheric mixing ratio
$\rho_{part}$	Particle density
$\overline{\rho_{part}}$	Average particle density below $h_m$
$\sigma$	Standard deviation
$\sigma_f$	A-priori flux uncertainty
$\sigma_{mod}$	Model uncertainty
$\sigma_{obs}$	Observation uncertainty
$\sigma_{tot}$	Total uncertainty
$\tau$	Lifetime of $CH_4$ in the atmosphere

## Numerical Variables

Notation	Numerical notation	Meaning
$b$	b_f	Parameter for soil
$biom$	biomt_par, biom	Biomass of termites
$C_0$	methane_0	Atmospheric CH <sub>4</sub> mixing ratio
$C_{soil}$	concout	CH <sub>4</sub> Concentration in soil
$CH_{4,term}$	uo CH4_term	CH <sub>4</sub> termite emissions
$CH_{4,veg}$	ebio (p_ch4term)	CH <sub>4</sub> emission from vegetation
$CH_{4,wet}$	CH4_vegetation CH4_wet	CH <sub>4</sub> wetland emissions
$D_{air}$	ebio (p_ch4wet)	Diffusivity of CH <sub>4</sub> in free air
$D_{soil}$	dch4_0	Diffusivity of CH <sub>4</sub> in top soil
$emiss_{day}$	dch4	Day CH <sub>4</sub> vegetation emission
$emiss_{night}$	emis_day	Night CH <sub>4</sub> vegetation emission
$et$	emis_night	Evapotranspiration
$f_{diff}$	sfevap	CH <sub>4</sub> diffusive flux
$f_{SM}$	flux_diff	Soil moisture factor
$f_{term}$	f_SM	CH <sub>4</sub> flux emitted by termites
$FAPAR_{PAV}$	emit_par emch4	Fraction of PAR absorbed by PAV
$G_{soil}$	vprm_in (p_evi)	Factor accounting for effect of soil structure
$G_T$	G_soil	Factor accounting for effect of temperature
$g(T_{soil})$	G_t	Soil temperature dependence of KWI
$GEE$	g_T	Gros Ecosystem Exchange
$h_r$	GEE_frac	Heterotrophic respiration
$I_{clay}$	HR	Clay content of soil
$I_{cult}$	clay_c	Measure of cultivation activity
$I_{sand}$	i_cult	Sand content of soil
$J_{CH_4}$	sand_c	CH <sub>4</sub> flux into the soil
$k_0$	soil_flux	Base oxidation rate
$k_d$	k_0	First-order oxidation rate in soil
$K_m$	k_d	Michaelis-Menten coefficient (5 $\mu$ M)
$k_r$	goxid	Carbon decomposition rate
$K_{soil}$	rkm	Unit conversion factor
	k_r	
	conv_Fk	

Notation	Numerical notation	Meaning
$NPP_{max}$	inppm	Maximum available substrate
$NPP_{org}$	inppt	Substrate availability
$NPP_{var}$	fin	Seasonal availability of substrate
$P_i$	P_1	Weighting factor
$P_{scale}$	Pscale	Variable accounting for the effect of leaf age on photosynthesis
$PAR_0$	rad0	Half-saturation value of PAR
$pcp$	rain_1 rain_2	Precipitation
$Q_{ebull}$	fluxbub	CH <sub>4</sub> ebullition flux rate
$Q_{plant}$	fluxplant	CH <sub>4</sub> plant-mediated transport rate
$r_N$	r_n	Cultivation factor
$R_{prod}$	wpro	CH <sub>4</sub> production rate
$r_{SM}$	r-sm	Soil moisture factor
$r_T$	vero	Temperature factor
$Resp$	RESP_frac	Respiration
$sm$	sm_tot sm_02	Soil moisture
$sm_{sat}$	soil_sat	Saturated soil moisture
$T$	Tair	(air) Temperature
$T_a$	T_a	Mean annual temperature
$T_{a,soil}$	tmean	Mean annual soil temperature
$T_{max}$	Tmax	Maximum temperature
$T_{min}$	Tmin	Minimum temperature
$T_{opt}$	Topt	Optimal temperature
$T_{scale}$	Tscale	Temperature dependence of photosynthesis
$T_{soil}$	T_soil rtd	Soil temperature
$V_m$	xvmax	Michaelis-Menten coefficient (20μM)
$V_p$	phi_soil	Total pore volume
$V_{thresh}$	rcmax	Threshold for CH <sub>4</sub> concentration in water
$W_{scale}$	Wscale	Variable accounting for the effect of water stress
$w_{flood}$	M_s	Floodplain scaling factor
$w_{peat}$	E_f	Peatland scaling factor
$z_d$	z_dsoil	Soil depth
$\alpha_v$	alpha	Adjustable VPRM parameter
$\beta_v$	RESP0	Adjustable VPRM parameter
$\epsilon$	eps	Air-filled porosity
$\lambda_v$	lambda	Maximum quantum yield
$\tau_0$	tau_10	Turnover time of fast carbon pool



**WRF specific variables**

Acronym	Meaning
chem	WRF-Chem 3D tracer variable
chem_source	WRF-Chem 2D flux variable
conv_rho	WRF-Chem conversion factor
CPOOL	Carbon pool
d01	30 km WRF coarse simulation domain
d02	10 km WRF nested simulation domain
dt	Time step
dz8	Height first model layer
ISLTYP	Soil type
LANDUSE	Landuse type
POTEVP	Potential evapotranspiration
RAINC	Precipitation from cumulus scheme
RAINNC	Precipitation from microphysics scheme
rho	Air density
SMOIS	Soil moisture
SWDOWN	Shortwave downward radiation
T2	2 m temperature
TSK	Skin temperature
WETMAP	Wetland inundation map

## Acronyms

Acronym	Meaning
3BEM	Brazilian Biomass Burning Emission Model
4DVAR	four Dimensional VARIational assimilation
<b>A</b>	
ABLE2	Amazon Boundary Layer Experiment
ABP	Arembepe
AGAGE	Advanced Global Atmospheric Gas Experiment
AMAZONICA	AMAZON Integrated Carbon Analysis project
AIRS	Atmospheric InfraRed Sounder
AP-CT	A-priori fluxes Carbon Tracker methane
AP-PB	A-priori fluxes TM5 simulations P. Bergamaschi
AP-SH	A-priori fluxes TM5 simulations S. Houweling
APR	April
ARW	Advanced Research WRF
ASC	Ascension Island
ATTO	Amazonian Tall Tower Observatory
AUG	August
AVHRR	Advanced Very High Resolution Radiometer
<b>B</b>	
BARCA	Balanco Atmosférico Regional de Carbono na Amazônia
BARCA-A	Airborne campaign within the BARCA project in November 2008
BARCA-B	Airborne campaign within the BARCA project in May 2009
BDS	Barbados
BETHY	Biosphere Energy Transfer and HYdrology model
BRAMS	Brazilian developments on the Regional Atmospheric Modeling System
BZ	Brazil
<b>C</b>	
CarbonSat	Carbon monitoring Satellite
CARIBIC	Civil Aircraft for Regular Investigation of the Atmosphere Based on an Instrument Container project
CCDAS	Carbon Cycle Data Assimilation System
CERES	Carbo Europe Regional Experiment Strategy
cg	coarse grid
CHIOTTO	Continuous HIGH-precisiOn Tall Tower Observations of green-house gases

Acronym	Meaning
COBRA	CO <sub>2</sub> Budget and Rectification Airborne study
CONTRAIL	Comprehensive Observation Network for Trace gases by Air-Liner
CRDS	Cavity Ringdown Spectroscopy technique
CSIRO	Commonwealth Scientific and Industrial Research Organization
<b>D</b>	
DEC	December
DMSF	Defense Meteorological Satellite Programm
DoI	Domain of Interest
<b>E</b>	
ECHAM	Global atmospheric circulation model
ECMWF	European Center for Medium-range Weather Forecast
EDGAR	Emission Database of Global Atmospheric Research
EF	Emission Factor
ENSO	El Niño Southern Oscillation
ENVISAT	European Space Agency ENVironmental SATellite
EPA	Environmental Protection Agency
ER	Emission Ratio
ERA-Interim	“Interim” ECMWF reanalysis
ERS	European Remote Sensing satellite
ESRL	Earth System Research Laboratory
ETOPO5	Earth Topography 5 min
EVI	Enhanced Vegetation Index
<b>F</b>	
FAST4x	temporal correlation length of one week
FEB	February
fg	fine grid
FLAT	a-priori CH <sub>4</sub> flux distribution of regional inversion using a constant CH <sub>4</sub> flux of 13 mg m <sup>-2</sup> d <sup>-1</sup>
FLAT-F4-S4	regional inversion with FLAT a-priori flux one week temporal and ~160 km spatial correlation length
FLAT-F4-S20	regional inversion with FLAT a-priori flux one week temporal and ~32 km spatial correlation length
FLAT-P	STILT forward simulation with FLAT a-priori flux
FLAT-Std	standard regional inversion with FLAT a-priori flux
FLT	Flight
FP	Full time Period
FT	lower Free Troposphere
FTS	Fourier-Transform Spectrometer
<b>G</b>	
G3	Grell 3 convective scheme
GAW	Global Atmospheric Watch
GC-FID	Gas Chromatography Flame Ionization Detector
GCM	Global Circulation Model
GD	Grell-Dévényi convective scheme
GEE	Gros Ecosystem Exchange

Acronym	Meaning
GEMS	Global and regional Earth-system (atmosphere) Monitoring using Satellite and in-situ data
GFED	Global Fire Emission Database
GHCN	Global Historical Climatology Network
GOES	Geostationary Operational Environmental Satellite
GOES WF_ABBA	Geostationary Operational Environmental Satellite - Wildfire Automated Biomass Burning Algorithm
GOSAT	Greenhouse gas Observing SATellite
GPCP	Global Precipitation and Climatology Project
GPNR	GPCP and TRMM based precipitation product
<b>H</b>	
HALOE	HALogen Occultation Experiment
HIPPO	HIAPER Pole-to-Pole Observations
HYSPLIT	HYbrid Single-Particle Lagrangian Integrated Trajectory
<b>I</b>	
IAGOS	In-service Aircraft for a Global Observing System
IAV	Interannual variability
ICOS	Integrated Carbon Observing System
IMAPv5.5	SCIAMACHY SRON retrievals version 5.5
IMAU	Institute for Marine and Atmospheric Research, Utrecht
INPE	Instituto Nacional de Pesquisas Espaciais
IPCC	Intergovernmental Panel on Climate Change
IPEN	Instituto de Pesquisas Energeticas Nucleares
ITCZ	InterTropical Convergence Zone
<b>J</b>	
JAN	January
JERS-1SAR	Japanese Earth Resources Satellite 1 Synthetic Aperture Radar
JUN	June
JUL	July
<b>K</b>	
K34	55 m high tower located 60 km north-west of Manaus
KWI	Kaplan Wetland Inventory
<b>L</b>	
LANDSAT	LAND remote sensing SATellite program
LBA	Large-scale Biosphere-Atmosphere experiment in Amazonia
LBA-CLAIRE	Cooperative LBA Airborne Regional Experiment
LPDM	Lagrangian Particle Dispersion Model
LPJ model	Lund-Jena-Postdam model
LPJ-WHyMe	LPJ Wetland Hydrology Methane model
LSWI	Land Surface Water Index
<b>M</b>	
MACC	Monitoring Atmospheric Composition and Climate
MAR	March
MAY	May

Acronym	Meaning
MCS	Mesoscale Convective System
MEI	Multivariate El Niño Index
MERLIN	Methane Remote Sensing Lidar Mission
MM5	PSU/NCAR mesoscale model
MODIS	Moderate Resolution Imaging Spectroradiometer
MOZAIC	Measurement of OZone and water vapour by Airbus In-service airCRAFT
MPI-BGC	Max Planck Institute for BioGeoChemistry
MYJ	Mellor-Yamada-Janjic PBL scheme
MYNN	Mellor-Yamada-Nakanishi-Niino PBL scheme
<b>N</b>	
N	North
NCAR	National Center of Atmospheric Research
NCEP	National Center for Environmental Protection
NDVI	Normalized Differenced Vegetation Index
NEE	Net Ecosystem Exchange
NITROEUROPE	The nitrogen cycle and its influence on the European greenhouse gas balance
NOAA	National Oceanic and Atmospheric Administration
NOAH-LSM	NOAH Land Surface Model
NOV	November
NPP	Net Primary Productivity
<b>O</b>	
OCT	October
<b>P</b>	
PAR	Photosynthetically Active Radiation
PAV	Photosynthetically Active portion of Vegetation
PBL	Planetary Boundary Layer
PDB	Pee Dee Belemnite
PDF	Probability Density Function
PoI	Period of Interest
PROVEG	atualização da representação da vegetação nos modelos numéricos
PSU	Pennsylvania State University
<b>Q</b>	
Q <sub>10</sub> approach	ratio of temperature responses with two temperatures of 10 K difference
<b>R</b>	
RADAR	RADio Detection And Ranging
RPB	Ragged Point Barbados
RRTM	Rapid Radiative Transfer Model
RRTMG	further development of RRTM
<b>S</b>	
S	South
SAR	Synthetic Aperture Radar
SAN	Santarém stationary airborne profiles
SCAR-B	Smoke, Clouds, And Radiation study



Acronym	Meaning
SCIAMACHY	SCanning Imaging Absorption spectroMeter for Atmospheric ChartographY
SEP	September
SHORT4x	spatial correlation length of ~160 km
SHORT20x	spatial correlation length of ~32 km
SMOW	Standard Mean Ocean Water
SRON	Netherlands Institute for Space Research
SSM/I	Special Sensor Microwave/Images
STILT	Stochastic Time Inverted Lagrangian Transport Model
STILT-ERA	STILT simulation with ERA-Interim driven wetland fluxes
<b>T</b>	
TCCON	Total Carbon Column Observation Network
TKE	Turbulent Kinetic Energy
TM2	Tracer transport Model version 2
TM3	Tracer transport Model version 3 also: global CH <sub>4</sub> inversion
TM3-P	TM3 simulation with a-priori fluxes
TM3-STILT	Jena two-step regional inversion scheme
TM3-TT34	global CH <sub>4</sub> inversion with TT34 observational constraints
TM5	Tracer transport Model version 5
TM5-CT	Carbon Tracker methane
TM5-PB	TM5 simulations P. Bergamaschi
TM5-PB-SCI	TM5 simulation P. Bergamaschi using SCIAMACHY observations
TM5-SH	TM5 simulations S. Houweling
TM5-SH-SCI	TM5 simulation S. Houweling using SCIAMACHY observations
TransCom	chemistry Transport model interComparison
TRMM	Tropical Rainfall Monitoring Mission
TRMM 3B42	3 h TRMM precipitation product
TROFFEE	Tropical Forest and Fire Emissions Experiment
TT34	35 m high tower located 60 km north-west of Manaus
<b>U</b>	
UK	United Kingdom
US	United States of America
USGS	U.S. Geological Survey
UTC	Universal Time Coordinated
UV	ultraviolet
<b>V</b>	
vfg	very fine grid
VPRM	Vegetation Photosynthesis and Respiration Model
<b>W</b>	
W	West

Acronym	Meaning
WJ	a-priori CH <sub>4</sub> flux distribution of regional inversion using WWM and JERS-1SAR wetland inundation map
WJ-F4-S4	regional inversion with WJ a-priori flux one week temporal and ~160 km spatial correlation length
WJ-F4-S20	regional inversion with WJ a-priori flux one week temporal and ~32 km spatial correlation length
WJ-P	STILT forward simulation with WJ a-priori flux
WJ-Std	standard regional inversion with WJ a-priori flux
WKK	WRF-GHG simulations with KWI and Kaplan wetland inundation map
WMO	World Meteorological Organization
WP	a-priori CH <sub>4</sub> flux distribution of regional inversion using WWM and Prigent wetland inundation map
WP-F4-S4	regional inversion with WP a-priori flux one week temporal and ~160 km spatial correlation length
WP-F4-S20	regional inversion with WP a-priori flux one week temporal and ~32 km spatial correlation length
WP-P	STILT forward simulation with WP a-priori flux
WP-Std	standard regional inversion with WP a-priori flux
WPS	WRF Preprocessing System
WRF	Weather Research and Forecasting model
WRF-Chem	Weather Research and Forecasting model with Chemistry
WRF-GHG	WRF GreenHouse Gas model
WRF-NMM	Non-hydrostatic Mesoscale Model
WSM5	WRF Single Moment 5-class scheme
WSM6	WRF Single Moment 6-class scheme
WWK	WRF-GHG simulations with WWM and Kaplan wetland inundation map
WWJ	WRF-GHG simulations with WWM and JERS-1SAR wetland inundation map
WWM	Walter Wetland Model
WWM-ERA	WWM forced by ERA-Interim meteorology
WWM-WRF-Chem	WWM forced by WRF-Chem meteorology
WWP	WRF-GHG simulations with WWM and Prigent wetland inundation map
WWP-ERA	WRF-GHG simulations with WWM forced by ERA-Interim meteorology and Prigent wetland inundation map
<b>X</b>	
xfg	extra fine grid
<b>Z</b>	
ZOTTO	Zotino Tall Tower Observatory

## Appendix C

# Data documentation

All models, model output, data, and analysis programs utilized within this work will be archived in a folder called “Dissertation\_Beck.tar.gz”, which can be requested from the Max Planck Institute for Biogeochemistry, Jena, Germany.

### Plotting routines

Name	Figure
methane.csv	Fig. 2.1
noaa_global_view_data.r	Fig. 2.2
isotopic_composition.r	Fig. 5.6
plot_global_kaplan.r	Fig. 2.5
barplots_precip.r	Fig. 2.7
plot_mei_el_nino.r	Fig. 2.8
read_wetland_map_new.r	Fig. 2.10
plot_wmo_stations.r	Fig. 3.2 and Fig. A.19
plot_wrf_d01_fluxes.r	Fig. 4.5 and Fig. 4.6
flighttrack_barca_paper.r	Fig. 5.1
scatterplots_for_flasks.r	Fig. 5.2 and Fig. 5.5a
ch4_data_fig_2.r	Fig. 5.3
total_tm5_barca_profiles.r	Fig. 5.8
bbm_profile.r	Fig. 5.5b
timeseries_barca_data.r	Fig. 5.7a
overlaid_footprints.r	Fig. 5.7b
stilt_footprint_tm5_budget_plot.r	Fig. 5.9a–b
tm5_influence_weighted_footprints.r	Fig. 5.9c–d
barca_data_6x4_footprints.r	Fig. A.5 and Fig. A.6
plot_global_fluxes_peter.r	Fig. A.1, Fig. A.2, and Fig. A.3
plot_global_fluxes_sander_apos.r	Fig. A.1, Fig. A.2, and Fig. A.3
plot_globale_fluxes_sander_lori.r	Fig. A.1, Fig. A.2, and Fig. A.3

Name	Figure
plot_wrf_domain.m	Fig. 6.1
wetland_map_diff_plot.r	Fig. 6.2
compare_radiosondes.r	Fig. 6.3, Fig. A.7, and Fig. A.8
plot_precip_wrf_trmm.r	Fig. 6.4 and Fig. A.9
plot_wrf_ch4_fluxes.r	Fig. 6.5 and Fig. A.12
plot_wrf_trmm_precip_3hr.r	Fig. 6.6, Fig. A.14, Fig. A.15, Fig. A.16, and Fig. A.17
wrf_cross_sections_scaled_ wetland_fluxes.r	Fig. 6.6
xsecplotdimo_barca.r	Fig. 6.6
wrf_taylor_good_bad.r	Fig. 6.7
wrf_profiles.r	Fig. 6.8
plot_precip_boxes.r	Fig. A.10 and Fig. A.11
plot_precip_footprints.r	Fig. A.14, Fig. A.15, Fig. A.16, and Fig. A.17
plot_wrf_tt34_obs_barca_ab.r	Fig. 7.1a
tt34_surroundings.r	Fig. 7.1b–d
plot_stilt_daily_budget.r	Fig. 7.2a and Fig. 7.11
plot_wrf_tt34_obs.r	Fig. 7.2b, Fig. 7.3
plot_yearly_timeseries_comparison.r	Fig. 7.4a and Fig. 7.7
plot_SAN_data.r	Fig. 7.4b
plot_tt34_footprints.r	Fig. 7.4c
plot_footprints_SAN.r	Fig. 7.4d
tm5_vs_tt34.r	Fig. 7.5
tm3_stilt_taylor.r	Fig. 7.6
stilt_regional_fluxes_plot.r	Fig. 7.8, Fig. A.26, and Fig. A.27
plot_BARCA-B_comparison.r	Fig. 7.9
plot_SAN_comparison.r	Fig. 7.10
plot_tt34_monthly_footprints.r	Fig. A.20 and Fig. A.21
plot_SAN_corr_length.r	Fig. A.22
plot_san_flight_footprint.r	Fig. A.24 and Fig. A.25
WRF_cross_sections_total.r	Fig. A.4 and Fig. A.13
xsecplotdimo_tot.r	Fig. A.4 and Fig. A.13
profiles_global_vs_regional.r	Fig. A.18

## WRF-GHG simulations

Name	Acronym	Description
run_169	WWK	WWK BARCA-A
run_170	WWK	WWK BARCA-B
run_171	WKK	WKK BARCA-B
run_172	WKK	WKK BARCA-A
run_177	-	19 <sup>th</sup> -21 <sup>th</sup> May 2009 simulation with Grell3 convection scheme
run_178	-	19 <sup>th</sup> -21 <sup>th</sup> May 2009 simulation with Kain-Fritsch convection scheme
run_179	-	19 <sup>th</sup> -21 <sup>th</sup> May 2009 simulation with Betts-Miller-Janjic convection scheme
run_180	-	19 <sup>th</sup> -21 <sup>th</sup> May 2009 simulation with Grell-Dévényi convection scheme
run_188	G3+SC	WWJ plus shallow convection option BARCA-A
run_189	G3+SC	WWJ plus shallow convection option BARCA-B
run_194	MYNN	MYNN meteorological set up BARCA-B
run_195	MYNN	MYNN meteorological set up BARCA-A
run_208	WWP	WWP BARCA-A
run_209	WWP	WWP BARCA-B
run_210	WWJ	WWJ BARCA-A
run_211	WWJ	WWJ BARCA-B
run_219	-	30 km d01 only BARCA-B simulation
run_238	WWP-ERA	Simulation with ERA-Interim forced wetland CH <sub>4</sub> fluxes for August 2009
run_240	-	WWP simulation for August 2009 same set up as for run_209
run_243	-	WWP simulation for August 2009 with daily constant fluxes

## Matlab scripts for WRF-GHG simulations

Name	Description
s_WRF_domain.m	Storage of WRF domain specific parameters
f_TM3_WRF_BARCA.m	Read TM3 CO <sub>2</sub> initial and boundary cond.
f_TM5_CH4_WRFin.m	Read TM5 CH <sub>4</sub> initial and boundary cond.
f_MACC_CO_WRFin.m	Read MACC CO initial and boundary cond.
f_CH4_NOAA_flask.m	Read extrapolated fields
f_CO2_NOAA_flask.m	from NOAA surface stations
f_CO_NOAA_flask.m	as boundary conditions
interp3TM5.m	Matlab 3-d interpolation for TM5 fields
co2_input_real_d01/d02.m	Script for WRF-GHG run_169-170
co2_input_real_kaplan_d01/d02.m	Script for WRF-GHG run_171-172
co2_input_real_con_d01/d02.m	Script for WRF-GHG run_177-180
co2_input_real_sc_d01/d02.m	Script for WRF-GHG run_188-189
co2_input_real_new_met_d01/d02.m	Script for WRF-GHG run_194-195
co2_input_co_d01.m	Script for WRF-GHG run_219
co2_input_real_jers_d01/d02.m	Script for WRF-GHG run_210-211
co2_input_realpnew_d01/d02.m	Script for WRF-GHG run_208-209
co2_input_walter_d01/d02.m	Script for WRF-GHG run_240
co2_input_walter_const_d01/d02.m	Script for WRF-GHG run_234
co2_input_era_const_d01/d02.m	Script for WRF-GHG run_238

## Global and regional inversions



Acronym	Name
TM3	OUTPUT12.086r8_2005-2010_fg.ch4.S01b_NEUch4_Std02mnPB_STATIONS_monthe6.tar.gz
TM3-TT34	OUTPUT12.086r8_2005-2010_fg.ch4.S01b_NEUch4_Std02mn_PB_STATIONS_TT34_DATA_monthe6.tar.gz
WP-Std	OUTPUT12.086_2009-2009_stiltam.ch4-D-_NEUch4_stilt_a_Std02mn_stiltamnew_prior_units2.tar.gz
WP-F4-S4	OUTPUT12.086_2009-2009_stiltam.ch4-D-_NEUch4_stilt_a_Std02mn_stiltam_SHORT4x_FAST4x_TT34_FAST4x_SHORT4x_new_prigent.tar.gz
WP-F4-S20	OUTPUT12.086_2009-2009_stiltam.ch4-D-_NEUch4_stilt_a_Std02mn_stiltam_SHORT20x_FAST4x_TT34_FAST4x_SHORT20x_prigent.tar.gz
WJ-Std	OUTPUT12.086_2009-2009_stiltam.ch4-D-_NEUch4_stilt_a_Std02mn_stiltamjers_normal.tar.gz
WJ-F4-S4	OUTPUT12.086_2009-2009_stiltam.ch4-D-_NEUch4_stilt_a_Std02mn_stiltam_SHORT4x_FAST4x_TT34_jers_new.tar.gz
WJ-F4-S20	OUTPUT12.086_2009-2009_stiltam.ch4-D-_NEUch4_stilt_a_Std02mn_stiltam_SHORT20x_FAST4x_TT34_FAST4x_SHORT20x_jers.tar.gz
FLAT	OUTPUT12.086_2009-2009_stiltam.ch4-D-_NEUch4_stilt_a_Std02mn_stiltam_fflat_prior.tar.gz
FLAT-F4-S4	OUTPUT12.086_2009-2009_stiltam.ch4-D-_NEUch4_stilt_a_Std02mn_stiltam_fl_SHORT4x_FAST4x_TT34_flat_short.tar.gz
FLAT-F4-S20	OUTPUT12.086_2009-2009_stiltam.ch4-D-_NEUch4_stilt_a_Std02mn_stiltam_fl_SHORT20x_FAST4x_flat_FAST4x_SHORT20x.tar.gz

## Regridding functions

Name	Description
regrid_wrf_to_stilt.ncl	WRF-Chem vegetation types to STILT grid
regrid_trmm.ncl	TRMM precipitation on WRF-Chem grid
regrid_trmm_fp.ncl	TRMM precipitation in footprint on WRF-Chem grid
regrid_tm5_fluxes.ncl	Get all TM5 fluxes on $6^{\circ} \times 4^{\circ}$ grid
regrid_prigent.ncl	Prigent wetland inundation map on WRF-Chem grid
regrid_prigent_stilt.ncl	Prigent wetland inundation map on STILT grid
regrid_ocean_lambert.ncl	TM3 ocean flux on STILT grid
regrid_kaplan_stilt.ncl	Kaplan wetland inundation map on STILT grid
regrid_jers_stilt.ncl	JERS-1SAR wetland inundation map on STILT grid
regrid_wetland_ncl.r	Kaplan and JERS-1SAR wetland inundation map,
regrid.ncl	carbon pool on WRF-Chem grid

## Flux preparation scripts

Name	Description
wrfout_data_matrix_d01.f90	Extracts WRF-Chem static fields for Walter wetland model (WWM)
wrfout_d02_May_09.f90	Extracts WRF-Chem meteorology for (WWM)
Sy_make.f90	Calculates bucket height (WWM)
regrid_dtmean.r	Mean annual soil temperature of corresponding grid cells (WWM)
regrid_elevation.r	Elevation for runoff calculation of corresponding grid cells (WWM)
regrid_npp.r	Substrate availability of corresponding grid cells (WWM)
r_to_fortran.r	Change to fortran compatible format (WWM)
npp_to_fortran.r	Change to fortran compatible format (WWM)
demand_d02.f90	Calculation evapotranspiration (WWM)
bucket_d02.f90	Calculation height of water table (WWM)
Gmain_d02.f90	Calculation CH <sub>4</sub> emissions per grid cell (WWM)
back_to_grid_trans_d02.f90	Transformation of CH <sub>4</sub> fluxes back to WRF-Chem grid (WWM)
tt34_data_stilt.r	TT34 observations in correct format for use in regional inversion
stilt_santarem.r	Santarém airborne data in correct format for use in regional inversion
edgar_accum.r	Creation WRF-Chem netcdf input for EDGAR from preprocessor
gpnr_soilm.m	Preparation of GPNR soil moisture data for WRF-GHG simulations
edgar_accum_new.r	Preparation of CH <sub>4</sub> fluxes for simulations with the official WRF-Chem release

Name	Description
tm3_stilt_wet.f	Wetland flux in TM3-STILT compatible format
tm3_stilt_bbm.f	Biomass burning flux in TM3-STILT compatible format
tm3_stilt_fossil.f	EDGAR flux in TM3-STILT compatible format
tm3_stilt_ocean.f	TM3 ocean flux in TM3-STILT compatible format
make_pfland_stiltam.pro	Land mask for TM3-STILT inversion
bbm_fluxes_stilt.tar.gz	Biomass burning fluxes for TM3-STILT inversion
bbm_fluxes_wrf.tar.gz	Biomass burning fluxes for WRF-GHG simulations
anthro_fluxes_stilt.tar.gz	EDGAR flux TM3-STILT inversion
anthro_fluxes_WRF.tar.gz	EDGAR flux for WRF-GHG simulation
wet_walter_kaplan_wrf.tar.gz	Wetland fluxes from WWM in combination with the Kaplan wetland inundation map for WRF-GHG simulations
wet_walter_jers_wrf.tar.gz	Wetland fluxes from WWM in combination with the JERS-1SAR wetland inundation map for WRF-GHG simulations
wet_walter_prigent_wrf.tar.gz	Wetland fluxes from WWM in combination with the Prigent wetland inundation map for WRF-GHG simulations
wet_walter_jers_stilt.tar.gz	Wetland fluxes from WWM in combination with the JERS-1SAR wetland inundation map for the TM3-STILT inversion
wet_walter_prigent_stilt.tar.gz	Wetland fluxes from WWM in combination with the Prigent wetland inundation map for the TM3-STILT inversion
ocean_fluxes_stilt.tar.gz	Ocean flux for TM3-STILT inversion
flat_fluxes_stilt.tar.gz	Flat a-priori flux for TM3-STILT inversion

## Data

Data source	Description
BARCA_1_flask_merged _19June2009.csv	BARCA-A flask observations
BARCA_B_all_flask_merged _July_24_2010.csv	BARCA-B flask observations
BARCA_all_A.tbl	BARCA-A continuous observations
BARCA_all_B.tbl	BARCA-B continuous observations
BARCA-A CH <sub>4</sub> isotopes Utrecht.xls	Isotope data selected BARCA-A flasks
BARCA-B CH <sub>4</sub> isotopes Utrecht.xls	Isotope data selected BARCA-B flasks
CH <sub>4</sub> data to Veronika.xlsx	Santarém airborne CH <sub>4</sub> observations
MEI.txt	Multivariate El Niño Index data
gv_ch4.tar	NOAA CH <sub>4</sub> GLOBALVIEW data
v2.prcp	Amazon precipitation data
focos.tar	Biomass burning locations from multiple satellites
EDGAR41.tar.gz	EDGAR v4.1 data input for preprocessor
global_wetland.nc	Kaplan wetland inundation map
lpj_cpool_2000.nc	LPJ carbon pool
.RData.basin.wetlands	JERS-1SAR wetland inundation map
wetland_new_1993_2007_Amazon	Prigent wetland inundation map
gpnr.tar.gz	GPNR soil moisture data for WRF-GHG simulations
TRMM.tar.gz	TRMM 3B42 data
TM5-PB.tar.gz	TM5-PB model output
TM5-PB-SCI.tar.gz	TM5-PB-SCI model output
TM5-SH.tar.gz	TM5-SH model output
TM5-SH-SCI.tar.gz	TM5-SH-SCI model output
TM5-CT.tar.gz	TM5-CT model output
picarro_LG_merged_hourly_data _Nov_2008_Feb_2010.txt	TT34 observations
Footprints_all.tar.gz	BARCA, Santarém, and TT34 footprints
radiosondes.tar.gz	BARCA-A radiosonde observations

## Models

Name	Description
WRFGHGV3.2.tar.gz	WRF-GHG model used for simulations in Ch. 6 and 7
WRFV3.4.tar.gz	Official WRF-Chem V3.4 distribution including the Greenhouse Gas model
STILT.tar.gz	STILT model code used for the footprint calculation
TM3-STILT.tar.gz	TM3 and STILT model code for the global and regional inversion
Prep_sources_chem_cptec_wrf_volc_degassing_Marcelo.tar.gz	Preprocessor for calculation of EDGAR and biomass burning CH <sub>4</sub> fluxes on WRF and STILT grid

## Analysis

Name	Description
read_tm5_3d_interp.m	Extract output along BARCA flight path from TM5-PB and TM5-PB-SCI
read_tm5_3d_interp_sh.m	Extract output along BARCA flight path from TM5-SH and TM5-SH-SCI
read_tm5_3d_interp_lb_alt.m	Extract output along BARCA flight path from TM5-CT
tm5_vs_barca_stat.r	Calculation of statistics for TM5-PB and TM5-PB-SCI vertical profiles
tm5_vs_barca_stat_2.r	Calculation of statistics for TM5-PB and TM5-PB-SCI vertical profiles
tm5_sh_vs_barca_stat.r	Calculation of statistics for TM5-SH and TM5-SH-SCI vertical profiles
tm5_sh_vs_barca_stat_2.r	Calculation of statistics for TM5-SH and TM5-SH-SCI vertical profiles
tm5_lb_vs_barca_stat.r	Calculation of statistics for TM5-CT vertical profiles
tm5_lb_vs_barca_stat_2.r	Calculation of statistics for TM5-CT vertical profiles
melack_budget_tm5_footprints.r	Calculation of TM5 CH <sub>4</sub> budgets
tm5_statistics_barca_ab.r	Calculation of $r^2$ of TM5 models for single BARCA flights
tm5_rsquare_regions.r	Calculation of $r^2$ of TM5 models for regions in the Amazon basin
tm5_extract_for_background.m	Extraction of TM5-PB and TM5-PB-SCI background mixing ratios

Name	Description
tm5_extract_for_background_sh.m	Extraction of TM5-SH and TM5-SH-SCI background mixing ratios
tm5_extract_for_background_lb.m	Extraction of TM5-CT background mixing ratios
tm5_background_comparison.r	Comparison background TM5 model simulations
read_radiosondes_wrf.r	Read radiosonde data and WRF-Chem model output
read_radiosondes_ecmwf.r	Read radiosonde data and ECMWF model output
compare_radiosondes.r	Calculation statistics for radiosonde comparison
precip_boxes2.r	Division TRMM and WRF-Chem precipitation fields in boxes
precip_boxes_trmm.r	Calculation hourly TRMM precipitation for each box
precip_boxes_wrf.r	Calculation hourly WRF-Chem precipitation for each box
precip_accum_wrf.r	Calculation accumulated WRF-Chem precipitation
precip_accum_new.r	Calculation accumulated TRMM precipitation
wrf_ch4_budgets_cal.r	Calculation of CH <sub>4</sub> budgets from WRF-GHG simulations
wrf_amazon_mainstream_wet.r	Calculation of CH <sub>4</sub> budgets for Amazon mainstream area from WRF-GHG simulations
plot_wrf_ch4_fluxes.r	Comparison of Kaplan wetland inventory and Walter wetland model
wrf_statistics.r	Statistics for each flight during BARCA-B
wrf_statistics_barca_a.r	Statistics for each flight during BARCA-A
wrf_stats_barca_b_flasks.r	Statistics of WRF-GHG simulations for BARCA-B flasks
wrf_rsquare_regions.r	Calculates $r^2$ for the different regions of the WRF-GHG BARCA comparison
wrf_barca_data_stat.r	Calculation for vertical profiles
wrf_barca_data_stat2.r	Calculation for vertical profiles
wrf_data_stat_change_wetland.r	Calculation for vertical profiles



Name	Description
trmm_wrf_precip_footprints.r	Accumulation WRF-Chem and TRMM 48 h precipitation
calculate_scaling_factors.r	Calculation of wetland scaling factors
f_cdf_var_ext.m	Function to read WRF-GHG netcdf output
f_dim_sav_out.m	Function to save the extracted model output
f_find_cell.m	Function to determine the grid cell for the extraction of model output
f_time.m	Function to extract model output at the correct time
f_grid_aircraft_d02/d01.m	Function to extract model output at the correct vertical level
s_WRF_Dim07_comp.m	Extraction of WRF-GHG model output along the flight track
s_WRF_Dimona_flasks.m	Extraction of WRF-GHG model output for BARCA-A flask locations
s_WRF_flasks_barca_b.m	Extraction of WRF-GHG model output for BARCA-B flask locations
wrf_tagged_tracer_new.r	Calculation tagged tracer contribution from WRF-GHG model output
tt34_mean.r	Calculation monthly mean CH <sub>4</sub> atmospheric mixing ratios of TT34 tower
wrf_tt34_extract.r	Extraction model output for TT34 observations from WRF-GHG simulations
tm3_for_tt34.m	Extraction of TM3 model output for the TT34 tower
tm5_for_tt34.m	Extraction of TM5 model output for the TT34 tower
tm3_melack_budget.r	Calculation TM3 CH <sub>4</sub> budget
stilt_melack_budget_seasonality.r	Calculation daily CH <sub>4</sub> budgets from regional inversion
stilt_melack_budget_all_mu.r	Calculation annual and monthly CH <sub>4</sub> budget from regional inversion
tm3_tm5_fluxes.r	Calculation of differences in the TM3 and TM5 a-priori fluxes
stilt_mixing_height.r	Extraction of STILT PBL height
plot_wrf_tt34_obs.r	WRF-GHG convection, PBL, and soil temperature output for the TT34 tower
stilt_san_48hrs_footprints.r	Calculation of 48 h precipitation in footprint upstream area
plot_actual_san_precip.r	Comparison of TRMM and ECMWF precipitation patterns for atmospheric transport evaluation



# List of Figures

2.1	Distribution of different CH <sub>4</sub> sources and sinks . . . . .	6
2.2	Time series of methane atmospheric mixing ratios at marine surface stations . . .	7
2.3	Isotopic composition of CH <sub>4</sub> sources . . . . .	9
2.4	Illustration of different pathways of CH <sub>4</sub> wetland emissions to the atmosphere .	10
2.5	The global wetland distribution based on the geographical potential wetland inundation map from Kaplan [2002] . . . . .	11
2.6	Illustration of the ITCZ location over the Amazon basin in January, July, and during the two BARCA campaigns . . . . .	17
2.7	Averaged monthly rainfall for the years 1950–2010 at three different stations in the Amazon basin . . . . .	18
2.8	Multivariate El Niño Index from 1950 to present . . . . .	20
2.9	Horizontal cross-section through the Amazon river, wetlands, and uplands . . . .	20
2.10	Wetland area of the Amazon lowland region (<500 m) as seen by JERS-1SAR . .	22
3.1	Calculation of greenhouse gas budgets with the top-down approach . . . . .	26
3.2	Overview over CH <sub>4</sub> and δ <sup>13</sup> CH <sub>4</sub> measurement locations . . . . .	30
3.3	Main components of the WRF model . . . . .	36
3.4	Two-step inversion scheme TM3-STILT . . . . .	43
4.1	Structure of the VPRM model . . . . .	48
4.2	Input parameters for the Brazilian Biomass Burning Emission Model (3BEM) . .	53
4.3	Structure of the Walter wetland model . . . . .	56
4.4	Embedded structure of the Greenhouse Gas model . . . . .	58
4.5	Different source components of CH <sub>4</sub> fluxes from official WRF-ChemV3.4 . . . .	66
4.6	Methane atmospheric mixing ratio distribution simulated by WRF-ChemV3.4 . .	67
5.1	Flight tracks of the two airborne campaigns BARCA-A and BARCA-B . . . . .	71
5.2	BARCA-A and BARCA-B CH <sub>4</sub> observations as function of latitude and longitude	73
5.3	BARCA-A and BARCA-B CH <sub>4</sub> atmospheric mixing ratios as function of SF <sub>6</sub> mixing ratios . . . . .	74
5.4	BARCA-A and BARCA-B CH <sub>4</sub> atmospheric mixing ratios as function of SF <sub>6</sub> mixing ratios . . . . .	75
5.5	Methane atmospheric mixing ratio as function of CO atmospheric mixing ratio for flasks collected during BARCA-A . . . . .	76

5.6	Keeling plot representation of the isotopic measurement results obtained on selected flasks during BARCA-A and BARCA-B . . . . .	78
5.7	Anthropogenic CH <sub>4</sub> emissions found on FLT 15 around Manaus city during BARCA-B . . . . .	80
5.8	500 m binned vertical profiles for observed CH <sub>4</sub> mixing ratios and five modeled CH <sub>4</sub> atmospheric mixing ratios from global atmospheric CH <sub>4</sub> inversions . . . . .	81
5.9	Monthly CH <sub>4</sub> budget for the five TM5-based global CH <sub>4</sub> inversions . . . . .	85
6.1	Topographic map illustrating the location of the two WRF-GHG simulation domains	91
6.2	Illustration of three different wetland inundation maps and differences . . . . .	92
6.3	Comparison of potential temperature, specific humidity, and wind speed from different WRF simulations, and ECMWF meteorological data to radiosondes profiles for Manaus during November 2008 . . . . .	94
6.4	Comparison of daily averaged precipitation from TRMM to WRF simulations . . . . .	95
6.5	Monthly mean CH <sub>4</sub> fluxes of the Kaplan wetland inventory and the Walter wetland model for November 2008 and May 2009 . . . . .	97
6.6	Comparison between CH <sub>4</sub> atmospheric mixing ratio, specific humidity, and precipitation observations of two flights during BARCA-B to WRF model simulations	100
6.7	Taylor diagram illustrating the comparison of the total CH <sub>4</sub> atmospheric mixing ratio to BARCA observations for flights during “good” and “bad” weather conditions	101
6.8	Comparison of BARCA-A and BARCA-B observations to four different WRF simulations binned in 500 m vertical profiles for five different regions in the Amazon basin . . . . .	108
7.1	Comparison of BARCA-B WRF-GHG simulations to TT34 observations and distribution of the inundated wetland area in vicinity of the TT34 tower . . . . .	117
7.2	Comparison between CH <sub>4</sub> fluxes driven by WRF-Chem and ERA-Interim meteorology . . . . .	118
7.3	Comparison between WRF-Chem and STILT atmospheric transport . . . . .	120
7.4	TT34 tower and Santarém airborne CH <sub>4</sub> observations including their footprints . . . . .	124
7.5	Comparison of TM5 and TM3 based global CH <sub>4</sub> inversion to TT34 observations for 2009 . . . . .	126
7.6	Taylor plot summarizing the results of different TM3-STILT regional inversion set ups . . . . .	128
7.7	Comparison of CH <sub>4</sub> atmospheric mixing ratios from the regional inversion to TT34 observations for 2009 . . . . .	129
7.8	A-priori and a-posteriori fluxes for three different regional inversion set ups for May 2009 . . . . .	130
7.9	Comparison of the latitudinal and longitudinal gradient of BARCA-B flasks to results from the regional inversion . . . . .	132
7.10	Comparison of CH <sub>4</sub> simulated atmospheric mixing ratios to aircraft observations close to Santarém . . . . .	135
7.11	Time series of daily CH <sub>4</sub> budget of the Amazon mainstream area and Amazon lowland region . . . . .	136

A.1	Monthly a-priori wetland CH <sub>4</sub> fluxes of the different TM5 global CH <sub>4</sub> inversions for November 2008 and May 2009 . . . . .	145
A.2	Monthly a-priori biomass burning CH <sub>4</sub> fluxes of different TM5 global CH <sub>4</sub> inversions . . . . .	146
A.3	Monthly a-posteriori total CH <sub>4</sub> fluxes obtained from five different global CH <sub>4</sub> inversions for November 2008 and May 2009 . . . . .	147
A.4	Vertical cross-section of BARCA-B observations and TM5 modeled CH <sub>4</sub> atmospheric mixing ratios . . . . .	148
A.5	Integrated footprints for observations obtained in the corresponding sampling regions during BARCA-A . . . . .	149
A.6	Integrated footprints for observations obtained in the corresponding sampling regions during BARCA-B . . . . .	150
A.7	Comparison of radiosonde profiles for potential temperature, specific humidity, and wind speed to WRF simulations for the city of Belém in November 2008 . .	151
A.8	Comparison of radiosondes profiles for potential temperature, specific humidity, and wind speed to WRF simulations for the city of Santarém in November 2008 .	152
A.9	Monthly mean average of TRMM precipitation in the d02 WRF simulation domain for November 2008 and May 2009 in comparison to precipitation output from three different WRF meteorologies . . . . .	153
A.10	Monthly averaged diurnal cycles of precipitation within the WRF d02 domain for simulations of different WRF meteorologies for November 2008 . . . . .	154
A.11	Monthly averaged diurnal cycles of precipitation within the WRF d02 domain for simulations of different WRF meteorologies for May 2009 . . . . .	155
A.12	Monthly mean CH <sub>4</sub> wetland fluxes of WRF-GHG d01 simulation domain for November 2008 and May 2009 . . . . .	156
A.13	Vertical cross-sections of BARCA-B observed and WRF-GHG simulated CH <sub>4</sub> atmospheric mixing ratios . . . . .	157
A.14	Comparison of WRF-Chem and TRMM precipitation patterns for FLT 3 to FLT 8 during BARCA-A . . . . .	158
A.15	Comparison of WRF-Chem and TRMM precipitation patterns for FLT 9 to FLT 14 during BARCA-A . . . . .	159
A.16	Comparison of WRF-Chem and TRMM precipitation patterns for FLT 2 to FLT 8 during BARCA-B . . . . .	160
A.17	Comparison of WRF-Chem and TRMM precipitation patterns for FLT 9 to FLT 15 during BARCA-B . . . . .	161
A.18	Comparison TM5 and WRF-GHG vertical profiles to BARCA observations . . .	162
A.19	Location of CH <sub>4</sub> surface observation stations for the global TM3 inversion . . .	163
A.20	Monthly footprints of the TT34 tower January to June 2009 . . . . .	164
A.21	Monthly footprints of the TT34 tower July to December 2009 . . . . .	165
A.22	Comparison of regional inversion results with different spatial and temporal correlation length to Santarém airborne profiles . . . . .	166
A.23	Comparison of regional inversion results with different spatial and temporal correlation length to Santarém airborne profiles . . . . .	167
A.24	Monthly footprints of the Santarém airborne profiles January to June 2009 . . . .	168
A.25	Monthly footprints of the Santarém airborne profiles August to December 2009 .	169

A.26 Monthly difference between a-priori and a-posteriori fluxes from the regional inversion for January to June 2009 . . . . .	170
A.27 Monthly difference between a-priori and a-posteriori fluxes from the regional inversion for July to December 2009 . . . . .	171



# List of Tables

2.1	Contributions of the individuals CH <sub>4</sub> source components to the global annual CH <sub>4</sub> budget. . . . .	8
2.2	PBL heights in the Amazon basin . . . . .	19
3.1	TM3 grid configurations . . . . .	38
4.1	Mapping of vegetation types defined by Sanderson [1996] to WRF vegetation types for the quantification of termite fluxes. . . . .	51
4.2	Tracer variables defined in <code>registry.ghg</code> . . . . .	58
4.3	Flux variables used in the WRF-GHG model . . . . .	59
4.4	Different options of the <code>namelist.input</code> file . . . . .	61
4.5	Additional namelist options required for WRF-GHG . . . . .	62
4.6	Main characteristics of the global models used as initial and lateral boundary conditions for greenhouse gas tracers in WRF-GHG . . . . .	63
4.7	Flux variables defined for the usage of the greenhouse gas module in the official WRF-Chem release . . . . .	64
4.8	Greenhouse gas tracer variables in the official WRF-Chem release . . . . .	65
4.9	Additional options of the <code>namelist.input</code> file for the official WRF-Chem release . . . . .	65
5.1	Detailed information about all flights conducted during BARCA-A and BARCA-B	72
5.2	Differences between the five TM5-based global CH <sub>4</sub> inversions . . . . .	79
6.1	WRF configurations, physics options, and updated land-surface maps used for the WRF-GHG simulations in the Amazon region. . . . .	93
6.2	Comparison of the CH <sub>4</sub> flux from the Kaplan wetland model (KWI) and the Walter wetland model (WWM) for grid cells specific for different wetland types . . .	99
6.3	Four different WRF-GHG CH <sub>4</sub> simulations with different configurations for wetland models and wetland inundation maps . . . . .	99
6.4	All flights conducted during BARCA-A and BARCA-B indicating their rating as “good” and “bad” flights . . . . .	103
6.5	Total CH <sub>4</sub> budget numbers and the wetland contributions of the four different WRF-GHG simulations for the Amazon lowland and Amazon mainstream region	110
7.1	Characteristics of the different regional TM3-STILT inversions in the Amazon basin	123
7.2	Budget estimates for different TM3-STILT regional inversion set ups . . . . .	137

8.1	Summary of CH <sub>4</sub> budget estimates for the Amazon basin . . . . .	142
A.1	Methane surface stations as constraint for the global TM3 inversion . . . . .	172

# Bibliography

- Abril, G., F. Guérin, S. Richard, R. Delmas, C. Galy-Lacaux, P. Gosse, A. Tremblay, L. Varfalvy, M. A. Dos Santos, and B. Matvienko, 2005: Carbon dioxide and methane emissions and the carbon budget of a 10-year old tropical reservoir (Petit Saut, French Guiana) *Glob. Biogeochem. Cycles*, **19**, GB4007, doi:10.1029/2005GB002457.
- Adamsen A. P. S. and G. M. King, 1993: Methane Consumption in Temperate and Subarctic Forest Soils: Rates, Vertical Zonation, and Responses to Water and Nitrogen *Appl. Environ. Microbiol.*, **59**(2), 485–490.
- Ahmadov, R., C. Gerbig, R. Kretschmer, S. Koerner, B. Neininger, A. J. Dolmann, and C. Sarat, 2007: Mesoscale covariance of transport and CO<sub>2</sub> fluxes: Evidence from observations and simulations using the WRF-VPRM coupled atmosphere-biosphere model *J. Geophys. Res.*, **112**, D22107, doi:10.1029/2007JD008552.
- Ahmadov, R., C. Gerbig, R. Kretschmer, S. Körner, C. Rödenbeck, P. Bousquet, and M. Ramonet, 2009: Comparing high resolution WRF-VPRM simulations and two global CO<sub>2</sub> transport models with coastal tower measurements of CO<sub>2</sub> *Biogeosciences*, **6**, 807–817.
- Alonso, M. F., K. M. Longo, S. R. Freitas, R. M. da Fonseca, V. Marécal, M. Pirre, and L. C. Klenner, 2010: An urban emission inventory for South America and its application in numerical modeling of atmospheric chemical composition at local and regional scales *Atmos. Environm.*, **44**(39), 5072–5083.
- Andreae M. O. and P. Merlet, 2001: Emission of trace gases and aerosols from biomass burning *Global Biochem. Cycles*, **15**(4), 955–966.
- Andreae, M. O., P. Artaxo, C. Brandaõ, F. E. Carswell, P. Ciccioli, A. L. da Costa, A. D. Culf, J. L. Esteves, J. H. C. Gash, J. Grace, P. Kabat, J. Lelieveld, Y. Malhi, A. O. Manzi, F. X. Meixner, A. D. Nobre, C. Nobre, M. d. L. P. Ruivo, M. A. Silva-Dias, P. Stefani, R. Valentini, J. von Jouanne, and M. J. Waterloo, 2002: Biogeochemical cycling of carbon, water, energy, trace gases, and aerosols in Amazonia: The LBA-EUSTACH experiments *J. Geophys. Res.*, **107**, D20, 8066, doi:10.1029/2001JD000524.
- Andreae, M. O., P. Artaxo, V. Beck, M. Bela, S. Freitas, C. Gerbig, K. Longo, J. W. Munger, K. T. Wiedemann, and S. C. Wofsy, 2012: Carbon monoxide and related trace gases and aerosols over the Amazon Basin during the wet and dry seasons *Atmos. Chem. Phys. Discuss.*, **12**, 8107–8168.
- Anisimov O. A., 2007: Potential feedback of thawing permafrost to the global climate system through methane emission *Environ. Res. Lett.*, **2**, doi:10.1088/1748-9326/2/4/045016.
- Archer D., 2007: Methane hydrate stability and anthropogenic climate change *Biogeosciences*, **4**, 521–544.
- Archer D., 2010: The Global Carbon Cycle *Princeton University Press*, Princeton, New Jersey, 2010.
- Arshinov, M. Y., B. D. Belan, D. K. Davydov, G. Inouye, S. Maksyutov, T. Machida, and A. V. Fofonov, 2009: Vertical Distribution of Greenhouse Gases above Western Siberia by the Long-Term Measurement Data *Atmospheric and Oceanic Optics*, **22**, 316–324.

- Aubinet, M., A. Grelle, A. Ibrom, U. Rannik, J. Moncrieff, T. Foken, A. S. Kowalski, P. H. Martin, P. Berbigier, C. Bernhofer, R. Clement, J. Elbers, A. Granier, T. Grunwald, K. Morgenstern, K. Pilegaard, C. Rebmann, W. Snijders, R. Valentini, and T. Vesala, 2000: Estimates of the Annual Net Carbon and Water Exchange of Forests: The EUROFLUX Methodology *Advances in Ecological Research*, **30**, 316–324.
- Aumann, H. H., M. T. Chahine, C. Gautier, M. D. Goldberg, E. Kalnay, L. M. McMillin, H. Revercomb, P. W. Rosenkranz, W. L. Smith, D. H. Staelin, L. L. Strow, and J. Susskind, 2003: AIRS/AMSU/HSB on the Aqua Mission: Design, Science Objectives, Data Products, and Processing Systems *IEEE Trans. Geosci. Remote Sensing*, **41**, 253–264.
- Aydin, M., K. R. Verhulst, E. S. Saltzman, M. O. Battle, S. A. Montzka, D. R. Blake, Q. Tang, and M. J. Prather, 2011: Recent decreases in fossil-fuel emissions of ethane and methane derived from firn air *Nature*, **476**, 198–201.
- Baird, A. J., I. Stamp, C. M. Heppell, and S. M. Green, 2009: CH<sub>4</sub> flux from peatlands: a new measurement method *Ecohydrology*, **3**, 360–367.
- Bakwin, P. S., P. P. Tans, D. F. Hurst, and C. Zhao, 1998: Measurements of carbon dioxide on very tall towers: results of the NOAA/CMDL program *Tellus B*, **50**, 401–415.
- Baldocchi, D., M. Detto, O. Sonnentag, J. Verfaillie, Y. A. Teh, W. Silver, N. Maggi Kelly, 2012: The challenges of measuring methane fluxes and concentrations over a peatland pasture *Agricult. For. Meteorol.*, **153**, 177–187.
- Bambace, L. A. W., F. M. Ramos, I. B. T. Lima, R. R. Rosa, 2007: Mitigation and recovery of methane emissions from tropical hydroelectric dams *Energy*, **32**, 1038–1046.
- Bartlett, K. B. and R. C. Harriss, 1993: Review and Assessment of Methane Emissions from Wetlands *Chemosphere*, **26**, 261–320.
- Bartlett, K. B., P. M. Crill, D. I. Sebacher, R. C. Harriss, J. O. Wilson, and J. M. Melack, 1988: Methane Flux From the Central Amazonian Floodplain *J. Geophys. Res.*, **93**, 1571–1582.
- Bartlett, K. B., P. M. Crill, J. A. Bonassi, J. E. Richey, and R. C. Harriss, 1990: Methane Flux From the Amazon River Floodplain: Emissions During Rising Water *J. Geophys. Res.*, **95**, 16,773–16,788.
- Bartlett, K. B., P. M. Crill, R. L. Sass, R. C. Harriss, and N. B. Dise, 1992: Methane Emissions From Tundra Environments in the Yukon-Kuskokwim Delta, Alaska *J. Geophys. Res.*, **97**, 16,645–16,660.
- Bastviken, D., L. J. Tranvik, J. A. Downing, P. M. Crill, A. Enrich-Prast, 2011: Freshwater Methane Emissions Offset the Continental Carbon Sink *Science*, **331**, 50.
- Baulch, H. M., P. J. Dillon, R. Maranger, and S. L. Schiff, 2011: Diffusive and ebullitive transport of methane and nitrous oxide from streams: Are bubble-mediated fluxes important? *J. Geophys. Res.*, **116**, G04028, doi:10.1029/2011JG001656.
- Beck, V., T. Koch, R. Kretschmer, J. Marshall, R. Ahmadov, C. Gerbig, D. Pillai, and M. Heimann, 2011: The WRF Greenhouse Gas Model (WRF-GHG) *Technical Report No. 25*, Max Planck Institute for Biogeochemistry, Jena, Germany, available online at <http://www.bgc-jena.mpg.de/bgc-systems/index.shtml>.
- Beerling, D. J., T. Gardiner, G. Leggett, A. McLeod, and W. P. Quick, 2008: Missing methane emissions from leaves of terrestrial plants *Global Change Biology*, **14**, 1821–1826.
- Bender, M. and R. Conrad, 1993: Kinetics of Methane Oxidation in Oxidic Soils *Chemosphere*, **26**, 687–696.

- Bergamaschi, P., C. Frankenberg, J. F. Meirink, M. Krol, F. Dentener, T. Wagner, U. Platt, J. O. Kaplan, S. Körner, M. Heimann, E. J. Dlugokencky, and A. Goede, 2007: Satellite chartography of atmospheric methane from SCIAMACHY on board ENVISAT: 2. Evaluation based on inverse model simulations *J. Geophys. Res.*, **112**, D02304, doi:10.1029/2006JD007268.
- Bergamaschi, P., C. Frankenberg, J. F. Meirink, M. Krol, M. G. Villani, S. Houweling, F. Dentener, E. J. Dlugokencky, J. B. Miller, L. V. Gatti, A. Engel, and I. Levin, 2009: Inverse modeling of global and regional CH<sub>4</sub> emissions using SCIAMACHY satellite retrievals *J. Geophys. Res.*, **114**, D22301, doi:10.1029/2009JD012287.
- Bergamaschi, P., M. Krol, J. F. Meirink, F. Dentener, A. Segers, J. van Aardenne, S. Monni, A. Vermeulen, M. Schmidt, M. Ramonet, C. Yver, F. Meinhardt, E. G. Nisbet, R. Fischer, S. O'Doherty, and E. J. Dlugokencky, 2010: Inverse modeling of European CH<sub>4</sub> emissions 2001–2006 *J. Geophys. Res.*, **115**, D22309, doi:10.1029/2010JD014180.
- Bloom, A. A., P. I. Palmer, A. Fraser, D. S. Reay, C. Frankenberg, 2010: Large-Scale Controls of Methanogenesis Inferred from Methane and Gravity Spaceborne Data *Science*, **321**, 322–325.
- Bogner, J. and K. Spokas, 1993: Landfill CH<sub>4</sub>: Rates, Fates, and Role in Global Carbon Cycle *Chemosphere*, **26**, 369–386.
- Boswell, R. and T. S. Collett, 2011: Current perspectives on gas hydrate resources *Energy and Environmental Science*, **4**, 1206–1215.
- Bousquet, P., P. Ciais, J. B. Miller, E. J. Dlugokencky, D. A. Hauglustaine, C. Prigent, G. R. Van der Werf, P. Peylin, E.-G. Brunke, C. Carouge, R. L. Langenfelds, J. Lathière, F. Papa, M. Ramonet, M. Schmidt, L. P. Steele, S. C. Tyler, and J. White, 2006: Current perspectives on gas hydrate resources *Nature*, **443**, 439–443.
- Bouwman, A. F., 1991: Agronomic aspects of wetland rice cultivation and associated methane emissions *Biogeochemistry*, **15**, 65–88.
- Bovensmann, H., J. P. Burrows, M. Buchwitz, J. Frerick, S. Noël, V. V. Rozanov, K. V. Chance, A. P. H. Goede, 1999: SCIAMACHY: Mission Objectives and Measurement Modes *J. Atmos. Sci.*, **56**, 127–150.
- Bovensmann, H., M. Buchwitz, J. P. Burrows, M. Reuter, T. Krings, K. Gerilowski, O. Schneising, J. Heymann, A. Tretner, and J. Erzinger, 2010: A remote sensing technique for global monitoring of power plant CO<sub>2</sub> emissions from space and related applications *Atmos. Meas. Tech.*, **3**, 781–811.
- Brass, M., and T. Röckmann, 2010: Continuous-flow isotope ratio mass spectrometry method for carbon and hydrogen measurements on atmospheric methane *Atmos. Meas. Tech.*, **3**, 1707–1721.
- Brenninkmeijer, C. A. M., D. C. Lowe, M. R. Manning, R. J. Sparks, and P. F. J. van Velthoven, 1995: The <sup>13</sup>C, <sup>14</sup>C, and <sup>18</sup>O isotopic composition of CO, CH<sub>4</sub>, and CO<sub>2</sub> in the higher southern latitudes lower stratosphere *J. Geophys. Res.*, **100**, 26,163–26,172.
- Brenninkmeijer, C. A. M., P. Crutzen, F. Boumard, T. Dauer, B. Dix, R. Ebinghaus, D. Filippi, H. Fischer, H. Franke, U. Friß, J. Heintzenberg, F. Helleis, M. Hermann, H. H. Kock, C. Koeppel, J. Lelieveld, M. Leuenberger, B. G. Martinsson, S. Miemczyk, H. P. Moret, H. N. Nguyen, P. Nyfeler, D. Oram, D. O'Sullivan, S. Penkett, U. Platt, M. Pucek, M. Ramonet, B. Randa, M. Reichelt, T. S. Rhee, J. Rohwer, K. Rosenfeld, D. Scharffe, H. Schlager, U. Schumann, F. Slemr, D. Sprung, P. Stock, R. Thaler, F. Valentino, P. van Velthoven, A. Waibel, A. Wandel, K. Waschitschek, A. Wiedensohler, I. Xueref-Remy, A. Zahn, U. Zech, and H. Ziereis, 2007: Civil Aircraft for the regular investigation of the atmosphere based on an instrumented container: The new CARIBIC system *Atmos. Chem. Phys.*, **7**, 4953–4976.

- Bubier, J. L., T. R. Moore, N. T. Roulet, 1993: Methane Emissions from Wetlands in the Midboreal Region of Northern Ontario, Canada *Ecology*, **74**, 2240–2254.
- Buchwitz, M., R. de Beek, S. Noël, J. P. Burrows, H. Bovensmann, O. Schneising, I. Khlystova, M. Bruns, H. Bremer, P. Bergamaschi, S. Körner, and M. Heimann, 2006: Atmospheric carbon gases retrieved from SCIAMACHY by WFM-DOAS: version 0.5 CO and CH<sub>4</sub> and impact of calibration improvements on CO<sub>2</sub> retrieval *Atmos. Chem. Phys.*, **6**, 2727–2751.
- Bustamante, M. M. C., M. Keller, and D. A. Silva, 2010: Sources and Sinks of Trace Gases in Amazonia and the Cerrado. In: Keller, M. (ed.) Amazonia and Global Change *Geophys. Monograph Series*, **186**, AGU, 10.1029/2008GM000847, 337–354 pp.
- Cantrell, C. A., 2008: Technical note: Review of methods for linear least-squares fitting of data and application to atmospheric chemistry problems *Atmos. Chem. Phys.*, **8**, 5477–5487.
- Cao, M., S. Marshall, and K. Gregson, 1996: Global carbon exchange and methane emissions from natural wetlands: Application of a process-based model *J. Geophys. Res.*, **101**, 14,399–14,414.
- do Carmo, J. B., M. Keller, J. D. Dias, P. B. de Camargo, and P. Crill, 2006: A source of methane from upland forests in the Brazilian Amazon *Geophys. Res. Lett.*, **33**, L04809, doi:10.1029/2005GL025436.
- Chanton, J. P., L. C. Chasar, P. Glaser, D. Siegel, 2005: Chapter 6, Carbon and hydrogen isotopic effects in microbial methane from terrestrial environments. In: Flanagan, L. B., Ehleringer, J. R., Pataki, D. E. (Eds.), Stable Isotopes and Biosphere-Atmosphere Interactions *Physiological Ecology Series*, Elsevier-Academic Press, Amsterdam, 85–105 pp.
- Chen, H., 2010: Development of a high-accuracy continuous CO<sub>2</sub>/CH<sub>4</sub>/H<sub>2</sub>O analyzer for deployment on board a commercial airliner *Dissertation*, Friedrich Schiller Universität Jena, 186 pp.
- Chen, H., J. Winderlich, C. Gerbig, A. Hofer, C. W. Rella, E. R. Crosson, A. D. Van Pelt, J. Steinbach, O. Kolle, V. Beck, B. C. Daube, E. W. Gottlieb, V. Y. Chow, G. W. Santoni, and S. C. Wofsy, 2010: High-accuracy continuous airborne measurements of greenhouse gases (CO<sub>2</sub> and CH<sub>4</sub>) using the cavity ring-down spectroscopy (CRDS) technique *Atmos. Meas. Tech.*, **3**, 375–386.
- Chen, Y.-H. and R. G. Prinn, 2006: Estimation of atmospheric methane emissions between 1996 and 2001 using a three-dimensional global chemical transport model *J. Geophys. Res.*, **111**, D10307, doi:10.1029/2005JD006058.
- Christensen, T., I. C. Prentice, J. Kaplan, A. Haxeltine, and S. Sitch, 1996: Methane flux from northern wetlands and tundra *Tellus B*, **48**, 652–661.
- Cicerone, R. J., R. S. Oreroland, 1988: Biogeochemical Aspects of Atmospheric Methane *Glob. Biogeochem. Cycles*, **2**, 99–327.
- Cooley, J. P., 1925: The infra-red absorption bands of methane *The Astrophysical Journal*, **2**, 73–83.
- Cosby, B. J., G. M. Hornberger, R. B. Clapp, and T. R. Ginn, 1984: A Statistical Exploration of the Relationships of Soil Moisture Characteristics to the Physical Properties of Soil *Water Resources Res.*, **20**, 682–690.
- Crevoisier, C., D. Nobileau, A. M. Fiore, R. Armante, A. Chédin, and N. A. Scott, 2009: Tropospheric methane in the tropics-first year from IASI hyperspectral infrared observations *Atmos. Chem. Phys.*, **9**, 6337–6350.
- Crill, P. M., 1991: Seasonal Patterns of Methane Uptake and Carbon Dioxide Release by a Temperate Woodland Soil *Glob. Biogeochem. Cycles*, **5**, 319–334.



- Crill P. M., K. B. Bartlett, J. O. Wilson, D. I. Sebacher, R. C. Harriss, J. M. Melack, S. MacIntyre, L. Lesack, L. Smith-Morrill, 1988: Tropospheric Methane From an Amazonian Floodplain Lake *J. Geophys. Res.*, **93**, 1564–1570.
- Crutzen, P. J. and M. O. Andreae, 1990: Biomass Burning in the Tropics: Impact on Atmospheric Chemistry and Biogeochemical Cycles *Science*, **250**, 1669–1678.
- Crutzen, P. J., I. Aselmann and W. Seiler, 1986: Methane production by domestic animals, wild ruminants, other herbivorous fauna, and humans *Tellus B*, **38**, 271–284.
- Davidson, E. A. and P. Artaxo, 2004: Globally significant changes in biological processes of the Amazon Basin: results of the Large-scale Biosphere-Atmosphere Experiment *Global Change Biology*, **10**, 519–529.
- Davidson, E. A., A. C. de Araújo, P. Artaxo, J. K. Balch, I. Foster Brown, M. M. C. Bustamante, M. T. Coe, R. S. DeFries, M. Keller, M. Longo, J. W. Munger, W. Schroeder, B. S. Soares-Filho, C. M. Souza Jr. and S. C. Wofsy, 2012: The Amazon basin in transition *Nature*, **481**, 321–328.
- Dedikov, J. V., G. S. Akopova, N. G. Gladkaja, A. S. Piotrovskij, V. A. Markellov, S. S. Salichov, H. Kaesler, A. Ramm, A. Müller von Blumencron, J. Lelieveld, 1999: Estimating methane releases from natural gas production and transmission in Russia *Atmos. Environ.*, **33**, 3291–3299.
- Delmas R., J. E. Lacaux, and D. Brochard, 1995: Determination of Biomass Burning Emission Factors: Methods and Results *Environm. Monitor. Assess.*, **38**, 181–204.
- Dentener, F., W. Peters, M. Krol, M. van Weele, P. Bergamaschi, and J. Lelieveld, 2003: Interannual variability and trend of CH<sub>4</sub> lifetime as a measure for OH changes in the 1979–1993 time period *J. Geophys. Res.*, **108**, D15, 4442, doi:10.1029/2002JD002916.
- Deutscher, N. M., D. W. T. Griffith, C. Paton-Walsh, and R. Borah, 2010: Train-borne measurements of tropical methane enhancements from ephemeral wetlands in Australia *J. Geophys. Res.*, **115**, D15304, doi:10.1029/2009JD013151.
- Devol, A. H., J. Richey, W. A. Clark, S. L. King, L. A. Martinelli, 1988: Methane Emissions to the Troposphere from the Amazon Floodplain *J. Geophys. Res.*, **93**, 1583–1592.
- Devol, A. H., J. Richey, B. R. Forsberg, L. A. Martinelli, 1990: Seasonal Dynamics in Methane Emissions from the Amazon River Floodplain to the Troposphere *J. Geophys. Res.*, **95**, 16,417–16,426.
- Dickens, G. R., 2011: Down the Rabbit Hole: toward appropriate discussion of methane release from gas hydrate systems during the Paleocene-Eocene thermal maximum and other past hyperthermal events *Clim. Past*, **7**, 831–846.
- Dlugokencky, E. J., L. P. Steele, P. M. Lang and K. A. Masarie, 1994: The growth rate and distribution of atmospheric methane *J. Geophys. Res.*, **99**, 17,021–17,043.
- Dlugokencky, E. J., K. A. Masarie, P. M. Lang, P. P. Tans, 1998: Continuing decline in the growth rate of the atmospheric methane burden *Nature*, **393**, 447–450.
- Dlugokencky, E. J., B. P. Walter, K. A. Masarie, E. M. Kasischke, 2001: Measurements of an anomalous global methane increase during 1998 *Geophys. Res. Lett.*, **28**, 499–502.
- Dlugokencky, E. J., S. Houweling, L. Bruhwiler, K. A. Masarie, P. M. Lang, J. B. Miller, and P. P. Tans, 2003: Atmospheric methane levels off: Temporary pause or a new steadystate? *Geophys. Res. Lett.*, **30**, 19, 1992, doi:10.1029/2003GL018126.

- Dlugokencky, E. J., R. C. Myers, P. M. Lang, K. A. Masarie, A. M. Croswell, K. W. Thoning, B. D. Hall, J. W. Elkins, and L. P. Steele, 2005: Conversion of NOAA atmospheric dry air CH<sub>4</sub> mole fractions to a gravimetrically prepared standard scale *J. Geophys. Res.*, **110**, D18306, doi:10.1029/2005JD006035.
- Dlugokencky, E. J., L. Bruhwiler, J. W. C. White, L. K. Emmons, P. C. Novelli, S. A. Montzka, K. A. Masarie, P. M. Lang, A. M. Croswell, J. B. Miller, and L. V. Gatti, 2009: Observational constraints on recent increases in the atmospheric CH<sub>4</sub> burden *Geophys. Res. Lett.*, **36**, L18803, doi:10.1029/2009GL039780.
- Dlugokencky, E. J., P. M. Lang, and K. A. Masarie, 2010: Atmospheric Methane Dry Air Mole Fractions from the NOAA ESRL Carbon Cycle Cooperative Global Air Sampling Network, 1983-2009, Version: 2010-08-12 available online at <ftp://ftp.cmdl.noaa.gov/ccg/ch4/flask/event/>.
- Dörr, H., L. Katruff, I. Levin, 1993: Soil Texture Parameterization of the Methane Uptake in aerated Soils *Chemosphere*, **26**, 697–713.
- Dolman, A. J., J. Noilhan, P. Durand, C. Sarrat, A. Brut, B. Pignatelli, A. Butet, N. Jarosz, Y. Brunet, D. Loustau, E. Lamaud, L. Tolk, R. Ronda, F. Miglietta, B. Gioli, V. Magliulo, M. Esposito, C. Gerbig, S. Körner, O. Glademard, M. Ramonet, P. Ciais, B. Neininger, R. W. A Hutjes, J. A. Elbers, R. Macatangay, O. Schrems, G. Perez-Landa, M. J. Sanz, Y. Scholz, G. Facon, E. Ceschia, and P. Beziat, 2006: The CarboEurope regional experiment strategy *Bull. Amer. Meteorol. Soc.*, **87**, 1367–1379.
- Draxler, R. R., and G. D. Hess, 1997: Description of the HYSPLIT\_4 modeling system *NOAA Tech. Memo. ERL ARL-224*, NOAA Air Resources Laboratory, Silver Spring, MD, 24 pp.
- Drevet, J. 2008: Modeling Study of the Interannual Variability in Global Tropospheric Hydroxyl Radical and Methane Concentrations Over the Last Two Decades, *Dissertation*, Ecole Polytechnique Fédérale de Lausanne, 114 pp.
- Dueck, T. A., R. de Visser, H. Poorter, S. Persijn, A. Gorissen, W. de Visser, A. Schapendonk, J. Verhagen, J. Snel, F. J. M. Harren, A. K. Y. Ngai, F. Verstappen, H. Bouwmeester, L. A. C. J. Voesenek, and A. van der Werf, 2007: No evidence for substantial aerobic methane emissions by terrestrial plants: a <sup>13</sup>C-labelling approach *New Phytologist*, **175**, 29–35.
- Easterling, D. R. and T. C. Peterson, 1995: A new method for detecting undocumented discontinuities in climatological time series *International journal of climatology Int. J. of Climatology*, **15**, 369–377.
- Edwards, M. O., 1989: Global gridded elevation and bathymetry (ETOPO5), Digital raster data on a 5-minute geographic (lat/lon) 2160\*4320 (centroid-registered) grid *NOAA Natl. Geophys. Data Cent.*, Boulder, CO, US.
- Engle, D. and J. M. Melack, 2003: Methane emissions from an Amazon floodplain lake: Enhanced release during episodic mixing and during falling water *Biogeochemistry*, **51**, 71–90.
- European Space Agency, 2011: Earth Observation Handbook, available online <http://database.eohandbook.com>.
- Etheridge, D. M., L. P. Steele, R. J. Francey, and R. L. Langenfelds, 1998: Atmospheric methane between 1000 A.D. and present: Evidence of anthropogenic emissions and climatic variability *J. Geophys. Res.*, **103**, 15,979–15,993.
- Etiopie, G., R. W. Klusman, 2002: Geologic emissions of methane to the atmosphere *Chemosphere*, **49**, 777–789.
- Etiopie, G. and A. V. Milkov, 2004: A new estimate of global methane flux from onshore and shallow submarine mud volcanoes to the atmosphere *Environmental Geology*, **46**, 997–1002.

- Etiopio, G., K. R. Lassey, R. W. Klusman, and E. Boschi, 2008: Reappraisal of the fossil methane budget and related emission from geologic sources *Geophys. Res. Lett.*, **35**, L09307, doi:10.1029/2008GL033623.
- Ferek, R. J., J. S. Reid, P. V. Hobbs, D. R. Blake, and C. Lioussé, 1998: Emission factors of hydrocarbons, halocarbons, trace gases and particles from biomass burning in Brazil *J. Geophys. Res.*, **103**, 107–132.
- Ferretti, D. F., J. B. Miller, J. W. C. White, K. R. Lassey, D. C. Lowe, and D. M. Etheridge, 2007: Stable isotopes provide revised global limits of aerobic methane emissions from plants *Atmos. Chem. Phys.*, **7**, 237–241.
- Fisch, G., J. Tota, L. A. T. Machado, M. A. F. Silva Dias, R. F. da F. Lyra, C. A. Nobre, A. J. Dolman, and J. H. C. Gash, 2004: The convective boundary layer over pasture and forest in Amazonia *Theor. Appl. Climatol.*, **78**, 47–59.
- Frankenberg, C., J. F. Meirink, M. van Weele, U. Platt, T. Wagner, 2005: Assessing Methane Emissions from Global Space-Borne Observations *Science*, **308**, 1010–1014.
- Frankenberg, C., T. Warneke, A. Butz, I. Aben, F. Hase, P. Spietz, and L. R. Brown, 2008: Pressure broadening in the  $2\nu_3$  band of methane and its implication on atmospheric retrievals *Atmos. Chem. Phys.*, **8**, 5061–5075.
- Frankenberg, C., I. Aben, P. Bergamaschi, E. J. Dlugokencky, R. van Hees, S. Houweling, P. van der Meer, R. Snel, and P. Tol, 2011: Global column-averaged methane mixing ratios from 2003 to 2009 as derived from SCIAMACHY: Trends and variability *J. Geophys. Res.*, **116**, D04302, doi:10.1029/2010JD014849.
- Fraser, P. J., R. A. Rasmussen, J. W. Creffield, J. R. French, and M. A. K. Kahlil, 1986: Termites and Global Methane - Another Assessment *J. Atmos. Chem.*, **4**, 295–310.
- Freitas, S. R., K. M. Longo, M. A. F. Silva Dias, P. L. Silva Dias, R. Chatfield, E. Prins, P. Artaxo, G. A. Grell, F. S. Recuero, 2005: Monitoring the Transport of Biomass Burning Emissions in South America *Environ. Fluid Mech.*, **5**, 135–167.
- Freitas, S. R., K. M. Longo, and M. O. Andreae, 2006: Impact of including the plume rise of vegetation fires in numerical simulations of associated atmospheric pollutants *Geophys. Res. Lett.*, **33**, L17808, doi:10.1029/2006GL026608.
- Freitas, S. R., K. M. Longo, M. A. F. Silva Dias, R. Chatfield, P. Silva Dias, P. Artaxo, M. O. Andreae, G. Grell, L. F. Rodrigues, A. Fazenda, and J. Panetta, 2009: The Coupled Aerosol and Tracer Transport model to the Brazilian developments on the Regional Atmospheric Modeling System (CCATT-BRAMS)–Part 1: Model description and evaluation *Atmos. Chem. Phys.*, **9**, 2843–2861.
- Freitas, S. R., K. M. Longo, M. F. Alonso, M. Pirre, V. Marecal, G. Grell, R. Stockler, R. F. Mello, and M. Sánchez Gácita, 2010: PREP-CHEM-SRC–1.0: A pre-processor of trace gases and aerosols emission fields for regional and global atmospheric chemistry models *Geosci. Model Dev.*, **4**, 419–433.
- Geels, C., M. Gloor, P. Ciais, P. Bousquet, P. Peylin, A. T. Vermeulen, R. Dargaville, T. Aalto, J. Brandt, J. H. Christensen, L. M. Frohn, L. Haszpra, U. Karstens, C. Rödenbeck, M. Ramonet, G. Carboni, and R. Santaguida, 2007: Comparing atmospheric transport models for future regional inversions over Europe - Part 1: mapping the atmospheric CO<sub>2</sub> signals *Atmos. Chem. Phys.*, **7**, 3461–3479.
- Geibel, M. C., C. Gerbig, and D. G. Feist, 2010: A new fully automated FTIR system for total column measurements of greenhouse gases *Atmos. Meas. Tech.*, **3**, 1363–1375.
- Geibel, M. C., J. Messerschmidt, C. Gerbig, T. Blumenstock, F. Hase, O. Kolle, J. V. Lavrič, J. Notholt, M. Palm, M. Rettinger, M. Schmidt, R. Sussmann, T. Warneke, and D. G. Feist, 2012: Calibration of column-averaged CH<sub>4</sub> over European TCCON FTS sites with airborne in-situ measurements *Atmos. Chem. Phys. Discuss.*, **12**, 1517–1551.

- Gerbig, C., J. C. Lin, S. C. Wofsy, B. C. Daube, A. E. Andrews, B. B. Stephens, P. S. Bakwin, and C. A. Grainger, 2003a: Toward constraining regional-scale fluxes of CO<sub>2</sub> with atmospheric observations over a continent: 1. Observed spatial variability from airborne platforms *J. Geophys. Res.*, **108**, D24, 4756, doi:10.1029/2002JD003018.
- Gerbig, C., J. C. Lin, S. C. Wofsy, B. C. Daube, A. E. Andrews, B. B. Stephens, P. S. Bakwin, and C. A. Grainger, 2003b: Toward constraining regional-scale fluxes of CO<sub>2</sub> with atmospheric observations over a continent: 2. Analysis of COBRA data using a receptor-oriented framework *J. Geophys. Res.*, **108**, D24, 4757, doi:10.1029/2003JD003770.
- Gerbig, C., A. J. Dolman, and M. Heimann, 2009: On observational and modeling strategies targeted at regional carbon exchange over continents *Biogeosciences*, **6**, 1949–1959.
- Gevaerd, R. and S. R. Freitas, 2006: Estimativa operacional da umidade do solo para iniciação de modelos de previsão numérica da atmosfera. Parte I: Descrição da metodologia e validação *Revista Brasileira de Meteorologia*, **21**, 1–15.
- Giglio, L., J. D. Kendall and C. O. Justice, 1999: Evaluation of global fire detection algorithms using simulated AVHRR infrared data *Int. J. Remote Sensing*, **20**, 1947–1985.
- Giglio, L., J. T. Randerson, G. R. van der Werf, P. S. Kasibhatla, G. J. Collatz, D. C. Morton, and R. S. DeFries, 2010: Assessing variability and long-term trends in burned area by merging multiple satellite fire products *Biogeosciences*, **7**, 1171–1186.
- Gloor, M., S.-M. Fan, S. Pacala, and J. Sarmiento, 2000: Optimal sampling of the atmosphere for purpose of inverse modeling: A model study *Glob. Biogeochem. Cycles*, **14**, 407–428.
- Gloor, M., P. Bakwin, D. Hurst, L. Lock, R. Draxler, and P. Tans, 2001: What is the concentration footprint of a tall tower? *J. Geophys. Res.*, **106**, 17,831–17,840.
- Göckede, M., A. M. Michalak, D. Vickers, D. P. Turner, and B. E. Law, 2010: Atmospheric inverse modeling to constrain regional scale CO<sub>2</sub> budgets at high spatial and temporal resolution *J. Geophys. Res.*, **115**, D15113, doi:10.1029/2009JD012257.
- Grell, G. A. and D. Dévényi, 2002: A generalized approach to parameterizing convection combining ensemble and data assimilation techniques *Geophys. Res. Lett.*, **29**, 14,1693, 10.1029/2002GL015311.
- Grell, G., S. E. Peckham, R. Schmitz, S. A. McKeen, G. Frost, W. C. Skamarock, and B. Eder, 2005: Fully coupled “online” chemistry within the WRF model *Atmos. Environ.*, **39**, doi:10.1016/j.atmosenv.2005.6904.6027.
- Grell, G., S. R. Freitas, M. Stuefer, and J. Fast, 2010: Inclusion of biomass burning in WRF-Chem: impact of wildfires on weather forecasts *Atmos. Chem. Phys. Discuss.*, **10**, 30613–30650.
- Guisasola, A., D. de Haas, J. Keller, Z. Yuan, 2008: Methane formation in sewer systems *Water Research*, **42**, 1421–1430.
- Guérin, F. G. Abril, S. Richard, B. Burban, C. Reynouard, P. Seyler, and R. Delmas, 2006: Methane and carbon dioxide emissions from tropical reservoirs: Significance of downstream rivers *Geophys. Res. Lett.*, **33**, L21407, doi:10.1029/2006GL027929.
- Gurney, K. Robert, R. M. Law, A. S. Denning, P. J. Rayner, D. Baker, P. Bousquet, L. Bruhwiler, Y.-H. Chen, P. Ciais, S. Fan, I. Y. Fung, M. Gloor, M. Heimann, K. Higuchi, J. John, T. Maki, S. Maksyutov, K. Masariek, P. Peylin, M. Prather, B. C. Pak, J. Randerson, J. Sarmiento, S. Taguchi, T. Takahashi and C.-W. Yuen, 2002: Towards robust regional estimates of CO<sub>2</sub> sources and sinks using atmospheric transport models *Nature*, **415**, 626–630.

- Guyon, P., G. P. Frank, M. Welling, D. Chand, P. Artaxo, L. Rizzo, G. Nishioka, O. Kolle, H. Fritsch, M. A. F. Silva Dias, L. V. Gatti, A. M. Cordova, and M. O. Andreae, 2005: Airborne measurements of trace gas and aerosol particle emissions from biomass burning in Amazonia *Atmos. Chem. Phys.*, **5**, 2989–3002.
- Hachikubo, A., A. Krylov, H. Sakagami, H. Minami, Y. Nunokawa, H. Shoji, T. Matveeva, Y. K. Jin, and A. Obzhirov, 2010: Isotopic composition of gas hydrates in subsurface sediments from offshore Sakhalin Island, Sea of Okhotsk *Geo-Mar Lett.*, **30**, 313–319.
- Harriss, R. C., S. C. Wofsy, M. Garstang, E. V. Browell, L. C. B. Molion, R. J. McNeal, J. M. Hoell Jr., R. J. Bendura, S. M. Beck, R. L. Navarro, J. T. Riley, and R. L. Snell, 1988: The Amazon Boundary Layer Experiment (ABLE 2A): Dry Season 1985 *J. Geophys. Res.*, **93**, 1351–1360.
- Harriss, R. C., M. Garstang, S. C. Wofsy, S. M. Beck, R. J. Bendura, J. R. B. Coelho, J. W. Drewry, J. M. Hoell Jr., P. A. Matson, R. J. McNeil, L. C. B. Molion, R. L. Navarro, V. Rabine, and R. L. Snell, 1990: The Amazon Boundary Layer Experiment: Wet Season 1987 *J. Geophys. Res.*, **95**, 16,721–16,736.
- Heimann, M., 1996: The global atmospheric tracer model TM2, *Technical Report 10* ISSN 0940-9327, Deutsches Klimarechenzentrum, Hamburg, Germany.
- Heimann, M., 2011: Enigma of the recent methane budget *Nature*, **476**, 157–158.
- Heimann, M., and S. Koerner, 2003: The Global Atmospheric Tracer Model TM3: Model description and user manual release 3.8a, *Technical Report No. 5*, Max Planck Institute for Biogeochemistry, Jena, Germany, available online at <http://www.bgc-jena.mpg.de/bgc-systems/index.shtml>.
- Hein, R., P. J. Crutzen, M. Heimann, 1997: An inverse modeling approach to investigate the global atmospheric methane cycle *Glob. Biogeochem. Cycles*, **11**, 43–76.
- Hendriks, D. M. D., A. J. Dolman, M. K. van der Molen, and J. van Huissteden, 2008: A compact and stable eddy covariance set-up for methane measurements using off-axis integrated cavity output spectroscopy *Atmos. Chem. Phys.*, **8**, 431–443.
- Hess, L. L., J. M. Melack, E. M. L. M. Novo, C. C. F. Barbosa, M. Gastil, 2003: Dual-season mapping of wetland inundation and vegetation for the central Amazon basin *Remote Sensing of Environment*, **87**, 404–428.
- Hess, L. L., A. A. Affonso, C. Barbosa, M. Gastil-Buhl, J. M. Melack and E. M. L. M. Novo, 2009: LBA-ECO LC-07 Basinwide Amazon Wetlands 100 m Mask based on JERS SAR Images (v.Apr08). Data set. Available online (<http://lba.cptec.inpe.br/>) from LBA Data and Information System, National Institute for Space Research (INPE/CPTEC), Cachoeira Paulista, Sao Paulo, Brazil.
- Houweling, S., T. Kaminski, F. Dentener, J. Lelieveld, and M. Heimann, 1999: Inverse modeling of methane sources and sinks using the adjoint of a global transport model *J. Geophys. Res.*, **104**, 26,137–26,160.
- Houweling, S., T. Röckmann, I. Aben, F. Keppler, M. Krol, J. F. Meirink, E. J. Dlugokencky, and C. Frankenberg, 2006: Atmospheric constraints on global emissions of methane from plants *Geophys. Res. Lett.*, **33**, L15821, doi:10.1029/2006GL026162.
- Iacono, M. J., J. S. Delamere, E. J. Mlawer, M. W. Shephard, S. A. Clough, and W. D. Collins, 2008: Radiative forcing by long-lived greenhouse gases: Calculations with the AER radiative transfer models *J. Geophys. Res.*, **113**, D13103, doi:10.1029/2008JD009944.
- Integrated Carbon Observing System, 2010: *Stakeholder Handbook* available online at [http://www.icos-infrastructure.eu/docs/pub/PO\\_stakebook2010\\_ref\\_201205.pdf](http://www.icos-infrastructure.eu/docs/pub/PO_stakebook2010_ref_201205.pdf), 117 pp.



- Intergovernmental Panel on Climate Change, 2001: Climate Change 2001: The Scientific Basis. Contribution of Working Group I to the Third Assessment Report of the Intergovernmental Panel on Climate Change *Cambridge Univ. Press*, Cambridge, UK, 881 pp.
- Intergovernmental Panel on Climate Change, 2007: Climate Change 2007: The Physical Science Basis. Contribution of Working Group I to the Fourth Assessment Report of the Intergovernmental Panel on Climate Change *Cambridge Univ. Press*, Cambridge, UK, 996 pp.
- Itoh, M., N. Ohte, K. Koba, 2009: Methane flux characteristics in forest soils under an East Asian monsoon climate *Soil Biology & Biochemistry*, **41**, 388–395.
- Judd, A. G., 2000: Geological Sources of Methane In: Khalil M. A. K. (Ed.) Atmospheric Methane: Its Role in the Global Environment, *Springer*, Berlin, 280–303 pp.
- Judd, A. G., M. Hovland, L. I. Dimitrov, S. García Gil, and V. Jukes, 2002: The geological methane budget at Continental Margins and its influence on climate change *Geofluids*, **2**, 109–126.
- Jung, M. K. Henkel, M. Herold, and G. Churkina, 2006: Exploiting synergies of global land cover products for carbon cycle modeling *Remote Sensing of Environment*, **101**, 534–553.
- Junk, W. J. and M. T. F. Piedade, 2005: The Amazon river basin. In: Fraser, L. H. and P. A. Keddy (Eds.) The World's Largest Wetlands: Ecology and Conservation, *Cambridge University Press*, Cambridge, UK, 36–117 pp.
- Justice, C. O., L. Giglio, S. Korontzi, J. Owens, J. T. Morisette, D. Roy, J. Descloitres, S. Alleaume, F. Petitcolin, Y. Kaufman, 2002: The MODIS fire products *Remote Sensing of Environment*, **83**, 244–262.
- Johnson, D. E., K. A. Johnson, G. M. Ward, and M. E. Branine, 2000: Ruminants and Other Animals. In: Khalil, M. A. K. (Ed.) Atmospheric Methane: Its Role in the Global Environment, *Springer*, Berlin, 112–133 pp.
- Johnson, R. H., Rickenback, T. M., Rutledge, S. A., Ciesielski, P. E., and W. H. Schubert, 1999: Trimodal Characteristics of Tropical Convection *Journal of Climate*, **12**, 2397–2418.
- Kai, F. M., S. C. Tyler, J. T. Randerson, and D. R. Blake, 2011: Reduced methane growth rate explained by decreased Northern Hemisphere microbial sources *Nature*, **476**, 194–197.
- Kaplan, J. O., 2002: Wetlands at the Last Glacial Maximum: Distribution and methane emissions *Geophys. Res. Lett.*, **29**, 6, 1079, doi:10.1029/2001GL013366.
- Kaplan, J. O., G. Folberth, and D. A. Hauglustaine, 2006: Role of methane and biogenic volatile organic compound sources in late glacial and Holocene fluctuations of atmospheric methane concentrations *Global Biogeochem. Cycles*, **20**, GB2016, doi:10.1029/2005GB002590.
- Keeling, C. D., R. B. Bacastow, A. E. Bainbridge, C. A. Ekdahl Jr., P. R. Guenther, and L. S. Waterman, 1976: Atmospheric carbon dioxide variations at Mauna Loa Observatory, Hawaii *Tellus B*, **28**, 538–551.
- Keller, M., M. Bustamente, J. Gash, and P. Silva Dias, 2009: Amazonia and Global Change *Geophys. Monograph Series*, **186**, AGU, 10.1029/2008GM000847.
- Kemenes, A., B. R. Forsberg, and J. M. Melack, 2007: Methane release below a tropical hydroelectric dam *Geophys. Res. Lett.*, **34**, L12809, doi:10.1029/2007GL029479.
- Kennett, J. P., K. G. Cannariato, I. L. Hendy, R. J. Behl, 2000: Carbon Isotopic Evidence for Methane Hydrate Instability During Quaternary Interstadials *Science*, **288**, 128–133.



- Keppler, F., J. T. G. Hamilton, M. Bra, T. Röckmann, 2006: Methane emissions from terrestrial plants under aerobic conditions *Nature*, **439**, 187–191.
- Khalil, M. A., R. A. Rasmussen, J. R. J. French, J. A. Holt, 1990: The Influence of Termites on Atmospheric Trace Gases: CH<sub>4</sub>, CO<sub>2</sub>, CHCl<sub>3</sub>, N<sub>2</sub>O, CO, H<sub>2</sub>, and Light Hydrocarbons *J. Geophys. Res.*, **95**, 3619–3634.
- Khalil, M. A., M. J. Shearer, and R. A. Rasmussen, 1999: Methane Sinks, Distribution and Trends. In: Khalil, M. A. K. (Ed.) *Atmospheric Methane: Its Role in the Global Environment*, Springer, Berlin, 86–97 pp.
- Kiese, R., B. Hewett, A. Graham, K. Butterbach-Bahl, 2003: Seasonal variability of N<sub>2</sub>O emissions and CH<sub>4</sub> uptake by tropical rainforest soils of Queensland, Australia *Glob. Biogeochem. Cycles*, **17**, 2,1043, doi:10.1029/2002GB002014.
- Kirchgessner, D. A., S. D. Pieeot, J. D. Winkler, 1993: Estimate of Global Methane Emissions from Coal Mines *Chemosphere*, **26**, 453–472.
- Knorr, W., 1997: Satellite remote sensing and modeling of the global CO<sub>2</sub> exchange of land vegetation: A synthesis study *Dissertation*, Max-Planck-Institut für Meteorologie, Hamburg, Germany.
- Kort, E. A., J. Eluszkiewicz, B. B. Stephens, J. B. Miller, C. Gerbig, T. Nehrkorn, B. C. Daube, J. O. Kaplan, S. Houweling, and S. C. Wofsy, 2008: Emissions of CH<sub>4</sub> and N<sub>2</sub>O over the United States and Canada based on a receptor-oriented modeling framework and COBRA-NA atmospheric observations *Geophys. Res. Lett.*, **35**, L18808, doi:10.1029/2008GL034031.
- Kozlova, E. A., A. C. Manning, Y. Kisilyakhov, T. Seifert, and M. Heimann, 2008: Seasonal, synoptic, and diurnal-scale variability of biogeochemical trace gases and O<sub>2</sub> from a 300 m tall tower in central Siberia *Glob. Biogeochem. Cycles*, **22**, GB4020, doi:10.1029/2008GB003209.
- Kretschmer, R., C. Gerbig, U. Karstens, and F.-T. Koch, 2012: Error characterization of CO<sub>2</sub> vertical mixing in the atmospheric transport model WRF-VPRM *Atmos. Chem. Phys.*, **12**, 2441–2458.
- Krol, M., S. Houweling, B. Bregman, M. van den Broek, A. Segers, P. van Velthoven, W. Peters, F. Dentener, and P. Bergamaschi, 2005: The two-way nested global chemistry-transport zoom model TM5: algorithm and applications *Atmos. Chem. Phys.*, **5**, 417–432.
- Kvovolden, K. A., T. D. Lorenson, 1993: Methane in Permafrost—Preliminary Results from Coring at Fairbanks, Alaska *Chemosphere*, **26**, 609–616.
- The Kyoto Protocol to the Framework Convention on Climate Change, 21 pp, available online at [http://unfccc.int/essential\\_background/kyoto\\_protocol/background/items/1351.php](http://unfccc.int/essential_background/kyoto_protocol/background/items/1351.php), 130 pp.
- Laing, A., J.-L. Evans, 2011: Introduction into Tropical Meteorology, A Comprehensive Online & Print Textbook, version 2.0, October 2011 available online at <http://meted.ucar.edu/>.
- Lambert, G. and S. Schmidt, 1993: Reevaluation of the oceanic flux of methane: uncertainties and long term variations *Chemosphere*, **26**, 579–589.
- Langenfelds, R. L., R. J. Francey, B. C. Pak, L. P. Steele, J. Lloyd, C. M. Trudinger, and C. E. Allison, 2002: Interannual growth rate variations of atmospheric CO<sub>2</sub> and its δ<sup>13</sup>C, H<sub>2</sub>, CH<sub>4</sub>, and CO between 1992 and 1999 linked to biomass burning *Glob. Biogeochem. Cycles*, **16**, 3,1048, doi:10.1029/2001GB001466.
- Lassey, K. R., M. J. Ulyatt, R. J. Martin, C. F. Walker and I. David Shelton, 1997: Methane Emissions measured directly from grazing Livestock in New Zealand *Atmos. Environm.*, **31**, 2905–2914.

- Lassey, K. R., D. M. Etheridge, D. C. Lowe, A. M. Smith, and D. F. Ferretti, 2007: Centennial evolution of the atmospheric methane budget: what do the carbon isotopes tell us? *Atmos. Chem. Phys.*, **7**, 2119–2139.
- Laubach, J., F. M. Kelliher, 2004: Measuring methane emission rates of a dairy cow herd by two micrometeorological techniques *Agricultural and Forest Meteorology*, **125**, 279–303.
- Laubach, J., F. M. Kelliher, 2005: Methane emissions from dairy cows: Comparing open-path laser measurements to profile-based techniques *Agricultural and Forest Meteorology*, **135**, 340–345.
- Lehner, B. and P. Döll, 2004: Development and validation of a global database of lakes, reservoirs and wetlands *J. Hydrology*, **296**, 1–22.
- Levine, J. S., W. R. Cofer III, and J. P. Pinto, 2000: Biomass Burning. In: Khalil, M. A. K. (Ed.) *Atmospheric Methane: Its Role in the Global Environment*, Springer, Berlin, 190–201 pp.
- Liebmann, B. and J. A. Marengo, 2001: Interannual Variability of the Rainy Season and Rainfall in the Brazilian Amazon Basin *J. Climate*, **14**, 4308–4318.
- Lin, J. C., C. Gerbig, S. C. Wofsy, A. E. Andrews, B. C. Daube, K. J. Davis, and C. A. Grainger, 2003: A near-field tool for simulating the upstream influence of atmospheric observations: The Stochastic Time-Inverted Lagrangian Transport (STILT) model *J. Geophys. Res.*, **108**, D16, 4493, doi:10.1029/2002JD003161.
- Lloyd, J., O. Kolle, H. Fritsch, S. R. de Freitas, M. A. F. Silva Dias, P. Artaxo, A. D. Nobre, A. C. de Araújo, B. Kruijt, L. Sogacheva, G. Fisch, A. Tielmann, U. Kuhn and M. O. Andreae, 2007: An airborne regional carbon balance for Central Amazonia *Biogeosciences*, **4**, 759–768.
- Longo, K. M., S. R. Freitas, M. O. Andreae, A. Setzer, E. Prins, and P. Artaxo, 2010: The coupled Aerosol and Tracer Transport Model to the Brazilian developments on the Regional Atmospheric Modeling System (CATT-BRAMS) - Part 2: Model sensitivity to the biomass burning inventories *Atmos. Chem. Phys.*, **10**, 5785–5795.
- Machida, T., H. Matsueda, Y. Sawa, Y. Nakagawa, K. Hirotani, N. Kondo, K. Goto, T. Nakazawa, K. Ishikawa, and T. Ogawa, 2008: Worldwide Measurements of Atmospheric CO<sub>2</sub> and Other Trace Gas Species Using Commercial Airlines *J. Atmos. Ocean. Tech.*, **25**, 1744–1754.
- Mahadevan, P., S. C. Wofsy, D. M. Matross, X. Xiao, A. L. Dunn, J. C. Lin, C. Gerbig, J. W. Munger, V. Y. Chow, and E. W. Gottlieb, 2008: A satellite-based biosphere parametrization for net ecosystem CO<sub>2</sub> exchange: Vegetation Photosynthesis and Respiration Model (VPRM) *Global Biogeochem. Cycles.*, **22**, GB2005, doi:10.1029/2006GB002735.
- Maltby, E., 2009: Functional Assessment of wetlands: Towards evaluation of ecosystem services *Woodhead Publishing Limited*, Cambridge, UK.
- Marengo, A., V. Tehouret, P. Nédélec, H. Smit, M. Helten, D. Kley, F. Karcher, P. Simon, K. Law, J. Pyle, G. Poschmann, R. von Wrede, C. Hume, and T. Cook, 1998: Measurement of ozone and water vapor by Airbus in-service aircraft: The MOZAIC airborne program, An overview *J. Geophys. Res.*, **103**, 25,631–25,642.
- Marengo, J. A., 2004: Interdecadal variability and trends of rainfall across the Amazon basin *Theor. Appl. Climatol.*, **78**, 79–96.
- Marengo, J. A., W. R. Soares, C. Saulo, and M. Nicolini, 2004: Climatology of the Low-Level Jet East of the Andes as Derived from the NCEP-NCAR Reanalyses: Characteristics and Temporal Variability *J. Climate*, **17**, 2261–2280.

- Marengo, J. A., 2007: Climate change and hydrological modes of the wet tropics In: Bush, M. B. and J. R. Flenley (Eds.) *Tropical Rainforest and Responses to Climate Change*, Springer, Berlin, 237–268 pp.
- Marengo, J. A., C. A. Nobre, J. Tomasella, M. D. Oyama, G. S. de Oliveira, R. de Oliveira, H. Camargo, L. M. Alves, and I. Foster Brown, 2008: The Drought of Amazonia in 2005 *J. Climate*, **21**, 495–516.
- Marquis, M., and P. Tans, 2008: Carbon Crucible *Science*, **320**, 460–461.
- Martinson, G. O., F. A. Werner, C. Scherber, R. Conrad, M. D. Corre, H. Flessa, K. Wolf, M. Klose, S. R. Gradstein, and E. Veldkamp, 2010: Methane emissions from tank bromeliads in neotropical forests *Nature Geosciences*, **3**, 766–769.
- Martius, C., R. Wassmann, U. Thein, A. Bandeira, H. Rennenberg, W. Junk, W. Seiler, 1993: Methane Emission from wood-feeding Termites in Amazonia *Chemosphere*, **26**, 623–632.
- Matsueda, H. and H. Y. Inoue, 1996: Measurements of Atmospheric CO<sub>2</sub> and CH<sub>4</sub> using a Commercial Airlines from 1993 to 1994 *Atmos. Environm.*, **30**, 1647–1655.
- Matthews, E., and I. Fung, 1987: Methane emissions from natural wetlands: Global distribution, area and environmental characteristics of sources *Global Biogeochem. Cycles.*, **1**, 61–86.
- Meirink, J. F., P. Bergamaschi, and M. C. Krol, 2008b: Four-dimensional variational data assimilation for inverse modeling of atmospheric methane emissions: method and comparison with synthesis inversion *Atmos. Chem. Phys.*, **8**, 6341–6353.
- Melack, J. M., 2009: Wetland ecology with a focus on the Amazon basin *Presentation at the tropical wetland workshop, NCGG5 Conference*, Wageningen.
- Melack, J. M., and L. L. Hess, 2011: Remote Sensing of the Distribution and Extent of Wetlands in the Amazon Basin. In: Junk, W. J., M. T. F. Piedade, F. Wittmann, J. Schöngart and P. Parolin (Eds.) *Amazonian Floodplain Forests Ecophysiology, Biodiversity and Sustainable Management*, *Ecological Studies* **210**, Springer, Berlin, 43–59 pp.
- Melack, J. M., L. L. Hess, M. Gastil, B. R. Forsberg, S. K. Hamilton, I. B. T. Lima and E. M. L. M. Novo, 2004: Regionalization of methane emissions in the Amazon Basin with microwave remote sensing *Global Change Biology*, **10**, 530–544.
- Messerschmidt, J., H. Chen, N. M. Deutscher, C. Gerbig, P. Grupe, K. Katrynski, F.-T. Koch, J. V. Lavrič, J. Notholt, C. Rödenbeck, W. Ruhe, T. Warneke, and C. Weinzierl, 2011a: Automated ground-based remote sensing measurements of greenhouse gases at the Bialystok site in comparison with collocated in-situ measurements and model data *Atmos. Chem. Phys. Discuss.*, **11**, 32245–32282.
- Messerschmidt, J., M. C. Geibel, T. Blumenstock, H. Chen, N. M. Deutscher, A. Engel, D. G. Feist, C. Gerbig, M. Gisi, F. Hase, K. Katrynski, O. Kolle, J. V. Lavrič, J. Notholt, M. Palm, M. Ramonet, M. Rettinger, M. Schmidt, R. Sussmann, G. C. Toon, F. Truong, T. Warneke, P. O. Wennberg, D. Wunch, and I. Xueref-Remy, 2011b: Calibration of TCCON column-averaged CO<sub>2</sub>: the first aircraft campaign over European TCCON sites *Atmos. Chem. Phys.*, **11**, 10765–10777.
- Michalak, A. M., L. Bruhwiler, and P. P. Tans, 2004: A geostatistical approach to surface flux estimation of atmospheric trace gases *J. Geophys. Res.*, **109**, D14109, doi:10.1029/2003JD004422.
- Michalakes, J., and D. Schaffer, 2004: WRF Tiger Team Documentation: The Registry, 17 pp. *NCAR/NOAA/FSL*, available online at [http://www.mmm.ucar.edu/wrf/WG2/software\\_2.0/registry\\_schaffer.pdf](http://www.mmm.ucar.edu/wrf/WG2/software_2.0/registry_schaffer.pdf),

- Michalakes, J., J. Dudhia, D. Gill, T. Henderson, J. Klemp, W. Skamarock, and W. Wang, 2005: The Weather Research and Forecast Model: Software Architecture and Performance. In: Zwiefelhofer, W. and G. Mozdzynski (Eds.) Proceedings of the Eleventh ECMWF Workshop on the Use of High Performance Computing in Meteorology, *World Scientific*, 156–168 pp.
- Mikaloff Fletcher, S. E., P. P. Tans, L. M. Bruhwiler, J. B. Miller, M. Heimann, 2004: CH<sub>4</sub> sources estimated from atmospheric observations of CH<sub>4</sub> and its <sup>13</sup>C/<sup>12</sup>C isotopic ratios: 2. Inverse modeling of CH<sub>4</sub> fluxes from geographical regions *Global Biogeochem. Cycles*, **18**, GB4005, doi:10.1029/2004GB002224.
- Miller, J. B., L. V. Gatti, M. T. S. d'Amelio, A. M. Crowell, E. J. Dlugokencky, P. Bakwin, P. Artaxo, and P. P. Tans, 2007: Airborne measurements indicate large methane emissions from the eastern Amazon basin *Geophys. Res. Lett.*, **34**, L10809, doi:10.1029/2006GL029213.
- Mlawer, E. J., S. J. Taubman, P. D. Brown, M. J. Iacono, and S. A. Clough, 1997: Radiative transfer for inhomogeneous atmospheres: RRTM, a validated correlated-k model for the longwave *J. Geophys. Res.*, **102**, D14, 16,663–16,682.
- Montzka, S. A., M. Krol, E. Dlugokencky, B. Hall, P. Jöckel, J. Lelieveld, 2011: Small Interannual Variability of Global Atmospheric Hydroxyl *Science*, **331**, 67–69.
- Morino, I., O. Uchino, M. Inoue, Y. Yoshida, T. Yokota, P. O. Wennberg, G. C. Toon, D. Wunch, C. M. Roehl, J. Notholt, T. Warneke, J. Messerschmidt, D. W. T. Griffith, N. M. Deutscher, V. Sherlock, B. Connor, J. Robinson, R. Sussmann, and M. Rettinger, 2011: Preliminary validation of column-averaged volume mixing ratios of carbon dioxide and methane retrieved from GOSAT short-wavelength infrared spectra *Atmos. Meas. Tech.*, **4**, 1061–1076.
- Nakanishi, M., H. Niino, 2004: An Improved Mellor-Yamada Level-3 Model with Condensation Physics: Its Design and Verification *Boundary-Layer Meteorology*, **112**, 1–31.
- Nehrkorn, T., J. Eluszkiewicz, S. C. Wofsy, J. C. Lin, C. Gerbig, M. Longo, S. Freitas, 2010: Coupled weather research and forecasting-stochastic time-inverted lagrangian transport (WRF-STILT) model *Meteorol. Atmos. Phys.*, **107**, 51–64.
- Nepstad, D., B. S. Soares-Filho, F. Merry, A. Lima, P. Moutinho, J. Carter, M. Bowman, A. Cattaneo, H. Rodrigues, S. Schwartzman, D. G. McGrath, C. M. Stickler, R. Lubowski, P. Piris-Cabezas, S. Rivero, A. Alencar, O. Almeida, O. Stella, 2009: The End of Deforestation in the Brazilian Amazon *Science*, **326**, 1350–1351.
- Nesbitt, S. W. and E. J. Zipser, 2003: The diurnal cycle of rainfall and convective intensity according to three years of TRMM measurements *J. Climate*, **16**, 1456–1475.
- Neue, H.-U. and P. A. Roger, 2000: Rice Agriculture: Factors Controlling Emissions. In: Khalil, M. A. K. (Ed.) Atmospheric Methane: Its Role in the Global Environment, *Springer*, Berlin, 134–169 pp.
- Nisbet, R. E. R., R. Fisher, R. H. Nimmo, D. S. Bendall, P. M. Crill, A. V. Gallego-Sala, E. R. C. Hornibrook, E. López-Juez, D. Lowry, P. B. R. Nisbet, E. F. Shuckburgh, S. Sriskantharajah, C. J. Howe and E. G. Nisbet, 2009: Emission of methane from plants *Proc. R. Soc. B*, **276**, 1347–1354.
- Nobre, C. A., G. Fisch, H. R. da Rocha, R. F. da F. Lyras, E. P. da Rocha, A. C. L. da Cosat, and V. N. Ubarana, 1996: Observations of the atmospheric boundary layer in Rondônia *Amazonian deforestation and climate*. Edited by J. H. C. Gash, C. A. Nobre, J. M. Roberts, and R. L. Victoria, Wiley.
- Norris, W. V. and H. J. Unger, 1933: Infrared Absorption Bands of Methane *Physical Review*, **43**, 467–472.
- Ojima, D. S., D. W. Valentine, A. R. Mosier, W. J. Parton, and D. S. Schimel, 1993: Effect of Land Use Change on Methane Oxidation in Temperate Forest and Grassland Soils *Chemosphere*, **26**, 675–685.

- Olivier, J. G. J., A. F. Bouwman, C. W. M. Van der Maas, J. J. M. Berdowski, C. Veldt, J. P. J. Bloos, A. J. H. Visschedijk, P. Y. J. Zandveld, J. L. Haverlag, 1996: Description of EDGAR Version 2.0: a set of global emission inventories of greenhouse gases and ozone depleting substances for all anthropogenic and most natural sources on a per country basis and on 18\_18 grid *RIVM Technical Report No. 771060 002, TNO-MEP Report No. R96/119, National Institute of Public Health and the Environment, Bilthoven/Netherlands Organisation for Applied Scientific Research, Apeldoorn.*
- Olivier, J. G. J., A. F. Bouwman, J. J. M. Berdowski, C. Veldt, J. P. J. Bloss, A. H. J. Visschedijk, C. W. M. van de Maas, and P. Y. J. Zandveld, 1999: Sectoral emission inventories of greenhouse gases for 1990 on per country basis as well as 10×10 *Environ. Sci. Policy*, **2**, 241–264.
- Olivier, J. G. J and J. J. M. Berdowski, 2001: Global emissions sources and sinks In Berdowski, J. J. M. et al. (Eds.) *The Climate System, A.A. Balkema, Lisse, Netherlands*, 33–78.
- Park, J. H., J. M. Russel, L. L. Gordley, S. R. Drayson, D. C. Benner, J. M. McInerney, M. R. Gunson, C. Toon, B. Sen, J.-F. Blavier, C. R. Webster, E. C. Zipf, P. Erdman, U. Schmidt, and C. Schiller, 1996: Validation of Halogen Occultation Experiment CH<sub>4</sub> measurements from the UARS *J. Geophys. Res.*, **101**, 10,183–10,203.
- Parker, R., H. Boesch, A. Cogan, A. Fraser, L. Feng, P. I. Palmer, J. Messerschmidt, N. Deutscher, D. W. T. Griffith, J. Notholt, P. O. Wennberg, and D. Wunch, 2011: Methane observations from the Greenhouse Gases Observing SATellite: Comparison to ground-based TCCON data and model calculations *Geophys. Res. Lett.*, **38**, L15807, doi:10.1029/2011GL047871.
- Patra, P., S. Houweling, M. Krol, P. Bousquet, L. Bruhwiler, D. Jacob, 2009: Protocol for TransCom CH<sub>4</sub> intercomparison version 6.2, 18 pp., available online via [http://www.jamstec.go.jp/frcgc/research/d4/prabir/papers/TC\\_CH4protocol\\_v6.2.pdf](http://www.jamstec.go.jp/frcgc/research/d4/prabir/papers/TC_CH4protocol_v6.2.pdf).
- Patra, P. K., S. Houweling, M. Krol, P. Bousquet, D. Belikov, D. Bergmann, H. Bian, P. Cameron-Smith, M. P. Chipperfield, K. Corbin, A. Fortems-Cheiney, A. Fraser, E. Gloor, P. Hess, A. Ito, S. R. Kawa, R. M. Law, Z. Loh, S. Maksyutov, L. Meng, P. I. Palmer, R. G. Prinn, M. Rigby, R. Saito, and C. Wilson, 2011: TransCom model simulations of CH<sub>4</sub> and related species: linking transport, surface flux and chemical loss with CH<sub>4</sub> variability in the troposphere and lower stratosphere *Atmos. Chem. Phys.*, **11**, 12813–12837.
- Peckham, S. E., G. A. Grell, S. A. McKeen, J. D. Fast, W. I. Gustafson, S. J. Ghan, R. Zaveri, R. C. Easter, J. Barnard, E. Chapman, C. Wiedinmyer, R. Schmitz, M. Salzmann, and S. R. Freitas, 2009: WRF/Chem Version 3.1 User's Guide, 82 pp.
- Pereira, L. G. and S. A. Rutledge, 2006: Diurnal Cycle of Shallow and Deep Convection for a Tropical Land and an Ocean Environment and Its Relationship to Synoptic Wind Regimes *Mon. Wea. Rev.*, **134**, 2688–2701.
- Peters, W., M. C. Krol, E. J. Dlugokencky, F. J. Dentener, P. Bergamaschi, G. Dutton, P. v. Velthoven, J. B. Miller, L. Bruhwiler, and P. P. Tans, 2004: Toward regional-scale modeling using the two-way nested global model TM5: Characterization of transport using SF<sub>6</sub> *J. Geophys. Res.*, **109**, D19314, doi:10.1029/2004JD005020.
- Petersen, A. K., T. Warneke, C. Frankenberg, P. Bergamaschi, C. Gerbig, J. Notholt, M. Buchwitz, O. Schneising, and O. Schrems, 2010: First ground-based FTIR observations of methane in the inner tropics over several years *Atmos. Chem. Phys.*, **10**, 7231–7239.
- Peterson, T. C. and D. R. Easterling, 1994: Creation of homogeneous composite climatological reference series *Int. J. of Climatology*, **14**, 671–679.



- Pétron, G., G. Frost, B. R. Miller, A. I. Hirsch, S. A. Montzka, A. Karion, M. Trainer, C. Sweeney, A. E. Andrews, L. Miller, J. Kofler, A. Bar-Ilan, E. J. Dlugokencky, L. Patrick, C. T. Moore Jr., T. B. Ryerson, C. Siso, W. Kolodzey, P. M. Lang, T. Conway, P. Novelli, K. Masarie, B. Hall, D. Guenther, D. Kitzis, J. Miller, D. Welsh, D. Wolfe, W. Neff, and P. Tans, 2012: Hydrocarbon emissions characterization in the Colorado Front Range: A pilot study *J. Geophys. Res.*, **117**, D04304, doi:10.1029/2011JD016360.
- Pickett-Heaps, C. A., D. J. Jacob, K. J. Wecht, E. A. Kort, S. C. Wofsy, G. S. Diskin, D. E. J. Worthy, J. O. Kaplan, I. Bey, and J. Drevet, 2011: Magnitude and seasonality of wetland methane emissions from the Hudson Bay Lowlands (Canada) *Atmos. Chem. Phys.*, **11**, 3773–3779.
- Pillai, D., 2011: Mesoscale simulations and inversions of atmospheric CO<sub>2</sub> using airborne and ground-based data *Dissertation*, Friedrich-Schiller Universität Jena, 191 pp.
- Pillai, D., C. Gerbig, J. Marshall, R. Ahmadov, R. Kretschmer, T. Koch, and U. Karstens, 2010: High resolution modeling of CO<sub>2</sub> over Europe: implications of representation errors of satellite retrievals *Atmos. Chem. Phys.*, **10**, 83–94.
- Pillai, D., C. Gerbig, R. Ahmadov, C. Rödenbeck, R. Kretschmer, T. Koch, R. Thompson, B. Neininger, and J. V. Lavrič, 2011: High-resolution simulations of atmospheric CO<sub>2</sub> over complex terrain - representing the Ochsenkopf mountain tall tower *Atmos. Chem. Phys.*, **11**, 7445–7464.
- Pillai, D., C. Gerbig, R. Kretschmer, V. Beck, U. Karstens, B. Neininger, and M. Heimann, 2012: Comparing Lagrangian and Eulerian models for CO<sub>2</sub> transport - a step towards Bayesian inverse modeling using WRF/STILT-VPRM *Atmos. Chem. Phys. Discuss.*, **12**, 1267–1298.
- Popa, M. E., M. Gloor, A. C. Manning, A. Jordan, U. Schultz, F. Haensel, T. Seifert, and M. Heimann, 2010: Measurements of greenhouse gases and related tracers at Bialystok tall tower station in Poland *Atmos. Meas. Tech.*, **3**, 407–427.
- Prigent, C., E. Matthews, F. Aires, and W. B. Rossow, 2001a: Remote sensing of global wetland dynamics with multiple satellite data sets *Geophys. Res. Lett.*, **28**, 4631–4634.
- Prigent, C., F. Aires, E. Matthews, and W. Rossow, 2001b: Joint characterization of vegetation by satellite observations from visible to microwave wavelengths: A sensitivity analysis *J. Geophys. Res.*, **106**, 20,665–20,685.
- Prigent, C., F. Papa, F. Aires, W. B. Rossow, and E. Matthews, 2007: Global inundation dynamics inferred from multiple satellite observations, 1993–2000 *J. Geophys. Res.*, **112**, D12107, doi:10.1029/2006JD007847.
- Prigent C., F. Papa, F. Aires, C. Jimenez, W. B. Rossow, and E. Matthews, 2012: Changes in land surface water dynamics since the 1990s and relation to population pressure *Geophys. Res. Lett.*, **39**, L08403, doi:10.1029/2012GL051276.
- Prinn, R. G., R. F. Weiss, P. J. Fraser, P. G. Simmonds, D. M. Cunnold, F. N. Alyea, S. O'Doherty, P. Salameh, B. R. Miller, J. Huang, R. H. J. Wang, D. E. Hartley, C. Harth, L. P. Steele, G. Sturrock, P. M. Midgley, and A. McCulloch, 2000: A history of chemically and radiatively important gases in air deduced from ALE/GAGE/AGAGE *J. Geophys. Res.*, **105**, 17,751–17,792.
- Prins, E. M., J. M. Feltz, W. P. Menzel, D. E. Ward, 1998: An overview of GOES-8 diurnal fire and smoke results for SCAR-B and 1995 fire season in South America *J. Geophys. Res.*, **103**, 31,821–31,835.
- Quay P., J. Stutsman, D. Wilbur, A. Snover, E. Dlugokenchy, and T. Brown, 1999: The isotopic composition of atmospheric methane *Global Biogeochem. Cycles*, **13**, 445–461.



- Querino C. A. S., C. J. P. P. Smeets, I. Vigano, R. Holzinger, V. Moura, L. V. Gatti, A. Martinewski, A. O. Manzi, A. C. de Araújo, and T. Röckmann, 2011: Methane flux, vertical gradient and mixing ratio measurements in a tropical forest *Atmos. Chem. Phys.*, **11**, 7943–7953.
- Raich, J. W., E. B. Rastetter, J. M. Melillo, D. W. Kicklighter, P. A. Steudler, B. J. Peterson, A. L. Grace, B. Moore III, C. J. Vorosmarty, 1999: Potential Net Primary Productivity in South America: Application of a Global Model *Ecol. Applic.*, **1**, 399–429.
- Rayner, P. J., M. Scholze, W. Knorr, T. Kaminski, R. Giering, and H. Widmann, 2005: Two decades of terrestrial carbon fluxes from a carbon cycle data assimilation system (CCDAS) *Glob. Biogeochem. Cycles*, **19**, GB2026, doi:10.1029/2004GB002254.
- Ridgwell, A. J., S. J. Marshall, and K. Gregson, 1999: Consumption of atmospheric methane by soils: A process-based model *Global Biochem. Cycles*, **13**, 59–70.
- Rigby, M., R. G. Prinn, P. J. Fraser, P. G. Simmonds, R. L. Langenfelds, J. Huang, D. M. Cunnold, L. P. Steele, P. B. Krummel, R. F. Weiss, S. O'Doherty, P. K. Salameh, H. J. Wang, C. M. Harth, J. Mühle, and L. W. Porter, 2008: Renewed growth of atmospheric methane *Geophys. Res. Lett.*, **35**, L22805, doi:10.1029/2008GL036037.
- Rinne, J., T. Riutta, M. Pihlatie, M. Aurela, S. Haapanala, J.-P. Tuovinen, E.-S. Tuitilla and T. Vesala, 2007: Annual cycle of methane emission from a boreal fen measured by the eddy covariance technique *Tellus B*, **59**, 449–457.
- Röckmann, T., M. Brass, R. Borchers, and A. Engel, 2011: The isotopic composition of methane in the stratosphere: high-altitude balloon sample measurements *Atmos. Chem. Phys.*, **11**, 13287–13304.
- Rödenbeck, C., 2005: Estimating CO<sub>2</sub> sources and sinks from atmospheric mixing ratio measurements using a global inversion of atmospheric transport *Technical Report 6*, Max Planck Institute for Biogeochemistry, Jena, Germany, 61 pp., available online at <http://www.bgc-jena.mpg.de/bgc-systems/index.shtml>
- Rödenbeck, C., S. Houweling, M. Gloor, and M. Heimann, 2003: CO<sub>2</sub> flux history 1982–2001 inferred from atmospheric data using a global inversion of atmospheric transport *Atmos. Chem. Phys.*, **3**, 1919–1964.
- Rödenbeck, C., C. Gerbig, K. Trusilova, and M. Heimann, 2009: A two-step scheme for high-resolution regional atmospheric trace gas inversions based on independent models *Atmos. Chem. Phys.*, **9**, 5331–5342.
- Romanovsky, V., M. Burgess, S. Smith, K. Yoshikawa, J. Brown, 2002: Permafrost Temperature Records: Indicators of Climate Change *Eos Trans AGU*, **83**, 598–600.
- Ruppel, C. D., 2011: Methane Hydrates and Contemporary Climate Change *Nature Education Knowledge*, 2(12):12.
- Sanderson, M. G., 1996: Biomass of termites and their emissions of methane and carbon dioxide: A global database *Global Biochem. Cycles*, **10**, 543–557.
- dos Santos, M. A., B. Matvienko, L. P. Rosa, E. Sikar, E. O. dos Santos, 2005: Gross Greenhouse Gas Emissions from Brazilian Hydro Reservoirs. In: Tremblay, A., L. Varfalvy, C. Roehm, M. Garneau (Eds.) *Greenhouse Gas Emissions - Fluxes and Processes Hydroelectric Reservoirs and Natural Environments Springer*, Berlin, 267–291 pp.

- Sarrat, C., J. Noilhan, P. Lacarrère, E. Ceschia, P. Ciais, A. J. Dolman, J. A. Elbers, C. Gerbig, B. Gioli, T. Lauvaux, F. Miglietta, B. Neininger, M. Ramonet, O. Vellinga, and J. M. Bonnefond, 2009: Mesoscale modeling of the CO<sub>2</sub> interactions between the surface and the atmosphere applied to the April 2007 CERES field experiment *Biogeosciences*, **6**, 633–646.
- Sass R. L., F. M. Fisher, and Y. B. Wang, 1992: Methane Emission from Rice Fields: The Effect of Floodwater Management *Glob. Biogeochem. Cycles*, **6**, 249–262.
- Schaefer, K., T. Zhang, L. Bruhwiler, and A. P. Barrett, 2011: Amount and timing of permafrost carbon release in response to climate warming *Tellus B*, **63**, 165–180.
- Schlesinger, W. H., 1997: Biogeochemistry: an analysis of global change *Academic Press*, San Diego, California.
- Schneising, O., M. Buchwitz, M. Reuter, J. Heymann, H. Bovensmann, and J. P. Burrows, 2011: Long-term analysis of carbon dioxide and methane column-averaged mole fractions retrieved from SCIAMACHY *Atmos. Chem. Phys.*, **11**, 2863–2880.
- Schneising, O., P. Bergamaschi, H. Bovensmann, M. Buchwitz, J. P. Burrows, N. M. Deutscher, D. W. T. Griffith, J. Heymann, R. Macatangay, J. Messerschmidt, J. Notholt, M. Rettinger, M. Reuter, R. Sussmann, V. A. Velasco, T. Warneke, P. O. Wennberg, and D. Wunch, 2012: Atmospheric greenhouse gases retrieved from SCIAMACHY: comparison to ground-based FTS measurements and model results *Atmos. Chem. Phys.*, **12**, 1527–1540.
- Schönwiese, C.-D., 2000: Praktische Statistik für Meteorologen und Geowissenschaftler, 3. Auflage *Gebrüder Borntraeger*, Stuttgart, Germany.
- Schuck, T. J., C. A. M. Brenninkmeijer, F. Slemr, I. Xueref-Remy, and A. Zahn, 2009: Greenhouse gas analysis of air samples collected onboard the CARIBIC passenger aircraft *Atmos. Meas. Tech.*, **2**, 449–464.
- Schulze, E. D., P. Ciais, S. Luyssaert, M. Schrumpf, I. A. Janssen, B. Thiruchuttampalam, J. Theloke, M. Saurat, S. Bringezu, J. Lelieveld, A. Lohila, C. Rebmann, M. Jung, D. Bastviken, G. Abril, G. Grassi, A. Leip, A. Freibauer, W. Kutsch, A. Don, J. Nieschulze, A. Börner, J. H. Gash, and A. J. Dolman, 2010: The European carbon balance. Part 4: integration of carbon and other trace-gas fluxes *Global Change Biology*, **16**, 1451–1469.
- Schütz, H., W. Seiler, R. Conrad, 1989: Processes involved in formation and emission of methane in rice paddies *Biogeochemistry*, **7**, 33–53.
- Schuur, E. A. G., J. Bockheim, J. G. Canadell, E. Euskirchen, C. B. Field, S. V. Goryachkin, S. Hagemann, P. Kuhry, P. M. Lafleur, H. Lee, G. Mazhitova, F. E. Nelson, A. Rinke, V. E. Romanovsky, N. Shiklomanov, C. Tarnocai, S. Venevsky, J. G. Vogel, and S. A. Zimov, 2008: Vulnerability of Permafrost Carbon to Climate Change: Implications for the Global Carbon Cycle *BioScience*, **58**(8), 701–714.
- Sebacher, D. I. and R. C. Harriss, 1982: A System for Measuring Methane Fluxes from Inland and Coastal Wetland Environments *J. Environ. Qual.*, **11**, 34–37.
- Seiler W., J. P. Crutzen, 1984: Estimates of Gross and Net Fluxes of Carbon between the Biosphere and the Atmosphere from Biomass Burning *Climatic Change*, **2**, 207–247.
- Seiler W., R. Conrad, and D. Scharffe, 1984: Field Studies of Methane Emission from Termite Nests into the Atmosphere and Measurements of Methane Uptake by Tropical Soils *J. Atmos. Chem.* **1**, 171–186.
- Setzer, A. W., M. C. Pereira, A. C. Pereira, 1997: Satellite studies of biomass burning in Amazonia - some practical aspects *Remote Sensing Reviews*, **10**, 91–103.

- Shakhova, N., I. Semiletov, A. Salyuk, V. Yusupov, D. Kosmach, Ö. Gustafsson, 2010: Extensive Methane Venting to the Atmosphere from Sediments of the East Siberian Arctic Shelf *Science*, **327**, 1246–1250.
- Shearer, M. J., M. A. K. Khalil, 2000: Rice Agriculture: Emissions. In: Khalil, M. A. K. (Ed.) *Atmospheric Methane: Its Role in the Global Environment*, Springer, Berlin, 170–189 pp.
- Singh, J. S., S. Singh, A. S. Raghubanshi, S. Singh, A. K. Kashyap and V. S. Reddy, 1997: Effect of soil nitrogen, carbon and moisture on methane uptake by dry tropical forest soils *Plant and Soil*, **196**, 115–121.
- Sippel, S. J., S. K. Hamilton, J. M. Melack, and E. M. M. Novo, 1998: Passive microwave observations of inundation area and the area/stage relation in the Amazon River floodplain *Int. J. Remote Sensing*, **19**, 3055–3074.
- Sitch, S., B. Smith, I. C. Prentice, A. Arneth, A. Bondeau, W. Cramer, J. O. Kaplan, S. Levis, W. Lucht, M. T. Sykes, K. T. Honicke, and S. Venevsky, 2003: Evaluation of ecosystem dynamics, plant geography and terrestrial carbon cycling in the LPJ dynamic global vegetation model *Global Change Biology*, **9**, 161–185.
- Skamarock, W. C., J. B. Klemp, J. Dudhia, D. O. Gill, D. M. Barker, M. G. Duda, X.-Y. Huang, W. Wang and J. G. Powers, 2008: A Description of the Advanced Research WRF Version 3, Tech. Note, NCAR/TN-475+STR, National Center for Atmos. Research, Boulder, Colorado, USA, 113 pp.
- Smeets, C. J. P. P., R. Holzinger, I. Vigano, A. H. Goldstein, and T. Röckmann, 2009: Eddy covariance methane measurements at a Ponderosa pine plantation in California *Atmos. Chem. Phys.*, **9**, 8365–8375.
- Smith, K. A., K. E. Dobbie, B. C. Ball, L. R. Bakken, B. K. Sitaula, S. Hansen, R. Brumme, W. Borken, S. Christensen, A. Priemé, D. Fowler, J. A. MacDonald, U. Skiba, L. Klemmedtsson, A. Kasimir-Klemmedtsson, A. Degórska, P. Orlanski, 2000: Oxidation of atmospheric methane in Northern European soils, comparisons with other ecosystems, and uncertainties in the global terrestrial sink *Global Change Biology*, **6**, 791–803.
- Snover, A. K., P. D. Quay, and W. M. Hao, 2000: The D/H content of methane emitted from biomass burning *Global Biochem. Cycles*, **14**, 11–24.
- Solomon, E. A., M. Kastner, I. R. MacDonald, I. Leifer, 2009: Considerable methane fluxes to the atmosphere from hydrocarbon seeps in the Gulf of Mexico *Nature Geoscience*, **2**, 561–565.
- Spahni, R., J. Chappellaz, T. F. Stocker, L. Loulergue, G. Hausammann, K. Kawamura, J. Flückiger, J. Schwander, D. Raynaud, V. Masson-Delmotte, J. Jouzel, 2005: Atmospheric Methane and Nitrous Oxide of the Late Pleistocene from Antarctic Ice Cores *Science*, **310**, 1317–1321.
- Spahni, R., R. Wania, L. Neef, M. van Weele, I. Pison, P. Bousquet, C. Frankenberg, P. N. Foster, F. Joos, I. C. Prentice, and P. van Velthoven, 2011: Constraining global methane emissions and uptake by ecosystems *Biogeosciences*, **8**, 1643–1665.
- Spivakovski, C. M., J. A. Logan, S. A. Montzka, Y. J. Balkanski, M. Forman-Fowler, D. B. A. Jones, L. W. Horowitz, A. C. Fusco, C. A. M. Brenninkmeijer, M. J. Prather, S. C. Wofsy, and M. B. McElroy, 2000: Three-dimensional climatological distribution of tropospheric OH: Update and evaluation *J. Geophys. Res.*, **105**, 8931–8980.
- Stedler, P. A., R. D. Bowden, J. M. Melillo, and J. D. Aber, 1989: Influence of nitrogen fertilization on methane uptake in temperate forest soils *Nature*, **341**, 314–316.
- Stedler, P. A., J. M. Melillo, B. J. Feigl, C. Neill, M. C. Piccolo, and C. C. Cerri, 1996: Consequence of forest-to-pasture conversion on CH<sub>4</sub> fluxes in the Brazilian Amazon Basin *J. Geophys. Res.*, **101**, 18,547–18,554.

- Stevens, C. M. and M. Wahlen, 2000: The Isotopic Composition of Atmospheric Methane and Its Sources. In: Khalil, M. A. K. (Ed.) *Atmospheric Methane: Its Role in the Global Environment*, Springer, Berlin, 25–41 pp.
- Stohl, A., 1998: Computation, Accuracy and Applications of Trajectories - a Review and Bibliography *Atmos. Environm.*, **32**, 947–966.
- Stohl, A., G. Wotawa, 1995: A Method for Computing Single Trajectories Representing Boundary Layer Transport *Atmos. Environm.*, **29**, 3235–3238.
- Stohl, A., C. Forster, A. Frank, P. Seibert, and G. Wotawa, 2005: Technical note: The Lagrangian particle dispersion model FLEXPART version 6.2 *Atmos. Chem. Phys.*, **5**, 2461–2474.
- von Storch, H. and F. W. Zwiers, 1999: *Statistical Analysis in Climate Research* Cambridge University Press, Cambridge, UK.
- Striegl, R. G., 1993: Diffusional Limits to the Consumption of Atmospheric Methane by Soils *Chemosphere*, **26**, 715–720.
- Stull, R. B., 1988: *An Introduction to Boundary Layer Meteorology* Kluwer Academic Publishers, Norwell, MA.
- Sussmann, R., W. Stremme, M. Buchwitz, and R. de Beek, 2005: Validation of ENVISAT/SCIAMACHY columnar methane by solar FTIR spectrometry at the Ground-Truthing Station Zugspitze *Atmos. Chem. Phys.*, **5**, 2419–2429.
- Takahashi, T., S. C. Sutherland, R. Wanninkhof, C. Sweeney, R. A. Feely, D. W. Chipman, B. Hales, G. Friederich, F. Chavez, A. Watson, D. C. E. Bakker, U. Schuster, N. Metzl, H. Yoshikawa-Inoue, M. Ishii, T. Midorikawa, Y. Nojiri, C. Sabine, J. Olafsson, T. S. Arnarson, B. Tilbrook, T. Johannessen, A. Olsen, Richard Bellerby, A. Körtzinger, T. Steinhoff, M. Hoppema, H. J. W. de Baar, C. S. Wong, B. Delille, and N. R. Bates, 2009: Climatological mean and decadal changes in surface ocean pCO<sub>2</sub>, and net sea-air CO<sub>2</sub> flux over the global oceans *Deep-Sea Res. II*, **56**, 554–577.
- Tarnocai, C., J. G. Canadell, E. A. G. Schuur, P. Kuhry, G. Mazhitova, and S. Zimov, 2009: Soil organic carbon pools in the northern circumpolar permafrost region *Global Biogeochem. Cycles*, **23**, doi:10.1029/2008GB003327.
- Taylor, K. E., 2001: Summarizing multiple aspects of model performance in a single diagram *J. Geophys. Res.*, **116**, 7183–7192.
- Teh, Y. A., W. L. Silver, O. Sonnentag, M. Detto, M. Kelly, and D. D. Baldocchi, 2011: Large Greenhouse Gas Emissions from a Temperate Peatland Pasture *Ecosystems*, **14**, 311–325.
- Thompson, R. L., A. C. Manning, E. Gloor, U. Schultz, T. Seifert, F. Hänsel, A. Jordan, and M. Heimann, 2009: In-situ measurements of oxygen, carbon monoxide and greenhouse gases from Ochsenkopf tall tower in Germany *Atmos. Meas. Tech.*, **2**, 573–591.
- Trenberth, K. E., 1984: Signal versus Noise in the Southern Oscillation *Mon. Wea. Rev.*, **112**, 326–332.
- Trusilova, K., C. Rödenbeck, C. Gerbig, and M. Heimann, 2010: Technical Note: A new coupled system for global-to-regional downscaling of CO<sub>2</sub> concentration estimation *Atmos. Chem. Phys.*, **10**, 3205–3213.
- U. S. Environmental Protection Agency, 2006: *Global Mitigation of Non-CO<sub>2</sub> Greenhouse Gases Report No. EPA/430-R-06-005*, Office of Atmospheric Programs, Washington D. C., 438 pp., available online at <http://www.epa.gov/climatechange/economics/downloads/GlobalMitigationFullReport.pdf>.

- van der Werf, G. R., J. T. Randerson, G. J. Collatz, L. Giglio, P. S. Kasibhatla, A. F. Arellano Jr., S. C. Olsen, E. S. Kasischke, 2004: Continental-Scale Partitioning of Fire Emissions during the 1997 to 2001 El Niño/La Niña Period *Science*, **303**, 73–76.
- van der Werf, G. R., J. T. Randerson, L. Giglio, G. J. Collatz, M. Mu, P. S. Kasibhatla, D. C. Morton, R. S. DeFries, Y. Jin, and T. T. van Leeuwen, 2010: Global fire emissions and the contribution of deforestation, savanna, forest, agricultural, and peat fires (1997–2009) *Atmos. Chem. Phys.*, **10**, 11707–11735.
- Verchot, L. V., E. A. Davidson, J. H. Cattânio, and I. L. Ackerman, 2000: Land-Use Change and Biogeochemical Controls of Methane Fluxes in Soils of Eastern Amazonia *Ecosystems*, **3**(25), 41–56.
- Verma, S. B., F. G. Ullman, D. Billesbach, R. J. Clement, J. Kim, E. S. Verry, 1992: Eddy Correlation Measurements of Methane Flux in a Northern Peatland Ecosystem *Boundary-Layer Meteorology*, **58**, 289–304.
- Vermeulen, A. T., 2007: CHIOTTO Final Report *ECN Energy research Centre of the Netherlands*, 116 pp., available online at <http://www.ecn.nl/docs/library/report/2007/e07052.pdf>.
- Vermeulen, A. T., R. Eismaa, A. Hensen, J. Slanina, 1999: Transport model calculations of NW-European methane emissions *Environmental Science & Policy*, **2**, 315–324.
- Vigano, I., H. van Weelden, R. Holzinger, F. Keppler, A. McLeod, and T. Röckmann, 2008: Effect of UV radiation and temperature on the emission of methane from plant biomass and structural components *Biogeosciences*, **5**, 937–947.
- Villani, M. G., P. Bergamaschi, M. Krol, J. F. Meirink, and F. Dentener, 2010: Inverse modeling of European CH<sub>4</sub> emissions: sensitivity to the observational network *Atmos. Chem. Phys.*, **10**, 1249–1267.
- Volz-Thomas, A., J.-P. Cammas, C. A. M. Brenninkmeijer, T. Machida, O. Cooper, C. Sweeney, A. Waibel, 2009: Civil Aviation Monitors Air Quality and Climate *Em Magazine, Air and Waste Management Association*, 16–19 pp, available online at [http://www.iagos.org/lw\\_resource/datapool/IAGOS-EM-Magazine.pdf](http://www.iagos.org/lw_resource/datapool/IAGOS-EM-Magazine.pdf).
- Walter, B. P., M. Heimann, R. D. Shannon, J. R. White, 1996: A process-based model to derive methane emissions from natural wetlands *Geophys. Res. Lett.*, **23**, 3731–3734.
- Walter, B. P. and M. Heimann, 2000: A process-based, climate-sensitive model to derive methane emissions from natural wetlands: Application to five wetland sites, sensitivity to model parameters, and climate *Global Biochem. Cycles*, **14**, 745–765.
- Walter, B. P., M. Heimann, and E. Matthews, 2001a: Modeling modern methane emissions from natural wetlands 1. Model description and results *J. Geophys. Res.*, **106**, 34,189–34,206.
- Walter, B. P., M. Heimann, and E. Matthews, 2001b: Modeling modern methane emissions from natural wetlands 2. Interannual variations 1982–1993 *J. Geophys. Res.*, **106**, 34,207–34,219.
- Walter, K. M., S. A. Zimov, J. P. Chanton, D. Verbyla, F. S. Chapin III, 2006: Methane bubbling from Siberian thaw lakes as a positive feedback to climate warming *Nature*, **443**, 71–75.
- Wania, R., 2007: Modeling northern peatland land surface processes, vegetation dynamics and methane emissions *Dissertation*, University of Bristol, 122 pp.
- Ward, D. E., R. A. Susott, J. B. Kauffman, R. E. Babbitt, D. L. Cummings, B. Dias, B. N. Holben, Y. J. Kaufman, R. A. Rasmussen, and A. W. Setzer, 1992: Smoke and Fire Characteristics for Cerrado and Deforestation Burns in Brazil: BASE-B Experiment *J. Geophys. Res.*, **97**, 14,601–14,619.



- Wassmann, R., H. Papen and H. Rennenberg, 1993: Methane Emission from Rice Paddies and Possible Mitigation Strategies *Chemosphere*, **26**, 201–217.
- Wassmann, R., U. G. Thein, M. J. Whiticar, H. Rennenberg, W. Seiler, and W. J. Junk, 1992: Methane Emissions from the Amazon Floodplain: Characterization of Production and Transport *Glob. Biogeochem. Cycles*, **6**, 3–13.
- Wecht, K. J., D. J. Jacob, S. C. Wofsy, E. A. Kort, J. R. Worden, S. S. Kulawik, D. K. Henze, M. Kopacz, and V. H. Payne, 2012: Validation of TES methane with HIPPO aircraft observations: implications for inverse modeling of methane sources *Atmos. Chem. Phys.*, **12**, 1823–1832.
- Whiticar, M. J., 1999: Carbon and hydrogen isotope systematics of bacterial formation and oxidation of methane *Chemical Geology*, **161**, 291–314.
- Whiting, G. J. and J. P. Chanton, 1993: Primary production control of methane emission from wetlands *Nature*, **364**, 794 – 795.
- Winderlich, J., 2011: Setup of a CO<sub>2</sub> and CH<sub>4</sub> measurement system in Central Siberia and modeling of its results *Dissertation*, Universität Hamburg, 125 pp.
- Winderlich, J., H. Chen, C. Gerbig, T. Seifert, O. Kolle, J. V. Lavrič, C. Kaiser, A. Höfer, and M. Heimann, 2010: Continuous low-maintenance CO<sub>2</sub>/CH<sub>4</sub>/H<sub>2</sub>O measurements at the Zotino Tall Tower Observatory (ZOTTO) in Central Siberia *Atmos. Meas. Tech.*, **3**, 1113–1128.
- Wofsy, S. C., 2011: HIAPER Pole-to-Pole Observations (HIPPO): fine-grained, global-scale measurements of climatically important atmospheric gases and aerosols *Phil. Trans. R. Soc. A*, **369**, 2073–2086.
- Wolter, K. and M. S. Timlin, 2011: El Niño/Southern Oscillation behaviour since 1871 as diagnosed in an extended multivariate ENSO index (MEI.ext) *Intl. J. Climatology*, **31**, DOI: 10.1002/joc.2336.
- Worthy, D. E. J., I. Levin, F. Hopper, M. K. Ernst, and N. B. A. Trivett, 2000: Evidence for a link between climate and northern wetland methane emissions *J. Geophys. Res.*, **105**, 4031–4038.
- Wuebbles, D. J. and K. Hayhoe, 2002: Atmospheric methane and global change *Earth-Science Reviews*, **57**, 177–210.
- Xiong, X., C. Barnet, E. Maddy, C. Sweeney, X. Liu, L. Zhou, and M. Goldberg, 2008: Characterization and validation of methane products from the Atmospheric Infrared Sounder (AIRS) *J. Geophys. Res.*, **113**, G00A01, doi:10.1029/2007JG000500.
- Yokelson, R. J., T. Karl, P. Artaxo, D. R. Blake, T. J. Christian, D. W. T. Griffith, A. Guenther, and W. M. Hao, 2007: The Tropical Forest and Fire Emission Experiment: overview and airborne fire emission factor measurements *Atmos. Chem. Phys.*, **7**, 5175–5196.
- Zahn, A., C. A. M. Brenninkmeijer, and P. F. J. van Velthoven, 2004a: Passenger aircraft project CARIBIC 1997–2002, Part I: the extratropical chemical tropopause *Atmos. Chem. Phys. Discuss.*, **4**, 1091–1117.
- Zahn, A., C. A. M. Brenninkmeijer, and P. F. J. van Velthoven, 2004b: Passenger aircraft project CARIBIC 1997–2002, Part II: the ventilation of the lowermost stratosphere *Atmos. Chem. Phys. Discuss.*, **4**, 1119–1150.
- Zhao, C., A. E. Andrews, L. Bianco, J. Eluszkiewicz, A. Hirsch, C. MacDonald, T. Nehrkorn, and M. L. Fischer, 2009: Atmospheric inverse estimates of methane emissions from Central California *J. Geophys. Res.*, **114**, D16302, doi:10.1029/2008JD011671.